UNCLASSIFIED

AD NUMBER

ADB283958

NEW LIMITATION CHANGE

TO

Approved for public release, distribution unlimited

FROM

Distribution authorized to U.S. Gov't. agencies only; Proprietary Info.; Aug 2002. Other requests shall be referred to US Army Medical Research and Materiel Comd., 504 Scott St., Fort Detrick, MD 21702-5012.

AUTHORITY

USAMRMC ltr, dtd 15 May 2003

THIS PAGE IS UNCLASSIFIED

AD______________

Award Number: DAMD17-99-1-9475

TITLE: Tissue Engineering Initiative

PRINCIPAL INVESTIGATOR: Vincent C. Hascall, Ph.D.

CONTRACTING ORGANIZATION: The Cleveland Clinic Foundation
Cleveland, Ohio 44195

REPORT DATE: August 2002

TYPE OF REPORT: Final

PREPARED FOR: U.S. Army Medical Research and Materiel Command
Fort Detrick, Maryland 21702-5012

DISTRIBUTION STATEMENT: Distribution authorized to U.S. Government agencies only (proprietary information, Aug 02). Other requests for this document shall be referred to U.S. Army Medical Research and Materiel Command, 504 Scott Street, Fort Detrick, Maryland 21702-5012.

The views, opinions and/or findings contained in this report are those of the author(s) and should not be construed as an official Department of the Army position, policy or decision unless so designated by other documentation.

20021114 248

NOTICE

USING GOVERNMENT DRAWINGS, SPECIFICATIONS, OR OTHER DATA INCLUDED IN THIS DOCUMENT FOR ANY PURPOSE OTHER THAN GOVERNMENT PROCUREMENT DOES NOT IN ANY WAY OBLIGATE THE U.S. GOVERNMENT. THE FACT THAT THE GOVERNMENT FORMULATED OR SUPPLIED THE DRAWINGS, SPECIFICATIONS, OR OTHER DATA DOES NOT LICENSE THE HOLDER OR ANY OTHER PERSON OR CORPORATION; OR CONVEY ANY RIGHTS OR PERMISSION TO MANUFACTURE, USE, OR SELL ANY PATENTED INVENTION THAT MAY RELATE TO THEM.

LIMITED RIGHTS LEGEND

Award Number: DAMD17-99-1-9475
Organization: The Cleveland Clinic Foundation

Those portions of the technical data contained in this report marked as limited rights data shall not, without the written permission of the above contractor, be (a) released or disclosed outside the government, (b) used by the Government for manufacture or, in the case of computer software documentation, for preparing the same or similar computer software, or (c) used by a party other than the Government, except that the Government may release or disclose technical data to persons outside the Government, or permit the use of technical data by such persons, if (i) such release, disclosure, or use is necessary for emergency repair or overhaul or (ii) is a release or disclosure of technical data (other than detailed manufacturing or process data) to, or use of such data by, a foreign government that is in the interest of the Government and is required for evaluational or informational purposes, provided in either case that such release, disclosure or use is made subject to a prohibition that the person to whom the data is released or disclosed may not further use, release or disclose such data, and the contractor or subcontractor or subcontractor asserting the restriction is notified of such release, disclosure or use. This legend, together with the indications of the portions of this data which are subject to such limitations, shall be included on any reproduction hereof which includes any part of the portions subject to such limitations.

THIS TECHNICAL REPORT HAS BEEN REVIEWED AND IS APPROVED FOR PUBLICATION.

Reproduced From
Best Available Copy

Copies Furnished to DTIC
Reproduced From
Bound Originals

REPORT DOCUMENTATION PAGE

Form Approved
OMB No. 074-0188

Public reporting burden for this collection of information is estimated to average 1 hour per response, including the time for reviewing instructions, searching existing data sources, gathering and maintaining the data needed, and completing and reviewing this collection of information. Send comments regarding this burden estimate or any other aspect of this collection of information, including suggestions for reducing this burden to Washington Headquarters Services, Directorate for Information Operations and Reports, 1215 Jefferson Davis Highway, Suite 1204, Arlington, VA 22202-4302, and to the Office of Management and Budget, Paperwork Reduction Project (0704-0188), Washington, DC 20503

1. AGENCY USE ONLY (Leave blank)	**2. REPORT DATE** August 2002	**3. REPORT TYPE AND DATES COVERED** Final (1 Aug 99 - 31 Jul 02)

4. TITLE AND SUBTITLE
Tissue Engineering Initiative

5. FUNDING NUMBERS
DAMD17-99-1-9475

6. AUTHOR(S)
Vincent C. Hascall, Ph.D.

7. PERFORMING ORGANIZATION NAME(S) AND ADDRESS(ES)

The Cleveland Clinic Foundation
Cleveland, Ohio 44195
E-Mail:
hascall@bme.ri.ccf.org

8. PERFORMING ORGANIZATION REPORT NUMBER

9. SPONSORING / MONITORING AGENCY NAME(S) AND ADDRESS(ES)

U.S. Army Medical Research and Materiel Command
Fort Detrick, Maryland 21702-5012

10. SPONSORING / MONITORING AGENCY REPORT NUMBER

11. SUPPLEMENTARY NOTES
report contains color

12a. DISTRIBUTION / AVAILABILITY STATEMENT
Distribution authorized to U.S. Government agencies only (proprietary information, Aug 02). Other requests for this document shall be referred to U.S. Army Medical Research and Materiel Command, 504 Scott Street, Fort Detrick, Maryland 21702-5012.

12b. DISTRIBUTION CODE

13. ABSTRACT ***(Maximum 200 Words)***

The Cleveland Clinic Foundation Tissue Engineering Initiative was proposed to initiate novel tissue engineering projects as a collaboration between connective tissue biochemists, bioengineers, prototype engineers, and physician researchers from the Department of Biomedical Engineering. The primary focus of these projects was to test applications of hylan gels (divinyl sulfone crosslinked, purified hyaluronan). Gels were formulated in-house, as well as evaluating specimens obtained from the Matrix Biology Institute. During the final year of this project, considerable effort was devoted to developing the technology to repeatably produce hylans with improved mechanical strength, as well as ways to improve cell attachment and proliferation on and within the gels. Significant improvement has been made in both of these areas over the results submitted in the 2000 and 2001 Annual Reports. However, hylan-cell composites have not yet been optimized for the described systems. Although funding for this award was not renewed, much of the research on these projects is ongoing. Any pertinent future publications arising from this continued work will be submitted for inclusion with this report.

14. SUBJECT TERMS
hylan, hyaluronan, matrix, bone, epidermis, tendon, cellular scaffold

15. NUMBER OF PAGES
182

16. PRICE CODE

17. SECURITY CLASSIFICATION OF REPORT Unclassified	**18. SECURITY CLASSIFICATION OF THIS PAGE** Unclassified	**19. SECURITY CLASSIFICATION OF ABSTRACT** Unclassified	**20. LIMITATION OF ABSTRACT** Unlimited

Table of Contents

Cover..

SF 298.. 2

Table of Contents.. 3

Introduction.. 4

Body.. 5

Key Research Accomplishments... 107

Reportable Outcomes... 109

Conclusions.. 114

References.. 115

Appendices... 120

INTRODUCTION

As proposed in the initial grant and reiterated in the 2000 and 2001 Annual Reports, the Department of Biomedical Engineering has been investigating a novel biomaterial, crosslinked hyaluronan (hylan), as a cellular scaffold for the formation and maintenance of the matrix of soft tissues (*i.e.* vascular, tendon, and epidermal tissues) and bone. This task has been undertaken by a multidisciplinary team with expertise in biomaterials science, cellular and molecular biology, connective tissue biochemistry, structural engineering, biomechanics and imaging.

Briefly, hyaluronan is a highly anionic biopolymer comprised of repeat disaccharide units of -4-glucuronic acid-β1,3-N-acetylglucosamine-β1-. The polymer can be formulated such as to have a variety of molecular weights up to several million. It is synthesized by almost all cells and forms a structural element of most extracellular matrices in the body. Highly purified hyaluronan has been shown to be a biocompatible, efficacious supplement for use in a variety of surgical procedures including as a vitreous replacement in eye surgery and as a synovial fluid supplement in osteoarthritis [1,2]. Dr. Endre Balazs, Director of the Matrix Biology Institute, developer of this technology, and a collaborator on this project, has now developed methods to introduce covalent divinyl sulfone crosslinks between hyaluronan molecules. It is this class of hyaluronan-based materials (hylans) that has been, and continues to be the focus of this work.

Common Abbreviations:	HA – Hyaluronic acid, hyaluronan
	DVS – Divinyl sulfone, crosslinking agent

TISSUE ENGINEERING OF SOFT TISSUES

Prior to this study, hylans had not been investigated as a cellular scaffold for tissue engineering. The first step in this study was to determine the mechanical properties as well as the cellular interactions of a variety of hylan formulations as substrates for the engineering of soft tissue replacements. The hylan formulations to be investigated were initially supplied by the Matrix Biology Institute (Ridgefield, NJ), a newly formed Foundation directed by Endre Balazs, M.D. after acquisition of his former company BioMatrix, Inc. by Genzyme, Corp. (Canton, MA). In the second year of this award, we have undertaken in-house formulation of these gels, although we also receive samples from the Matrix Biology Institute.

DETERMINATION OF SUBSTRATES – Project 1 (PI: Ivan Vesely)

The objective of this project is to determine the correlation between the biomechanical properties of hylan preparations and two parameters of the material, namely the concentration of hyaluronan in the preparation and the extent of bifunctional crosslinking by the divinyl sulfone. Initial efforts in this area were conducted in collaboration with Dr. Hascall's lab. The results of these early experiments were summarized in the 2000 Annual Report as well as Ms. Maida Ludwig's Master's thesis [16] (See Appendix, 2000 Annual Report).

Gel development

During year one of this award, testing was conducted exclusively using series of hylan specimens provided by BioMatrix, Inc, (Ridgefield, NJ) for evaluation in our laboratories. During this time, a bid was made by Genzyme, Corp. (Cambridge, MA) to acquire BioMatrix, Inc. This transaction ultimately led to the formation of Genzyme Biosugery and the Matrix Biology Institute. However, lengthy resolution of merger issues delayed the supply of specimens for testing or culture studies. As a result, we set out to develop the technology of hylan formulation in our laboratories. In-house development of hylans has been undertaken as a collaborative effort among several of the PIs on this project. The in-house hylan development was initially conducted under the guidance of Endre Balazs, M.D. (Director) and Julie Whetstone of the Matrix Biology Institute, using United States Patent No. 4,582,865 – Example 14 [11] as the initial protocol. Within the third year of this granting period, Anand Ramamurthi, Ph.D., and a group of intern students within Dr. Vesely's lab carried out most of this work.

The appearance and mechanical properties of these gels were consistent with gels previously obtained from BioMatrix, Inc. The degree of crosslinking, determined via Fluorophore-Activated Carbohydrate Electrophoresis (FACE), and hyaluronan content in gels, determined using a hexuronic acid assay, confirmed that CCF fabricated gels were comparable to similar gels provided by BioMatrix, Inc. Our ability to replicate the formulation process described in the patent enabled us to further innovate protocols to create gels that were better suited to the various applications described in the initial proposal.

There are a myriad of variables that can be altered to affect the gel properties. These include the molecular weight and concentration of HA, salt content, solvent selection, crosslinking ratio, temperature, and duration of gelation and washing. Increased amounts of DVS gives the gel greater mechanical integrity, but at the cost of rendering the gel brittle. Decreased crosslinking results in increased swelling, thereby increasing water content and diminishing mechanical strength. Low molecular weight HA ($< 1 \times 10^6$) produces brittle gels. Therefore, all in-house formulations were made using HA of molecular weight $\geq 1.3 \times 10^6$. The primary trade off of using high molecular weight HA is that the gels swell significantly more than those prepared from low molecular weight HA. However, swelling can be controlled to some degree by the addition of sodium chloride to the gel prior to crosslinking. Additionally, alcohol washing increases the rigidity of hylan. Washing gels in a combination of alcohol and salt solution results in elastic gels. It is clear that there are a vast number of permutations that can be investigated in gel formulation. In consultation with the Matrix Biology Institute, we directed our efforts at reducing swelling and increasing elasticity of the gels in order to achieve our goal of improved mechanical strength.

As described in the previous two years' reports, the mechanical properties of the hylan gel preparations provided by the former BioMatrix, Inc. precluded testing by tensile stress-strain methods because of the difficulty in clamping ends of the pliant materials without significant damage. Therefore, only compressive properties, which were of limited value for the end-uses intended, were measured for most preparations prior to 2002. Further chemical and structural modifications of hylan gels were necessary to improve their strength. Elasticity imparted to the gels by washing with alcohol/salt made the gels more suitable for use in our studies. Many in-house gel formulations did achieve the mechanical integrity necessary for tensile testing. These mechanical testing data are presented within the context of ***Project 4***. It has not yet been determined what effect these formulation changes may have on biocompatibility.

Quantification of mechanical properties was conducted in parallel with ongoing culture studies. We were successful in modulating gel properties for cell culture via surface treatment and UV-irradiation. We continued to evaluate these techniques on elastic gels to further assess their utility as cellular scaffolds for tissue engineering. We also continued our efforts to verify that gel reinforcement via synthesis of a collagen and elastin-rich matrix by attached cells can contribute to added gel strength and/or elasticity. The mechanical properties of the current hylan preparations, while not entirely sufficient, are approaching levels that would be satisfactory for long term use in cell culture models, in which controlled, variable strain would be a parameter under study. The results of these efforts are also explained in great detail later in this report (***Project 4***).

In summary, this project continues to investigate hylan gels as substrates for cell culture and ultimately tissue engineering applications. Relying on the expertise of the Matrix Biology Institute and our own emerging proficiency, we have continued our efforts to develop and characterize hylan gels for the proposed tissue engineered constructs.

KERATINOCYTE MODEL - Project 2 (PI: Vincent Hascall)

Last year, we reported that the organotypic rat epidermal keratinocyte (REK) cell line is unable to attach to crosslinked hyaluronan. Therefore, with our collaborators in Finland, we continued to explore the mechanisms by which these cells regulate hyaluronan metabolism and how modulating synthesis and catabolism parameters influences their ability to migrate in scratch wound models and to undergo stratification and epidermal differentiation.

We completed the study of the keratinocyte clones with stable transfects of sense and antisense hyaluronan synthase 2 (Has2) [3]. As noted last year, clones expressing sense Has2 synthesized increased amounts of hyaluronan and migrated faster in scratch wound assays, while clones expressing antisense Has2 synthesized decreased amounts of hyaluronan and migrated more slowly. These results, in combination with the study showing that epidermal growth factor upregulates Has2, increases hyaluronan synthesis, and increases migration [4], provide convincing evidence for a direct role of hyaluronan synthesis in the process of epidermal regeneration during wound repair.

Because the epidermis is separated from the underlying dermis by a basement membrane, hyaluronan metabolism is regulated entirely within the epidermis. Hyaluronan synthesis has been the main focus of attention in this work. It has been shown both in organ culture of normal skin biopsies and in the stratified REK cultures that the half-life of newly synthesized hyaluronan in the epidermis is less than a day. As the concentration of hyaluronan is maintained in steady state, the catabolic mechanism must balance the high rate of synthesis. We investigated the mechanism of hyaluronan catabolism in monolayer cultures of REKs [5]. The results uncovered a novel, previously unknown pathway that involves the cell surface hyaluronan receptor, CD44. A hyaluronan-specific probe was used to monitor uptake of hyaluronan by both histological and biochemical methods. An antiserum to CD44 that blocks the ability of the receptor to interact with hyaluronan, inhibited further uptake whereas inhibitors of all known endocytotic pathways had no effect. This new pathway involves internalizing large fragments of hyaluronan, most likely produced by a cell surface hyaluronidase acting in concert with CD44, and rapidly (less than 10 minutes) depositing them in large, flattened vesicles near the cell surface with recycling of CD44 to the cell surface. Metabolic labeling experiments showed that the internalized hyaluronan fragments rapidly exit this unique compartment and enter an intracellular pathway that eventually (2 – 3 hours) leads to lysosomes and complete degradation. This pathway probably evolved to degrade hyaluronan directly and is likely to be common to all cells that actively catabolize hyaluronan.

The other major study this past year, investigated how removing hyaluronan from the intercellular matrix affects subsequent epidermal differentiation. REK cultures were prepared on reconstituted collagen fibrils on which an intact basement membrane had previously been deposited by MDCK cells [6] as described in the 2000 Annual Report. At near confluence, the cultures were lifted to the air/liquid interface to initiate epidermal differentiation and stratification. Some cultures were incubated in the continuous presence of Streptomyces hyaluronidase (HSD), an enzyme that specifically degrades hyaluronan, in order to remove all intercellular hyaluronan and to degrade all newly synthesized hyaluronan. Controls showed that the keratinocytes were not adversely affected by the enzyme treatment and that cultures were devoid of hyaluronan. The results showed that in the absence of hyaluronan, the keratinocytes accelerated their differentiation program by early expression of keratin 10, an early differentiation marker, and by the production and early appearance of significantly larger "giant" keratohyaline granules in the stratum corneum, a late differentiation marker. This suggests that the concentration of hyaluronan around basal cell keratinocytes can be instructive in the stratification and differentiation pathways, with increased hyaluronan correlating with delayed differentiation and possibly a thicker, more stratified and multi-layered epidermis.

We are seeking funds (NIH) to continue work with this model. We now have stable REK clones with inducible promoters and plan to use them to modulate both synthetic and catabolic pathways involved in hyaluronan metabolism. Understanding the underlying mechanisms and how to manipulate them can provide important insight into how to promote more rapid and complete re-epithelialization in wound situations. We also hope that we can continue to develop a facilitative, biocompatible substrate for epidermal tissue engineering to meet the overall objectives set forth for this project initially. The REK model continues to be the most promising one for meeting these objectives.

VASCULAR ENDOTHELIAL CELL MODEL – Project 3 (PI: Hiroaki Harasaki)

As stated in previous reports, the focus of this project was to develop and optimize the cell seeding technology necessary for endothelial cell coating of vascular grafts and the evaluation of such constructs *in vitro*. Early gel formulations did not have enough mechanical integrity to withstand circulatory flow conditions as a stand-alone graft. For this reason, a composite vascular graft was proposed, whereby the other materials (e-PTFE, Dacron mesh) could provide the necessary backing strength for the graft to survive the flow conditions it would be subjected to. It was initially hypothesized that DVS crosslinked hylans possessing a surface coat of collagen type IV could provide a substrate suitable for endothelial cell seeding in the lumen of such a construct. The primary obstacle to overcome is to prevent detachment of such cell coatings under fluid shear.

Based on experiments with neonatal rat aortic smooth muscle cells in year 1 of this award (***Project 4***), it was shown that cell attachment on uncoated hylan gels was sparse. Significant cell attachment was only achieved through surface coating with matrix factors. This observation has 2 ramifications. First, the endothelial cell seeding on the luminal side of a vascular graft could be achieved using the collagen type IV coating described. Secondly, the inertness of unmodified hylan is an attractive characteristic to prevent smooth muscle cell (SMC) proliferation within the remainder of the composite graft. Two of the leading causes of vascular graft failure are SMC hypertrophy leading to graft occlusion and thrombosis resulting from the absence of a protective endothelial cell lining. The characteristics of hylan gels as described, could help to greatly reduce graft failure as a result of these phenomena.

In year 2 of this award, culture experiments with SMCs presented a result that was detrimental to this project. Although cells could attach and proliferate on the surface of collagen coated hylans, when long-term cultures (3 weeks or more) remained at confluence and began to form multi-layers, they had a propensity for the cell layer to peel away from the gel surface (***Project 4***). One possible hypothesis is that the contractile forces between the SMCs exceeded the bond strength of the gel's surface coating. This is quite likely, as the coatings are merely surface adhesions, and their strength and efficiency are a function of the electrostatic interactions between the coating factor and the hylan gel surface.

If intercellular forces were able to remove these surface cell coatings, there would be no practical reason to believe that they would be able to withstand shear and other mechanical forces that they may ultimately be subjected to *in vivo*. The limitations presented by the weak adherence of surface coatings led us to abandon our efforts along this line of work. It was then proposed that we expend further effort into the transfection of endothelial cells with pSPORT-NOS to suppress platelet aggregation and SMC proliferation [7] in combination with conventional vascular grafts. This approach was briefly described in the 2000 annual report.

Significance and Future Work

Since the submission of the 2001 Annual Report, Dr. Harasaki has retired and left the institution. Therefore, no further work was done in regard to the endothelial cell transfection approach at the Cleveland Clinic. All unused funds from this project were redistributed amongst the other projects that were showing more significant progress.

Development of biological substrates for fabrication of a composite artificial heart valve

The overall objective of this project is to develop suitable biological composite materials for fabrication of biocompatible and functional aortic heart valves. Ideal for this purpose would be a viscoelastic, mechanically anisotropic material that is capable of supporting cell attachment and growth. The traditional tissue-engineering concept of using biodegradable scaffolds may be inappropriate for fabricating aortic heart valves due to unsuitable mechanical characteristics of the polymer matrices and because of the limited remodeling experienced by the aortic valve construct *in vivo*. The materials that we develop are therefore based on non-biodegradable natural polymers, and the structures into which they are to be formed are intended to have nearly physiologic biomechanical properties. Divinyl sulfone-crosslinked hyaluronan substrates (hylans) were selected for study due to their biocompatibility and mechanical versatility. Hyaluronan is a polysaccharide widely distributed in connective tissues. In previous years, we determined that hylan gels poorly support cell attachment, vital to their use as tissue engineering scaffolds. Texturing of the gel surface and alteration of bulk gel properties by exposure to low wavelength UV light were found to dramatically enhance cell attachment. The encouraging results of work performed in the first 2 years of this study have led us in year 3 to focus on the complete characterization of these modified gels, and study their reinforcement with extracellular matrix elements such as collagen and elastin, synthesized by seeded cells. The research goals in the third year of this study thus were:

Specific Aim 1: Characterize UV-modified hylan gels to determine chemical and biological changes incurred during the irradiation process.

Specific Aim 2: Evaluate the synthesis of an extracellular matrix (ECM) by cells attached on hylan gels via quantitative and qualitative experiments.

Specific Aim 3: Initiate the development of a composite of collagen fiber bundles and elastin-reinforced hylan gels that would replicate the multilayered morphology of aortic valve cusps.

Necessity for cell seeding on gels

Cell seeding is necessary to enable complete integration of the scaffold material with native tissue upon implantation. Several studies have suggested that the degradation or absence of structural tissue molecules such as collagen and elastin in aortic valve allografts and xenografts is caused by a lack of cells in implanted tissues. In fact, Mulholland and Gotlieb [8] showed that aortic valve interstitial cells have considerable biosynthetic activity in some animal models. The deterioration of structural components has been thought to lead to ultimate tissue failure. The absence of a protective surface cell lining has also been related to enhanced thrombogenicity of the tissue. Our rationale for culturing viable cells on hylans therefore aims to address the above issues. Previously, biodegradable hyaluronan sponges seeded with mesenchymal progenitor cells were used for tissue-engineered repair of bone and cartilage. However, very limited information is available pertaining to feasibility of cell culture on divinyl sulfone-crosslinked hylan gels. In the first year of this study, we evaluated cell attachment on a variety of hylan formulations obtained from BioMatrix, Inc. (Ridgefield, NJ). These experiments showed that cells attach very sparsely to unmodified hylan gels. And surface coating with matrix factors was necessary to enable cell attachment. In year 2, we performed qualitative and quantitative experiments to compare different surface treatments and also investigated modifications to the gel necessary to either restrict cells to a surface lining or enable cell infiltration. Cell binding properties of gels were either altered via surface coating or UV irradiation, as described below. The results of these studies performed in the first 2 years of the project are summarized as below.

Evaluation of cell-binding properties of divinyl sulfone-crosslinked hylan gels

Hylan gels were either pre-coated with cell-binding matrix factors such as collagen (type I, from rat tail), extra cellular matrix (ECM) gel (from mouse sarcoma), laminin, and fibronectin (from bovine plasma) or were left uncoated (controls). For each surface treatment, three different amounts of factors ranging from 10 μg – 100 μg were used to prepare coating suspensions. Coating suspensions were overlaid on circular disks of hylan (Area = 1.9 cm^2; thickness ~2 – 4 mm) and incubated in a humid atmosphere at 37 °C for 5 hours. The gels were subsequently rinsed with PBS for 5 minutes to remove unbound factors. Neonatal rat smooth muscle cells were isolated from the aortae of 1- to 3-day old rat pups using methods adapted from Oakes *et al.* [9], and seeded on gels at counts of $\sim 2 \times 10^5$ cells/well in a 24-well plate. Neonatal rat aortic cells were selected for this study since they prolifically synthesize large quantities of collagen and elastin, which we expect to improve the mechanics of the gel. Cells were cultured on the hylan gels for 7 – 28 days. All experimental trials were performed in triplicate. The culture medium was changed twice weekly for up to 3 weeks of culture and more often thereafter. Cell attachment and subsequent proliferation on hylan gels was assessed quantitatively using the (MTT) assay and confirmed using a DNA assay (Fig. 1).

Results

Cells attached very sparsely to unmodified control solid or particulate hylan gels. Significant cell attachment occurred only when the hylan gels were coated with matrix factors. Once attached, the

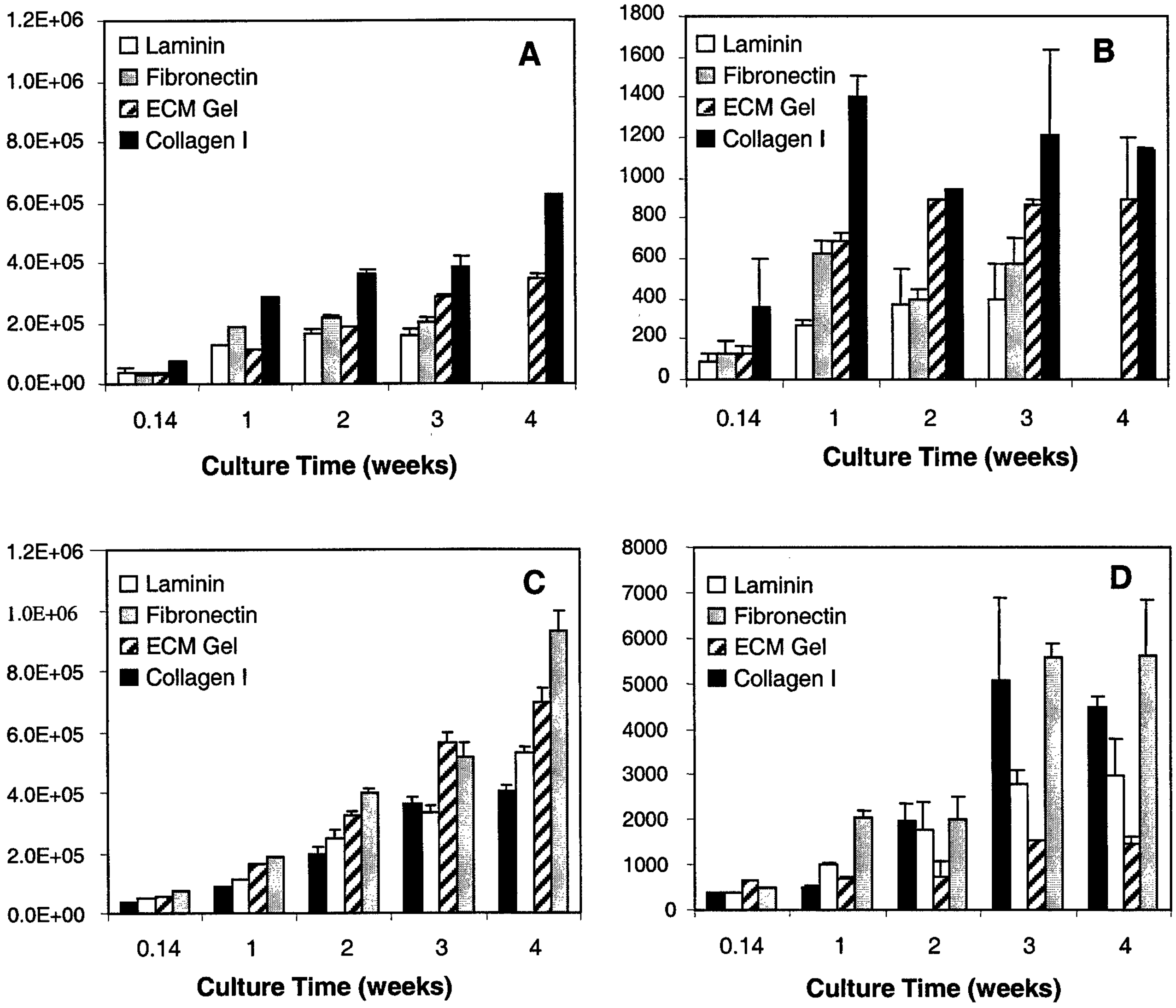

Figure 1: Proliferation of neonatal art aortic smooth muscle cells on solid hylan gels expressed in total number of cells attached (**A**) and cellular DNA (**B**). Similar results are shown for proliferation on particulate hylan gels expressed in total number of cells attached (**C**) and cellular DNA (**D**). Cells were cultured on gels (1.9 cm^2) coated with collagen I, ECM gel, laminin, or fibronectin. Values shown are Mean ± SD for n = 3. The average DNA per cell was 7.8 ± 1.2 pg.

cells proliferated over a 4-week period, and surfaces were confluent with cells within 10 days of seeding (Fig. 2). Collagen I was most appropriate as a coating agent, since cells attached on both solid and particulate collagen-coated hylan gels and maintained their normal proliferative phenotype. Cell morphology appeared to be influenced by both the identity of the matrix factors coated and the hylan type (solid vs. particulate). Immunofluorescence studies showed that the uneven surface of particulate gels induced more protein deposition and the subsequent attachment of cells, relative to smooth-surfaced gels (Fig. 3).

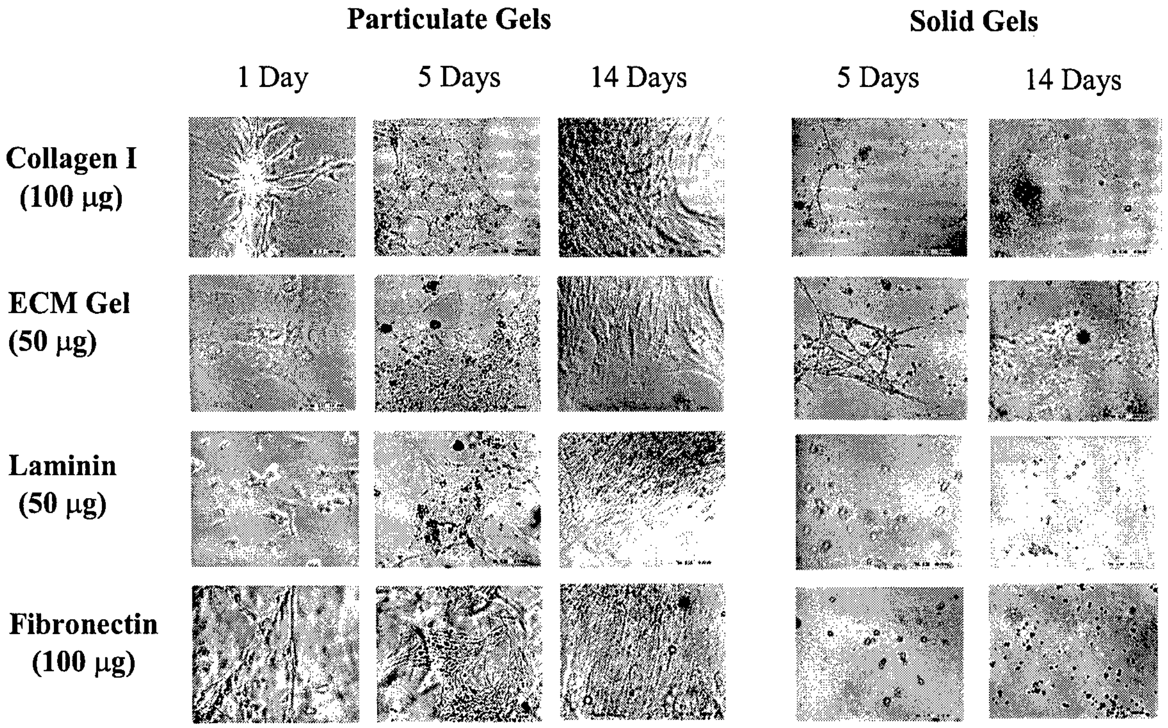

Figure 2. Neonatal rat aortic smooth muscle cells cultured on particulate hylan gels, shown at 1, 5, and 14 days after seeding. Gel surfaces were coated with adhesion proteins to facilitate cell attachment. Note the spreading and proliferation of cells on particulate gels. Also shown are cells on solid gels at 5 and 14 days after seeding (right panels). Note the presence of rounded and non-proliferative cells on laminin and fibronectin coated solid gels. Culture area = 1.9 cm^2. Magnification: 40X.

Conclusions

Hydrogels based on DVS-crosslinked hyaluronan (hylans) do not support the attachment of neonatal rat aortic smooth muscle cells, likely due to their extreme hydrophilicity. However, surface treatment of the hylans with matrix factors stimulates cell attachment and proliferation. The identity, amounts and coating efficiencies of matrix factors influence cell attachment. Coating efficiencies are a function of the electrostatic interaction between these factors and the hylan surface. The study showed that hylan gels with identical composition, but different surface textures, can elicit different responses to protein deposition and cell attachment. Surface texturization of hylan gels, can thus be possibly used to modulate the cellular response in this case, by influencing protein deposition.

Modification of hylan gels to enhance their cell binding properties

A constraint of the above approach of coating gels with matrix factors is that the factors are only physically adsorbed on the gel surface and can thus be detached by shear and other mechanical forces. Second, the gels required some modification to enable cell infiltration, - necessary for its use in tissue engineering applications. Since low-intensity ultraviolet (UV) radiation has been used previously to tailor pore-sizes in hydrogels [10], we attempted to enhance cell attachment and infiltration into hylan gels by altering the surface and bulk gel properties by exposure to UV light.

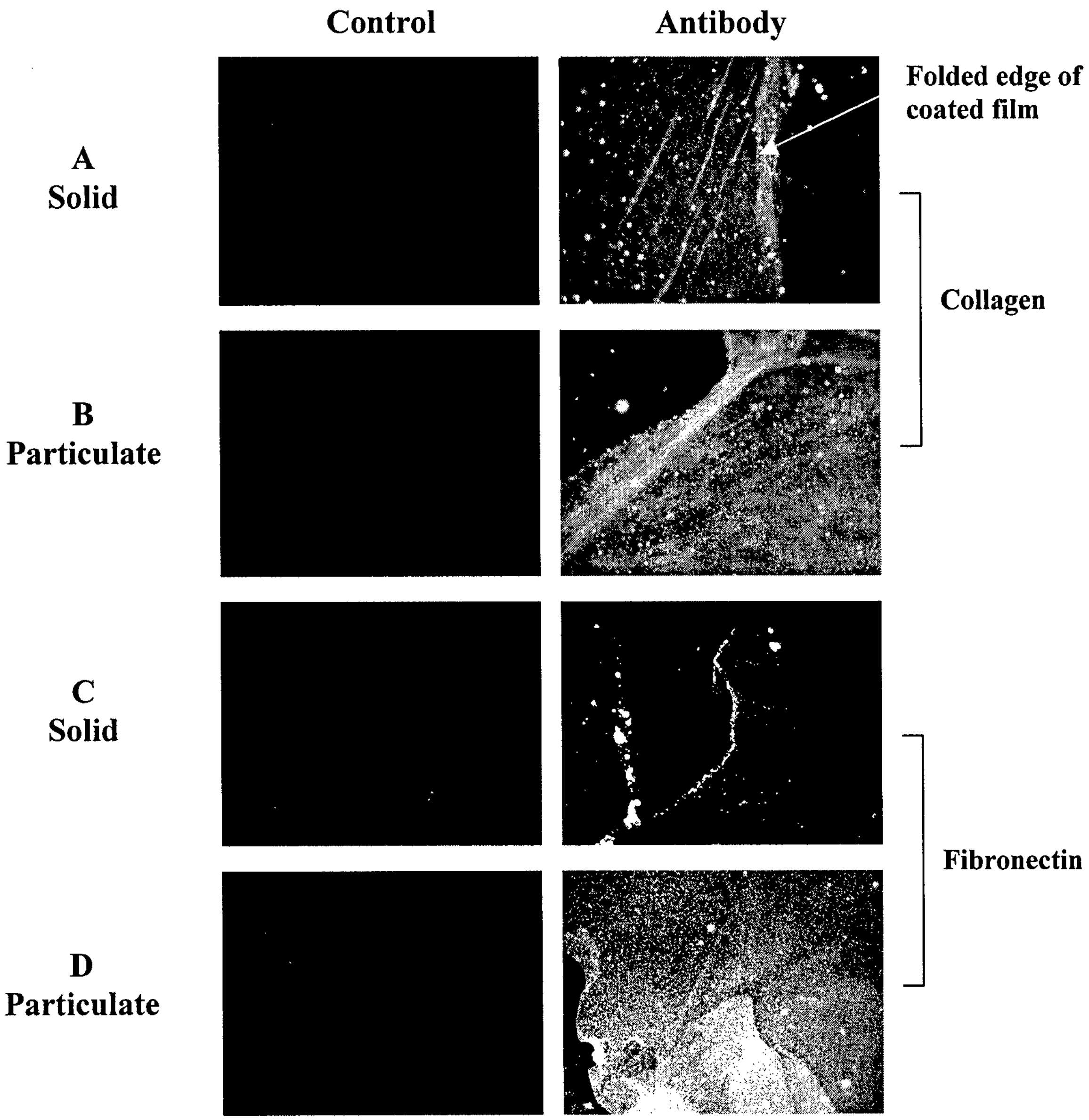
Control
Antibody
Folded edge of coated film
A
Solid
Collagen
B
Particulate
C
Solid
Fibronectin
D
Particulate

Figure 3. Coating of cell adhesion factors on solid (**A** and **C**) and particulate (**B** and **D**) hylan gels. Gels were overlaid with 100 μg of collagen type I (rat tail; **A** and **B**) or fibronectin (from bovine plasma; **C** and **D**). Non-controls were treated with rabbit polyclonal primary antibodies against bovine fibronectin and rat collagen I, respectively. Adhesion proteins were visualized with a secondary antibody conjugated with Texas-Red fluorophore (λ = 594 nm). Untreated control gels were not treated with primary antibodies. Note the uniform coating of collagen on both solid (**A**) and particulate (**B**) gels, and the sparse coating of fibronectin on the solid gel (**C**). This may explain the poor adherence of cells to fibronectin-coated solid gels. Gels were imaged at their edge to clearly distinguish between background fluorescence and fluorescence from the protein coat.

Hydrogel preparation and modification

For this study, hylan gels were prepared in-house. Gel formulation was based on methods previously patented by Balazs et al. [11]. The gels consisted of long chain hyaluronan (HA) crosslinked with divinyl sulfone (DVS). All gels were prepared from high molecular weight ($> 1.5 \times 10^6$) HA as sodium hyaluronate (NaHA), obtained from Genzyme Biosurgicals (Cambridge, MA). Briefly, 230 mg of NaHA was mixed with 0.2 M NaOH, pH 13.0 and stirred over ice, for 30 minutes. The HA was then crosslinked with 44 μl of divinyl sulfone (Sigma Chemical Co., St. Louis, MO). The HA solution was immediately transferred using a syringe to 100 mm petri dishes, and the gel was allowed to form over 15 minutes. After an additional 2 hours, the gel was placed in one liter of distilled water and allowed to swell overnight. Unreacted DVS was removed through multiple washes with distilled water. In all gels, the ratio of hyaluronan to DVS was approximately 3:1 by weight. The HA content in the hydrated gels was roughly 3% by weight. All gels were optically clear with a smooth surface, and were roughly 1 mm thick. Although all gels were prepared aseptically in a biological culture hood, irradiated gels were sterilized by exposure to UV light.

Gel modification

Sterile hylan gels were equilibrated with serum-free Dulbecco's Modified Eagle's Medium with an F-12 supplement (DMEM:F12; Life Technologies, Grand Island, NY). Control gels, designated as 'C', were unmodified. Those in a second group (D) were oven dehydrated at 30 °C for 36 hours. A third group of gels (UV) was modified by irradiation with UV light ($\lambda = 254$ nm) for 48 hours in a biological hood. These gels were maintained hydrated during the period of UV irradiation. A fourth group of gels (DUV) was first dehydrated for 36 hours and then irradiated with UV light for the same period of time as the UV gels. Prior to cell culture, gels in all groups were equilibrated with serum-free DMEM: F12 culture medium.

Cell culture and quantitative assessment of cell proliferation

Neonatal rat smooth muscle cells were harvested from the aortas of 3-day old rat pups using methods previously described by Oakes et al [9]. Briefly, aortas from 20 Sprague-Dawley rat pups were excised and split longitudinally in sterile PBS (with 2 mM Ca^{2+}, 4 °C). The collagenous matrix was digested with type II collagenase (2 mg/ml in serum-free medium; Worthington Chemical Corp., Lakewood, NJ) for 10 minutes at 37 °C. DMEM:F12 culture medium (3 ml; pH 7.3) containing 10% fetal bovine serum (FBS), was added to the digested segments. The endothelium on the inner wall of the aortal segment was stripped off using a sterile cell scraper. The segments were then minced into 0.5 mm long pieces and transferred to a petri dish pre-wetted with sterile culture medium. The explants were removed after 1 week of culture. The primary cells were cultured to confluence and passaged. Cells used in this study were of the sixth passage.

Prior to culture on hylan gels, stock cells were trypsinized (0.25% trypsin/ 0.1% EDTA; Life Technologies, Grand Island, NY), pelleted by centrifugation, and then resuspended in DMEM:F12 (containing 10% FBS and 1% penicillin-streptomycin). The cells were seeded onto treated or untreated (control) hylan gel samples that occupied the entire area of wells in a 24-well tissue culture plate (1.9 cm^2). Each well was seeded with 4×10^5 cells (2×10^5 cells for the cell proliferation assays) and initially incubated with a minimal volume (200 μl) of DMEM:F12 (containing 10% FBS and 1% penicillin-streptomycin) per well, to facilitate cell attachment. Two hours after seeding, the volume of the medium was increased to 1000 μl per well. Cells were cultured on the hylans for up to 3 weeks, with the culture medium changed twice weekly. All trials were performed in triplicate.

The total cellular DNA content was measured to evaluate cell proliferation atop and within UV-irradiated gels. The results were compared to data previously obtained for cultures atop similar hylan gels coated with collagen, and unmodified hylan gels. Based on the observations of our previous work [12], the amount of DNA per cell was assumed to remain unchanged through the period of culture. Cell proliferation on unmodified control and UV-irradiated gels was compared to that on gels coated with rat-tail collagen (100 μg/100 μl; Collaborative Biomedical Products, Bedford, MA), which was previously shown to significantly enhance cell adhesion and proliferation.

Hylans with adherent cell layers were carefully transferred to fresh wells, gently rinsed with 1% (v/v) PBS, overlaid with 1 ml of 0.25% trypsin / 0.1% EDTA per well and incubated at 37 °C for 10 minutes. The released cells were pelleted by centrifugation and then pooled with other cells that were removed in a second cycle of trypsinization. Multiple cycles of trypzinizing were required to remove cells from the interior of the gels. Cells on collagen-coated gels were disrupted with trypsin-EDTA containing collagenase (2 mg/ml; 2 mM of Ca^{2+} as $CaCl_2$) at 37 °C and removed by scraping. The wash was centrifuged and the cell pellet resuspended in Pi buffer (50 mM Na_2HPO_4, 2 mM EDTA, 0.02% Na azide, pH 7.4). In each case, the cell suspensions were sonicated over ice, and the DNA in the homogenate was measured in a spectrophotometer using standard techniques.

Confocal microscopy

Confocal microscopy was used to investigate the degree of cell infiltration into the interior of gels and to visualize the 3-D structure of dehydrated and UV-irradiated (DUV) and non-irradiated (D) gels. All UV-irradiated gels observed with confocal microscopy were typically less than 1 mm thick. Gels that were dehydrated before irradiation were much thinner (< 100 μm). Cells were visualized by labeling the actin cytoskeleton with the fluorescent probe Alexa 488 Phalloidin (Molecular Probes, Inc., Eugene, OR). Briefly, the cell layers were rinsed with PBS (1% v/v) at 37 °C, fixed with cold acetone for 5 minutes, and rinsed again in an excess of cold PBS. Alexa 448 Phalloidin was diluted in a 1:20 ratio with PBS, and 50 μl was layered atop gels (Area = 1.9 cm^2). The samples were incubated at room temperature for 20 minutes, and then rinsed with PBS once again. Cell nuclei were labeled with 4',6-diamino-2-phenylindole dihydrochloride (DAPI; Molecular Probes, Inc., Eugene, OR) dissolved in PBS. The hylan gel itself was visible due to its auto-fluorescence. After labeling, the thin gels were transferred to glass slides and mounted with Vectashield mounting medium (Vector Laboratories, Burlingame, CA).

Scanning electron microscopy

Scanning electron microscopy was performed to determine if irradiation with UV light altered the texture of the hylan gel surface. In preparation for SEM, gels were frozen in a – 80 °C freezer overnight and then rapidly quenched in a bath of liquid nitrogen. Samples were then freeze-dried for 48 hours. The dried gel samples were coated with gold by a SPI-Module Sputter Coater (Structure Probe, Inc., West Chester, PA).

Results

Cells attached very sparsely to unmodified control hylan gels (C). Dehydration of gels (D) prior to reconstitution with culture medium marginally improved cell attachment. In both the above cases, however, the cells did not survive beyond 4 days of culture after seeding. Gels irradiated with UV light (UV, DUV) showed significantly higher levels of cell attachment than non-irradiated gels (Fig. 4). Cells atop UV and DUV gels proliferated to confluence within ten days of seeding, and then formed multilayered sheets on the gel surface.

DNA assay for cell proliferation

Cell counts obtained using hemocytometry were used to determine the average DNA per cell. Our value of 7.8 ± 1.2 pg of DNA/cell agrees with the accepted value of 6 pg/cell. Cells that attached to C- and D-type gels were too few in number to be quantified. Cells attached readily to dehydrated, UV-irradiated gels (DUV) and continued to proliferate over time (Fig. 5). These results were compared to our previously published data on collagen-precoated, hylan gels [12]. On coated gels, cellular DNA levels increased rapidly within 2 – 3 days after seeding and reached a plateau within 10 days (Fig. 5). The cellular DNA content of cultures on DUV gels, however, does not necessarily represent the number of cells attached to the gel surface, since many cells also migrated into the gel interior. The total DNA from these cell cultures measured at 1, 2, 3, and 4 weeks of culture were 2.6, 4.0, 6.0, and 9.3 times that measured 1 day after seeding. These cells began to proliferate rapidly at day 7 and continued to do so for the remainder of the 4-week duration of the study.

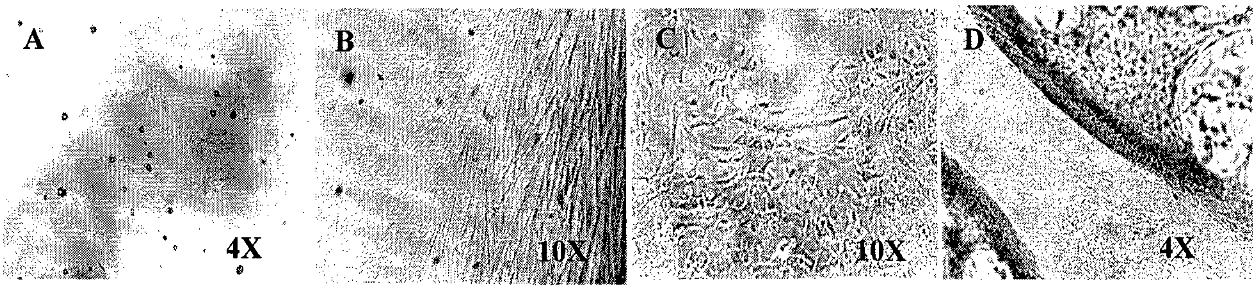

Figure 4. Irradiation of hylan gels with ultraviolet light increases cell attachment. Neonatal rat aortic smooth muscle cells attached sparsely and remained rounded and non-proliferative atop unmodified control (**A**, C-type) and non-irradiated but dehydrated gels (**B**, D-type). UV-irradiated gels without dehydration (**C**, UV-type) and with prior dehydration (**D**, DUV-type) improved cell attachment and proliferation. The striations in **B** are from the topography of the dehydrated gel, not from the attached cells. Note the thick cell layer atop DUV gels that can be peeled off.

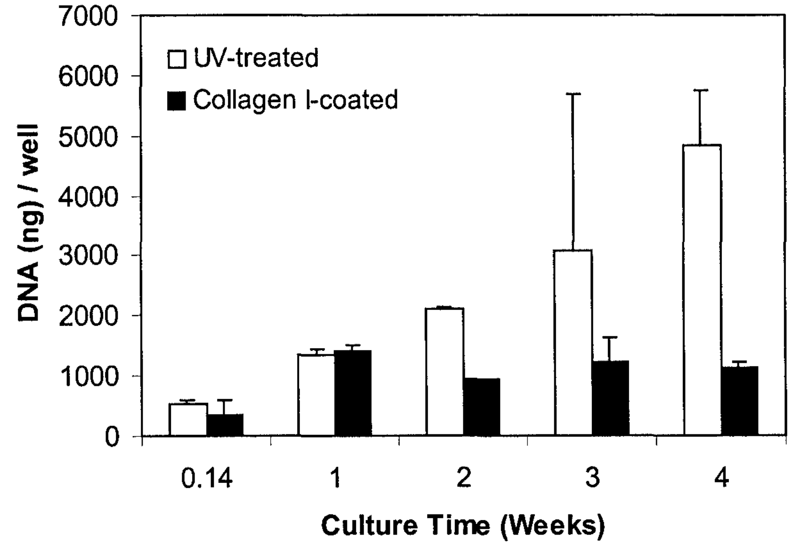

Figure 5. Proliferation of neonatal rat smooth muscle cells on modified hylan gels expressed in terms of the DNA content of the cultures. Cells were cultured on gels (1.9 cm^2) that were either coated with collagen I (rat-tail) or were first dehydrated and then UV-exposed for 48 hours. Note that UV-irradiation is more effective than coating with type I collagen. Values shown are mean ± SD of 3 trials. $*p < 0.05$ for significance.

Morphology of attached cells

The type of modification done to the hylan substrates affected the morphology of the seeded aortic smooth muscle cells. The few cells that attached to the control (C-type) hylan gels were rounded and non-proliferative. The cells that attached to the previously dehydrated gels (D-type) were also rounded, although a few spindle shaped cells were observed. The cells cultured on the UV and DUV gels were either highly extended or irregularly shaped. Cells appeared to align themselves along the pattern of cracks created on the gel surface by exposure to UV light, and then proliferated to confluence. Cell infiltration into the interior was observed only in the DUV gels, not in the UV gels.

Hylan gels as 3-dimensional cell scaffolds

Confocal imaging confirmed that cells did not penetrate into the interior of the UV gels, and cell growth was restricted to the surface only (Fig. 6A). In contrast, cells infiltrated into, and populated the entire thickness (< 100 μm) of the DUV gels at 7 weeks of culture (Fig. 6B). The migrating cells were highly extended, with multiple anchoring feet (Fig. 6C). The observation of dividing nuclei confirmed the presence of actively proliferating cells (Fig. 6D). Three-dimensional reconstruction and re-projection images were used to elucidate the mode of cell migration into the interior of DUV gels. Because of the auto-fluorescence of HA, pore and crevice-like structures were visible in the confocal images, with migrating cells within (Fig. 7). No such migrating cells were visible in the UV and D-type gels. Differences in cell behavior most likely resulted from the surface and interior morphologies of the different hylan gels.

Ultraviolet light-induced modification of surface and bulk characteristics of hylan gels

Optical microscopy performed on D-type gels revealed the presence of small, randomly distributed cracks on the surface. During rehydration, the cracks slowly became invisible as the gels swelled. Their surface, however, remained slightly corrugated relative to the smooth, unmodified (C-type) gels. Gels exposed to ultraviolet light (UV, DUV) had honeycomb-like ridges on their surface in addition to the cracks (Fig. 8A). This pattern of ridges was denser in the DUV than on the UV gels. During culture, cells appeared to align along the ridges on the gel surface (Fig. 8B).

Since confocal microscopy is a planar imaging technique, it does not yield detailed information about surface characteristics of the gel. However, the technique can detect density variation in the imaging plane near the gel surface, and confirmed the differences between gels. D-type gels had a smooth but undulating surface (Fig. 9A), while DUV gels had irregularities that resembled ridges, pores and cracks (Fig. 9B). Similar differences were also observed between the non-dehydrated gel groups (C-type and UV gels). The gel interior was imaged in 1 μm increments up to a depth of 68 μm for DUV gels and 30 μm for D-type gels beneath the surface. The interior of the D-type and DUV gels resembled their respective surfaces, appearing featureless (Fig. 9C) or porous and irregular (Fig. 9D). The surface characteristics of swollen D-type and DUV gels were compared using SEM. When these gels were prepared using freeze-drying, the D-type gels showed a non-porous and non-textured surface (Fig. 10A), while the DUV gels were patterned with ridges and troughs (Fig. 10B). The ridges were roughly 1 μm thick and 10 μm apart. Small cracks were visible between the ridges, reminiscent of the cracks seen under a light microscope.

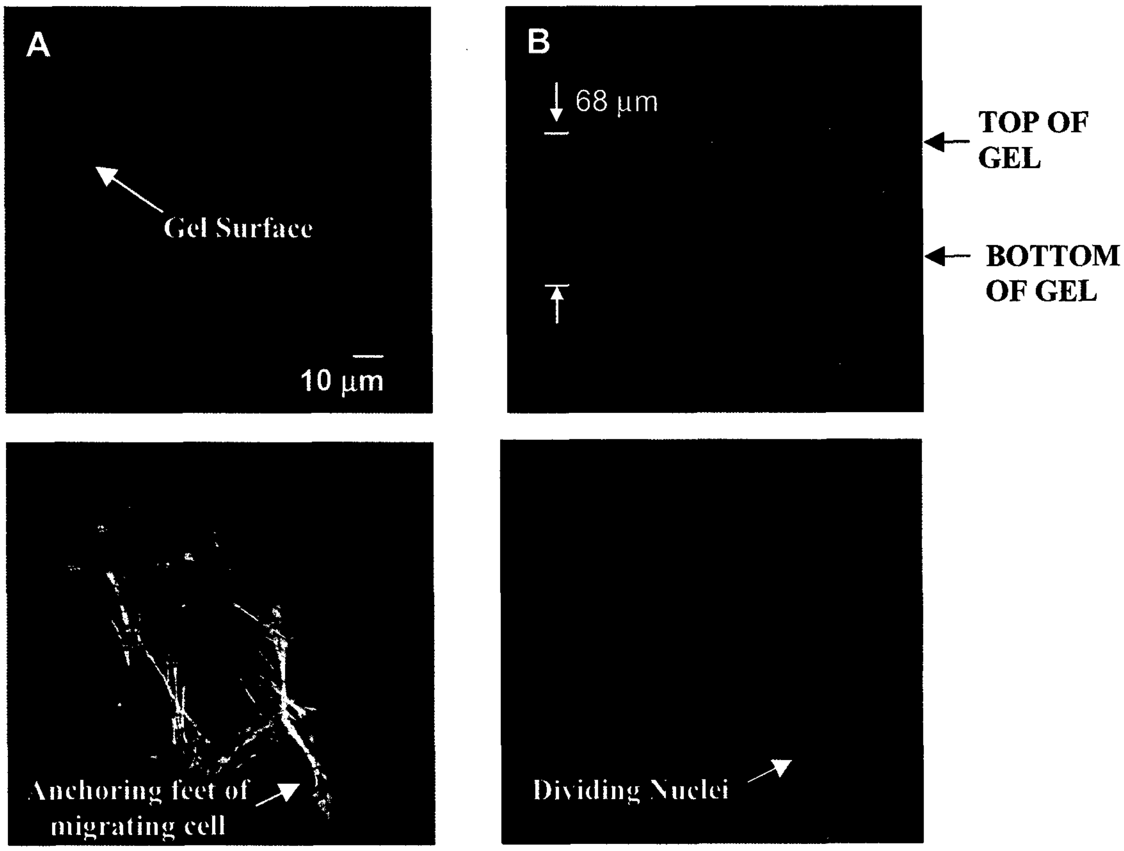

Figure 6. Confocal images of cells seeded on UV-irradiated hylan gels. Cell attachment was restricted to the surface of gels that were not dehydrated prior to UV-irradiation (**A**: UV). Dehydration of hylan gels prior to UV-irradiation enabled cells to penetrate into the interior of the gels (**B**: DUV). Cells in the gel interior were highly extended (**C**) and proliferative at the time of fixation, as evident from the presence of dividing nuclei (**D**). Cellular actin was labeled with Alexa 488 Phalloidin and cell nuclei with DAPI. Magnification: 40X (**A**,**B**), and 63X (**C**, **D**).

Conclusions

Despite their high biocompatibility, hylan gels are naturally poor tissue engineering scaffolds due to their poor cell-binding properties. Cell binding is primarily limited by the negative surface charge of hyaluronan chains, which are not conducive to cell attachment. The significance of this work is that we have developed techniques for the controlled modification of the surface and the bulk properties of DVS-hylan gels to enhance their performance as a cellular scaffold for tissue engineering applications. Depending on the treatment, cells can be either confined to the surface of the gel, or be induced to infiltrate into the interior.

Characterization of UV-modified hylan gels

We realize that a thorough evaluation of the modified hylan gels is necessary to determine if UV-exposure causes significant and possibly undesirable changes to the gel chemistry that may in turn prove detrimental to gel mechanics and biocompatibility. In this section of the study, we compared the chemistries, mechanics, hydrophobicity, and hemocompatibility of UV-modified hylan gels with that of unmodified control gels. The results of this study are essential to demonstrate that such modified gels can be reliably used as cell scaffolds for engineering soft tissues.

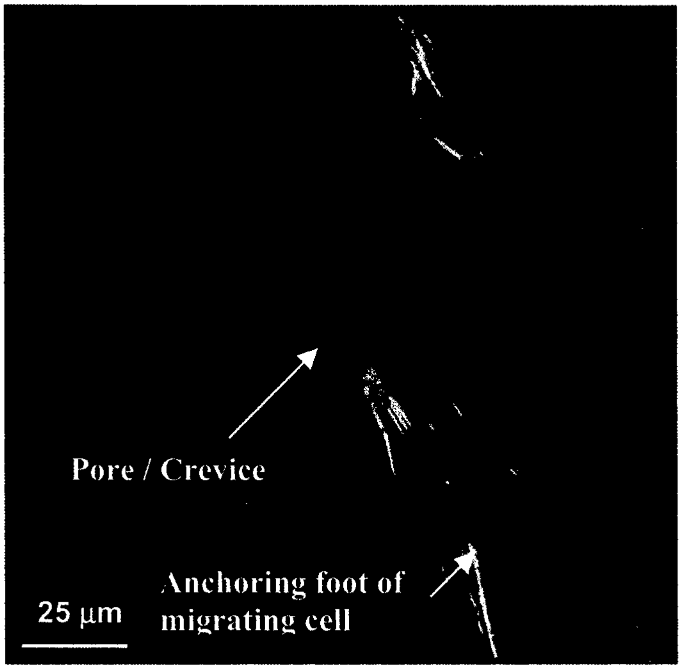

Figure 7. Cell migration within hylan gels. The confocal image shows an interior plane within a DUV gel, at a depth of 20 μm. The hylan gel appears red due it's autofluorescence. Cells in green were labeled for smooth muscle cell actin. The image suggests that cells infiltrate the gel via cracks that were likely created by the UV-irradiation process.

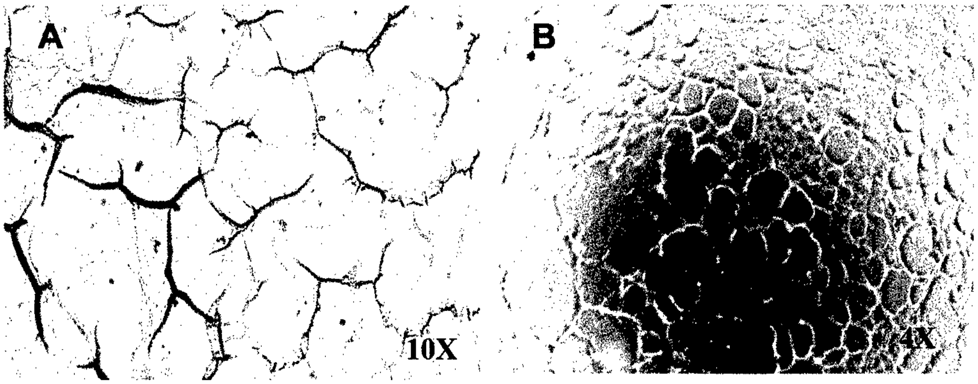

Figure 8. Exposure of hylan gels to UV light created honeycomb-like surface patterns of ridges and cracks (**A**). Cells initially aligned along these ridges and cracks, prior to proliferating to confluence (**B**). Cells in **B** are shown at 1 week of culture, and were imaged using a phase contrast microscope.

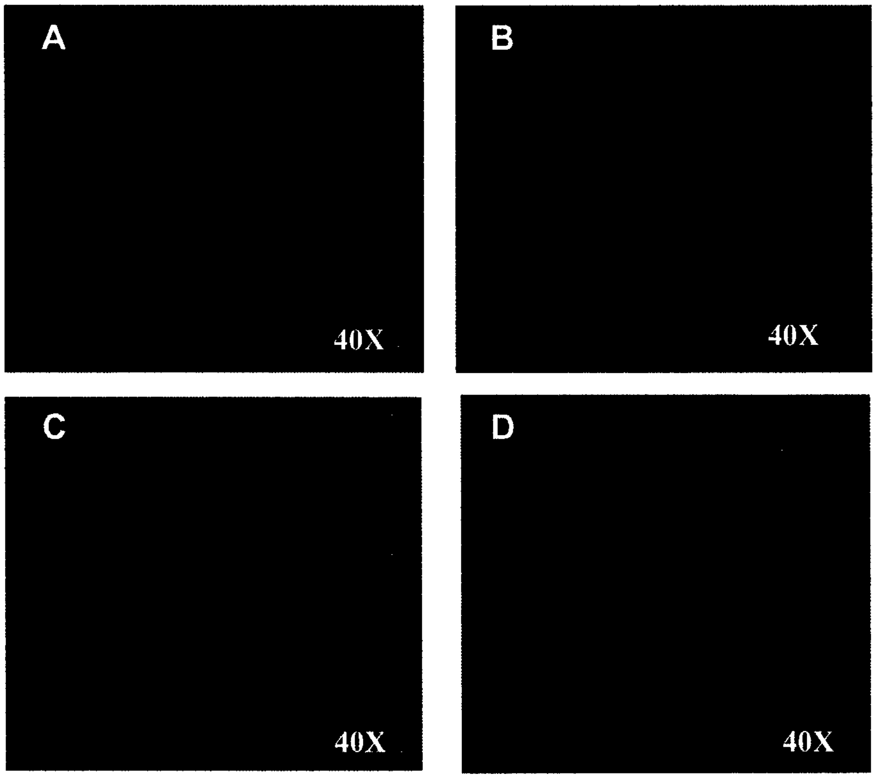

Figure 9. Texturing of hylan gels by ultraviolet light. Ridges and cracks were created on the surface of UVD hylan gels (**B**). Non-irradiated (D-type) gels did not show such patterning (**A**), although the gel surfaces displayed gentle undulations on a scale much larger than that of cell adhesion. The interior layers of irradiated gels (**D**) were identical to the surface, while in the case of the non-irradiated gels, no discernable features were apparent (**C**). The selected interior plane was located 14 μm from the surface.

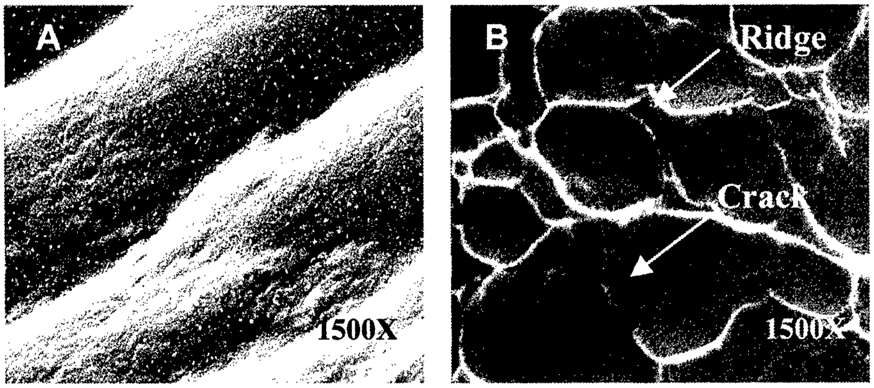

Figure 10. (**A**) SEM photograph of the surface of a dehydrated, non-irradiated (D-type) gel. Gentle undulations were observed in some regions of these gels. (**B**) SEM photograph of the surface of a UV-irradiated (DUV) gel. In contrast to the D-type gels (**A**), the surfaces of irradiated gels showed a textured, honeycomb-like pattern, with numerous thin ridges, approximately 1 μm across.

Methods

UV-induced changes to hylan gel chemistry

Fluorophore-Assisted Carbohydrate Electrophoresis (FACE) was used to analyze the effects of ultraviolet irradiation on hyaluronan gel structure and chemistry. FACE is a simple and sensitive assay for the identification and quantification of oligosaccharides generated by the enzyme- or non-enzyme-mediated breakdown of larger carbohydrate structures, such as hyaluronan. In the assay, the terminal reducing groups on these oligosaccharides are fluorescently labeled and identified as bands on a electrophoresis gel. The fluorescence of each band is dependent solely on the molar amounts of labeled product.

A first set of experiments investigated if irradiation of uncrosslinked HA and hylan gels with UV light induced changes in the digestibility of the HA chains. A reduction in enzymatic breakdown would indicate that UV irradiation crosslinks the HA chain structure. For the first set of experiments, 100 μg of HA in an uncrosslinked form or crosslinked with DVS into gels, were exposed to UV light for periods ranging from 0 – 60 hours, and then enzymatically digested in preparation for FACE. A second set of experiments investigated if UV light instead caused breakdown of HA. For this second set of experiments, aliquots of uncrosslinked high molecular weight hyaluronan (100 μg/100 μl in ammonium acetate, pH 7.0) were exposed to UV in a 24-well plate for 0 – 120 hours. These samples were not digested with enzyme prior to analysis using FACE.

After exposure to UV light for various time periods, samples in the enzymatic digestion experiment were reconstituted in 100 μl of ammonium acetate (pH 7.0) and broken down with 10 U of hyaluronidase from Streptococcus diglycidae (HSD; Seikagaku America, Falmouth, MA) for 4 hours at 37 °C. The enzymatic breakdown of HA results in the creation of saccharide fragments containing end reducing groups that may be fluorescently labeled. Thus digested samples were lyophilized and then derivatized with 40 μl of a 12.5 mM solution of 2-aminoacridone hydrochloride (AMAC; Molecular Probes, Eugene, OR), a fluorescent probe, at room temperature for 15 minutes. For experiments not involving enzyme digestion, irradiated HA samples were reconstituted in ammonium acetate (100 μl; pH 7.0) and then directly labeled with AMAC as described above.

After labeling with AMAC, 40 μl of a 1.25 M solution of sodium cyanoborohydride (Sigma Chemical Co., St. Louis, MO) was mixed with each sample and allowed to incubate in a 37 °C water bath for 16 hours. Glycerol was added to each sample to bring the volume to 100 μl. Five μl aliquots of labeled samples were run on a monosaccharide gel (Glyko Corporation, Novoto, CA), imaged under UV illumination with a cooled Quantix CCD camera (Roper Scientific, Trenton, NJ), and the band intensities were quantified using Gel Pro® 3.1 software (Media Cybernetics, Des Moines, IA).

All experiments were performed in triplicate. In both sets of experiments, non-irradiated samples (hylan and HA) served as controls.

Tensile Testing of Hylan Gels

Tensile testing was performed to correlate mechanical properties with the observed chemical effects of UV irradiation. Non-irradiated, but dehydrated gels (D-type) were compared with DUV hylan gels. All gels tested were 1 mm thick. Gels were cut into rectangular pieces 10 mm in length and 5 mm in width. Tensile testing was performed on a model 5543 Instron (Instron Corporation, Canton, MA). Gels were preconditioned by cyclically loading them to roughly half the measured failure strength of that sample. The tensile modulus of the material was calculated from the slope of the obtained stress-strain curve in the post-transitional linear region. The gels were then loaded to failure, and the failure stress and maximal percentage strain were obtained.

Swelling Studies

Swelling studies were performed to determine the degree of rehydration of hylan gels. Hylan gels were cast in 12-well plates (5 cm^2 per well; 2 ml hylan per well) as previously described. The gels were washed in a mixture of isopropanol and 1 M NaCl, and then equilibrated with a solution of 1 M NaCl. The gels were then divided into 3 groups. Gels designated as C-type were left unmodified. The D-type gels were dehydrated in an oven at 32 °C, and then reconstituted with 1 M NaCl. DUV gels were dehydrated and then reconstituted with 1 M NaCl and irradiated under low-wavelength UV-light for 48 hours. These gels were then reconstituted in 1 M NaCl. All gels were then frozen in liquid nitrogen and lyophilized overnight.

Each group ($n = 3$) of lyophilized gels was individually weighed and then immersed in 10 ml of culture medium (DMEM: F12 containing 10% FBS) at room temperature. Gels were removed and pat-dried with bilious paper, weighed at ten-minute intervals (over the first 2 hours) and at hourly intervals thereafter for up to 24 hours. After each weighing, the gels were replaced in the aliquot of culture medium. The relative swelling of the gel groups was determined by measuring the degree of their rehydration as calculated by the following equation.

$$\mathit{Swelling\ Ratio} = \left(\frac{\mathit{Weight}(t) - \mathit{Weight}(t=0)}{\mathit{Weight}(\mathrm{t}=0)} \right)$$

Results

Effects of UV-light on hylan gel chemistry

Exposure of uncrosslinked hyaluronan and crosslinked hylan gels to UV light decreased their susceptibility to digestion with hyaluronidase SD (HSD). Digestion with HSD completely broke down the non-irradiated HA, producing a single band of disaccharides on the FACE gel (First lane; Fig. 11). Irradiation with UV over the first 12 hours resulted in reduced digestibility by HSD. Only 39 ± 7% of the HA appeared in the ΔDiHA band relative to controls (Table 1). This suggests that UV induces some changes in the structure of HA that makes it resistant to HSD digestion. Irradiation of HA samples for periods greater than 12 hours did not produce any further decrease in the intensities of ΔDiHA bands suggesting no cumulative effect of UV irradiation on HA digestibility.

Digestion of crosslinked hylan gels with HSD yielded two bands; an intense band corresponding to ΔDiHA and a lighter band corresponding to DVS-crosslinked fragments of HA. Relative to the intensities of the bands in the control lane, the intensities of the bands corresponding to ΔDiHA and the DVS-crosslinked fragments were lower by one order of magnitude after 22 hours of UV irradiation and by two orders of magnitude after 60 hours of irradiation (Table 2).

In both sets of experiments above, the lanes loaded with non-control (i.e. irradiated) samples also contained very faint bands containing HA fragments of length greater than two saccharide units (Fig. 12). The normalized intensity values of these bands did not change with the duration of exposure to UV-light. Note that the new HA fragments were not present in either the non-irradiated HA or the DVS-crosslinked gel (Table 1).

Band	**Band Intensities normalized to intensity of ΔDiHA band at t = 0 hours**				
UV Exposure:	**t = 0**	**t = 12**	**t = 36**	**t = 48**	**t = 120**
ΔDiHA	1.0 ± 0.0	0.39 ± 0.07	0.37 ± 0.09	0.43 ± 0.01	0.30 ± 0.05
HA fragment 1			0.012 ± 0.009	0.019 ± 0.002	0.018 ± 0.01
HA fragment 2			0.011 ± 0. 005	0.008 ± 0.0	0.003 ± 0.01

Table 1. FACE analysis of uncrosslinked HA. Identical weights (100 μg) of uncrosslinked HA were exposed to UV light for periods ranging from 0 – 120 hours, digested with hyaluronidase SD, and then run on a FACE gel. The mean ± SD of obtained band intensities is shown normalized to the intensity of the single (HA disaccharide) band obtained for UV-unexposed control samples (t = 0; n = 3).

The second set of experiments demonstrated that the amount of new HA fragments increased with UV exposure, particularly beyond 72 hours of exposure (Fig. 13). We know that the source of these new HA fragments is the UV irradiation because these fragments were not seen in either control (1: non-irradiated, no HSD, or 2: non-irradiated, HSD). The absence of these new HA fragments in control 2 indicates that they resulted only from UV irradiation, and not from HSD digestion.

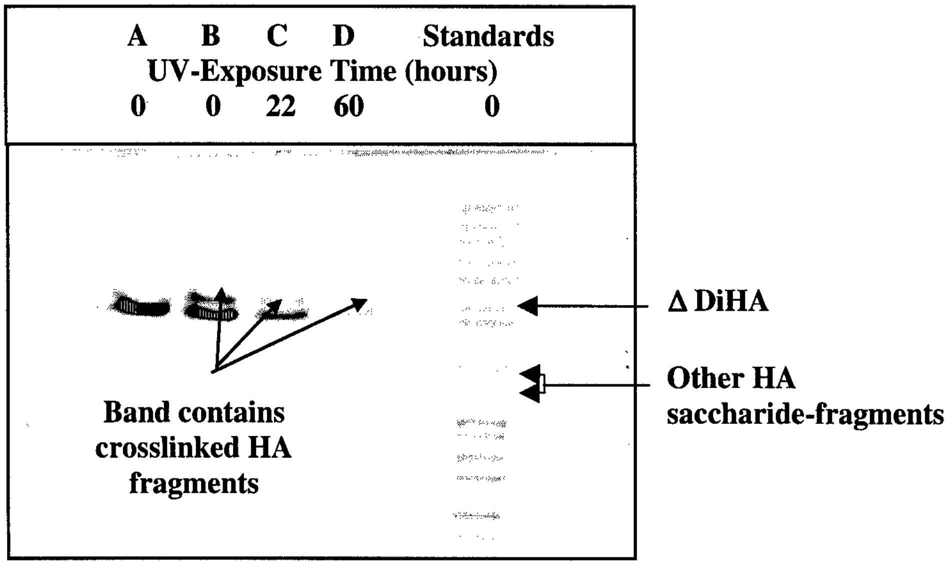
A B C D Standards
UV-Exposure Time (hours)
0 0 22 60 0
Band contains crosslinked HA fragments
Δ DiHA
Other HA saccharide-fragments

Figure 11. FACE analysis of uncrosslinked hyaluronan (**A**; 100 μg/100 μl) and DSV-crosslinked HA gels, exposed to UV light for periods of 0 (**B**), 22 (**C**), and 60 (**D**) hours and then digested with HSD to yield HA disaccharides (ΔDiHA). UV-irradiation altered the chemical structure of HA, reducing its susceptibility to HSD digestion. After 22 hours of UV-irradiation, other HA saccharide-fragments were also generated, likely due to UV-mediated breakdown of HA. However, these fragments are not easily seen without over-exposing the gel.

Band	**Uncrosslinked HA (A)**	**HA Gel (No UV) (B)**	**HA Gel (UV for 22h) (C)**	**HA Gel (UV for 60h) (D)**
DVS-Crosslinked fragments		(9.5 ± 1.2) E+5	(1.1 ± 1.4) E+4	(3.5 ± 4.8) E+3
ΔDiHA	(3.8 ± 2.2) E+7	(2.7 ± 0.6) E+6	(6.5 ± 1.4) E+5	(2.0 ± 2.5) E+4

Table 2. FACE analysis of uncrosslinked HA (**A**; control) and DVS-crosslinked HA gels undergoing 0 (**B**), 22 (**C**), and 60 (**D**) hours of UV light exposure. Mean ± SD of fluorescence intensities of the bands, measured using GELPRO® software (*n* = 3) are presented. All samples contained 100 μg of HA (MW > 1.5 x 10^6) and were digested by hyaluronidase SD (10 U). Irradiation with UV light interfered with the enzyme-mediated breakdown of the HA polysaccharide to yield HA disaccharides (ΔDiHA) and other products, relative to non-irradiated controls.

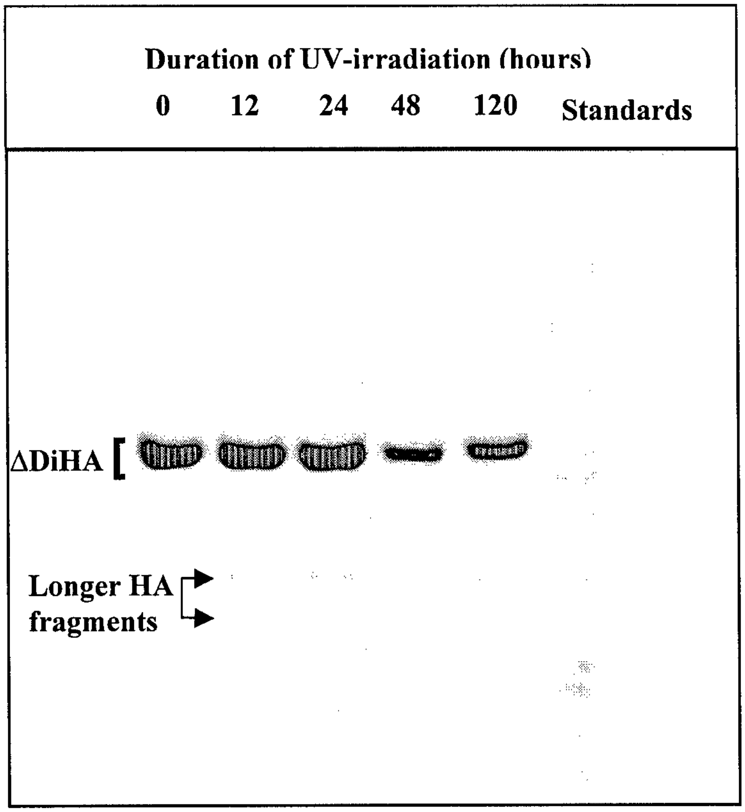

Figure 12. FACE analysis of uncrosslinked HA (100 μg/100 μl), exposed to UV light for periods ranging from 0 – 120 hours and then digested with HSD to yield HA disaccharides (ΔDiHA). UV-irradiation altered the chemical structure of HA, reducing its susceptibility to HSD digestion. After 12 hours of UV-irradiation, other HA saccharide-fragments were also generated, either due to UV-mediated breakdown of HA or indirectly, as a byproduct of HSD-digestion.

Effects of UV-light on hylan gel mechanics

UV-irradiated (DUV) gels were less stiff and more extensible than dehydrated (D-type) gels. The modulus measured at a tensile stress value of 12.7 kPa (applied load of 6. 5 grams) was lower for DUV gels than that for the D-type gels (9.6 ± 4.6 kPa vs. 17.4 ± 10.1 kPa). The irradiated gels were also more extensible than controls (37 ± 12 % vs. 27 ± 0.3 %) and failed at greater strain (90.7 ± 13.5% vs. 58.5 ± 4.7%) and lower stresses (19.1 ± 7.7 kPa vs. 28.0 ± 6.8 kPa).

Effects of UV-irradiation on swelling properties of hylan gels

When immersed in culture medium at room temperature, lyophilized, unmodified hylan gels (C-type) rehydrated to provide a steady state swelling ratio of 10.3 ± 0.09 at approximately 60 minutes after immersion. No further swelling occurred in the next 23 hours indicating that equilibrium had been attained (Fig. 14A). Low-heat drying of D-type gels in an oven prior to rehydration and lyophilization did not produce any structural changes in the gel as reflected by similar ultimate swelling ratios as the unmodified gels (10.5 ± 0.1), although steady-state hydration was attained within 30 minutes (Fig. 14C). However, hylan gels that were first dehydrated and then irradiated with UV light demonstrated a significantly lower degree of rehydration. Similar to the D-type gel, the UV gels reached a steady state level of swelling within 30 minutes. However, the ultimate swelling ratio was only 6.0 ± 0.2 (Fig. 14B).

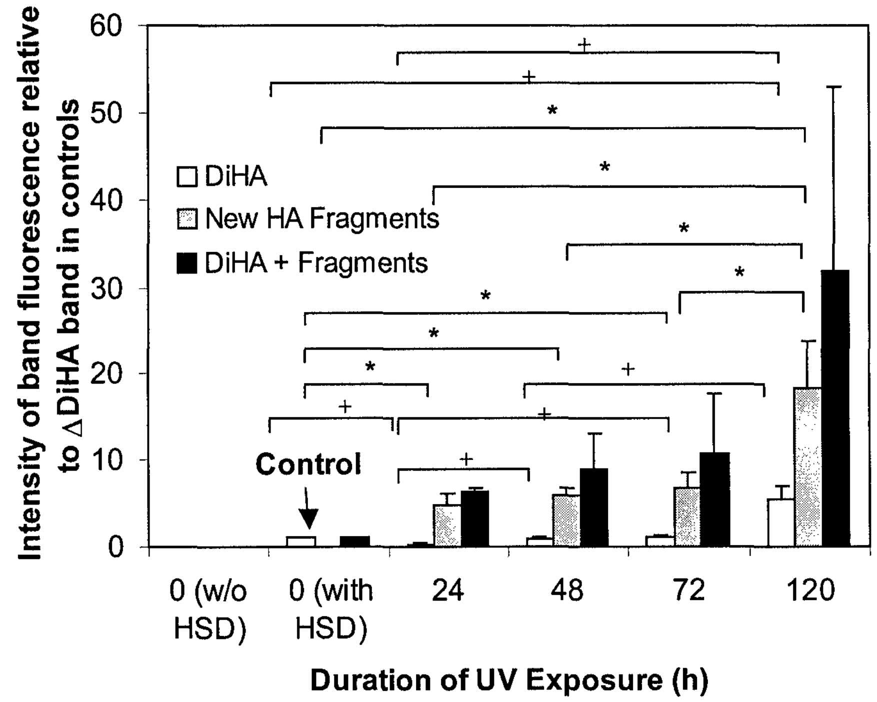

Figure 13. FACE analysis of uncrosslinked HA (10 μg/100 μl), exposed to UV light for periods ranging from 0 – 120 hours, and then fluorescently labeled for FACE, without HSD digestion. Irradiation of the HA polysaccharide broke it down into ΔDiHA and other HA fragments in the first 24 hours of UV-exposure although a significant increase in these amounts was only seen after 72 hours of exposure. Results shown are the mean ± SD of the band intensities normalized to the intensity of the HA disaccharide band, obtained upon digestion of HA with 10 U HSD. $p < 0.05$ at significance for new HA fragments (*) and ΔDiHA (+).

Conclusions and significance of study

Although highly biocompatible, hyaluronan-based materials are not good tissue engineering scaffolds due to the negative charge of hyaluronan, which is not conducive to cell attachment. In this study, we have shown that the surface and bulk properties of hylan gels can be modified to enhance cell attachment and enable cellular ingrowth. When hylan gels were dried and then rehydrated, gentle undulations were created on the otherwise smooth gel surface (group D). This surface, however, did not enhance cell attachment, possibly because the scale of texturing was larger (10 μm) than the scale

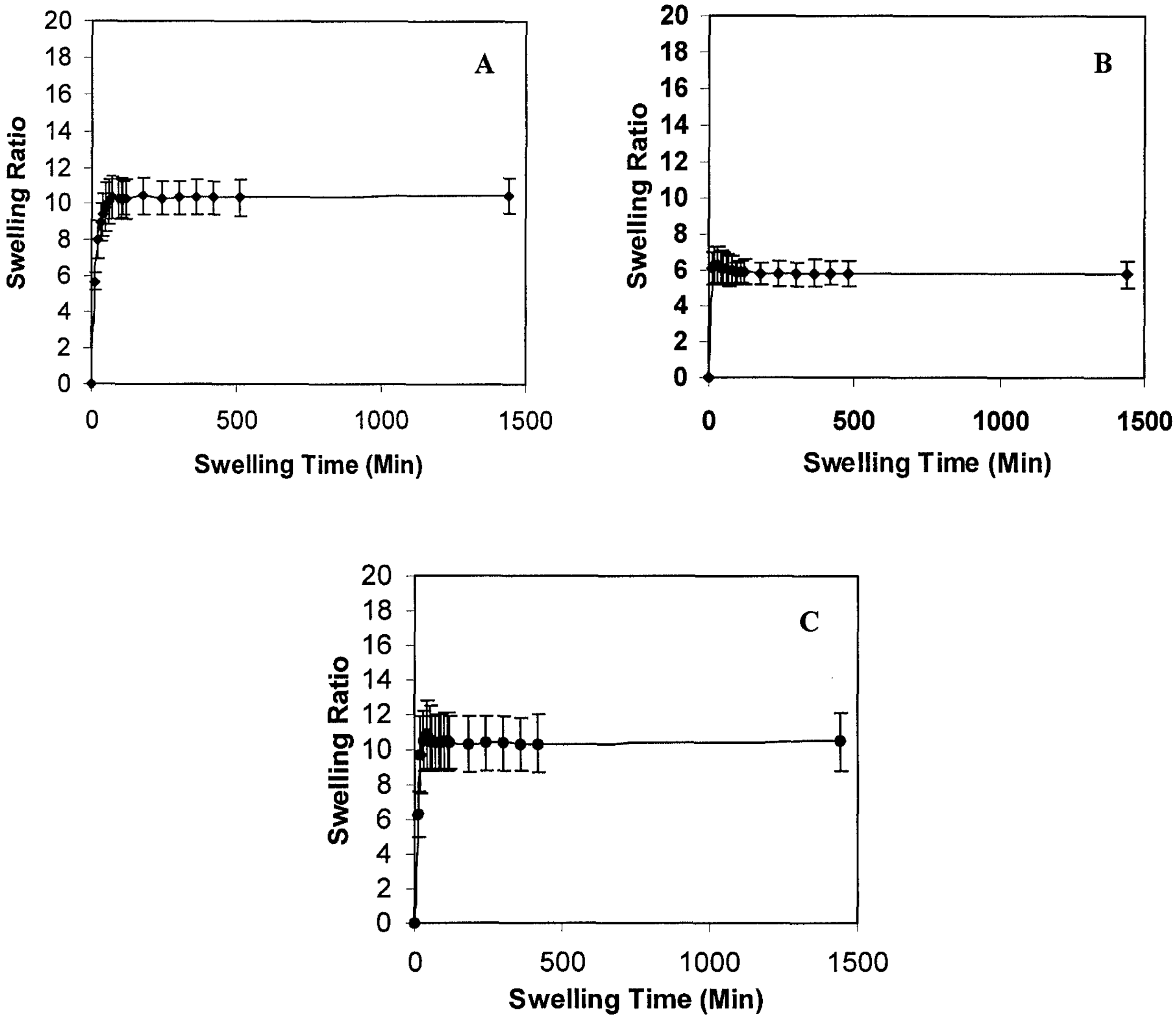

Figure 14. Time profile of swelling of (**A**) unmodified hylan gels, (**B**) oven-dried and then UV-irradiated gels, and (**C**) oven-dried gels. All gels were reconstituted in water after treatment, and lyophilized prior to swelling in serum-rich culture medium.

of cell attachment (1 μm). Such large-scale texturing is therefore insufficient to overcome the effect that negative charge has on cell adhesion. Irradiation with low-wavelength UV light was found to produce a fine honeycomb-like pattern of ridges and cracks on the hylan gel surface. The ridges were approximately 1 μm across and likely provided anchorage for the cells since cells aligned along them. Cells attached and proliferated readily atop the UV-irradiated gels, demonstrating highly extended and irregular morphologies, quite unlike the rounded or spindle-shaped cells that adhered sparsely to unmodified (C-type) hylan gels. However, cells did not migrate into the interior of the gels unless they had been dried prior to irradiation. Confocal microscopy demonstrated that UV irradiation after dehydration transforms the apparently featureless hylan matrix into one filled with irregular pore-like structures. Therefore UV-irradiation was much more effective in penetrating the dehydrated gels than it was on fully swollen, hydrated gels due to the smaller thickness of the former (< 100 μm vs. < 1000 μm).

Besides physical and textural cues, cells are known to respond to various biochemical stimuli that are part of the substrate. The FACE assays showed the presence of new chemical species. Since the total intensity of the bands in the lane loaded with crosslinked hylan gel was roughly 10% of the intensity of the single ΔDiHA band from the lane loaded with uncrosslinked HA, it can be assumed that only 10% of the total HA of the crosslinked gel is digestible by HSD. Ultraviolet irradiation reduced the digestibility of HA further, with the greatest reduction in digestibility occurring after the first 12 hours of UV exposure (Table 1). This suggests that UV-induced crosslinks reinforce the hyaluronan molecule, making it resistant to digestion. To confirm crosslinking, the tensile properties of irradiated and non-irradiated hylan gels were compared. Irradiated gels however were more elastic, less stiff, and failed at lower stresses than the non-irradiated hylan gels. This suggests that any reduction in HSD digestibility of the gels, caused by UV-induced crosslinking, was overcome by a physical break-up of the structural DVS-crosslinks that are responsible for the mechanical properties of the gels. Earlier studies by others have suggested that other forms of irradiation such as gamma rays, cause some breakdown of HA chains [13].

Even though UV-irradiated gels were weaker, the presence of UV-induced crosslinking was confirmed through FACE. Besides exhibiting reduced HSD digestibility, irradiated samples also produced new HA fragments. These new, non-ΔDiHA fragments could have been produced directly by UV-induced breakdown of HA or indirectly upon enzymatic digestion of UV-irradiated HA. However, FACE assays performed on the non-HSD-digested samples of irradiated hyaluronan also produced a ladder of various lengths of new HA fragments, thus confirming that UV alone can breakdown the HA molecule. These findings are supported by previous work, which showed that microbial hyaluronate depolymerizes upon exposure to UV light, producing shorter saccharide chains. The cause of the reduced HSD digestibility following UV irradiation remains unknown, but is likely related to the presence of new UV-induced crosslinks within the gel.

One potential concern in modifying hylan gels to enhance cell adhesion is the loss of biocompatibility. Certainly, one possible reason that crosslinked hylan gels are so biocompatible is that cells do not recognize and adhere to their surface. The generation of new non-ΔDiHA fragments could potentially reduce the biocompatibility of the gel. Fortunately, the absence of non-ΔDiHA bands on the FACE gel, except at very high camera exposure times, demonstrated that the new HA fragments are produced in very small amounts. This result was expected considering the fact that only a small fraction of the HA is digestible, and also because of the lower penetration of UV light into the gel, relative to uncrosslinked HA. The swelling experiments performed on unmodified (C-type) and DUV gels with identical compositions showed clearly that the unmodified gels hydrate to give swelling ratios approximately 40% higher than that of the DUV gels. The lower water content of the UV-irradiated gels is strongly indicative that they have a decreased swelling capacity when compared to the unmodified gels.

While the specific physical and molecular mechanisms behind the much enhanced attachment and proliferation of cells atop and within UV-irradiated hylans relative to non-irradiated control gels are beyond the scope of this manuscript, we propose two possibilities. The first is that UV-induced ridges and cracks both atop and within the gel provide anchorage for cell attachment, while the crevices allow cells to infiltrate into the gel. The second may be that the new HA fragments created by the UV-induced breakdown of HA elicit a cellular response. This mechanism is supported by the results of earlier studies that have shown that different saccharides elicit very different responses from cells, in a cell-specific manner [14,15]. Further studies are necessary to establish that UV irradiation of crosslinked hylan gels is not detrimental to its biocompatibility.

Conclusions

The significance of this work is that we have developed a technique for the modification of DVS-crosslinked hyaluronan (hylans) to enhance its performance as a cellular scaffold for tissue engineering applications. Depending on the treatment, cells can be either confined to the surface of the gel, or be induced to infiltrate into the interior. Since the hylan gels are altered structurally and chemically, binding of cells to the material is likely to be more permanent than possible by other approaches, such as coating of cell-adhesive matrix factors on the gel surface, described previously.

Evaluation of the synthesis of an extracellular matrix (ECM) by cells attached on hylan gels via quantitative and qualitative experiments

The unique mechanical characteristics of native aortic valve cusps are a result of their complex multilayered morphology (Fig. 15). The fibrosa, composed mainly of collagen bundles, is the primary load-bearing layer of the tissue. The ventricularis contains elastin sheets and fibers that keep the fibrosa in a compressed state. The central spongiosa layer contains glycosaminoglycans (GAGs) that keep the cusp hydrated, and permits shear between the fibrosa and ventricularis during tissue loading and unloading.

The mechanical properties of valve tissues are dependent on the amounts and distribution of the above three primary structural extracellular components. A major goal towards development of tissue-engineered valves is mimicking the components and structure that contribute to the unique mechanical properties of the native tissue. The hylan scaffolds that we use have remarkable mechanical versatility but may require additional reinforcement with the above structural molecules. Our approach to engineering of the aortic valve is to integrate the above essential components into a composite cusp, once each has been fabricated separately *in vitro*. The immediate goals of this project are to fabricate a spongiosa-like layer using hyaluronan, and then stimulate cells seeded atop this layer to synthesize elastin sheets and fibers with morphology similar to that of the ventricularis (Fig. 16).

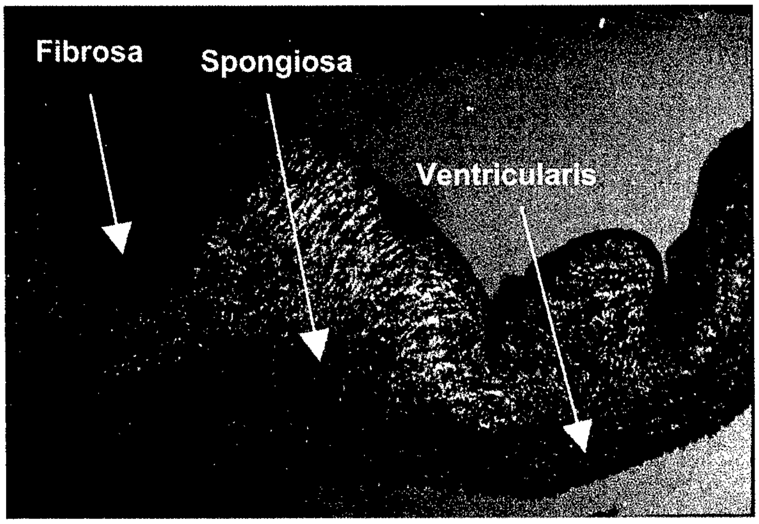

Figure 15. Multilayered morphology of the aortic valve cusp.

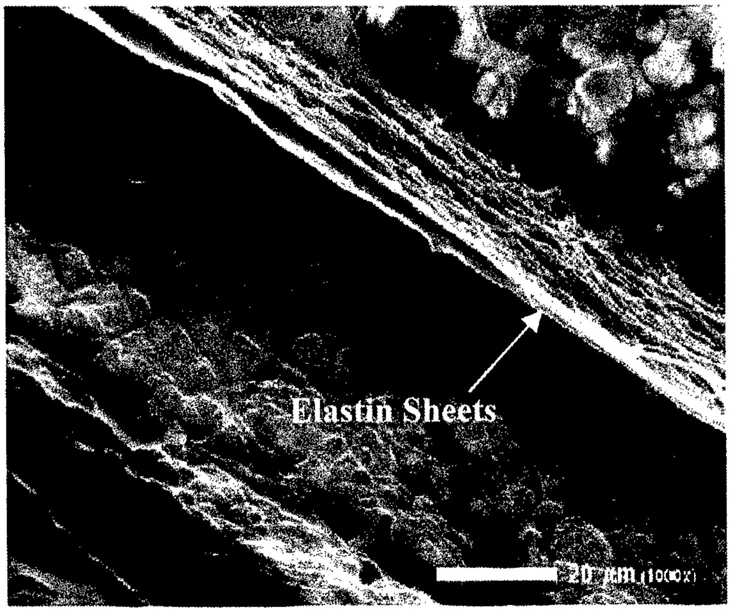

Figure 16. SEM image showing elastin in the ventricularis organized into sheets.

The progression of this project has been planned so as to address the following specific aims towards the fabrication of extracellular matrix–reinforced hylan scaffolds. The two major aims of this study are to:

(i) Select a cell type based on ability to synthesize large amounts of collagen and insoluble elastin. Compare ECM synthesis by cells cultured on hylan and non-hylan substrates.

(ii) Characterize the types, amounts, and orientation of extracellular collagen and elastin synthesized by cells cultured on unmodified and UV-irradiated hylan substrates.

Methods

In the first year of this study, neonatal rat aortic smooth muscle cells were cultured in petri dishes over varying lengths of time. These cells were selected since they were previously reported to prolifically synthesize collagen and elastin, important to the goals of this study. Collagen and elastin were quantified over culture periods ranging from 1 – 5 weeks. Our initial studies showed that the cultures could be induced to produce significant amounts of collagen and elastin. Collagen was deposited into the matrix in measurable amounts only post 6 weeks of culture. Cells however started synthesizing both soluble tropoelastin and insoluble elastin within 1 week of seeding. We determined that by supplementing the culture medium with Copper (II) ions (5 μM), elastin synthesis could be shifted in favor of production of insoluble elastin (Fig. 17A, B).

Previously, we used TEM to determine the structural form and distribution of elastin and collagen secreted by cells in culture. Since then, we cultured cells atop hylan gels that were coated with cell adherence matrix factors such as collagen and fibronectin. Extracellular matrix synthesis by cells cultured on hylan gels was investigated. Cell layers on hylans were treated with primary antibodies against rat elastin, which was visualized using a Texas Red fluorophore conjugated to a secondary antibody. Cellular actin was labeled with Alexa 488 Phalloidin while the nuclei were labeled with DAPI.

Cell Culture

Neonatal rat aortic smooth muscle cells were selected for study due to their demonstrated ability to prolifically synthesize elastin [9]. Cells (passages 6 – 8) suspended in DMEM: F12 (containing 10% FBS and 1% penicillin-streptomycin) were seeded atop the hylan films at a count of 4×10^6 cells/gel (Culture area = 100 mm^2; n = 3) and cultured for up to 6 weeks.

Biochemical assay for elastin synthesis

Cell layers atop hylan films were harvested and assayed for elastin at 2, 4, and 6 weeks of culture. Cell layers were trypsinized with 0.25% Trypsin-EDTA for 15 minutes, at 37 °C, scraped off the films, and then centrifuged with culture medium to isolate a pellet containing hylan and cells. The pellet was dried in an oven at 110 °C, weighed, and then re-hydrated with distilled water. After another cycle of centrifugation and drying, the pellet was digested with 0.1 M NaOH (98 °C, 48 hours). The long period of digestion was necessary to breakdown the large amount of crosslinked hylan. Matrix elastin alone survived digestion, and was pelleted, weighed, solubilized with oxalic acid (0.25 N, 95 °C, 1 hour, 3 cycles) and finally quantified using a dye-binding Fastin Assay (Accurate Scientific and Chemical, Westbury, NY). The digestate was also assayed to quantify any matrix elastin that was leached out during digestion.

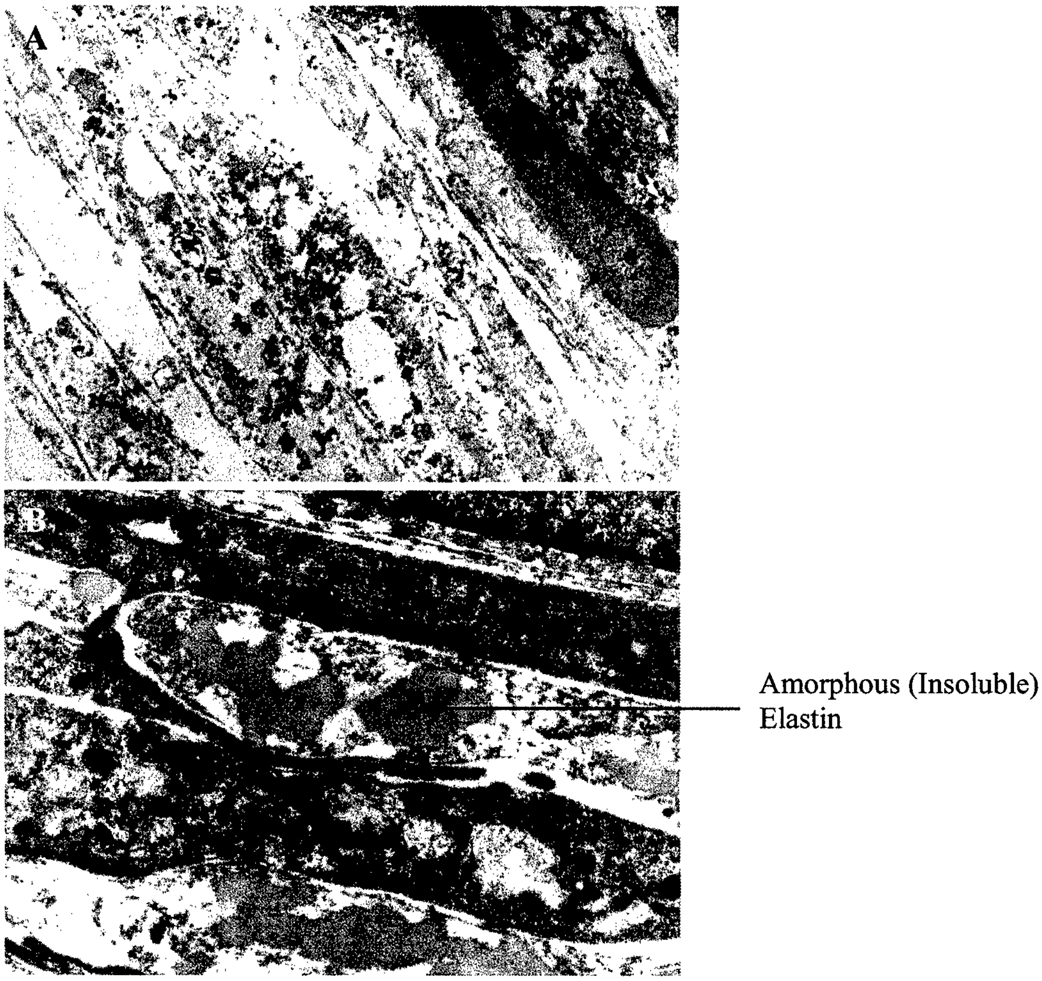

Figure 17. **A.** TEM of neonatal rat aortic smooth muscle cell layer (4600X). Cells were cultured for 3 weeks. A very low percentage of the elastin synthesized by the cells is present in the form of insoluble elastin. **B.** TEM of neonatal rat aortic cell layer showing the presence of amorphous (non-fibrillar) elastin. Cells were cultured for 3 weeks in the presence of 5 μM Cu^{2+} in the culture medium. Copper promotes crosslinking of elastin synthesized by cells and renders it insoluble. Magnification: 13,000X.

Microscopy

Segments of hylan films (< 100 μm thin) with adherent cell layers (at 4 weeks) were immobilized on a steel holder and digested in 0.1 M NaOH (20 minutes, 75 °C). Elastin samples surviving the digestion were frozen in a – 80 °C freezer overnight and then rapidly quenched in a bath of liquid N_2. Samples were lyophilized and then sputter-coated with gold for 90 seconds. Cell-free hylan films and detached 4-week old cell layers from petri dishes were also digested similarly and processed for SEM. For TEM, gels with adherent cells were fixed with a 2.5% solution of glutaraldehyde in sodium cacodylate buffer. Samples were post-fixed in OsO_4 in sodium cacodylate, and then dehydrated in a graded series of ethanol solutions. Samples were then embedded in araldite following which thin sections were cut in the plane perpendicular to the substratum. Sections were mounted on a grid and stained with uranyl acetate and lead citrate. Cell-free hylan films and non-irradiated hylan films were used as controls.

Results

Elastin synthesis within culture dishes

Neonatal rat aortic smooth muscle cells cultured on petri dishes deposited large amounts of insoluble elastin starting one week to ten days after seeding. Elastin was deposited mostly in a disorganized amorphous form. Organization into fibers, responsible for tissue elasticity, was limited. In comparison, elastin in valvular tissues is highly organized into fibers (Fig. 18). At 3 weeks, immunolabeling studies performed on cell layers atop collagen-coated particulate hylan gels also showed uniform distribution of what appears to be amorphous elastin. Transmission electron microscopy performed on 7-week old cell cultures on UV-exposed gels confirmed the presence of multiple cell layers. Interestingly, uniform basement matrix formed the interface between these cell

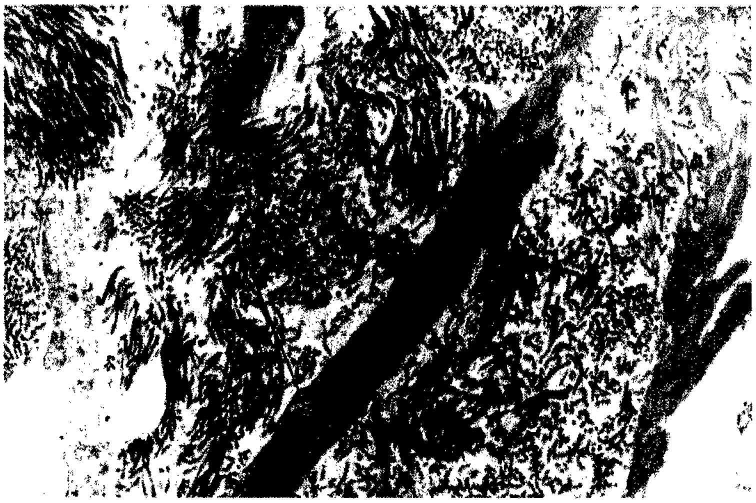

Figure 18. TEM image showing elastin organized into fibers.

layers and the gel surface. The appearance of the matrix in regions resembled previously obtained images of amorphous elastin deposits in dish cultures. The thickness of this layer was approximately 10 – 12 μm.

Elastin synthesis atop hylan substrates: biochemical analysis

Elastin synthesized by cells atop irradiated hylan gels was incorporated into the extracellular matrix in increasing amounts over the period of culture (Fig. 19). At, 2 weeks, all the elastin was retained in the matrix. However, 17 ± 10% and 20 ± 1% of the matrix elastin in the 4- and 6-week old cell layers respectively, were soluble in alkali.

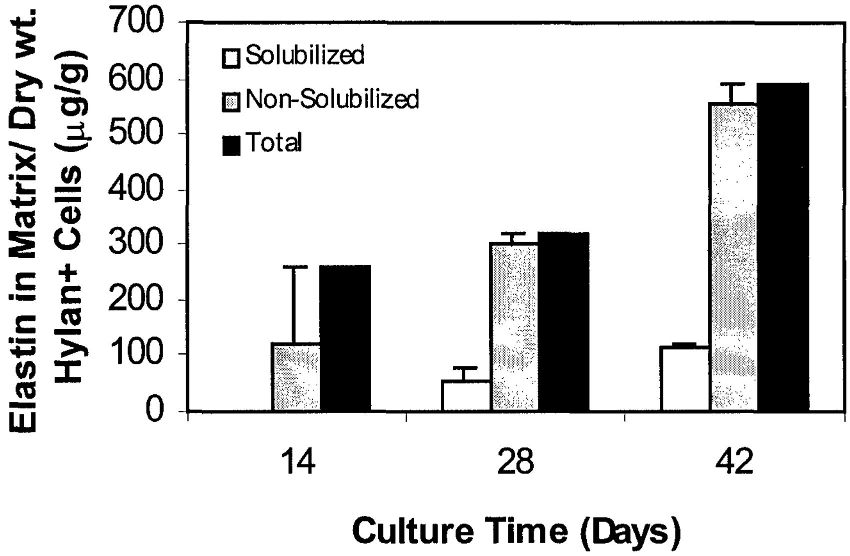

Figure 19. Elastin synthesis atop UV-irradiated hylan films.

Elastin synthesis atop hylan substrates: Microscopy

SEM of alkali-digested cell layers from petri dishes, or atop hylan films both showed the presence of fenestrated sheets (likely elastin) and of fibrillar elastin networks (Fig. 20). TEM images show multiple layers of cells atop hylan films. At 2 weeks, small clumps of amorphous elastin were deposited between cells. Also, the beginnings of thin basal layer of matrix (likely elastin) were visible at the cell-hylan interface (Fig. 21A). At 4 weeks, a much greater amount of elastin was found distributed between cells. A thick, well-defined basal matrix layer was also laid down which was roughly 25 μm thick by the 8th week of culture (Fig. 21B). Cell attachment and matrix were not observed on control hylan films.

Conclusions

Our studies indicate that neonatal rat aortic smooth muscle cells synthesize a large amount of elastin within 2 weeks, when cultured atop irradiated hylan films. Although most of the elastin is

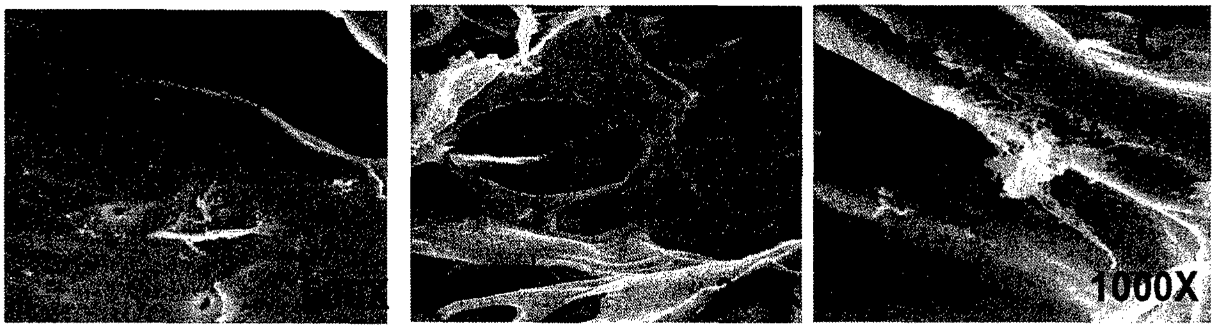

Figure 20. SEM images of elastin structures isolated by alkali-digestion of cell layers from petri dishes (**A**) or hylan films (**B**, **C**). Fibrils, likely fibrillar elastin, were also seen (**C**).

present as sheets, some elastin fibrils were also seen. In future work, biochemical and mechanical stimuli will be provided to enhance elastin synthesis and obtain the desired ultrastructure. The study is promising towards the development of a tissue engineered aortic valve cusp.

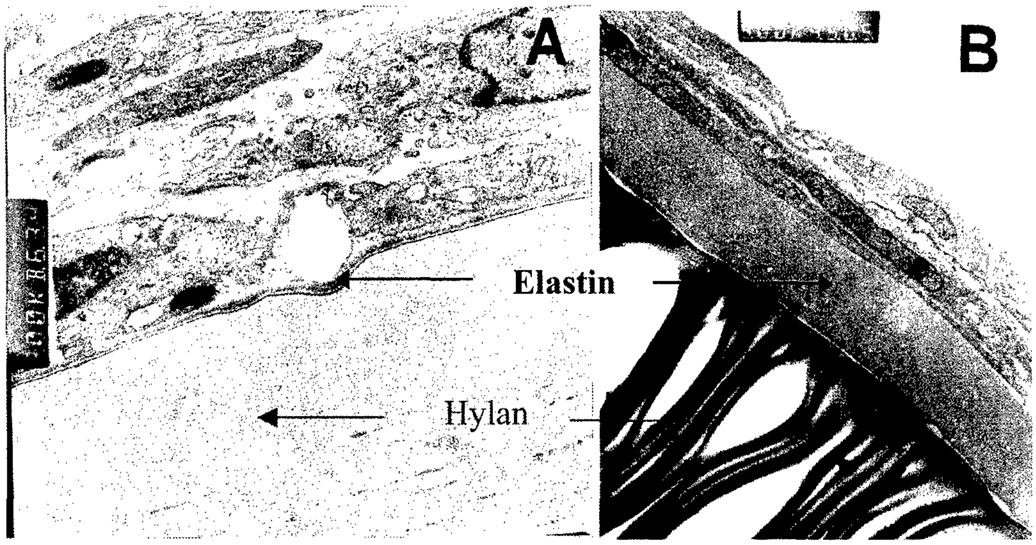

Figure 21. TEM images of elastin synthesized atop hylan films for (**A**) 2 wks, and (**B**) 8 wks of culture. Magnification: (**A**) 3000X, (**B**) 8000X.

Significance and future approach

Neonatal rat aortic smooth muscle cells were demonstrated to synthesize large amounts of elastin. However we determined that a low fraction of synthesized elastin is incorporated as a structural component of the extracellular matrix. By culturing cells in the presence of copper ions and other growth factors/stimulants we significantly enhanced production of insoluble extracellular elastin. We also showed that cells cultured on modified hylan gels are able to produce amorphous elastin and likely other matrix molecules. Since cells populate the interior of the hylan gels, it is also likely that an extracellular matrix is generated within the gels. While some fibrillar elastin is seen, most of the deposited elastin is in the amorphous crosslinked form. Thus, our immediate challenges are to develop methods to organize the deposited elastin into fibrillar networks as seen in native valve tissues. However, a great success of this work is that we have demonstrated that cells cultured atop hylan gels/films synthesize fenestrated hylan sheets similar to what we see in native heart valve tissues. The elastin synthesized atop hylan gels thus forms a composite structure resembling the combined structure of the spongiosa-ventricularis as seen in the aortic valve cuspal tissue. The results of this study establish that we can now create such a composite structure that may be integrated with collagen networks to create a composite tissue resembling the native valve cusp.

Development of a collagen fiber and elastin-reinforced composite hylan gel to replicate the multilayered morphology of aortic valve cusps

The aortic valve cusp, like most connective tissues, consists of collagen, elastin and glycosaminoglycans organized into structures that serve highly specialized roles. Our approach to tissue engineering the aortic valve has been to attempt to fabricate these structures individually and then assemble them into a functioning valve cusp. Such an approach has several attractive features, in that it:

(i) Does not require remodeling or regrowth of morphologically complex tissues.
(ii) Provides a matrix able to withstand cardiac load immediately upon implantation.
(iii) Can be designed and fabricated using engineering principles, rather than depending on unknown or uncharacterized biologic processes.

Thus far, we have been able to fabricate all of the basic building blocks that are required to assemble such a valve cusp. These are:

(i) Collagen fiber bundles, both straight and branched, of variable diameter.
(ii) Elastin tubes and sheets.
(iii) A viscoelastic glycosaminoglycan (GAG) matrix.

The viscoelastic GAG matrix is based on divinyl sulfone-crosslinked hyaluronan (hylan), the collagen fiber bundles have been fabricated using the principle of directed collagen gel shrinkage, and the elastin sheets and tubes have been grown on both the hylan and on the collagen bundles. Our ongoing research has three primary requirements. These are:

(i) Improvement in the mechanical properties of each of these components.
(ii) Definition of an optimal fabrication process for these components.
(iii) Assembly of the components to produce an aortic valve cusp with the appropriate mechanical function.

The specific aims for the assembly of this tissue engineered valve cusp are as follows:

Specific Aim 1: Develop collagen fiber bundles using the principle of directed collagen gel shrinkage.

Specific Aim 2: Develop a viscoelastic substrate to integrate the network of collagen fiber bundles and elastin sheets, using divinyl sulfone-crosslinked hyaluronan (hylan) that has been textured using UV-irradiation (see previous goals of the main project).

Specific Aim 3: Integrate the above three materials (collagen fibers, elastin sheets, hylan matrix) into a complete multilayered construct and evaluate its mechanical properties relative to those of native aortic valve cusps.

Summary of methods and results

Collagen fiber bundles

Collagen fiber bundles were fabricated using a method based on the principle of directed collagen gel shrinkage [17,18]. The principle involves first mixing soluble, fibrillar collagen with cells, neutralizing the mixture to induce gelation, and maintaining the system in culture. When the system gels, cells become entrapped within the collagen gel and begin to interact with the collagen fibrils [19,20]. These cells facilitate reorganization of the surrounding collagen matrix, contracting it and excluding water. In many ways, this in vitro contraction mimics wound healing *in vivo* [21]. When the gel is mechanically constrained from shrinking in one direction, the collagen fibrils align in the direction of constraint [20,22]. Highly aligned, compacted collagenous constructs can thus be fabricated. Since the fabrication of collagen fiber bundles is not part of the aims of this project, the fabrication methods will not be discussed in detail.

Within several hours of gelling, the collagen gel detached from the walls of the well and began to contract. Contraction was rapid initially, eventually slowed down but continued for up to 8 weeks. The original transparent gel became a dense, cylindrical construct with well-aligned collagen fibrils (Fig. 12). The rate of initial collagen gel contraction depended on cell type, cell seeding density, initial collagen concentration, and serum concentration. All of these parameters were optimized through exhaustive experiments. The final constructs had the typical non-linear stress-strain curve of tendonous materials, an extensibility of 14%, a stiffness of 5 MPa and failure strength of 2 MPa. Although the stiffness and strength are still an order of magnitude or more lower than what is required, our constructs are already 10 to 100 times stronger than similar collagen-based materials fabricated previously [23]. Ultrastructural analyses have shown that the main reason for the good strength of our constructs is the very high collagen fibril density. Because the constructs are relatively simple, one-dimensional collagen bundles, they compacted from two directions, producing an area shrinkage ratio that is greater than 99% (from an area of 324 mm^2 to less than 1 mm^2). When fully compacted, the collagen fiber density visually approaches that of mitral valve chordae. The obvious main differences are less collagen fiber crimp than is present in most collagenous structures and lower failure strength. We have had some success in inducing collagen fiber crimp in our constructs by controlling the tension applied upon them during shrinkage, but clearly not to the same degree as native tendon.

Since collagen fiber bundles in heart valves are branched, we have also attempted to fabricate branched structures, with encouraging results (Fig. 22). The key to these geometries is to ensure that tension is properly controlled during the shrinkage process so that the constructs do not tear away from the holders during the early stages. As the images demonstrate, different branching angles and parent/daughter ratios can be engineered with the use of appropriate molds.

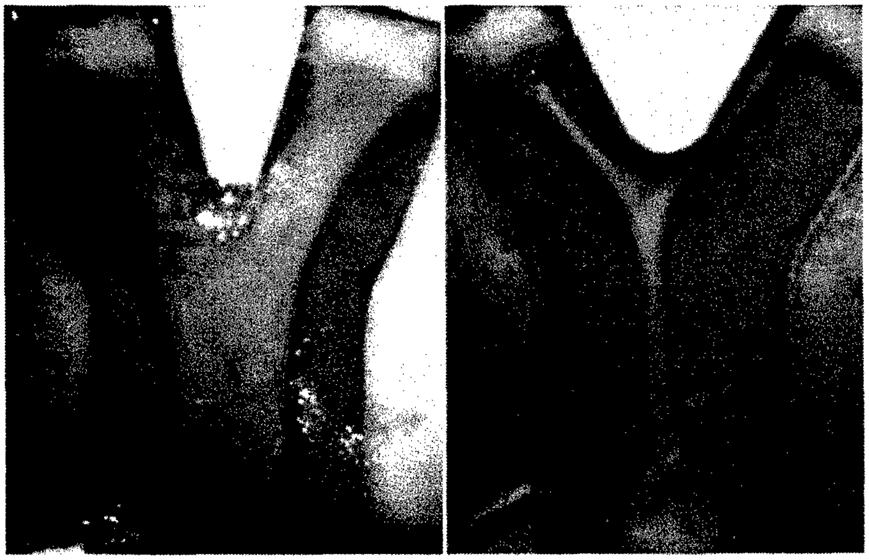

Figure 22. Images showing branched collagen constructs at 1 and 8 weeks of culture.

The final phase of this study will integrate the two separately cultured constructs (collagen bundles and elastin-hyaluronan composites) into a composite structure that is intended to mimic an aortic valve cusp. This next step will demonstrate that these technologies can be used together to achieve the desired goals. In our initial experiments, collagen constructs were fabricated using the method described above, and harvested at 3 weeks of culture. Hylan gels were formulated and cultured with neonatal rat aortic smooth muscle cells to confluence over a 2-week period. Thereafter, the collagen constructs were removed along with their end holders and pinned down into the cell-confluent hyaluronan-elastin composite and cultured for an additional period of 2 weeks. At the end of this period, the collagen-hyaluronan-elastin composite was cryofrozen in liquid nitrogen, lyophilized and then mounted on an SEM holder. The specimen was sputter-coated with gold and observed using a scanning electron microscope. In the limited culture period, the collagen construct gradually integrated with the confluent cell layer atop the hylan gel as seen in the SEM image (Fig. 23). In our ongoing experiments, which are being performed in quadruplicate, collagen fiber bundles at various stages of maturity (3 – 5 weeks old) were pinned onto hylan-elastin composites (3 – 5 weeks old) and cultured for time periods ranging from 3 – 5 weeks.

Conclusions

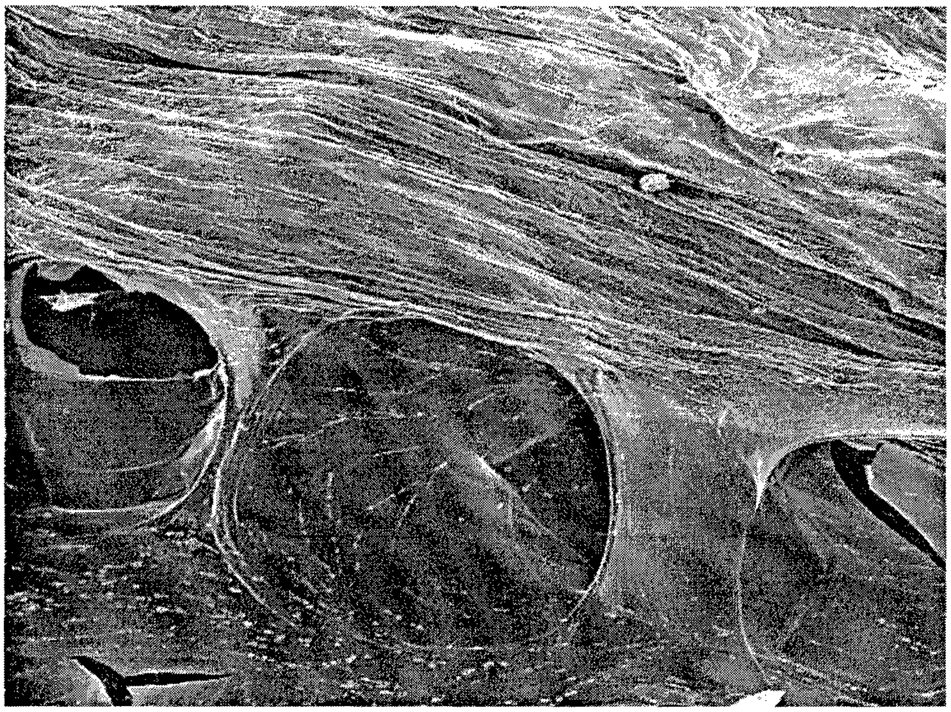

Figure 23. SEM image of collagen construct integrating with the hylan gel. Composite shown at 2 weeks of combined culture. Magnification 35X.

Although many of the methodologies have already been developed, some of the specific details of the integration are under development at this time. Encouragingly, we have found that the tissue layers appear to integrate on their own, when cultured in contact with each other. Some of the current unknowns are issues such as size of the entire construct, keeping in mind that the edges will need to be gripped by some fixtures to enable handling and pre-strain. It is also well known that the fibrosa is preloaded in compression in its central zone. The specific means by which this will be achieved is not yet clear. Most likely, we will preload the ventricularis layer in tension, allow the fibrosal layer to bond to it in culture for several days, and then release the tension on the ventricularis. Given our current level of experience in manipulating the geometry and matrix synthesis of our existing constructs and the additional experience we will obtain during the course of the first three phases, we expect to be able to overcome the majority of the challenges that are sure to arise in completing the fabrication for the composite valve.

TENDON MECHANOBIOLOGY – Project 5 (PI: Kathleen Derwin)

Over the 3 years of this grant we have worked to establish *in vitro* culture models of tendons, bioartificial scaffolds, and cells to investigate various metabolic parameters and their relationship to the mechanical loading environment of tendon. Included in previous reports were the development of various geometric, biochemical and biomechanical techniques for the characterization of tendon properties. Baseline data from a small number of tendons were included. Since that time, the geometric, biochemical and biomechanical variabilities of canine *flexor digitorum superficialis* (FDS) tendons have been assessed in a cohort of normal controls. Methods to harvest tendon explants under sterile conditions and quantify cell number and viability have been established. Investigation into the effect of no load, static load, and cyclic mechanical load on FDS tendon explants has been studied. A prototype loading-chamber that successfully maintains sterility in long-term organ culture has been designed and built. Finally, initial studies into the development of bioartificial tendon analogs comprised of isolated primary tenocytes cultured on and within porcine-derived small intestine submucosa (SIS) have begun. Details of the accomplishments of the 3-year granting period are now described.

Homotypic variation of canine flexor tendons

To date we have used canine *flexor digitorum superficialis* (FDS) tendons for *in vitro* organ culture studies (Fig. 24). Flexor tendons are a clinically relevant model in that in humans these tendons are involved in carpal tunnel syndrome [24], a condition believed to result at least in part from repetitive loading conditions [25]. FDS tendons have a high aspect ratio, lending themselves to mechanical loading experiments. Specifically, the two inner FDS tendon branches from the region of the tendon between the distal tarsal bones and the metacarpophalangeal joints were studied. We adopted the terminology medial inner (MI) and lateral inner (LI) to described these two tendon branches based on their anatomical location (Fig. 24A). Tendon segments can be readily isolated from the hind paws and cleaned of attached muscle and sheath material with the aid of a stereomicroscope (Fig. 24B, 24C, 24D). Although a flexor tendon model has been used in numerous organ culture studies [26,27,28], tendon variability in a cohort of normal controls has not been investigated. Canine FDS tendons were retrieved at sacrifice from 24 adult (24 – 30 kg) male mongrel dogs (four per dog, n = 96). Tendons were frozen at –20° C until analysis.

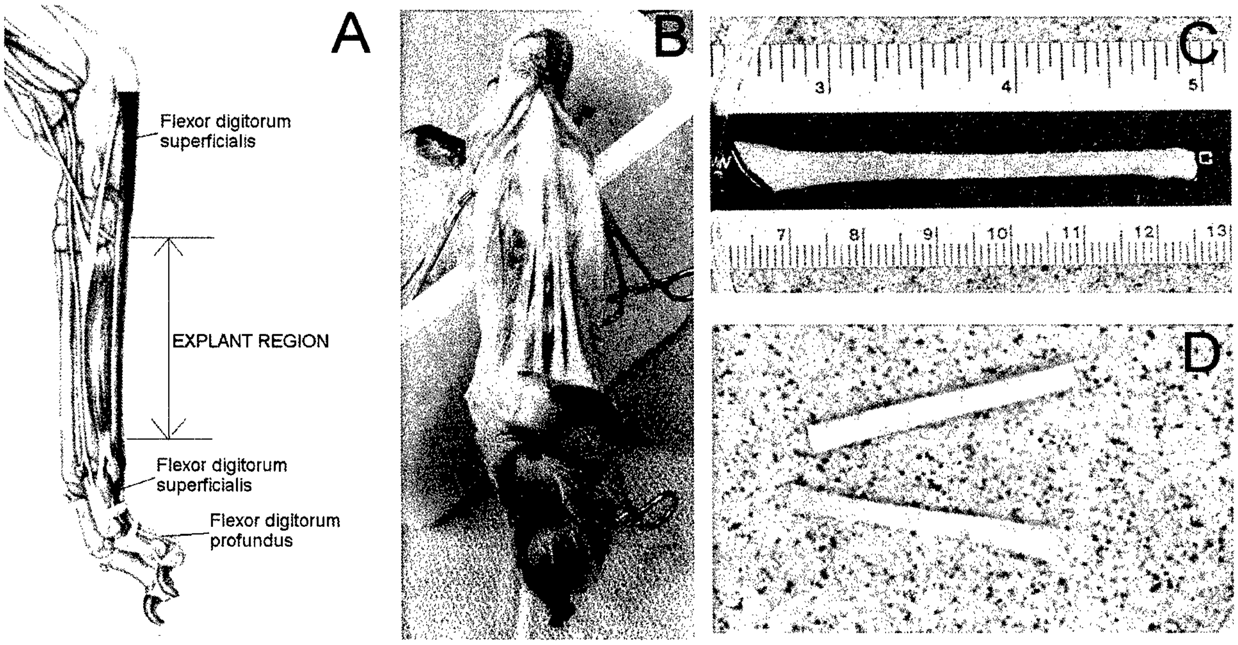
A
Flexor digitorum superficialis
EXPLANT REGION
Flexor digitorum superficialis
Flexor digitorum profundus
B
C
D

Figure 24. Anatomy and dissection of canine *flexor digitorum superficialis* (FDS) tendons. **A.** Lateral view of the canine hindpaw depicting the FDS tendon. Arrows denote region of tendon used for preliminary studies. **B.** Palmar view of canine hindpaw with the four branches of the FDS tendon exposed. **C.** An isolated FDS tendon segment. **D.** Two FDS tendon segments after being cleaned of muscle and sheath material and cut to 3.5 cm in length.

Forty-eight tendons were analyzed for biochemical variability, specifically water, collagen and chondroitin/dermatan sulfate glycosaminoglycan (GAG) content. From the mid-section of each tendon, two 4 mm segments were weighed, dried at 60° C for 72 hours and reweighed. Water content was determined by calculating the percent decrease in mass due to drying ($n = 96$). One segment from each tendon was hydrolyzed and analyzed for hydroxyproline content. Collagen content was calculated by assuming hydroxyproline is solely derived from collagen and is 13% of this protein by weight. The second segment was digested and analyzed for GAG content using fluorophore-assisted carbohydrate electrophoresis (FACE) [29,30]. We consistently observed that ΔDi4S was the predominant disaccharide present in the GAG chains, although measurable amounts of ΔDi6S and small amounts of ΔDi0S were also present (Fig. 25).

Additionally, forty-eight tendons were analyzed for geometric and biomechanical variabilities, specifically cross-sectional area, stiffness and elastic modulus. To measure cross-sectional area, tendons were clamped in custom grips (Fig. 26A), mounted in a custom device (Fig. 26B) and nominally tensioned and rotated 360° while viewed under a stereomicroscope. Cross-sectional area was estimated

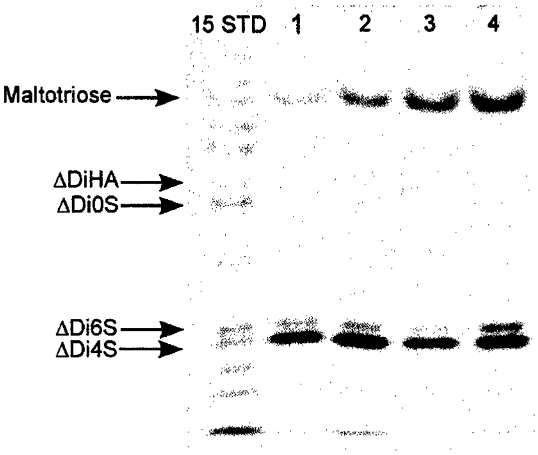

Figure 25. FACE analysis of canine FDS tendons to determine their glycosaminoglycan content.

from optical analysis of images captured during rotation. For mechanical testing, gripped tendons were then mounted in a testing tank containing physiologic saline at 37° C. Optical (surface) markers were placed on the tendons and tracked with a video system during the test. The optical system was synchronized with an Instron 5543 load system, such that load vs. local displacement curves were readily generated. Tendons were preconditioned 10X to loads representing 15 MPa stress, then tested at 10 mm/min to loads representing 30 MPa stress. Load and optical (local) displacement data were either plotted directly or normalized by cross-sectional area and initial gauge length to generate load-displacement or stress-strain curves. Stiffness was estimated from the linear portion of the load-displacement curve. Elastic modulus was estimated similarly from the stress-strain curve. The results for these analyses are presented in Table 3.

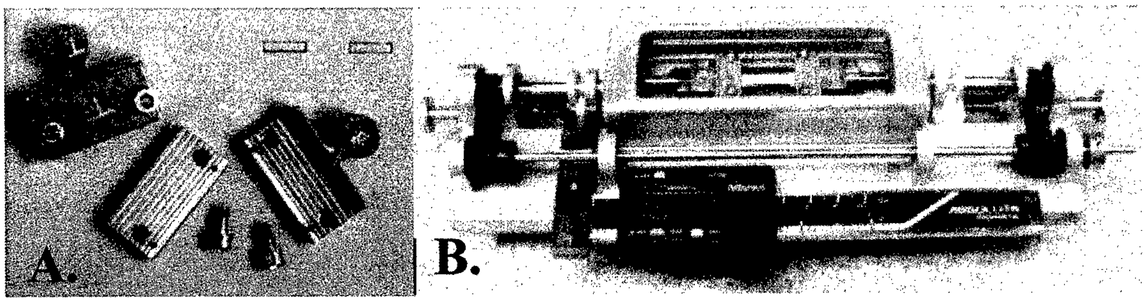

Figure 26. A. Custom sinusoidal tissue grips. **B.** Gripped FDS tendon mounted in custom device used for cross-sectional area determination.

Within- and between-dog variance in parameters was compared using the modified (median) Levene's test [31]. Within-dog variance includes both right-left (leg) and medial-lateral (tendon) variability. The variances of parameters normalized by tissue mass (i.e., water, collagen, GAG contents) or tissue geometry (i.e., modulus) were not statistically larger between-dogs than within-dogs. However,

Table 3. Variability of canine FDS tendons (n = 48, each parameter, except water content n = 96)

Parameter	Range	Mean ± SD	Within-dog variance[1]	Between-dog variance[2]	P-value[3]
Water content (%)	64.9 - 74.1	68.41 ± 1.86	1.04	1.30	0.19
Collagen content (%)	69.2 - 97.6	80.9 ± 6.63	4.5	5.2	0.41
GAG content (μg/mg$_{dw}$)	0.45 - 1.46	0.84 ± 0.24	0.14	0.18	0.15
Cross-sectional area (mm^2)	2.00 - 5.07	3.38 ± 0.68	0.31	0.55	0.005
Stiffness (N/mm)	467.5 - 1237.7	885. ± 166.5	88.2	132.0	0.030
Modulus (MPa)	729.8 - 1861.9	1319.0 ± 255.7	154.9	200.9	0.16

[1] Avg. absolute deviation from median of dog. [2] Average absolute deviation from overall median. [3] Levene's test for variances around median [31].

the variances of the non-normalized parameters (i.e., cross-sectional area and stiffness) were significantly greater between-dogs than within-dogs. In all cases, the within-dog variance was mostly from right-left leg comparisons. These results suggest that a paired, within-leg or within-tendon design would give optimal statistical power since variability between dogs and between legs within a dog would be removed. However, because the variability is not greater between dogs than within a dog, these data also suggest that it is appropriate to utilize a historical data set for controls as long as the sample size is chosen to provide sufficient power to detect differences. This latter design, though not optimal from a variance standpoint, is considerably more practical for the types of experiments we conduct.

In an additional eight fresh FDS tendon segments (7 mm), the cell number per unit tissue area was determined. Specifically, tendon segments were fixed in 10% zinc formalin for 48 hours and processed routinely for embedding in paraffin. Longitudinal sections were cut (4 μm), deparaffinized, rinsed with PBS and covered with Vectashield mounting medium (Vector Laboratories, Burlingame, CA) containing DAPI, a fluorescent DNA dye that stains cell nuclei. Sections were viewed with a Leica DMXRA motorized epifluorescent microscope equipped with an x-y-z stage to visualize the DAPI-positive nuclei. For each tissue section, a series of 590 x 430 μm digital images were captured (20X) and montaged (Fig. 27). Using custom software, DAPI-positive nuclei were counted and normalized by the imaged tissue area to give a representative cell density in fresh FDS tendon. The tissue cell density ranged from 393 – 657 cells/mm^2 (Mean ± SD = 546 ± 110).

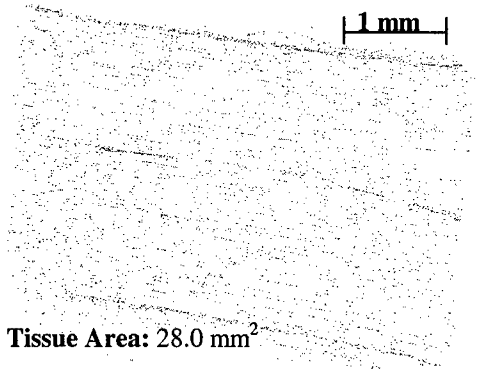

Figure 27. A montaged tissue section stained with DAPI to visualize cell nuclei.

The effect of no load and static mechanical load on canine flexor tendons

Our initial study into the effect of mechanical load on FDS tendons in organ culture is described here. Eight FDS tendon explants were retrieved aseptically as described previously. From each paw, two explants of 4.5 cm were harvested from the branches of the FDS tendon extending to the 3rd and 4th digits, in the region between the distal tarsal bones and the metacarpophalangeal joints. Each explant was divided into 3 segments. A 5 mm piece was immediately fixed in 10% neutral buffered formalin (NBF) and served as a fresh control. A second 5 mm piece was cultured in the absence of mechanical load. A third segment (3.5 cm) was placed in a custom device (Fig. 28) that utilized a spring to apply a constant static load to the tendon (200 - 500 g). With the tendons mounted, the actual spring displacements and explant cross-sectional areas were measured optically, and the applied stress on each tendon was computed.

Unloaded and statically loaded explants were cultured for 9 days in M199 containing 2% fetal bovine serum (FBS) at 37° C and 5% CO_2. Medium was supplemented with 1% antibiotic / antimycotic solution for the first 48 hours only and changed every other day. At the end of the culture period, a 5 mm segment from the center of each loaded explant's gauge length was harvested. Loaded and unloaded tissue segments were fixed in 10% NBF. Fresh, unloaded and loaded tissue segments were processed for routine histology, embedded in paraffin, and sectioned (4 μm).

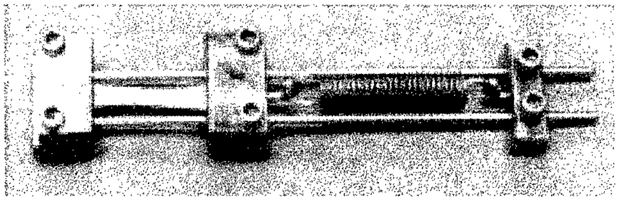

Figure 28. Device for applying static loads to tendon explants in culture.

From deparaffinized histologic sections, the TUNEL method was used to identify cells undergoing apoptosis, while DAPI was used to identify total cell nuclei. Fluorescent imaging of tissue sections was performed using a 1317 x 1035 Quantix 1401E 12-bit digital camera (Roper Scientific) attached to Leica DMXRA motorized microscope equipped with an x-y-z stage. Sections (20X) were viewed under wide interference blue (WIB) light to identify apoptotic nuclei (TUNEL-positive) and wide interference ultraviolet (UV) light to identify total nuclei (DAPI-positive). For each tissue section, twenty pairs of digital images (WIB and UV, each 590 x 430 μm) were captured and montaged. The images were collected using Metamorph software (v4.6). The montaged image area was 5.074 mm^2 inclusive and located in the central portion of each tissue section. From the montaged images, total cell number per mm^2 (DAPI-positive nuclei) was determined automatically using custom software, except for areas of clustered cells, which were masked and counted manually. Apoptotic cells (TUNEL-positive nuclei) were counted manually. Manual counts were done by at least two and as many as four independent counters depending on variability of the results. A percentage of apoptotic cells was computed as the ratio between total apoptotic cells and total cells. Repeated Measures ANOVA followed by a Bonferroni *post hoc* test was used to test for significant differences between groups ($p < 0.016$ required for significance).

One loaded explant slipped from its grips during the culture period and was excluded from analysis. No measurable creep was observed in the remaining loaded explants ($n = 7$) after 9 days of culture. The cross-sectional area of the loaded explants averaged 3.53 ± 0.69 mm^2 (Mean ± SD) corresponding to applied stresses of 0.4 to 1.4 MPa. Histologically, there were no gross differences observed among the groups. Tendon fibroblasts were ubiquitously distributed on all tissue sections. Spindle-shaped nuclei were seen arranged in rows or individually throughout the matrix (Fig. 29A). Regions of clustered, cuboidal nuclei were also observed on all sections (Fig. 29B). These clusters are indicative of intrinsic tendon vasculature.

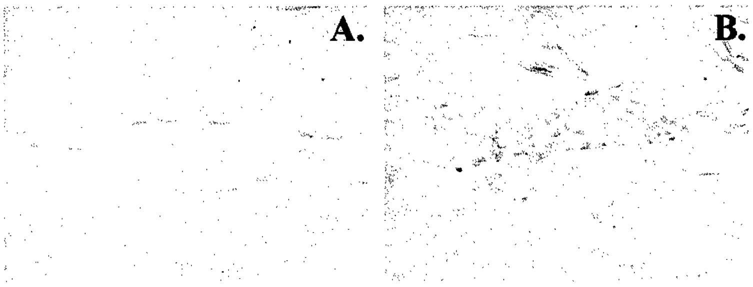

Figure 29. Hematoxylin and eosin (H&E) stained sections of cultured explants (40X). **A.** Spindle-shaped nuclei were seen arranged in rows or individually throughout the matrix. **B.** Regions of clustered, cuboidal nuclei were also observed on all sections.

Quantitative results are presented in Table 4. There was no significant difference in cell number per mm^2 between any of the groups. There was, however, a statistically significant increase in the percentage of apoptotic cells between the fresh and unloaded groups ($p = 0.01$). The increase in percent apoptotic cells between fresh and loaded groups was not statistically significant ($p = 0.03$) when the Bonferroni's correction for multiple comparisons was applied. No significant difference was found in the percentage of apoptotic cells between loaded and unloaded groups ($p = 0.97$).

Here we demonstrate a semi-automated method to quantitatively determine cell number and viability in tendon. Quantitating cell number in this manner provides a more physical description of cellularity than methods reporting DNA content per mg tissue or mg hydroxyproline. From our data the number of cells per tissue volume could also be estimated. Further, it is interesting to note that the cell number per mm^2 varied considerably even among fresh tissue specimens. Future work will investigate whether this variability is observed along the length of FDS tendons as well. The implications of differences in cellularity may be reflected by regional variations in tendon biochemical and/or material properties.

Table 4. Cell number and percent apoptotic cells in FDS tendon explants

Group (n = 7)	**Cell number per mm^2** (Mean ± SD)	**Apoptotic cells (%)** (Mean ± SD)
Fresh	666 ± 166	0.06 ± 0.07
Unloaded	584 ± 106	1.93 ± 0.97*
Loaded	660 ± 122	1.96 ± 1.71

* = Significantly different from fresh.

Although the percentage of apoptotic cells was higher in the cultured tendons (unloaded and loaded) than fresh tissue, we argue that the difference in practice is negligible. We conclude from our data that cell number and viability are essentially maintained similar to fresh tissue in tendon explants cultured for 9 days in the presence or absence of low levels of static load under the conditions described. It is acknowledged that longer culture times may have revealed that an increasing proportion of the cells in one or both of the cultured cases become apoptotic. However, for culture times on the order of one week the cells appeared to be maintained. These results provide the basis for our future studies investigating the response of tendon fibroblasts to various load magnitudes, frequencies and durations.

Development of a device for applying cyclic mechanical load to tendon explants and cell-seeded constructs

A bioreactor device for applying cyclic mechanical loads to tendon explants and cell-seeded scaffolds has been built in our laboratory. This bioreactor allows explanted tendon or scaffold segments of 1 – 3 cm in length to be clamped in custom grips and mounted in stainless steel chambers (Fig. 30A). A faceplate with a silicone gasket seals the chambers and allows for visualization of the specimens (Fig. 30B). The chambers interface with a stainless steel stopcock and septum for medium changes. A stainless steel lid attaches to the upper grip assembly and translates with it. For cyclic loading, chambers are individually placed on a loading frame. Otherwise, the chambers are placed on stainless steel stanchions where they are subjected to continuous, low, static load (Fig. 30B). For cyclic loading, the chambers interface directly with custom electronics to apply controlled mechanical loads to the cultures in a controlled incubator environment (Fig. 30B). The system consists of a load cell (Sensotec, Inc., Columbus, OH), linear stepping motor (Haydon Switch and Instrument, Waterbury, CT), and motion controller and power drive (Intelligent Motion Systems, Inc., Marlborough, CT). The stepper motor and load cell reside within the incubator on the loading frame. The stepper motor allows 2 cm of linear displacement with an accuracy of ± 10 μm. The load resolution is 0.1% of the full scale of the load cell used (10 or 100 lb). Cycling frequencies of 0.1 to 5 Hz are possible. The motor and load cell cabling exit the incubator via a sealed pass-through and connect to the power drive and control electronics. The system is controlled by a desktop computer interfaced to a PCI AIAO board (Measurement Computing, Middleboro, CT) for data acquisition and waveform generation. Custom software has been written in Visual Basic to allow variable command signals and data acquisition sequences.

Figure 30. **A.** Gripped tendon mounted in an open chamber. **B.** Assembled chambers in the incubator: static loading stanchion (right) and custom loading frame with electronic computer interface (left).

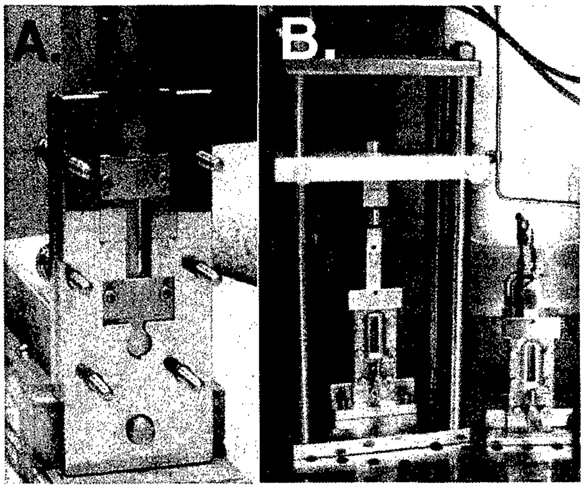

Specimens can be cycled in displacement or load control, at user specified magnitudes and frequency, in one of three waveforms: sine, triangle, or triangle with hold. We are currently modifying the system from a static culture to a flow-through design to take advantage of bulk flow and gas permeable tubing to improve nutrient and oxygen delivery to the cultures. We are also designing and fabricating multi-sample chambers to increase our testing capacity. Pilot studies have been undertaken to evaluate gripping torques and mechanical and electrical performance.

Several novel aspects of the design of our device should be noted. First, the 2 – 3 ml chamber volume allows use of expensive medium supplements or radioactive precursors to be practical. Second, explants can be cycled in load control at loads customized to the cross-sectional size of an individual tendon. In this manner, *in vivo* loads/stresses measured in tendons during various activities can be directly modeled. Third, loading conditions with variable waveforms are possible: (a) sine wave -- all of the energy at the primary frequency [32] (b) triangle wave -- simplest for digital control, and (c) triangle with hold -- approximates the *in vivo* loading profile of some tendons [33,34]. Fourth, variable length tendons may be tested (1 – 3 cm gauge length).

The effect of dynamic load on canine flexor tendons

In one pilot study utilizing the loading device, four FDS tendons were aseptically harvested from an adult mongrel dog and clamped with 20 in-oz. torque leaving a 2 cm gauge length. Gripped tendons were placed in loading chambers and cultured for a total of 72 hours. All tendons were assumed to be 3 mm^2 in cross-sectional area. Specimen 1 was cycled (1 Hz triangle, 6 – 30 N) during the first 6 hours of Day 1, and specimen 3 was cycled at the same conditions during the first 6 hours of Day 2. Specimens 2 and 4 were not cycled and served as controls. If or when not being cycled, specimens were submitted to a constant static load of 50 g. Specimens 1 and 4 were cultured in medium M199 without FBS on Day 1, while specimens 2 and 3 were cultured in M199 without FBS on Day 2. Otherwise, M199 was supplemented with 2% FBS. Culture medium was collected daily and frozen at –80° C. Samples of collected culture medium without FBS were used for gelatin metalloproteinase (MMP) evaluation by zymography and a fluorescent-protein conjugate digestion assay (EnzChek™, Molecular Probes, Inc., Eugene, OR). A tissue sample from each tendon was processed for histologic assessment of cell number and viability.

All cultured tendons showed increased MMP-2 in the medium, all in the pro- or latent form (Fig. 31A). MMP-9 was not detected. Pro-MMP-2 was greater in the medium from unloaded tendons (#4, #2) than their respective loaded pair (#1, #3). As expected, the fluorescence assay did not show any net gelatinase activity in the medium samples. A bacterial collagenase positive control was run with both the fluorescence digestion assay and zymography to confirm that the sensitivities of the two methods were similar. Both methods are able to detect enzyme activity as low as 5 X 10^{-3} U/ml (Fig. 31B). At this time we have not analyzed MMPs/TIMPs in the tissues themselves, nor investigated levels of the collagenases (MMP-1, MMP-13, MMP-14) or stromelysin (MMP-3), so these preliminary results are difficult to interpret. They do, however, demonstrate the utility of these methods for assessing MMP production and net proteolytic potential.

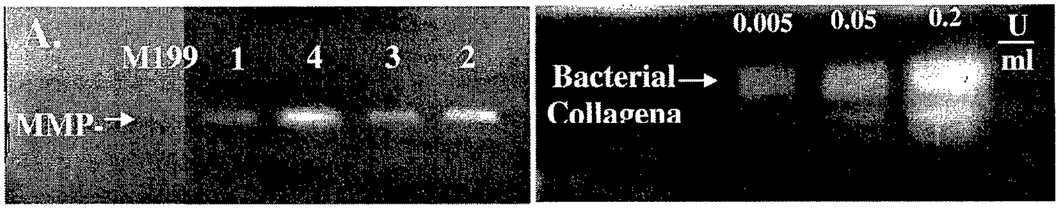

Figure 31. MMPs and cellularity in cultured tendon samples. **A.** Gelatin zymogram showing MMP-2 expression in all samples. **B.** Gelatin zymogram showing sensitivity of technique.

Natural biomatrices as scaffolds for tendon tissue engineering

Small intestine submucosa (SIS)

We have begun investigations of porcine small intestine submucosa (SIS) as a natural bioscaffold for tendon tissue engineering. Depuy Orthopaedics, Inc. (Warsaw, IN) supplied funding and the SIS for our initial pilot study. The in vivo studies are now described.

When natural (bioresorbable) scaffolds are used as grafts for replacing functional tissues such as tendon, the goal has been to maximize the strength of the graft. However, this goal must be balanced by the biologic requirements of cell attachment and migration into the scaffold, as well as appropriately timed scaffold resorption. With a canine flexor digitorum profundus (FDP) tendon (Fig. 33A) application as our objective, various configurations of SIS grafts were designed and fabricated including layered, braided, twisted, and wrapped designs. Various processing (drying) methods were also assessed including air, vacuum and lyophilization drying. SIS grafts were mechanically tested and compared to fresh canine flexor tendon. Briefly, grafts or tendons were mounted in a testing tank containing physiologic saline at 37° C and tested at a rate of 10 mm/min to failure. Stiffness was estimated from the linear portion of the load-displacement curve and failure load as the first peak of the curve. An example of our biomechanical data is presented in Table 5. Figure 32 shows load-displacement plots of various SIS graft configurations and an FDP tendon. Regardless of the configuration, all SIS grafts were an order of magnitude less stiff and strong than fresh FDP tendon. Based on these data, an *in vivo* animal model has been chosen that allows the graft site to be immobilized (casted) and only passively loaded for the evaluation of SIS as a bioscaffold for tendon repair.

Sterilized porcine-derived SIS grafts are being assessed for flexor digitorum profundus (FDP) tendon replacement in a canine model (Fig. 33A) [35]. The SIS grafts consist of a 25-layer, vacuum dried inner core that is subsequently wrapped with a piece of hydrated SIS and lyophilized (implanted product is fabricated and sterilized by Depuy Orthopaedics, Inc.). The graft dimensions are

Table 5. Mechanical properties of SIS grafts		
Experimental Groups	Stiffness (N/mm)	Failure Load (N/mm)
Group I: 25-layer core, wrapped, vacuum-dried/lyophilized (n = 2)	5.4 ± 0.05	27.5 ± 2.5
Group II: 25-layer core, wrapped, air dried (n = 3)	6.6 ± 2.8	80.8 ± 7.0
Group III: Twisted core, wrapped, air dried (n = 3)	4.4 ± 0.1	72.2 ± 4.9
Group IV: Twisted core, wrapped, vacuum-dried (n = 3)	4.1 ± 0.8	70.0 ± 4.4
Fresh FDP (n = 8)	63.0 ± 2.8	216.5 ± 23.6

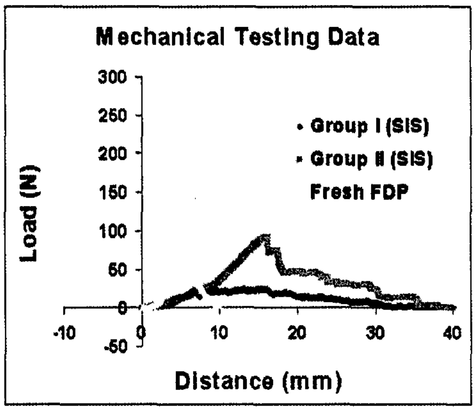

Figure 32. Representative mechanical testing data of fresh FDP tendon and SIS grafts.

approximately 2.5 mm wide by 1 mm thick. A 7 – 8 cm length of graft is used to replace the native FDP tendon in the intrasynovial region of the second and fifth digits of the left forepaw. The operated limb is casted, and rehabilitation consists of passive flexion of the wrist and digits at a rate of 0.5 Hz, twice daily for 5-minute intervals, 6 days/week, starting on the first postoperative day (Fig. 33B). At sacrifice the grafts are assessed by gross observation for adhesions/scarring, functionality, and healing. The grafted digits are then excised *en bloc* for histological evaluation (hematoxylin and eosin stained).

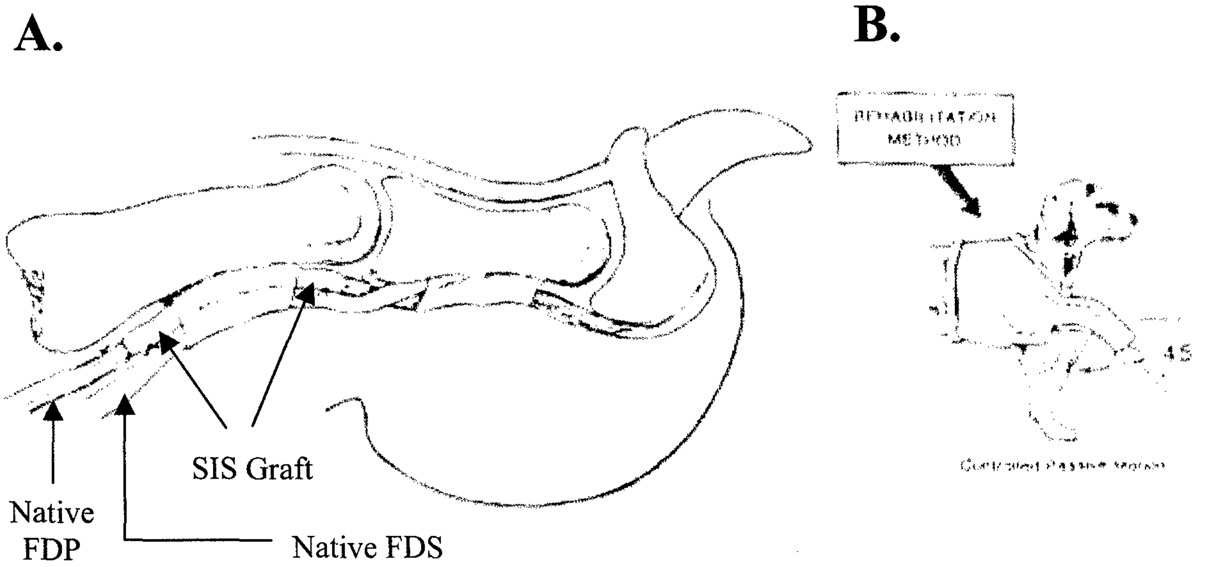

Figure 33. **A.** Representation of the FDP site (→) showing SIS graft replacement (→). FDS tendon is also shown (→). **B.** Demonstration of the immobilization casting method and passive motion rehabilitation [36].

Our initial results on the use of SIS as a biological scaffold for flexor tendon repair are encouraging. To date we have completed two animals in our study (n = 4 grafts at 3 weeks). Gross observation showed minimal to extensive scarring of the graft to adjacent tendons and tissues at the proximal repair site in all four digits. After removal of the scar tissue, however, the FDP/SIS could be readily differentiated from the adjacent FDS tendon. To evaluate functionality, the FDP/SIS and FDS were independently pulled to determine the degree of distal interphalangeal (DIP) joint motion contributed by each. In three digits the distal phalanx moved similarly whether pulling on the FDP/SIS or the FDS tendon. This suggests some scarring/adhesions between the tendons in these digits. Histologically, a mononuclear cell infiltrate was observed throughout the length and width of all grafts (Fig. 34). All grafts appeared to be well vascularized along their lengths. In some regions, the SIS appeared integrated with the adjacent FDS tendon, in others the SIS appeared to be distinct from the FDS. In all digits the proximal repair demonstrated direct apposition and integration between the native tendon and SIS. At the distal repair, the SIS appeared to be integrated with the surrounding tissue and the bony phalanx. The SIS grafts were sufficiently strong to withstand isometric muscle loads and loads introduced during passive motion rehabilitation.

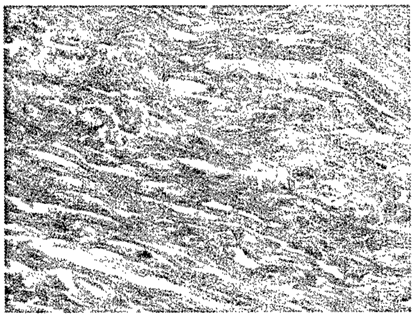

Figure 34. H&E stained section of SIS 3 weeks after implantation in a canine flexor tendon site (40X). A mononuclear cell infiltrate was observed.

An initial pilot study has been done to determine if cyclic mechanical load would improve the ability of cells to adhere and migrate into SIS (Restore®, Depuy Orthopaedics, Inc). Strips of Restore® were gripped in custom fixtures (Fig. 26A) leaving a 2 cm grip-to-grip gauge length for load cultures. Two centimeter length strips of Restore® were cut and kept ungripped for no load cultures. Prior to seeding, all scaffolds were rehydrated and conditioned for 4 hours in Dulbeco's Modified Eagles Medium – Low Glucose (DMEM-LG) supplemented with 1% antibiotics and 10% FBS. The wet scaffolds were then removed from conditioning medium, placed in specially designed silicone chambers, and statically seeded with an aliquot of primary canine tenocytes in order to achieve 1×10^6 tendon cells/cm^2. After 4 hours a small volume of fresh medium was added to cover the scaffolds, and the scaffolds were cultured for an additional 20 hours. Gripped/seeded scaffolds were then transferred to the chambers of a bioreactor for mechanical loading (Fig. 30B). No load cultures were kept in the silicone chambers. Cell-seeded scaffolds were maintained for 7 and 14 days under no load, static load or cyclic load conditions. The cyclic load constructs were cycled twice daily for one-hour intervals between 0 – 2 mm (0 – 10% strain) at 0.1 Hz. The static load cultures were subjected to 50 g continuous load. Scaffolds were cultured in DMEM-LG supplemented with 1% antibiotics and 10% FBS. Scaffolds were incubated in 5% CO2 at 37° C, and the complete medium changed three times per week for no load cultures and daily for load cultures.

The results of this preliminary study demonstrated that the application of mechanical load to cell-seeded Restore® SIS increased the number of cells that infiltrated the graft compared to the no load condition. In no load cultures, cells did adhere and layer along the surface of the scaffold but did not infiltrate the SIS (Fig. 34A). In cyclic load cultures, cells were observed on the surface of the scaffold as well as within the scaffold. The cells also had begun to align themselves along the direction of load (Fig. 34B). The results were qualitatively similar between static and cyclic load conditions.

Figure 34. DAPI stained sections to visualize cell infiltration (10X): **A.** 7-day no load construct, **B.** 7-day cyclic load construct.

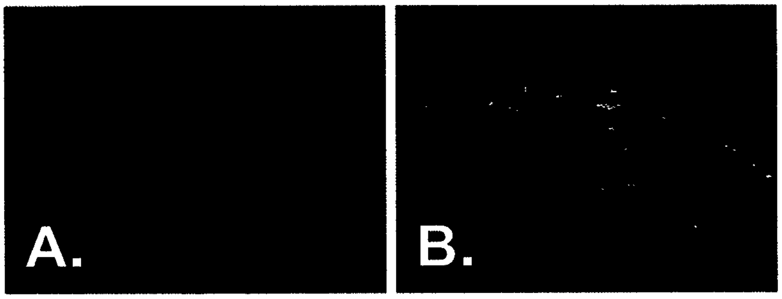

Hylan

Our initial studies into using hylan as a material for tendon tissue engineering have been motivated by the work described in ***Project 4*** (Aortic Smooth Muscle Cell Model). From this work, it was clear that fibroblast-type cells would not adhere to or penetrate pure hylan gels without surface modification. Based on this work, we have refocused our attention on the development of hylan coatings for potential applications related to anti-adhesive surface coatings. We have undertaken these investigations in collaboration with Ron Midura, Ph.D., and they are described in detail in ***Project 8*** (Optimizing Matrix for Attachment and Differentiation of Bone Precursors *In Vitro*).

Briefly, the inability of AKR1 cells to adhere to DVS crosslinked hylan coatings is demonstrated in Figure 31a (***Project 8***, p. 60, 2001 Annual Report). This result is comparable to the inability of rat neonatal aortic smooth muscles cells (SMCs) to bind to the unmodified surface of hylan gels (***Project 4*** - Fig. 1A, p. 14, 2001 Annual Report). Both the SMCs and AKR1 cells are lacking the CD44 receptor necessary to bind hyaluronan. Because tendon fibroblasts are also lacking the CD44 receptor, we hypothesize they also will not bind to hylan coatings. Future studies could include investigation of the binding capacity of inflammatory cells to cross-linked hyaluronan. These cells are associated with wound healing, and thereby the adhesion formation common to surgical repair of tendon injuries. Prevention or reduction of the formation of adhesions through the use of hylan coated tendon grafts could significantly reduce morbidity associated with recovery from these types of injuries. These studies have not yet been completed as significant time was invested into the development of the cyclic loading device as well as development of the *in vivo* tendon graft model. Should the progress of our collaborators (***Projects 4 & 8***) make such anti-adhesive coatings practical, we could employ them in conjunction with our SIS graft *in vivo* model.

Engineering Design

The Engineering Design and Analysis Group, under the management of Mark Goodin, M.S., has provided considerable support to the PI in the area of device development. Working closely with a design engineer in the group (Michael Nilsson, M.S., P.E.) as well as the Mechanical Prototype and Electronics Core Facilities, several new devices have been designed and manufactured. As described previously, grips for tendon mechanical testing (Fig. 26A), a device for mounting and rotating tendons to determine cross-sectional area (Fig. 26B), a device for applying static loads to tendon explants (Fig. 28), and a prototype loading device for tendon explant cultures (Fig. 30) have been developed. These devices allow the PI to make quantitative geometric and mechanical property measurements on tendons and tissue engineered constructs, as well as to study the effect of mechanical load on tendon fibroblasts.

Image Processing

The Image Processing Group, under the direction of Kim Powell, Ph.D., has provided considerable support to the PI in the development of software for the quantitative analysis of tendon histology and morphology. To date, four analysis programs have been written, verified, and utilized for cell counting, collagen-fibril diameter measurements, tendon width measurements, and optical marker tracking for determination of local strains on tendon specimens during mechanical testing. The software allows the PI to perform automated or semi-automated analyses of large data sets that would be prohibitive to quantitate manually. The PI has extensively utilized the 1317 x 1035 Quantix 1401E12-bit digital camera (Roper Scientific) attached to the Leica DMXRA motorized microscope equipped with an x-y-z stage (Figs. 27,34). This equipment was purchased with monies from this award (DOD No. DAMD 17-99-1-9475).

The previous sections discuss the merits of the given tissue replacement models based on the intrinsic properties of the constructs. Another factor that is crucial to the evaluation of tissue-engineered replacements is their interaction with the implantation site. In the case of skin replacements (***Project 2***), even an ideal graft would be rendered useless if it were prone to delamination from the underlying tissue under the application of physical forces. This project has developed methods of determining the strength of skin and its bond with underlying tissues in normal and diseased patients. These techniques can be applied to tissue engineered constructs at the appropriate state of development.

The influence of diabetes on mechanical properties of skin

Approximately 16 million people in the United States suffer from diabetes. An estimated 385,000 people in the United States die from diabetes every year, making it the nation's sixth leading cause of death by disease. Diabetic patients are at high risk for serious foot problems. It has been estimated that 15% of all diabetic patients will have a foot ulcer during their lifetime. About one in five hospitalizations among diabetic patients are directly related to foot ulceration. An estimated 56,200 people lose their foot or leg due to diabetes each year. The mortality rate in patients with diabetic foot ulceration is also high and is approximately twice that of patients without ulceration. The cost of treating these complications accounts for ~25% of the hospitalization costs of diabetes care, but the indirect costs can be much more.

Foot ulceration is a major complication of diabetes and consumes a major portion of the resources for the treatment of diabetes. The development of ulceration is preventable. Patient education regarding foot hygiene, skin care, proper footwear, and appropriate foot care administrated by qualified professionals can reduce injuries that may lead to foot ulceration. Therefore, identifying the at-risk patients is probably the most important step in reducing the rate of foot ulceration. A number of risk factors have been examined and found to be associated with diabetic foot ulceration, including peripheral neuropathy, previous ulceration, high dynamic plantar foot pressures, and limited joint mobility. Peripheral neuropathy is the most important component cause of foot ulceration, as well as foot deformity and trauma. The plantar surface of the foot is the most common site of neuropathic foot ulcers, especially the area under the metatarsal heads (MTHs). Peripheral neuropathy is associated with hyperextension of the metatarsophalangeal joints, clawing of the toes, and distal migration of the fibro-fatty pad on the plantar aspects of the forefoot. This process may subsequently lead to increased forefoot pressures.

Decreased sweating and dryness of skin secondary to autonomic neuropathy results in callus building up under areas of increased pressure, which in turn further increases the pressure.

Various screening techniques have been proposed and are currently in use for the identification of the patient at high risk for foot ulceration. These include the evaluation of vibration perception threshold (VPT), plantar foot pressure measurements, joint mobility and 5.07 Semmes-Weinstein monofilament (SWF) testing. In addition, a history of previous foot ulceration, a $TcPO_2$ level of < 30 mm Hg, and the existence of foot deformities have also shown to be risk factors for the development of diabetic foot ulceration.

Diabetes mellitus is also a serious risk factor for cutaneous alteration. In particular, the skin at the extremities of diabetic patients becomes thick and stiff. Monnier [37] found that glycosylation in diabetic patients causes excessive crosslinking between collagen strands. Pierard *et al.* [38] investigated the biomechanical properties of diabetic skin using the Cutometer SM 474 (CK Electronic GmbH, Köln, Germany). Evaluations were made on the dorsum of the hands and on the volar aspect of the forearms. They found that in Type I diabetic patients, the extensibility (maximum deformation) of skin decreased while values of thickness and elasticity increased. These alterations were most prominent on the hands. Similar modifications, although less pronounced, were also found in Type II diabetic subjects.

Reihsner *et al.* [39] examined the viscoelastic properties of long-term glycated human skin samples using a biaxial testing method. A marked increase of the direction-dependent stiffness was found upon long-term incubation with glucose-6-phosphate. The increase was statistically significant for the maximum principal elastic stress component, which was highly correlated with the degree of non-enzymatic collagen modification. They also found that the biomechanical and biochemical effects of long-term glycation could be partially reversed by aminoguanidine, a potential therapeutic agent for patients with diabetes mellitus.

Although mechanical factors are now generally recognized as important in understanding formation of diabetic foot ulceration, the effects of principal mechanical factors, including changes in tissue stiffness, shear and pressure, are not fully understood. In a number of studies [40,41,42], the conclusions were that elevated plantar pressures constituted a major biomechanical factor in the etiology of skin ulceration. Pollard *et al.* [43], however, showed that diabetic neuropathic ulceration occurred at sites of maximal shear stress under the foot. Some studies found that the loading rate had great effect on formation of foot ulcer. Landsman *et al.* [44] have suggested that the stiffening of viscoelastic tissue decreases its ability to quickly deform in response to a given load, making the tissue more susceptible to cracking in response to the rapid deformation associated with high velocity foot impact. There are also a number of studies focused on identification of threshold of plantar pressure that leads to foot ulceration. However, a recent study showed that only 65% of foot ulceration is pressure specific.

Mechanical factors are important in the understanding of the formation of foot ulcers. Foot ulceration is generally associated with high plantar pressure. The mechanical property changes in the skin of diabetic patients may change the internal stress distribution under the foot. The overall purpose of this study was to investigate the influence of diabetes on the mechanical properties of skin.

There have been clinical reports that diabetic ulcers may originate internally [45]. In addition, there are numerous reports describing failure mechanisms in structures that are made of more than a single material where adjacent regions have different stiffness values. Previous 2-D plain strain finite element modeling [46] showed that a peak of first principal stress occurs near the skin-fat interface, and that the peak stresses were significantly elevated (up to 50%) in diabetic patients. These modeling efforts (1) assumed skin properties could be predicted from simple uniaxial tests, and (2) were limited by an absence of data related to the strength of the skin-fat interface. Therefore, the current study focused on the mechanical properties of skin that are likely to affect stress at the skin-fat interface.

Methods

Skin-fat interface strength testing

In this study, 21 diabetic (68 ± 2.4 years) and 17 non-diabetic (74.6 ± 3.8 years) foot specimens were studied. For each specimen, the plantar skin surface was cut into a 9 x 2 array from the first metatarsal head (row 1) to the anterior heel (row 9) and divided down the medial/lateral axis (Fig. 35).

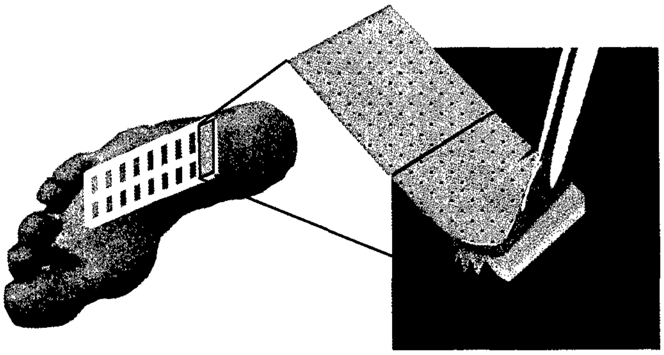

Figure 35. The plantar surface on each foot was cut into 18 strips, in a 2 x 9 array. The medial edge of each strip was attached to a claw grip that was connected to the actuator of an MTS mechanical testing machine.

Each strip of skin was 1 cm wide and 2 mm deep. The skin was clamped to a load cell and tension was applied at a rate of 1 mm/sec as the skin was peeled off the underlying fat tissue. During testing, the foot specimen was held in a supine position in a custom jig, designed and fabricated by our department's Mechanical Prototype Facility. The jig was placed on top of a transitional unit that could move in both x and y directions to keep the peeling force vertical to the peeling site (Fig. 36). This unit was then mounted on a universal material testing system (MTS Systems Corp., Eden Prairie, MN). The peeling force and the displacement of the loading head were recorded at a sampling rate of 60 Hz. The mean peeling force over the entire removal process was calculated and normalized to the width of the skin strip (F = N/cm).

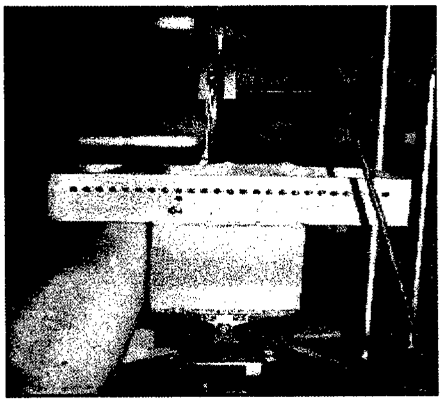

Figure 36. A jig was used to rigidly attach the foot to the MTS machine. Note the dovetail mortice beneath the jig that allowed each foot to be positioned directly under the MTS actuator for each strip that was tested.

Biaxial skin property test

Ten non-diabetic skin specimens and 9 diabetic specimens were tested. The age of the non-diabetic group ranged from 44 – 88 years, with a mean ± SD of 71.9 ± 14.3 years, while the age of diabetic group ranged from 48 – 85 years, with a mean ± SD of 69.9 ± 11.0 years. All skin specimens were acquired from the heel region (Fig. 37) of the cadaveric foot specimens used in the skin-fat interface peeling testing. After the peeling test, the heel region of the foot specimen was dissected. Subcutaneous fatty tissue was removed, leaving only the epidermis and dermis intact. The skin specimen was then trimmed to a 4 cm x 4 cm square and stored in a freezer at – 20 °C until needed for testing. On the day of testing, the skin specimens were thawed at room temperature for two hours.

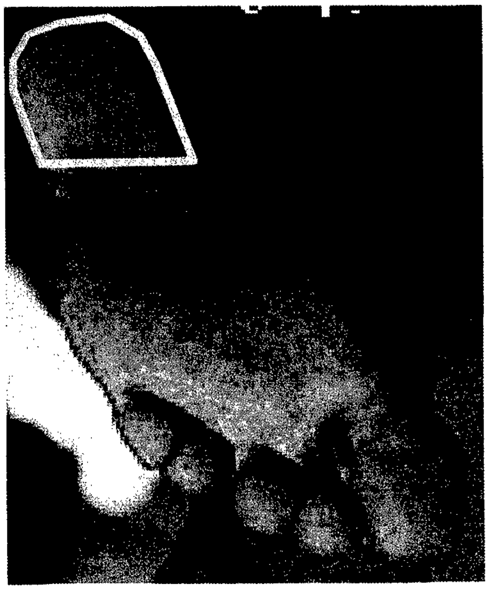

Figure 37. Skin specimen obtained for biaxial testing.

A biaxial strain measuring system was developed to measure the biaxial mechanical properties of the skin specimens. The system consists of a loading device, a motion capture system and a pressure measuring system (Fig. 38). The loading device, a custom designed device to deform skin biaxially, is essentially a hollow cylinder. During a test, a ring clamp held the skin specimen at one end of the cylinder. The skin specimen was inflated by adding a physiological salt solution to the cylinder using a syringe. A cyclic load was applied. A motion capture system (MacReflex; Qualysis Inc., Sävebalden, Sweden) equipped with Qtrac® software captured the movement of the markers and, thus, the deformation of the skin specimen. Nine reflective tape markers were placed on the surface of the skin specimen. To obtain the stereo images, 3 cameras were set up in such a way that each camera viewed the skin specimen at a different angle. The setup insured that at any instant of the test each marker on the skin specimen was viewed by at least 2 cameras. The pressure in the cylinder was measured with a pressure collecting system. The pressure transducer was placed at the mid height of the cylindrical chamber and synchronized with the motion capture system. Both the marker data and pressure data were collected via Qtrac® software at a sampling rate of 60 Hz. Cyclic loading was applied, with a target loading rate of 10 seconds per cycle and peak pressure of 200 mm Hg. However, as the cyclic loading was controlled manually, there was variance of loading rate and peak pressure values in loading curves (Fig. 39) between different trials.

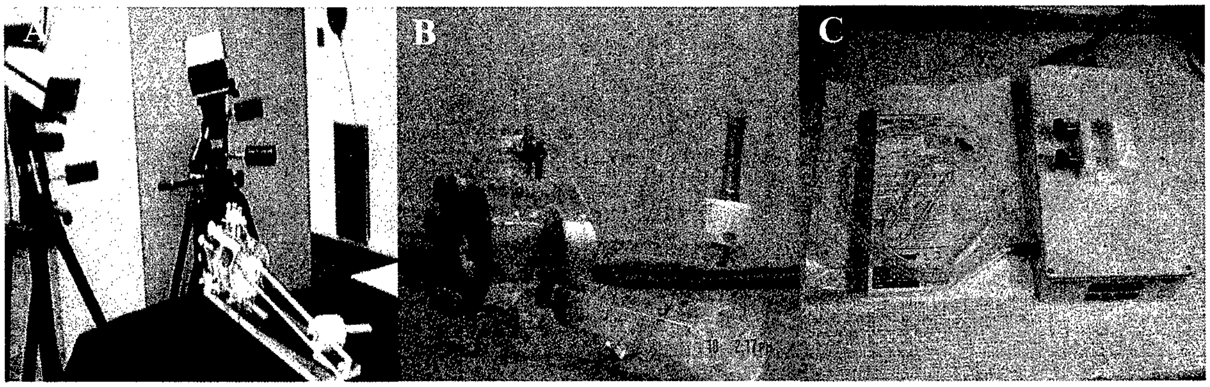

Figure 38. The biaxial skin testing apparatus consisting of (**A**) loading device, (**B**) pressure measurement system and (**C**) motion capture system.

Following tracking and the processing of 2-D camera data, 3-D position (x, y, z coordinated) data of the markers was obtained (Fig. 40). With nine markers on the skin, strains were calculated for each trial for eight regions of the specimen (Fig. 41). The strain was calculated from the following equation:

$$\text{Strain} = \frac{(l - l_o)}{l_o}$$

Where l_o was the original length between corresponding markers before the loading. It is noteworthy that strain calculated from the above equation represents average tissue strain between the corresponding two optical markers and does not reflect the variance of strain along the line. The strain data of strain 5 to strain 8 were very noisy; these data were excluded from further analysis.

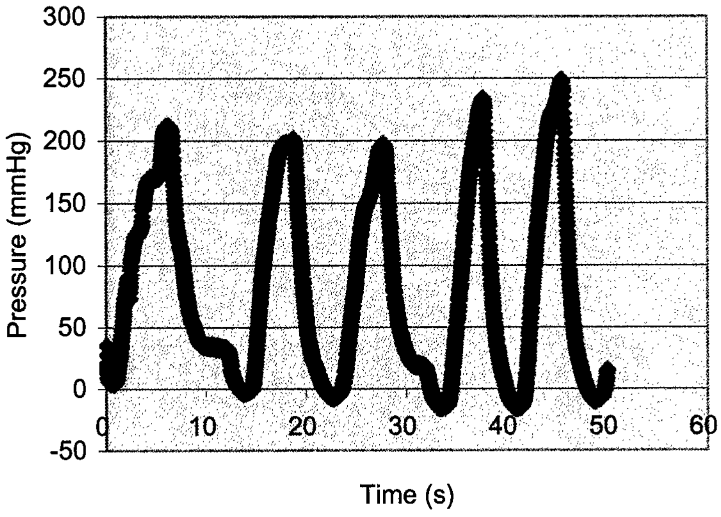

Figure 39. A typical loading curve for the biaxial testing system.

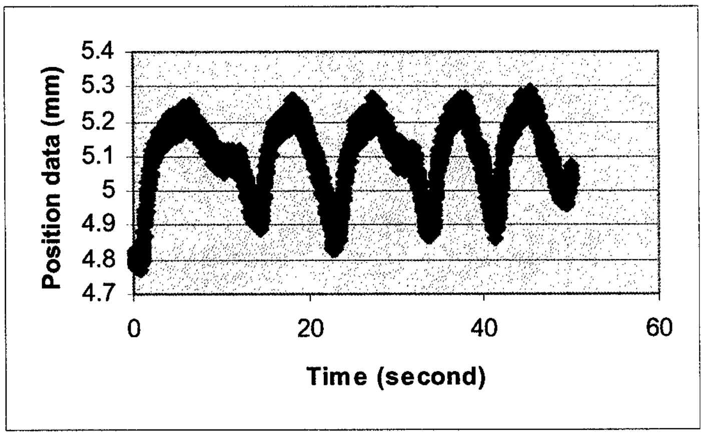

Figure 40. Representative marker position data (x, y, z coordinates).

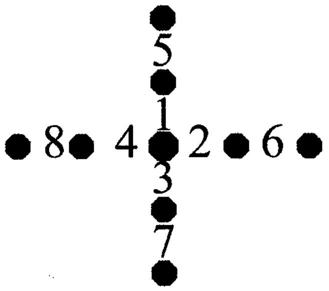

Figure 41. Diagram of the eight regions where strains were calculated.

Results

Skin-fat interface strength testing

Generally, the peeling force increased quickly to a certain level in the initial loading stage (Fig. 42). In the mid-peeling process, there are several peaks and valleys; this is because the skin and underlying fat tissue were connected by connective fibers. Each time a fiber was broken, there was a decrease in force. The peeling force returned to zero rapidly as the whole skin strip was removed from the underlying fat tissue. It is important to note that although each loading curve has the characteristic phases of initial loading, mid-loading and final loading, the peak forces and the pattern in the mid-loading stage varied greatly between foot specimens and different strips within one foot specimen.

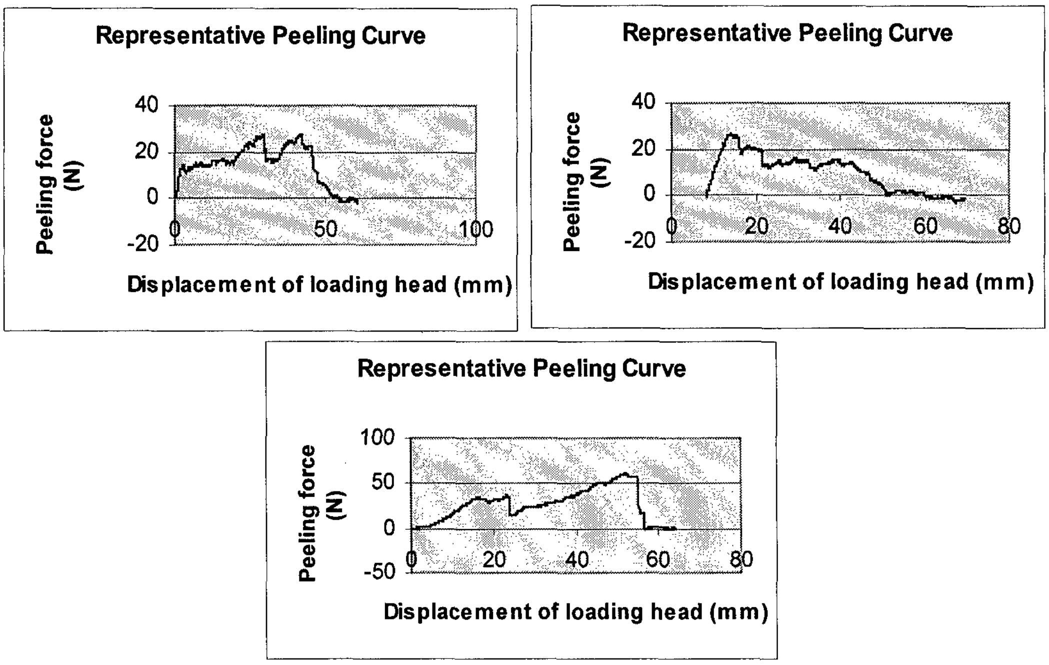

Figure 42. Graphic representation of how the different samples had unique loading curves. Note that each has a rapid initial loading phase, mid-loading phase of varying degrees, and an unloading phase where the peeling force rapidly drops to zero.

In this study, the variable of interest was the mean force required to peel the dermis off of the underlying subcutaneous tissue. The mean force over the entire removal process was estimated and normalized to the width of the skin strip (F = N/cm). This variable is less susceptible to the influence of a few collagenous strands that might result in localized peak stress at the skin-fat interface. The mean force was used as the interface strength of the site and compared between strips and specimens. It is important to note that data collected in this study were obtained from regions of the foot where the skin surface was intact. Thus, if the skin-fat interface was compromised by the presence of an ulcer, the region was not tested.

Regional differences

As mentioned earlier, the plantar surface of the foot was cut into a 9 x 2 array from the first metatarsal head (row 1) to the anterior heel (row 9) and divided down the medial/lateral axis. Mean ± SD of the strength of the skin-fat interface at different regions for the 38 feet specimens are presented in Table 6.

Paired t-tests revealed that there were no significant differences of skin-fat interface strength between the medial and lateral strips ($p = 0.483$). An analysis of variance (ANOVA) showed that the means of the strength in different row groups were significantly different ($p < 0.001$). Generally, the strength of the skin-fat interface was significantly higher in the metatarsal head and heel regions. Tukey tests were conducted to compare these rows. Row 9 was significantly different from all the other rows and rows 1 and 2 were different from rows 3 – 6. As illustrated in Figure 43, the strength of the skin-fat interface was higher in the forefoot and heel regions and lower in the mid-arch region of the foot. It is important to note that high interface strength regions (forefoot and heel regions) experienced high stress compared with low interface strength regions (mid-arch region). These results suggest that there may be an association between the external stress and the skin-fat interface strength.

Row/Column	Medial	Lateral
1	30.38 ± 12.45	33.89 ± 11.97
2	30.46 ± 10.56	30.89 ± 13.99
3	28.56 ± 8.86	27.66 ± 11.63
4	26.61 ± 8.35	26.78 ± 10.43
5	24.5 ± 7.68	25.49 ± 8.67
6	25.02 ± 9.93	27.25 ± 8.89
7	28.33 ± 10.58	29.45 ± 9.60
8	32.14 ± 9.70	31.32 ± 10.83
9	41.83 ± 16.32	38.97 ± 15.01

Table 6. The mean ± SD for the strength (N/cm) of the skin-fat interface at different regions across the plantar surface of the foot ($n = 38$).

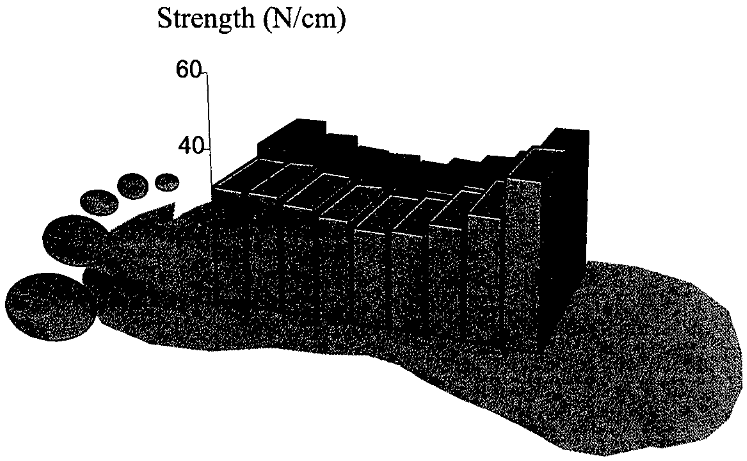

Figure 43. The mean skin-fat interface strength at different regions across the plantar surface of the foot.

The thickness of the skin strips ranged from 0.33 mm – 2.97 mm, with a mean ± SD of 1.30 ± 0.52 mm. There was a negative correlation between thickness of the skin strip and age of the specimen (correlation = 0.188, $p < 0.001$), indicating that older people have thinner skin compared with younger people. A series of 2-sample t-tests revealed that there was no significant difference in thickness of skin strips between males and females ($p > 0.05$). There was a positive correlation between the strength of the skin-fat interface and the thickness of the skin at the site ($p < 0.001$), which means thicker skin strips required a higher force to peel them off.

For age effects, there was a negative correlation between the strength of the skin-fat interface and the age of the donor of the foot specimen (correlation = – 0.277, $p < 0.001$), indicating that the strength of the skin-fat interface decreased with age. A series of 2-sample t-tests were conducted to compare the mean strength of the skin-fat interface in the female and male groups. The mean strength of the skin-fat interface was higher in the male group than in the female group ($p < 0.001$, Fig. 44).

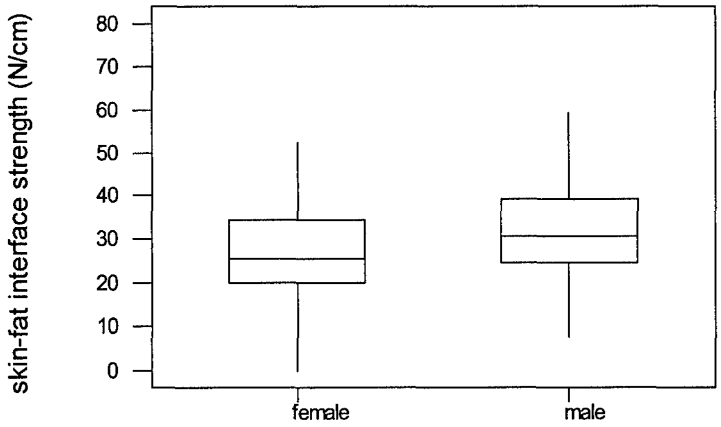

Figure 44. Graphic comparison of the skin-fat interface strength as a function of gender.

Diabetic vs. non-diabetic

A two-way ANOVA model was utilized (diabetic vs. control and medial vs. lateral) with age as a covariate for the statistical analyses. The strength of the skin-fat interface was significantly different ($p < 0.05$) with the diabetic strips requiring greater skin removal force. There was no significant difference between medial and lateral strips ($p > 0.05$). In both groups, the skin-fat interface strength was significantly higher in the forefoot, heel, and lower in the mid-arch region of the foot ($p < 0.05$).

A series of 2-sample t-tests showed that the thickness of the skin strips in the diabetic group was significantly thicker than in the non-diabetic group ($p < 0.001$), with a mean of 1.46 mm in diabetic group and 1.11 mm in the non-diabetic group (Fig. 45). There was a positive correlation between skin-fat interface strength and the thickness of skin at the site in both groups. In the diabetic group, the correlation was 0.352 ($p < 0.001$) while in non-diabetic group the correlation was 0.266 ($p < 0.001$). The mean ± SD for the mean skin-fat interface strength (N/cm) in these 2 groups is shown in Table 7.

	Diabetic group (n = 21)		**Non-diabetic group (n = 17)**	
	Medial	**Lateral**	**Medial**	**Lateral**
Row 1	32.2 ± 6.7	38.2 ± 10.6	31.9 ± 13.6	30.8 ± 9.6
Row 2	33.2 ± 9.2	36.1 ± 12.7	29.0 ± 9.4	30.4 ± 7.9
Row 3	30.7 ± 8.7	31.2 ± 11.4	26.0 ± 8.5	25.1 ± 9.3
Row 4	28.1 ± 8.0	28.7 ± 9.1	24.7 ± 8.6	24.4 ± 10.5
Row 5	26.1 ± 7.5	26.4 ± 7.1	22.5 ± 7.7	24.4 ± 10.5
Row 6	28.3 ± 9.5	29.6 ± 7.8	22.7 ± 7.9	24.4 ± 9.5
Row 7	32.7 ± 10.0	31.9 ± 9.0	24.5 ± 8.7	26.5 ± 9.8
Row 8	34.4 ± 9.9	34.2 ± 10.7	29.3 ± 8.9	27.7 ± 10.2
Row 9	46.7 ± 16.5	42.5 ± 15.3	35.9 ± 14.4	34.7 ± 13.9

Table 7. Mean ± SD for the mean skin-fat interface strength (N/cm) in diabetic and non-diabetic groups.

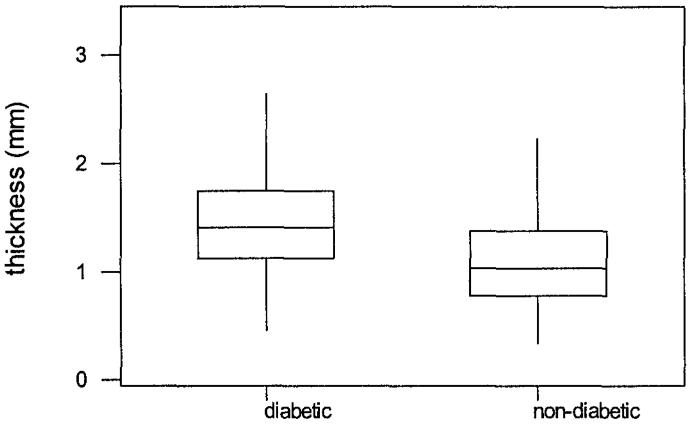

Figure 45. Thickness of skin strips in the diabetic group and non-diabetic groups.

In the non-diabetic group, there was a negative correlation of – 0.487 between the age of the specimen and the skin-fat interface strength ($p < 0.05$; Fig. 46), indicating older people have lower skin-fat interface strength. However, in the diabetic group there was not a significant correlation between the age of the specimen and the skin-fat interface strength.

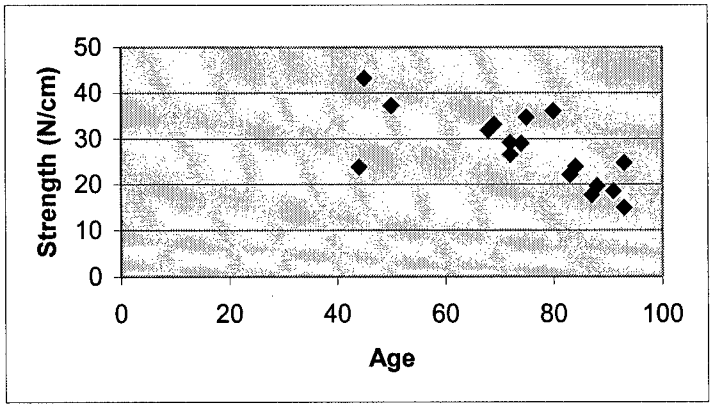

Figure 46. Skin-fat interface strength versus age in the non-diabetic group.

Since many factors are known to be related to the strength of the skin-fat interface, in order to identify the useful subset of predictors for skin-fat interface strength, a stepwise regression model was utilized. The predictor variables entered were: sex (male or female), age, diabetic or non-diabetic, thickness of skin, rows, medial or lateral. Five predictor variables were significant in the regression model. The five predictor variables in the order of importance in the regression model were thickness of skin, age, rows, sex, and medial or lateral location. The diabetic or non-diabetic factor was not identified as significant in the subset of predictors.

In summary, the skin-fat interface strength was higher in the diabetic group than in the non-diabetic group, and higher in the forefoot and heel regions than in the mid-arch region of foot. Forefoot and heel regions are weight-bearing regions, thus they experience higher vertical stresses compared with the mid-arch region. Due to tissue property changes and bone deformity, diabetic patients usually experience elevated vertical stress at the foot-ground interface. The higher strength of the skin-fat interface in the diabetic group might be an adaptive response to this elevated vertical stress. The positive correlation between skin-fat interface strength and thickness of skin indicates that both skin thickness and skin-fat interface strength are adaptive to vertical stress. The result of this study suggests a "skin equivalent" to Wolff's law for bone, i.e., higher stresses lead to stronger tissue. The trend with age in the non-diabetic group might also be explained by this assumption. In general, people become less active with age, which implies less stress under the foot, and thus lower skin-fat interface strength. In the diabetic group, as age increases, the stress concentration may be greater because of changes taking place in the foot due to diabetes, thus the decreasing interface strength trend with age did not exist in the diabetic group.

Biaxial skin mechanical property test

As in most living tissue, the stress-strain relationship of skin is nonlinear and viscoelastic. The stress of skin not only depends on the strain alone, but also on the loading history and time. According to Fung, the stress-strain relationship can be separated into two parts: an elastic part and a history-dependent part [47]. The elastic part defines a unique stress-strain relationship, i.e., the "elasticity" of the material. The reversible portion of the elastic response can be obtained from an infinitely slow process of loading. Since such an idealized device is complicated, we may derive the elastic relation from dynamic results. Fung described a simple procedure to extract the elastic portion of the response from dynamic results as follows. For a given strain rate, a relaxation experiment is performed in which the specimen is loaded at the specified rate and then held fixed and then the stress history is measured. The asymptotic stress is defined as T_∞, and T_∞ is proportional to the peak stress T_1. T_∞ is the stress that would have been obtained had the load been applied slowly. Hence, if the dynamic stress were reduced by the factor T_∞/T_1, the result would correspond to the elastic curve.

The history-dependent part is time-dependent; it is related to the hysteresis, stress relaxation, creep, and other non-conservative phenomena. It is exceedingly difficult to represent the history-dependent portion of the stress-strain law analytically. Previous tests on skin have shown that the hysteresis loop is almost independent of the strain rate, indicating that the stress-strain law of skin is nonlinear viscoelastic. It is well known in engineering structure analysis that if a material is linear viscoelastic, the hysteresis varies with the strain rate.

Figure 47 shows a typical hysteresis curve for a skin specimen. The blue loop is the first cycle; the purple one represents the last cycle. The stress-strain curve shifted to the right with loading cycles and the area between one loading and unloading cycle decreased as the number of cycles increased.

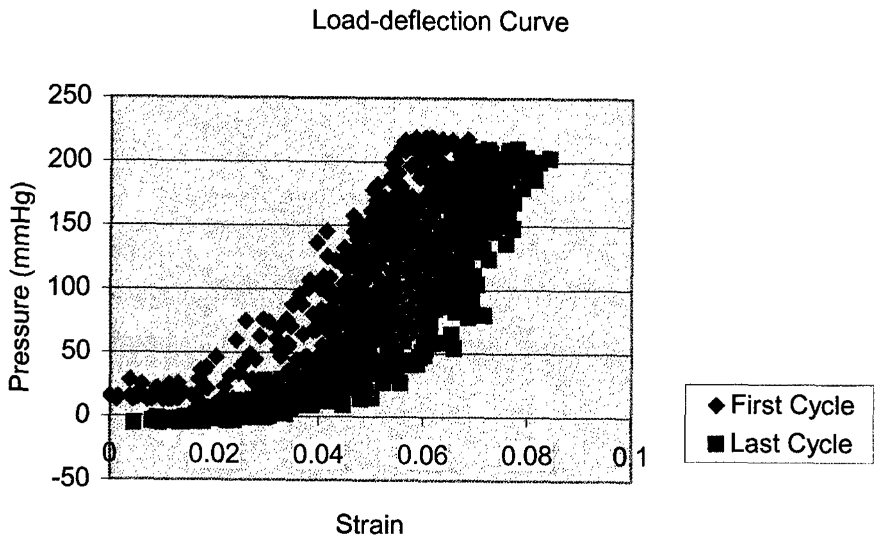

Figure 47. A typical hysteresis curves of a skin specimen.

Under cyclic loading and unloading, the skin showed pseudo-elasticity. After repeating a specific cyclic process a number of times, the stress-strain curve became repeatable and predictable. One could then speak of pseudo-elasticity: of describing the stress-strain relationship in loading as if the material is elastic, and in unloading as another elastic material. Generally, all the published elasticity data on soft tissues are such pseudo-elastic functions.

Many different mathematical expressions have been used to describe the experimental results of stress-strain curves of skin. Of these, polynomials and exponential functions are the two most extensively explored. In this study, third order polynomials were used to describe the loading stress strain relation for the loading curve while an exponential function was used to describe the unloading curve. A typical curve is shown in Figure 48.

In this study, the parameters of interest were Young's modulus at 150 mm Hg of pressure (P) and the area of hysteresis. These values were calculated based on the curve fitting results of the loading-deflection curves for both the first cycle and the last cycle. Young's modulus was estimated as the slope of the loading-deflection curve where P = 150 mm Hg. The area of hysteresis is the area inside one loading and unloading cycle.

When cyclic loading is applied on the tissue, the stress-strain curve is gradually shifted to the right. After a number of such cycles, the mechanical response of the tissue enters a stationary phase and the results become reproducible from one cycle to the next. The last two cycles of the loading and deflection of all the skin specimens are observed to be similar so we assumed at the last cycle, the skin specimen has entered a stationary state. The parameters calculated from the last cycle reflect this stationary phase while the parameters from the first cycle reveal more of the viscoelastic response.

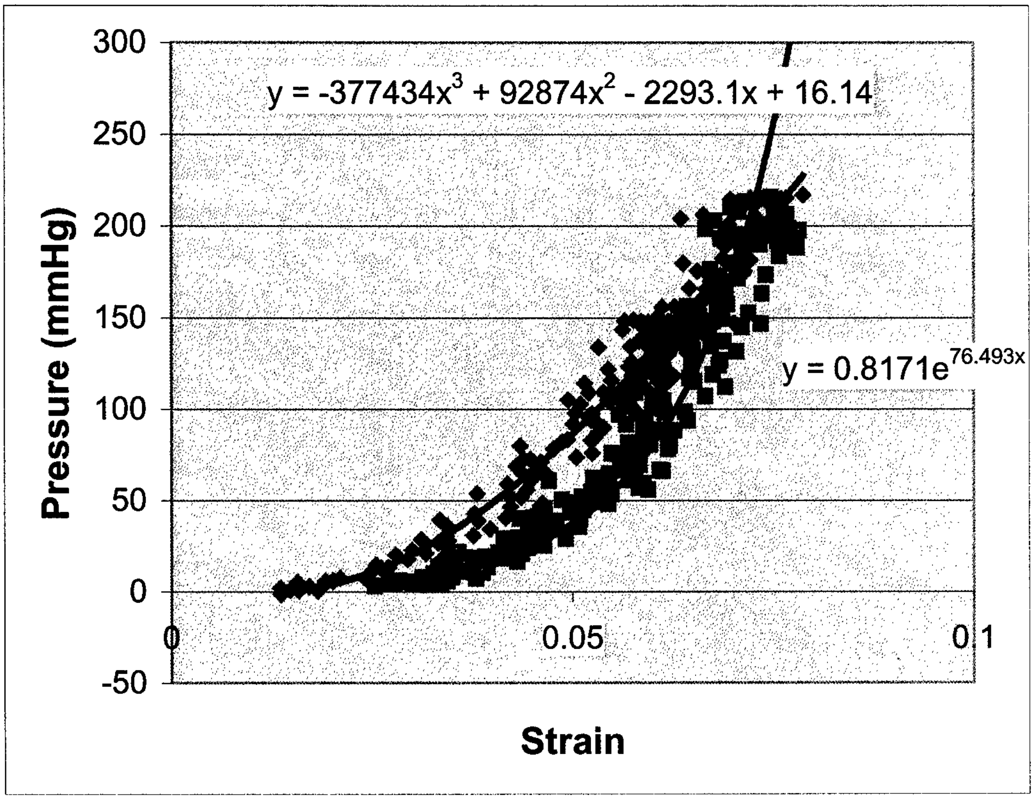

Figure 48. A typical curve fitting of loading and unloading curves for a given cycle.

The mean ± SD of Young's modulus at $P = 150$ mm Hg for the first and last loading cycles in the diabetic group and non-diabetic group are shown in Table 8. For the first loading cycle, Young's modulus was significantly higher in the diabetic group than in the non-diabetic group ($p < 0.05$), with a mean of 4747 mm Hg in diabetic versus 4203 mm Hg in non-diabetic. However, for the last loading cycle there was no difference between the diabetic and non-diabetic groups ($p > 0.05$).

	Diabetic group (mm Hg)	**Non-diabetic group (mm Hg)**
First cycle	4747 ± 1080	4203 ± 926
Last cycle	5212 ± 1546	5134 ± 1445

Table 8. The mean ± SD of Young's modulus at $P = 150$ mm Hg in diabetic and non-diabetic specimens.

The results show that in the first loading cycle, diabetic skin was stiffer compared to non-diabetic skin in the exponential area of the stress-strain curve. However, after several cycles of loading and unloading (preconditioning), the stiffness difference between diabetic and non-diabetic groups decreased. It is important to note that for the last cycle, the pressure and strain had a repeatable loading and unloading portion, indicating the tissue had entered a stationary state so the viscous influences could be neglected. After preconditioning, the tissue can be modeled as pseudo-elastic, where the loading and unloading curves are treated as separate materials. The Young's modulus for the last cycle reveals most of the elastic portion of skin response to loading, while the Young's modulus for first cycle includes the viscous component of response. The results suggested that the differences in the viscoelastic behavior of diabetic and non-diabetic skin were due more to differences in the viscous component of the response rather than the elastic component.

As mentioned previously, there were variances of loading rate and peak pressure between different trials. Since the response of skin was time- and loading history-dependent, this variance in loading pattern will have an effect on values of Young's modulus calculated from the last cycle. The Young's modulus from the first cycle is not influenced by this variance.

While the Young's modulus at $P = 150$ mm Hg was significantly higher in the diabetic group, the strain for the first cycle was significantly lower in the diabetic group ($p < 0.05$), with a mean ± SD of 0.0666 ± 0.015 in the diabetic group and 0.0884 ± 0.0392 in the non-diabetic group. Typical loading curves of diabetic and non-diabetic skin specimens are shown in Figure 49. Following initial elastic deformation, the slope of the stress strain curve of diabetic skin increased dramatically while the slope of the stress strain curve of non-diabetic skin specimen increased much more slowly. Diabetic skin specimens had less overall extensibility compared to non-diabetic skin. Pierard *et al.* [38] reported similar results; decreased extensibility of skin in diabetic patients based on the evaluation made on the dorsum of the hands and on the volar aspect of the forearms.

In the diabetic group, the Young's modulus at $P = 150$ mm Hg was significantly higher (Figure 50) in the anterior-posterior direction (5365 mm Hg) than in the medial-lateral direction (4594 mm Hg). There was no significance directional difference in the non-diabetic group. These results suggest that the skin stiffness change in diabetic patients was direction dependent.

For age effects, there was a significant negative correlation between Young's modulus at $P = 150$ mm Hg and age in both diabetic (-0.344, $p < 0.05$) and non-diabetic groups (-0.264, $p < 0.05$), indicating that in both groups the stiffness of skin decreased with age. While the specimens in the

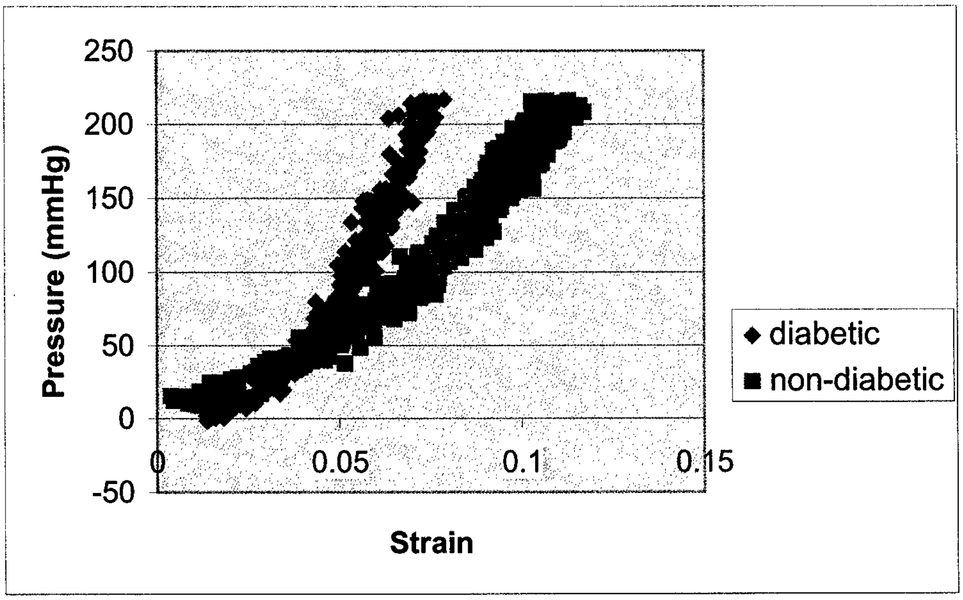

Figure 49. Typical loading curves of diabetic and non-diabetic skin specimens.

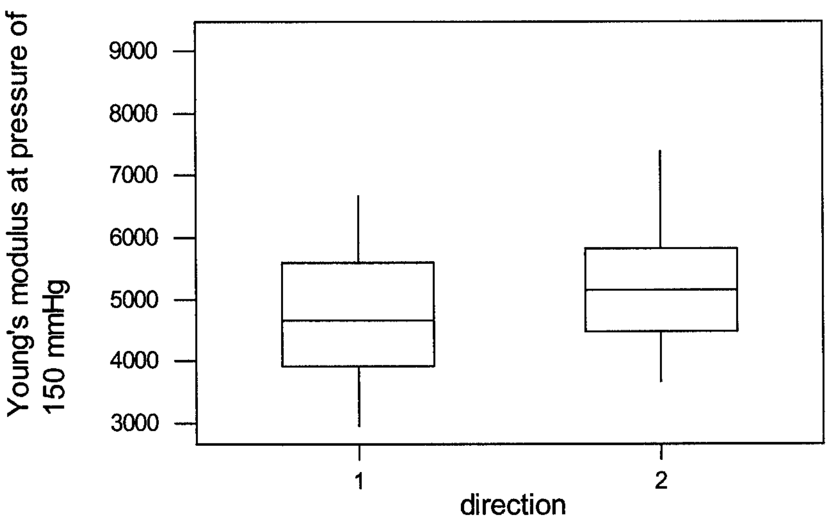

Figure 50. Directional difference of Young's modulus at P = 150 mm Hg in the diabetic group. (1 = medial-lateral direction, 2 = anterior-posterior direction).

diabetic group were younger than those in the non-diabetic group, age effects should be considered when comparing the Young's modulus between these two groups. Considering age as a covariate, analysis of variance using a general linear model showed that Young's modulus for the first cycle was significantly higher in the diabetic group than in the non-diabetic group ($p < 0.05$).

In summary, diabetic skin is stiffer and less extensible compared to non-diabetic skin. In both diabetic and non-diabetic groups, the stiffness of skin decreased with increasing age.

Area of hysteresis

As a viscoelastic material, the loading and unloading curve obtained from a force-deformation test do not follow the same path. The difference in the calculated area under the loading and unloading curves is termed the area of hysteresis. Area of hysteresis is characteristic of viscoelastic materials and is a measure of the energy dissipated by anelastic processes such as fluid movement. The area of hysteresis has been considered as an important physical parameter to determine the anabolic response of bones to cyclic mechanical simulation [48]. Kunnel *et al.* also suggests that fluid flow is a major mechanism involved in the response of bone to cyclic loading. In this study, the area of hysteresis revealed the viscous component of the response of skin to cyclic loading.

The area of hysteresis was calculated based on the curve results for loading and unloading. Areas of hysteresis for both the first loading cycle and last loading cycle were calculated. The area of hysteresis for the first loading cycle was significantly greater in the non-diabetic group than in the diabetic group ($p < 0.05$), with a mean ± SD of 2.583 ± 0.958 in the diabetic group versus 3.22 ± 1.36 in the non-diabetic group (Table 9). However, the area of hysteresis for the last loading cycle was not significantly different between diabetic and non-diabetic groups. Since area of hysteresis represents the energy dissipated by anelastic processes such as fluid flow, a higher area of hysteresis in the diabetic group indicates a higher influence of the viscous component in the viscoelastic behavior of diabetic skin.

	Diabetic group (mm Hg)	**Non-diabetic group (mm Hg)**
First cycle	2.583 ± 0.958	3.22 ± 1.36
Last cycle	1.6 ± 1.07	1.824 ± 0.590

Table 9. The mean ± SD of the area of hysteresis in diabetic and non-diabetic groups.

There was no significant difference found for the area of hysteresis in different directions ($p > 0.005$). In the diabetic group, there was a positive correlation of area of hysteresis and skin specimen donor age (correlation = 0.301, $p < 0.05$). No significant correlation was found in the non-diabetic group. These results indicated that in the diabetic group, the area of hysteresis increased with increasing age.

In summary, this test measured the biaxial mechanical property of skin specimens from diabetic donors and non-diabetic donors using an in-house biaxial strain measurement system. The results demonstrated that the skin specimens from the diabetic group were significantly stiffer, and the resultant change in stiffness of diabetic skin was direction-dependent. In addition, the investigation of the area of hysteresis revealed that the diabetic skin specimens had a higher influence of the viscous component in regard to viscoelastic behavior.

Conclusions

Foot ulceration is a common complication of diabetes and consumes a major portion of the resources allocated for the treatment of diabetes. The mortality rate in patients with diabetic foot ulceration is approximately twice that of patients without such ulceration. Although the end results of diabetic foot ulceration may be devastating, the development of ulceration is potentially preventable. Therefore, there is considerable research interest in identifying risk factors for foot ulceration in diabetic patients. A number of risk factors have been examined and found to be associated with diabetic foot ulcers, including peripheral neuropathy, previous ulceration, high dynamic plantar foot pressures, and limited joint mobility. Of these, high plantar pressure with neuropathy is considered as the major cause of diabetic foot ulceration. Previous research has found high stress at the skin-fat interface of the plantar surface of the diabetic foot. This study investigated the bonding between skin and subcutaneous tissue at the plantar surface of both non-diabetic and diabetic feet. The results showed that the skin-fat interface strength was higher in the diabetic group. The regional differences of skin-fat interface strength across the plantar surface of the foot and higher skin-fat interface strength in diabetic group suggests a "skin equivalent" to Wolff's law for bone, i.e., higher stresses lead to stronger tissue. Though the exact mechanisms for diabetic foot ulcer formation are as yet unknown, this study provided data related to the bonding of the skin-fat interface of the plantar surface of foot, which might be the initial site of foot ulcer formation.

SELECTION AND CONCENTRATION OF BONE PRECURSOR CELLS –

Project 7 (PI: Maciej Zborowski)

We have continued to support work on precursor cells by providing service of isolating the precursor cells from bone marrow. Precursor cells have a potential, under suitable culture conditions, to differentiate into bone-forming cells (osteoblasts) *in vitro*, and other tissues, and therefore are a necessary cellular component of any future tissue replacement therapy. The precursor cells are rare, approximately at 1 for every 20,000 nucleated cells. Moreover, the molecular makeup of the cell surface of the early precursor cell distinguishing them from committed progenitor cells is poorly understood. Those two factors contribute to significant technical difficulties of isolating the precursor cells from the bone marrow aspirates.

We have extended the class of the putative precursor cells targeted for isolation from the last year to include the cells that express complex of differentiation (CD) 105, an epitope on the endoglin molecule. Endoglin is a glycoprotein expressed on human vascular endothelium, and it is a component of the TGF beta signaling system. The recent publications indicate that endoglin may participate in interactions between hematopoietic and mesenchymal stem cells in the marrow. Also, the presence of the CD105 epitope on hematopoietic progenitor cells is predictive of the presence of early, or immature, progenitor cells that may have the potential of differentiating into tissues other than blood (such as connective and neural tissues). In the first year of the project, we used hyaluronan as the sole candidate molecular marker of the bone precursor cell.

The human bone marrow cell suspensions were obtained from normal donors through the collaboration with Dr. Muschler (***Project 9***). The cells were obtained as mostly mononuclear cell preparations depleted of red blood cells by centrifugation on a density cushion (Ficoll, Amersham Pharmacia Biotech, Inc., Piscataway, NJ). The cells were targeted with a primary monoclonal antibody against the CD105 epitope (Becton-Dickinson Biosciences, San Jose, CA) conjugated to fluorescein isothiocyanate (FITC), and magnetically labeled using an anti-FITC magnetic colloid (MACS nanospheres, Miltenyi Biotec, Auburn, CA). The magnetically labeled CD105 positive cells were isolated from the cell mixture using either a prototype magnetic cell sorter developed in our laboratory, or by a commercial magnetic cell separator (MiniMACS, Miltenyi Biotec).

The distinguishing feature of the prototype magnetic cell sorter is that it allows for direct deposition of the magnetically labeled cells on the microscope slide. This system has been selected as being most suitable for isolation of rare cells, such as the bone precursor cell, because of its high recovery of the separated cells. A schematic illustration of the magnetic deposition system is shown in Figure 51.

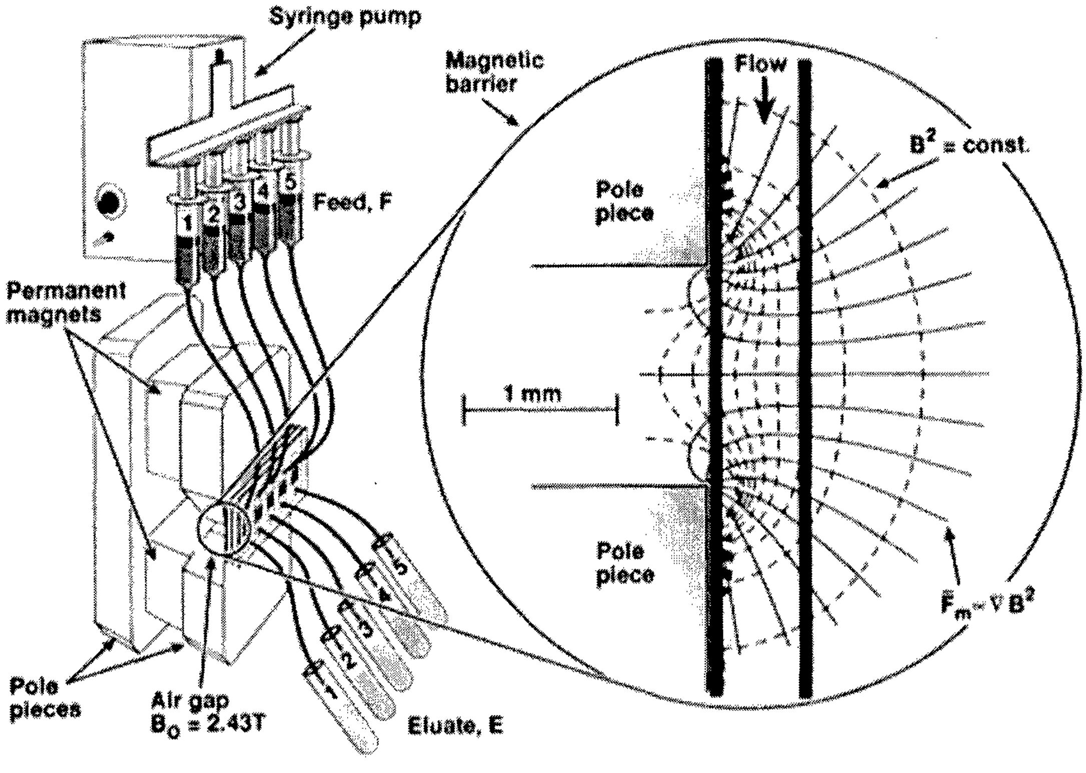
Syringe pump
Magnetic barrier
Flow
B^2 = const.
Pole piece
1
2
3
4
5
Feed, F
Permanent magnets
1 mm
Pole piece
$F_m \sim \nabla B^2$
Pole pieces
Air gap
B_0 = 2.43T
Eluate, E

Figure 51. Magnetic cell sorter prototype showing an enlarged magnetic cell deposition area.

The system comprises a syringe pump with a set of five syringes, a magnet, and a set of five flow channels with connecting tubing. A characteristic feature of the magnet is a narrow interpolar gap that generates a highly non-uniform, well-defined fringing field. The interpolar gap, the source of the fringing field, is a strong attractor of magnetically susceptible material, in particular, the magnetically labeled cells. Before operation, the target cells are tagged using a suitable magnetic label; the flow channel is assembled, placed on the magnet and filled with the carrier medium. The flow channels are oriented in a perpendicular fashion to the interpolar gap. The test procedure consists of loading the cell samples into the syringes and activating the syringe pumps. The stream of cells passing across the interpolar gap is exposed to a strong, highly localized magnetic field that deflects the magnetic cells from the sample stream towards the channel wall facing the magnet. As a result, the magnetized cells are precipitated from the flowing solution onto the glass slide, forming a narrow band at the interpolar gap. Once the entire volume of the cell sample has been pumped across the interpolar gap, the flow channels are disassembled and the glass slide is detached from the flow channel (Fig. 52). Cell adhesion to the glass slide prevents cell losses from the deposition band during fixation and staining steps or for subsequent culture. The non-tagged cells are washed away from the slide, thus providing a clear and unobstructed view of the few, deposited target cells (bone precursor cells). The stained slide is mounted on a standard microscopic substrate slide and is available for analysis. During year 2, we extended the application of the system to include wet mounts of the cells deposited on the slide. The wet mounts were used for seeding the CD105 positive progenitor cells in culture.

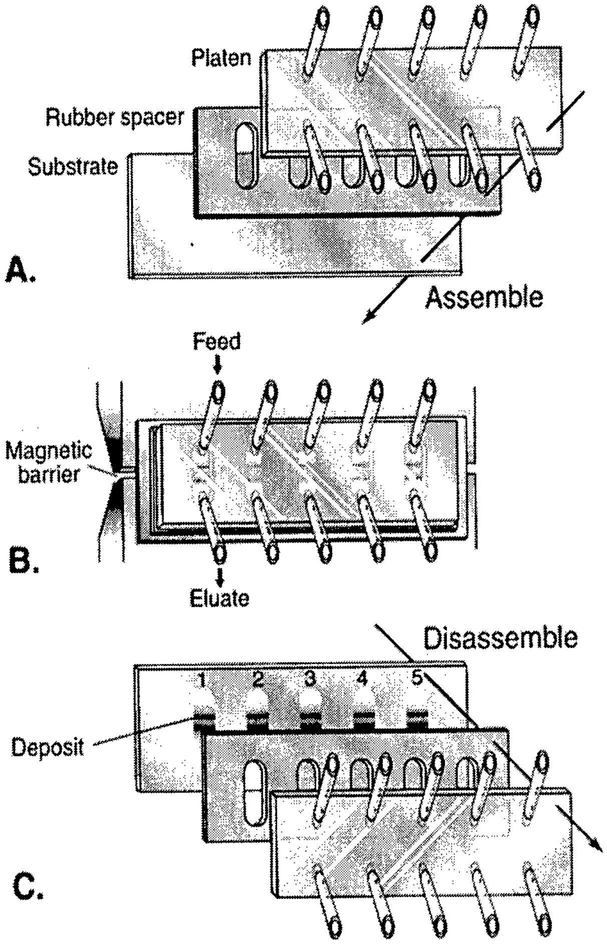

Figure 52. An illustration of the flow chamber assembly and disassembly showing the area of magnetic cell deposition.

The other magnetic cell separation system used in this study was a commercial magnetic column by Miltenyi Biotec. The magnetically labeled cells were trapped inside the column, while the unlabeled cells flow through the column and were collected as a negative fraction. The labeled cells were collected by removing the column from the magnet (and thus deactivating the magnetic attraction between the labeled cells and the solid substrate of the column), and by flushing the column outside the magnet. The designation "negative" and "positive" refers to the expression (or lack thereof) of the CD105 marker on the cell.

The separated cell fractions were returned to the laboratory of Dr. Muschler for further analysis and cell culture. Altogether, 13 bone marrow samples were processed, of which four samples were separated using our magnetic cell sorter prototype. The most promising results were obtained when using our magnetic cell sorter prototype. An example of the most promising results is shown in Figure 53.

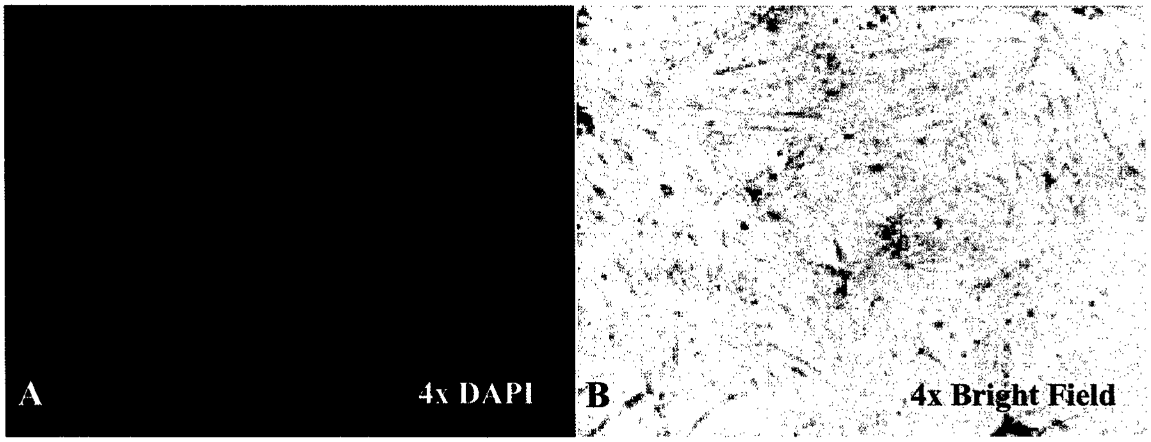

Figure 53. Fluorescence (**A**) and visible light (**B**) images of cells captured on the magnetic deposition slide, followed by 9 days culture. Note cell growth on the slide.

Conclusions

The participation in this project enabled us to test the magnetic flow sorter prototype on cell samples relevant for bone progenitor cell research. In the process, we provided service to the program by isolating putative bone progenitor cells from bone marrow samples and making them available for further analysis and cell culture in the laboratory of the collaborator (***Project 9*** - Muschler). As a result, we generated significant new information regarding the performance of the prototype magnetic cell sorter, in particular, with regards to its potential use for preparation of wet mounts of the progenitor cells. Such wet mounts could be used in the future for improved cell culture seeding. A continuation of this part of the project is planned after the expiration of the current DOD grant support, with the funds that will be sought from other sources (NIH). The search for the distinguishing markers of early precursor cells led us to the evaluation of hyaluronan and endoglin as candidate markers. The preliminary results showed the feasibility of the proposed methods to isolate the hyaluronan and the endoglin expressing cells from the bone marrow. The work on demonstrating the proliferative capacity of the CD105 (endoglin) positive cells is continuing and is expected to continue beyond the duration of the current DOD project. In summary, the participation in the DOD project enabled the evaluation of the magnetic cell sorting technology on new types of precursor cell, and suggested new directions in the magnetic sorter development.

OPTIMIZING MATRIX FOR ATTACHMENT AND DIFFERENTIATION OF BONE PRECURSOR CELLS *IN VITRO* – Project 8 (PI: Ron Midura)

Distribution of HA in bone

Hyaluronan has been shown to have several biological functions in connective tissues, including influencing cell differentiation, proliferation, migration, motility, tissue hydration and wound healing [49,50,51,1]. The function of HA in bone is not known. HA participates in the early events of bone formation and repair. Using a highly specific staining procedure for detecting HA in tissue sections, strong HA staining was found in the calcifying zone of growth cartilages of young animals [52,53]. During bone repair, HA was found to distribute abundantly at many sites throughout the fracture callus, including regions of fibrous connective tissue, the extracellular matrix of hypertrophic cartilage and the lacunae of osteocytes resembling cortical bone [54]. In the long shaft of bone (diaphysis), HA was detected in all bone cell layers. Intense staining was observed in outer periosteal cell layers, strong staining around osteocytes, and faint staining on the apical surfaces of mature osteoblasts lining the bone tissue (Fig. 54). The transition of HA staining correlating with bone cell phenotype is shown in Figure 54. The matrix surrounding mature osteoblasts stains poorly for HA, while the matrix surrounding osteocytes stains intensely for the presence of HA. This finding suggests that the presence of HA in the extracellular matrix correlates with bone cell differentiation.

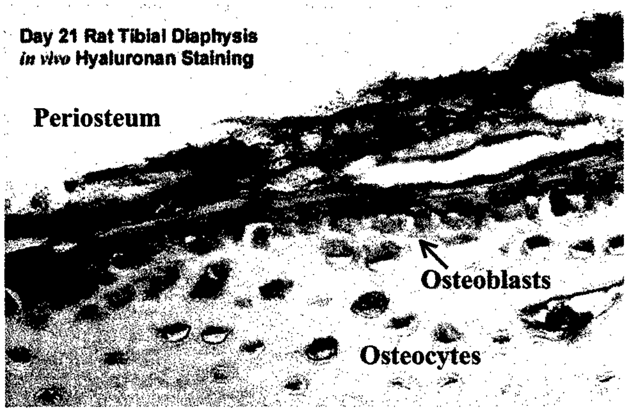

Figure 54. HA staining of tibial diaphyseal bone *in vivo*. Diaphyseal bone shaft isolated from 21 day-old rat tibia, and stained with a highly specific biotinylated HA-binding complex. Brown color is HA staining while the blue color is the hematoxylin counterstain.

The amount of HA in tibial diaphyses in periosteum and bone has been measured by fluorophore assisted carbohydrate electrophoresis (FACE). Tibial diaphyses averaging 8 mm long and 2 mm in diameter were recovered from 21 day-old rats. Periosteum was surgically removed from the outer bone surface. Bone wax was inserted from either open end of the bone to seal the empty medullary cavity. Both periosteum and bone were extracted sequentially with: (1st) a denaturing solution consisting of 4 M guanidine HCl, 1% CHAPS and protease inhibitors, followed by extensive washing, (2nd) the same extraction solution as above but now containing 20 mM EDTA followed by extensive washing, and finally (3rd) the same extraction solution but now containing 40 mM EDTA. Following extraction, the solubilized samples were concentrated and further treated for FACE analysis. An image of FACE results from the extractions is shown in Figure 55. Altogether, roughly 200 ng of HA present in periosteum and 22 ng of HA are present in bone. This result is consistent with the results of immunostaining, where the HA signal in periosteum appeared considerably greater than that in bone tissue (Fig. 54).

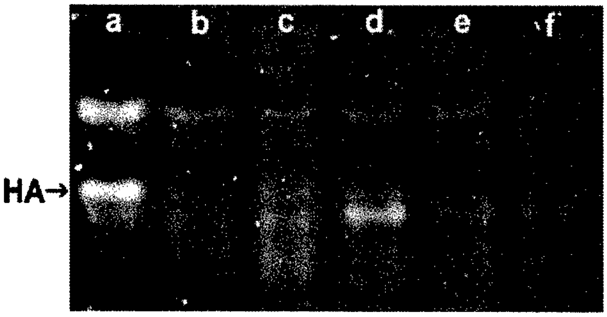

Figure 55. FACE analysis of HA disaccharides extracted from young rat tibia. Lanes **a-c** correspond to fractions from periosteum and lanes **d-f** correspond to fractions from bone tissue extracted without EDTA (**a,d**), with 20 mM EDTA (**b,e**), or with 40 mM EDTA (**c,f**).

HA synthesis by osteoblasts

Osteoblasts synthesize HA [55,56]. HA production by osteoblasts can be greatly enhanced by parathyroid hormone (PTH) [55,56]. PTH is a potent anabolic factor for bone formation and is one of the most promising prospects for the prevention of bone loss and the treatment of osteoporosis [57]. We have studied the stimulation of HA synthesis by PTH with the UMR106-01 osteoblastic cell line. Cells were plated at 1000 cells/mm^2 and cultured in 10% FBS in EMEM medium. At 40 hours, 10 nM $\mathrm{PTH}_{1\text{-}34}$ or 1 mM 8-bromo-cAMP was added to the culture medium for a 12-hour treatment. After incubation, the media were collected and the cell-matrix layers were washed. Both the medium and cell layer were further treated with Proteinase K (250 µg/ml, 37 °C for 4 hours), and the released glycosaminoglycans (GAGs; including newly synthesized HA) were subsequently digested for 4 hours at 37 °C with hyaluronidase SD (HSD; 10 mU), and for 3 hours at 37 °C with chondroitinase ABC (cABC; 10 mU; Seikagaku America, Falmouth, MA). Aliquots from the digests were assayed for their content of HA disaccharides by FACE.

PTH rapidly enhances the production of HA threefold (Fig. 56) in serum-free medium (0.5% BSA in EMEM). In serum containing medium, the increase in HA synthesis by PTH is twice that of control (data not shown). The production of HA in serum containing medium is an order of magnitude greater than cultures in serum-free medium. In cell layers, the amount of HA is the same in cultures in the presence and absence of serum. PTH treatment increased HA synthesis by approximately 1.5 times in cell layers.

Figure 56. PTH stimulates HA synthesis in osteoblast cultures. FACE quantitation of the HA contents in culture medium from osteoblast cultures treated with 10 nM PTH for 12 hours. The inset box outlines the HA disaccharide band used for quantitation. The intense bands above the HA disaccharide bands are glucose contaminants from the culture medium.

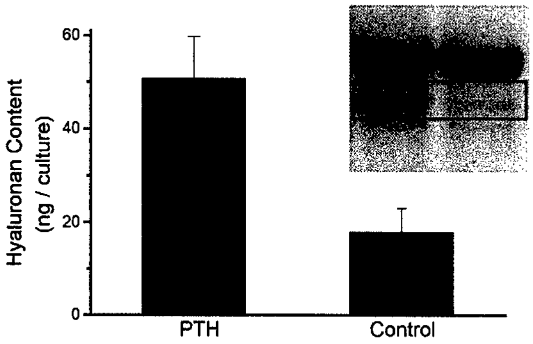

HA is synthesized by HA synthases (HASes) on the inner leaflet of the plasma membrane, and the HA chain is subsequently extruded out of the cell through the central pore of HASes [58]. Three HAS isoforms (HAS1-3) have been identified in eukaryotic cells, although HAS2 appears to be the only HAS gene exhibiting inducible expression by hormones [58]. A quantitative RT-PCR approach [4] was used to assess which of the HASes it is that PTH predominantly stimulates in the UMR 106-01 cell line. UMR106-01 cells were plated at 1000 cells/mm^2 and cultured in EMEM medium containing 10% FBS. At 40 hours, cultures received fresh media (0.5% BSA in EMEM) with or without a 10 nM PTH$_{1\text{-}34}$ supplement for an additional 12 hours of incubation. RNA from the cells was isolated with TRIzol®-reagent. RT-PCR reactions were done with an RNA PCR Core Kit (PerkinElmer Life Sciences, Branchburg, NJ). So far, we have only used HAS-2 primers for the RT-PCR reaction. Results show that HAS-2 is expressed in the UMR 106-01 cell line (Fig. 57). Quantification of HAS2 mRNA by using internal standards in PTH treated and control culture is under investigation.

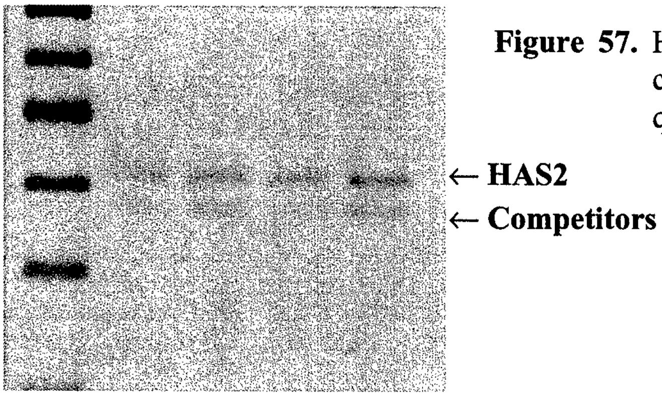

Figure 57. HAS2 expression in the UMR106-01 osteoblastic cell line. mRNA levels were assessed using quantitative RT-PCR.

The presence of HA in bone and the fact that HA can be produced by an osteoblastic cell line compel us to better understand HA's functions in bone tissue. We hypothesize that the possible function(s) of HA in bone are:

(i) To promote or diminish osteoblast (or osteocyte) adhesions to their surrounding extracellular matrix

(ii) HA regulates osteoblast/osteocyte differentiation. To answer these questions, it is necessary to produce HA-coated substrates.

Preparation of HA-coated substrates for cell culture

To understand whether HA functions as an adhesive extracellular matrix that regulates osteoblast/osteocyte differentiation, it is necessary to produce an HA coated substrate. Very little HA stably binds to native cell culture plate surfaces (data not shown). Thus, producing a stable HA-coated substrate became a technical goal of this study. In this section, we present evidence that we have been successful in coating HA either on cell culture inserts (Millicell®-CM, Millipore, Bedford, MA) or onto polystyrene cell culture plates. To obtain a coating in cell culture plates, a pre-coat of 15% BSA gel is needed. In both cases, HA is chemically linked to the insert membrane surface or BSA gel using divinyl sulfone (DVS).

The cross-linking reaction of HA to either insert membranes or BSA gels was performed at room temperature. The process involved soaking the insert membranes or BSA gels for 15 minutes with DVS, followed by removal of DVS and addition of HA to the inserts and plates. Both cell culture inserts and plates were dried for two hours at room temperature, and then extensively washed with PBS at 37 °C. The last wash lasted overnight at 37 °C and was routinely collected for FACE analysis. HA-coated inserts and plates were digested for 1 hour at 37 °C with HSD. Aliquots from the digests were assayed for their content of HA disaccharides by FACE. The results are shown in Figure 58. For cell culture inserts, ~2 $\mu g/cm^2$ was linked to the insert membrane by DVS. For comparison, ~0.1 $\mu g/cm^2$ HA was bound to the insert membrane in the absence of DVS cross-linking agent. For BSA-coated plates, ~10 $\mu g/cm^2$ was linked to the plates in the presence of DVS, while only ~0.12 $\mu g/cm^2$ HA was bound to the plates (with or without BSA coating) in the absence of DVS. These results show that high MW HA can be chemically linked to both cell culture inserts and cell culture plates.

To investigate if the HA coating of these culture surfaces is homogeneous, portions of the HA-coated insert membrane were stained with a biotinylated HA-binding complex [40], followed by a

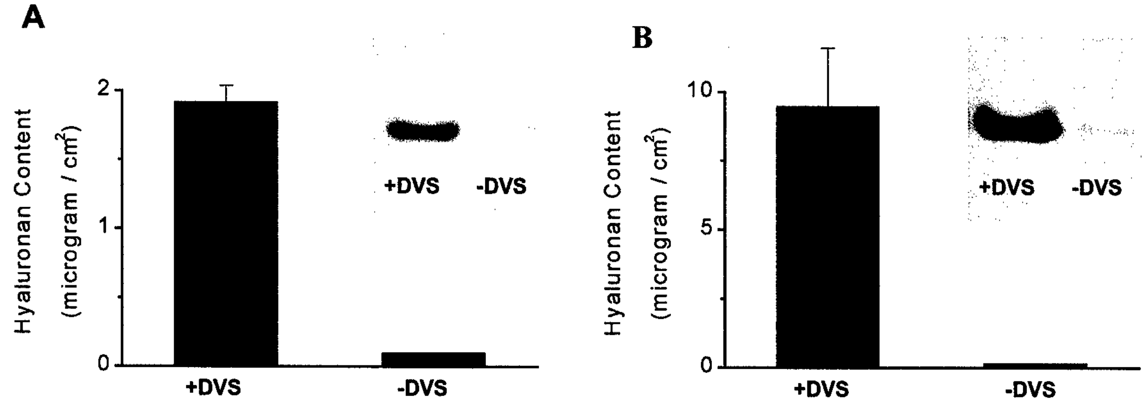

Figure 58. Amount of HA bound to cell culture inserts (**A**) and BSA-coated cell culture plates (**B**) by DVS cross-linking.

peroxidase-linked streptavidin conjugate, and subsequent detection using a Ni-enhanced DAB substrate kit (Vector ABC; Vector Laboratories, Burlingame, CA). Figure 59 shows that a continuous HA coating on the insert membrane has been achieved.

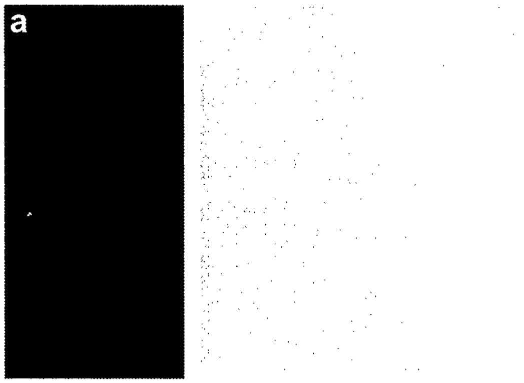

Figure 59. Images of HA staining with a Ni-enhanced DAB substrate kit for peroxidase. (**a**) HA-coated insert membrane (**b**) HA-coated insert membrane predigested with HSD (**c**) HA labeling in the presence of HA18 oligosaccharides. A positive signal consists of a black-colored precipitate.

The next issue was whether the HA coating was biologically active for cell culture. To address this question, a cell culture experiment was conducted using the TFX 3224.17.14 cell line. TFX 3224.17.14 cells stably express wild type mouse CD44H, and bind to HA through these CD44 receptors [59,60]. AKR1 cells, which are negative for CD44 expression and do not bind to HA matrices, were used as controls. Cells were seeded onto HA-coated inserts at a density of 1000/mm^2 in EMEM growth medium containing 0.5 % BSA. After 2 hours of incubation, the cells that were not attached to HA were removed by washing the cultures 3 times with culture medium and counted with a hemacytometer. The adherent cell numbers were calculated and plotted in Figure 60. About 90% of the TFX 3224.17.14 cells bound to the HA-coated inserts. Only 23% of TFX 3224.17.14 cells bound to the insert membrane without an HA coating. The results show that the HA coating we produced is biologically active for cell culture.

Figure 60. Binding efficiency of TFX 3224.17.14 cells and AKR1 cells on HA-coated substrates. TFX-mAb is a control and represents cultures of TFX cells in the presence of inhibiting mAb KM81 specific for CD44.

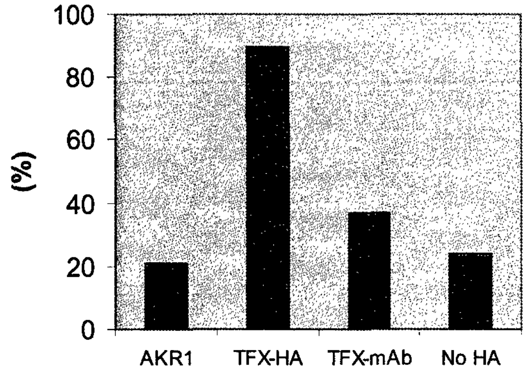

Cell culture experiment on HA-coated substrates

To date, four kinds of cells have been tested for their adhesion on HA-coated substrates:

(i) UMR106-01rat osteoblastic cell line

(ii) MC3T3 E1 murine osteoblastic cell line

(iii) Human osteoprogenitor cells from bone marrow

(iv) Rat osteoprogenitor cells from bone marrow

Cells were plated at 1000 cells/mm^2 and cultured in serum free medium (0.5% BSA in EMEM) or 10% fetal bovine serum (FBS) supplemented EMEM medium. At 1 and 16 hours after presenting the osteoblasts to the HA-coated substrates, phase-contrast images of the live cells at 10X were recorded from each culture before and after removing the nonadherent cells. These images provided information on the adhesion capacity by 1 hour and the spreading of cells by 16 hours.

UMR106-01 and MC3T3 cells do not adhere to HA-coated substrates. Figure 61 shows phase contrast images of UMR106-01 and MC3T3 cells before and after washing to remove non-adherent cells at 16 hours. Both cells formed large clumps, i.e., they adhered to one another rather than to HA substrates. Thus, HA is an anti-adhesive substrate for these cells.

Less than 10% of human osteoprogenitor cells adhered to HA-coated substrates. These cells had been cultured in 50 μg/ml ascorbate and 10^{-8} M dexamethasone in α-MEM for 9 days and they already underwent osteoblastic differentiation. Some of them spread on HA substrate, as seen in Figure 62b. These cells also adhered to BSA substrate, but they remain rounded. In comparison to human osteoprogenitor cells, rat osteoprogenitor cells were cultured in EMEM for one week before plating them in cell culture dishes; these culture conditions should help maintain their progenitor status. Interestingly, 30 – 40 % of rat osteoprogenitor cells adhered to HA-coated substrates. Some rat progenitor cells also adhered to BSA-coated substrate, but they were much less in number and remained rounded for up to 4 days, after which they died off.

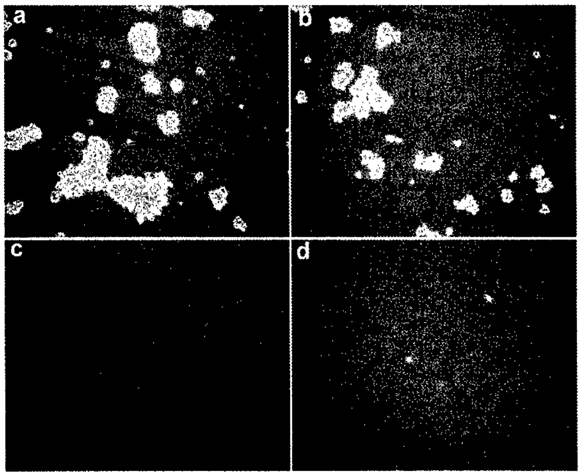

Figure 61. Phase contrast images of UMR106-01 and MC3T3 cells on HA-coated substrates at 16 hours. (**a**) UMR106-01 cells before removal of non-adherent cells (**b**) MC3T3 cells before removal of non-adherent cells (**c**) UMR106-01 cells after removal of non-adherent cells (**d**) MC3T3 cells after removal of non-adherent cells.

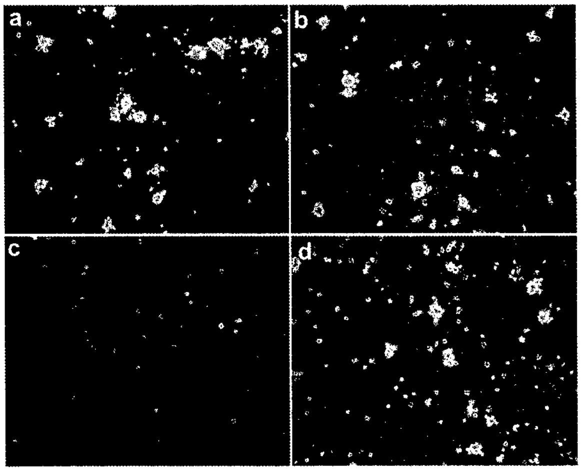

Figure 62. Phase contrast images of human and rat osteoprogenitor cells on BSA- and HA-coated substrates at 16 hours. (**a**) Human progenitor cells on BSA-coated substrate. (**b**) Human progenitor cells on HA-coated substrate. (**c**) Rat progenitor cells on BSA-coated substrate. (**d**) Rat progenitor cells on HA-coated substrate.

Figure 63 shows the morphological changes of the adherent rat progenitor cells on an HA-coated substrate over increasing incubation time. Interestingly, they eventually spread on the HA-coated substrate. However, it does not appear that they proliferate with increasing incubation. The phenotype of the cells that adhered to HA substrates is not yet known. The fact that they were not proliferating suggested that such cells are in a quiescent mitotic state. This experiment showed the possibility that these HA-coated substrates can be used to screen for and isolate select cells having a phenotype which allows for adhesion to HA.

HA-coated substrates can be subsequently exposed to varying amounts of type I collagen or fibronectin to form composite coatings that promote the adhesion of osteoblasts (Fig. 64, see also ***Project 4***). Such an experimental design can be used to address the following issues: (1) how does the HA content in the surrounding extracellular matrix influence osteoblast adhesion to other matrix molecules, (2) how does the presence of HA in the surrounding matrix influence the intracellular signaling of other adhesion ligands, and (3) how does HA in the surrounding matrix regulate the proliferation and differentiation of osteoblasts.

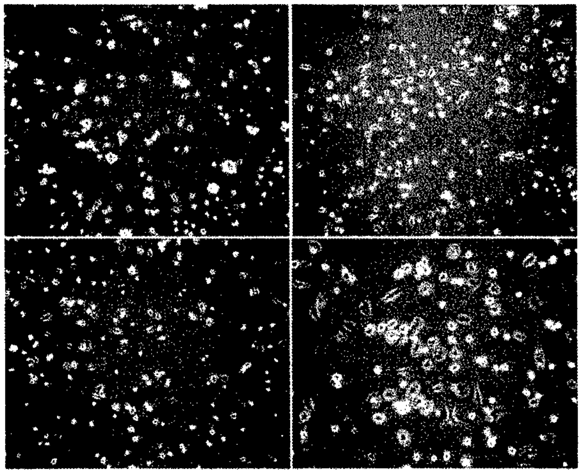

Figure 63. Phase contrast images of rat progenitor cells on HA-coated substrates at (**a**) 16 hours, (**b**) 40 hours, (**c**) 70 hours, and (**d**) 40 hours at higher magnification. Images **a** – **c** were taken at 10X, while **d** was taken at 20X to view the spreading of the cells.

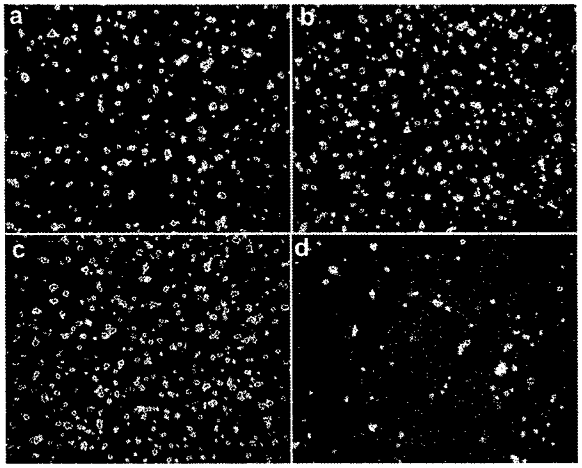

Figure 64. Phase contrast images of UMR106-01 osteoblastic cell line cultured on collagen/HA and fibronectin/HA substrates. HA-coated substrates were presented with collagen type I concentrations of (**a**) 10 μg/ml, (**b**) 50 μg/ml, and (**c**) 200 μg/ml; while (**d**) was coated with 10 μg/ml of fibronectin.

OPTIMIZING CELL-MATRIX COMPOSITES FOR BONE REGENERATION *IN VIVO* –

Project 9 (PI: George Muschler)

Performance of a cell-matrix composite *in vivo* will be influenced by several parameters that cannot be adequately modeled *in vitro*. These factors include:

i. Diffusion rate of nutrients from extracellular fluid through the implanted matrix
ii. Balance between the metabolic activity of implanted cells and diffusion, prior to revascularization
iii. Rate and extent of revascularization of graft sites or defects
iv. Vascularity of the local soft tissue
v. Quality and viability of local osseous and periosteal tissue
vi. Capacity of the cell-matrix composite to induce prompt revascularization of the grafted defect

Evaluation of these variables requires a model system in which the volume of the grafted defect is of sufficient size to make the limitations of diffusion and revascularization a limiting factor in a least part of the defect (at least 1 cm in size). Furthermore, the anatomic site must be relevant to the bone environment in which most grafting for trauma is performed (*i.e.* the diaphysis of a long bone). A canine femoral defect model that satisfies these design requirements was described in the initial proposal and reiterated in the 2000 annual report.

Selection of graft matrix materials

Previous work had investigated the ability of Connective Tissue Precursor Cells (CTPs) to form osteoblastic colonies (Colony Forming Units – Osteoblastic, CFU-Os). These studies had looked at allograft cancellous bone and allograft bone powder for their ability to selectively concentrate CFU-Os. The methods used for the investigation of these materials were applied to the study of hylan beads (~ 1000 μm) as a matrix material.

It was reported in the first year of the project that the hylan beads (Hylan B) could not be used effectively as a component in an affinity column. The beads proved to be too deformable, and as a result, progressively limited the flow of fluid and cells through the column and also resulted in clogging of the porous filters used to retain the beads in the column. Furthermore, when cells and matrix were mixed as a slurry, we found that we were unable to separate the beads from the non-attached suspended cells, because the beads were isodense with the cells (*i.e.* did not settle from solution, even with the aid of centrifugation). These difficulties led us to investigate the use of a non-crosslinked, dense, fibrous freeze-dried HA matrix provided by the Matrix Biology Institute. This preparation demonstrated improved function in a column. Fibrous clumps of matrix rehydrated leaving channels of sufficient size to allow fluid and cells to flow. However, clogging was still prevalent, as longer periods of rehydration were used, the matrix showed continual swelling making it progressively more restrictive to fluid flow and softening the gel to a state which was sufficiently deformable to clog the porous filter (as above).

Pursuant to the difficulties in identifying a suitable matrix, we conducted an on-site visit with Dr. Balazs, and members of his research staff from the Matrix Biology Institute, on June 14th, 2001 at the Cleveland Clinic Foundation. From these discussions, concerns were raised about the reproducibility of working with non-crosslinked HA as a matrix. Therefore, the difficulties experienced in early trials with hylan beads (mean diameter ~ 1000 μm) were revisited. Stemming from these discussions, several changes were made to the cell-loading regimen in an attempt to improve cell attachment. Rather than loading cells using an affinity column, the cells are mixed with the beads in a 10-fold volume dilution in physiologic saline and then passed through a 70 μm mesh. The added volume reduces the viscosity of the cell suspension and the beads, reducing clogging and helping to elute unbound cells. These beads provide a particle bed presenting an accessible three-dimensional surface for cell attachment and a void volume with a pore size that is compatible with cell migration. The bound cell-matrix composite graft is then recovered from the mesh for implantation into the bone defect.

In Vitro Experiments

A series of *in vitro* experiments has been initiated to verify the efficacy of these procedural changes. To date we have conducted 2 trials, and the results are summarized in Table 10.

Hylan Volume (μl)	Dilution Factor	Additional Rinse Volume (ml)	Cells Loaded	Cell Retention (%)
700	10	10	500×10^6	26
700	10	-	200×10^6	72

Table 10. Summary of in vitro cell loading experiments on hylan beads (~1000 μm).

The high cell loading in the first trial was overly viscous and therefore needed additional rinsing to elute unattached cells. As a result, fewer cells were loaded in the second trial, with much improved cell retention.

***In vivo* model system**

In vivo experiments were designed to evaluate the Hylan B formulation of HA using the previously described canine femoral defect model. In this model, a lateral biceps splitting approach is made followed by extraperiosteal exposure of the entire lateral surface of the proximal femoral diaphysis. Four identical cylindrical defects (1.0 cm diameter x 1.5 cm deep) are created in the canine proximal femur using a template fixed as a drill guide (Fig. 65). Each is separated by 1.5 cm of normal marrow. Grafts having dimensions of 0.95 cm diameter and 1.0 cm in height and a volume of approximately 700 μl are placed in each defect using a 3 ml syringe as a delivery device to insert the graft material directly into the defect site. Oxygen tension is reported telemetrically using a custom implanted device developed with the aid of the Department of Biomedical Engineering's Electronics Prototype Facility, taking advantage of technologies and expertise gained in the Total Artificial Heart Program. The initial design of this device has been further streamlined by reducing the size of the circuit board and components (including the power requirements and battery size) from that shown in (Fig. 65B-C). The telemetry device is now fabricated within a one-piece device held on the femur. In animals in which oxygen tension was measured, a one-piece assembly of the oxygen sensors and telemetry system is placed using the proximal and distal screw sites from the drill template for fixation (Fig. 66). One electrode is positioned in the center of each of the four defects. One electrode is also placed in normal non-traumatized vascular marrow space as a normally oxygenated tissue site control. On animals without oxygen tension measurement, each site was closed using a press fit polycarbonate cap to contain the graft material.

Outcome assessment was designed to quantitatively assess bone formation (micro CT analysis), histologic response and vascularity (undecalcified and decalcified histology), and oxygen tension within the graft site (*in vivo* telemetry system and platinum based oxygen electrodes). Two experiments were designed. *Experiment 1* compared sites grafted with HA to sites left ungrafted in three dogs. *Experiment 2* compared sites grafted with HA to sites grafted with autogenous cancellous bone graft harvested from the proximal humerus in nine dogs. These experiments were reduced significantly in scope from the 42 animals proposed in the initial proposal due to the additional basic work needed to identify the most appropriate formulation of HA to evaluate and due to time and budget constraints late in the project. All experiments are designed to distribute groups equally with respect to site, to control for potential performance bias at different site levels of the canine femur.

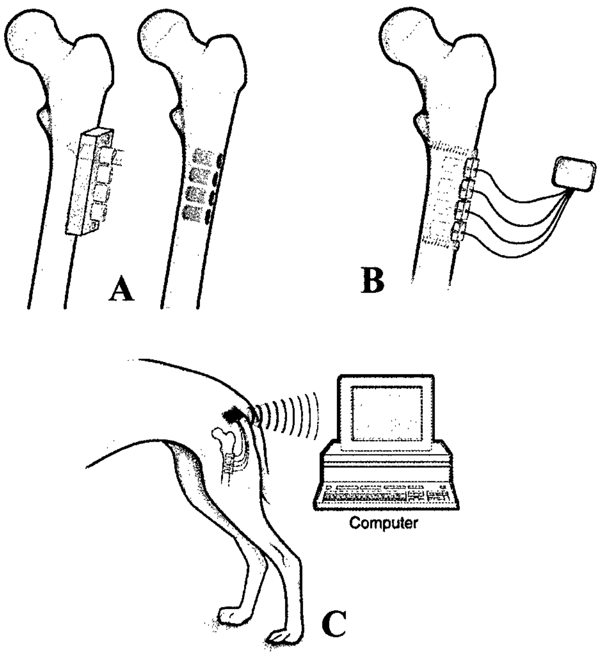

Figure 65. Schematic representation of the canine femoral defect model and oxygen tension data acquisition. **A)** Placement of the defect template over the lateral aspect of the femur and a representation of the femur following placement of the 4 grafts. **B)** Defect caps with oxygen sensors in place. **C)** Telemetric data collection system designed by the Cleveland Clinic Foundation, Department of Biomedical Engineering's Electronics Prototype Facility.

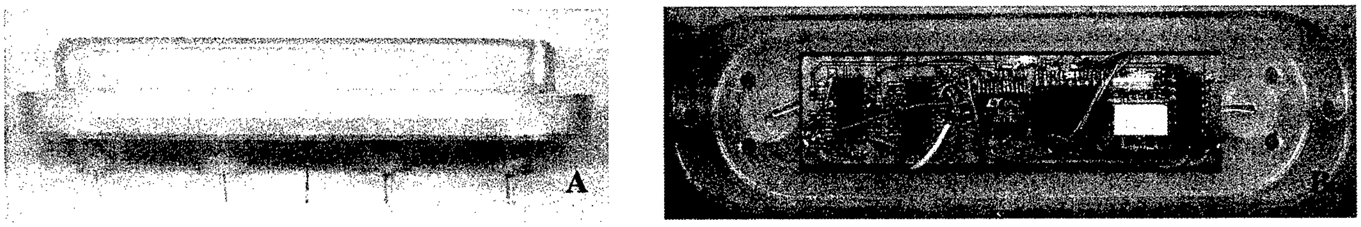

Figure 66. Telemetry Plate Construct: **A)** side view of plate assembly with five O_2 sensors. Note that the proximal and distal two sensors are positioned at the center of each respective graft site or implant. The center sensor is positioned through a small cortical drill hole into normal marrow. **B)** Top down view of circuit board of the telemetry device with cover plate removed. Note that the temperature sensor is placed within the plate.

Experimental design

Experiment 1

Specific Aim 1: To define the baseline performance of Hylan B in the femoral defect model in regard to bone formation (evaluated by micro CT) and tissue formation (histologic evaluation).

Specific Aim 2: To evaluate the rate of revascularization of Hylan B implants, as compared to empty defects.

Experimental groups: A – Hylan B alone (HA), B – Empty defect (-)

Table 11

Dog ID	Time (wks)	Site 1	Site 2	Site 3	Site 4
01D-271	1	HA	(-)	HA	(-)
01D-331	2	(-)	HA	(-)	HA
01D-367	3	(-)	HA	(-)	HA

Experiment 2

Specific Aim 1: To test the hypothesis that Hylan B will have comparable efficiency to autogenous bone as assessed by bone formation (evaluated by micro CT) and tissue formation (histologic evaluation).

Experimental groups: A – Hylan B alone (HA), B – Autogenous bone (AB)

Table 12

Dog ID	Time (wks)	Site 1	Site 2	Site 3	Site 4
02D-100	1	HA	AB		AB
02D-115	1	HA	AB		
02D-210	1	HA	AB		AB
02D-177	2	HA	AB	HA	AB
02D-072	6	HA	AB	HA	AB
02D-088	6	AB	HA	AB	HA
02D-097	6	AB	HA	AB	HA
02D-114	6	AB	HA	AB	HA
02D-178	6	AB	HA	AB	HA

Results

At the time of this report all surgery has been completed, all animals have been euthanized and all specimens have been collected. Table 13 below summarizes the processing that is planned in the analysis of these specimens for both Experiments 1 and 2. Tables 14 and 15 illustrate the distribution of these samples with respect to the time point of assessment.

Table 13

Experiment 1

Dog ID	Time (wks)	Site 1	Site 2	Site 3	Site 4	Labeling	Notes
01D-271	1	HA	(-)	HA	(-)		Telemetry data = 2 days
01D-331	2	(-)	HA	(-)	HA		Telemetry data = 7 days
01D-367	3	(-)	HA	(-)	HA		Telemetry data = 18 days

Experiment 2

Dog ID	Time (wks)	Site 1	Site 2	Site 3	Site 4	Labeling	Notes
02D-100	1	HA	AB		AB		Fx
02D-115	1	HA	AB				Fx
02D-210	1	HA	AB		AB		Fx
02D-177	2	HA	AB	HA	AB		Fx
02D-072	6	HA	AB	HA	AB		
02D-088	6	AB	HA	AB	HA		
02D-097	6	AB	HA	AB	HA	Calcein	
02D-114	6	AB	HA	AB	HA	Tetracyline. Calcein	
02D-178	6	AB	HA	AB	HA	Tetracyline. Calcein	

☐	Histology only (14)
▨	Histology & micro CT (30)

Table 14
Micro CT Analysis – 30 Sites

Time (wks)	AB	HA	(-)
1	2		
2	2	2	
3		2	2
6	10	10	

Table 15
Histologic Analysis – 44 Sites

Time (wks)	AB	HA	(-)
1	5	5	2
2	2	4	2
3		2	2
6	10	10	

Bone formation

As of the date of this report, data from micro CT images from samples is still being collected, and has not been subjected to quantitative analysis.

Histologic assessment

At the time of this report, histologic analysis has been performed only on graft sites from the first two dogs in *Experiment 1.* The histologic analysis of these samples provided by Dr. Bauer and images from these samples is presented as an Appendix to this report.

Oxygen tension within the graft site

Oxygen tension analysis was attempted on only the three animals in *Experiment 1.* These efforts were cut short by the malfunction of electrodes in the first two animals. Data collected from sites in the third animal is presented in Figure 67. These data demonstrate equilibration of oxygen tension in normal bone marrow in the range of 7%. The data from the graft sites demonstrates a dramatic fall in oxygen tension in all four sites during the first 4 days after implantation. This fall is followed by progressive recovery of oxygenation within the graft site into the normal tissue range in three of the four sites. One site, containing HA failed to recover. This finding will be correlated with histologic observations as they become available. Use of this oxygen tension assessment in *Experiment 2* was unfortunately precluded by budgetary limitations.

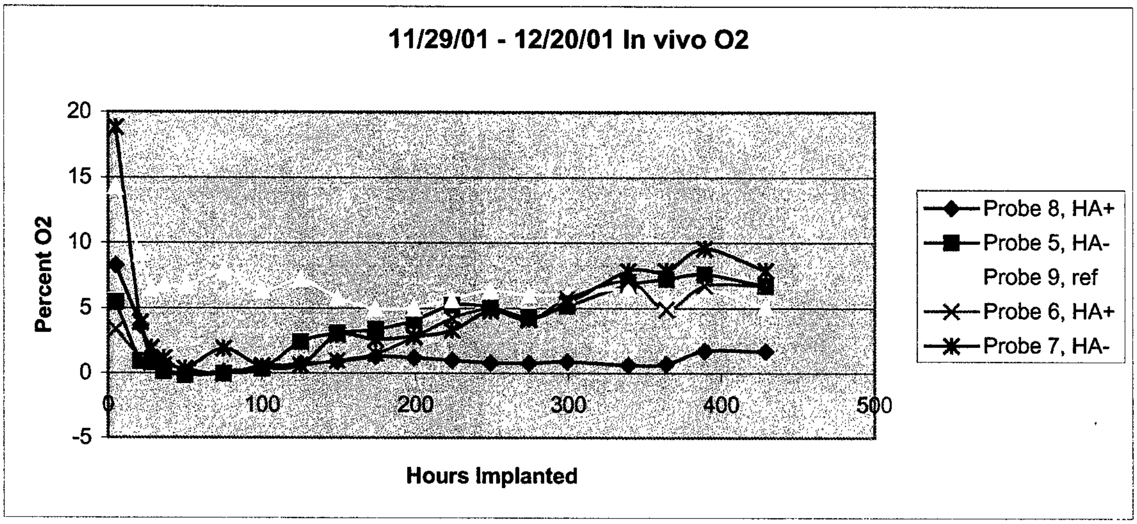

Figure 67. Oxygen tension within graft sites – *Experiment 1* (01D-367)

A MULTI-AXIAL EXTENSOMETER FOR GLOBAL MEASUREMENT OF BONE STRAIN – Project 10 (PI: Brian Davis)

An extensometer that measures displacements in 3D and converts the data into global bone strain magnitudes and rates was described in the 2000 Annual Report. This device is capable of monitoring physiological strains *in vivo,* and because of its 3D configuration can differentiate between bending and axial strains. The extensometer uses six paired capacitive sensors mounted to intraosseous pins and allows measurement of principal strain magnitudes and their direction, and maximum shear strain. Researchers on this project have focused on measurement of strain in bone to more fully understand the adaptation of bone to its functional environment.

Based on the data presented in "Design and testing of an extensometer for global measurement of bone strain suitable for use in vivo in humans," [61] (see Appendix of 2000 Annual Report) the extensometer is suited for measuring strains above 100 με. This type of device (Fig. 68) is capable of tracking strain up to strain rates in excess of 90,000 με/sec. As described previously, this device has significant advantages over current methods.

As tissue engineered bone becomes available for testing, this technology can be applied to the novel constructs for strain evaluation. These measurements can then be compared to strain readings taken from native bone for direct comparison. Future testing will be performed on bone regenerated *in vivo* in the canine femoral defect model (***Project 9***), as well as specimens from Dr. George Muschler's canine spinal fusion model (from an independent, related study not supported by this award).

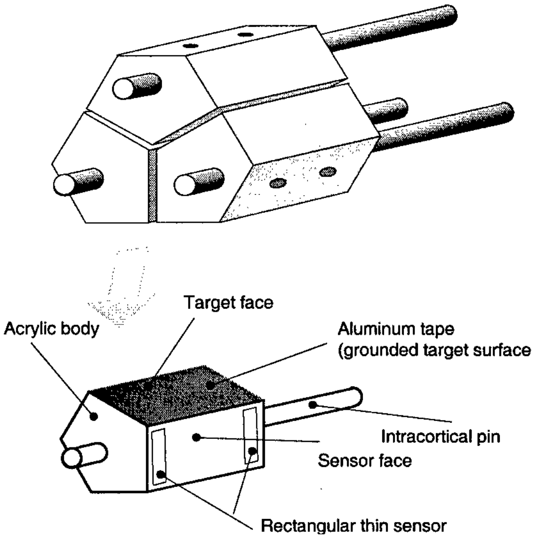

Figure 68. The 3D extensometer uses six capacitive sensors mounted to acrylic bodies that are attached to intraosseous pins. The acrylic bodies are mounted to the protruding ends of the pins after implantation.

Image Processing Group

The Image Processing Group is developing and employing technologies necessary to serve the needs of all relevant projects. The group provides prompt and definitive histologic, immunologic, and *in situ* analysis for bioengineered tissue specimens.

Confocal Laser Microscope Imaging

As described in the initial proposal, engineered tissues need to be evaluated for their spatial and temporal expression of specific biological markers that are present in native tissue. For reasons previously stated, the confocal laser microscope is the ideal tool for this analysis. A Leica TCS SP Confocal Microscope was purchased with the funds allocated. The instrument was fully operational as of September 2000. The images presented in Figures 6, 7, and 9 (***Project 4***) were all collected using the confocal microscope. Additionally, the bone grafts from ***Project 9*** excised following the completion of each animal trial will be evaluated using this microscope.

Phosphoimager

As described in the initial proposal, engineered tissues will need to be evaluated for the quality and quantity of specific gene expression patterns unique to their native tissue homologues. This type of imager has the capacity to handle fluorescence, as well as phospholuminescence. When combined with specific DNA and RNA probes, a phosphoimager can unambiguously identify and accurately measure these gene expression patterns. One specific application for use of this instrument would be for the quantification of radiolabeled protein and GAGs, for determination of synthesis and turnover rates in tendon organ cultures (***Project 5***). The Storm 860 phosphoimager (Molecular Dynamics, Inc.) described in the initial proposal was purchased and is currently operational in our labs.

Micro CT Station

As described in the 2000 and 2001 Annual Reports, a Micro CT Station and an Octane/SSE Workstation were to be purchased as capital equipment for support of the Image Processing Group. The Micro CT will allow us to analyze tissue engineered constructs with 3D volume imaging at a high spatial resolution (~20 μm). Rather than purchasing a commercially available Micro CT Station, the funds allocated for the Micro CT and Octane/SSE Workstation were combined to allow for the purchase of components to build a more sophisticated Micro CT Station, with the assistance of the Department of Biomedical Engineering's Mechanical and Electrionic Prototype Facilities. A high-powered Pentium Workstation was integrated to support the custom Micro CT. The Mechanical Prototype Facility completed the assembly of this system in April 2001. It is currently in use for the imaging of rat tibias by Ron Midura, Ph.D. on a related project. Additionally, this system is being used to scan the canine femurs recently explanted at various stages of *in vivo* bone formation (***Project 9***).

Automated Quantitative Microscopy

The traditional method of analysis of tissue sections and cellular data has been, and continues to be, manual light microscopic interpretation. The accuracy of such tedious and laborious manual methods depends largely on the skill of the user, and these methods do not allow further analysis of cell shapes and locations. In recent years, however, advanced histologic techniques have been combined with computerized image processing and analysis. These techniques continue to evolve in response to the recognized limitations of subjective or semi-quantitative data analysis and growing needs for obtaining large amounts of objective, quantitative data.

Our Department's Biomedical Imaging Group (http:\\www.ccf.org\ri\bme\image) has developed and continues to refine an automated image analysis system for use in quantitative microscopy. This system is versatile; allowing analysis of stained tissue sections, *in situ* hybridizations, confocal images, or cell cultures and provides the data in unambiguous statistical terms. This system also provides information that is difficult or impossible to obtain from manual assessment (*e.g.* size, shape, and orientation). The system will have immediate application in this proposal for quantification of the following:

- Cell morphology, including total cell counts, determination of cell area, cell color, shape analysis, and position/location data. These analyses will be aided by routines that perform opening and closing operations, boundary detection, global filling and decomposition.
- Immunochemical or routine stain analysis, by chromagen color, purity, and intensity.
- Gross morphologic features such as cellularity, blood vessel luminal area, vascular density, extent of collagen infiltration, tissue cell density, collagen fibril size, and continuity of elastin fibers.
- Grain counting techniques using grey-scale analysis of *in situ* hybridizations.
- *In situ* hybridization chromagen distribution using advanced color segmentation algorithms.

- Determination of local optical strain by tracking surface markers in mechanical test systems.
- Quantification of fluorescence intensity in immunohistochemically stained tissue.

The software for this automated image analysis system is complete. It is currently functional on high-powered UNIX workstations and is being adapted for application and usage on Windows NT systems. The holdup in adaptation for the PC is that this system requires 1 GB of RAM. Very few PCs have this capacity; therefore this analysis tool is currently still available only on UNIX workstations. However, the file server purchased in year one (see below), allows the data to be stored remotely and then accessed from either PC or UNIX workstation.

These quantitative microscopy techniques have been used extensively in the analysis of data presented here in ***Project 4*** (Vesely), ***Project 5*** (Derwin), ***Project 8*** (Midura), and ***Project 9*** (Muschler). The Image Processing group under the direction of Kim Powell, Ph.D., developed software specific to each of these cases. As new applications arise, they will be called on to write code for new software development.

File Server

A highly sophisticated F520-8N-256-14D9 File Server (StorNet, Inc., West Chester, PA) was purchased in the first year of this award and is currently being used by all investigators in the Tissue Engineering Initiative and Image Processing Group. This equipment is installed and fully functional. It has been networked to support multiple image data collection systems within the scope of the Tissue Engineering Initiative. It facilitates the remote storage of image files too immense for analysis on a PC, such that those files may be processed using UNIX stations, yet the data can still be accessed from any PC within the department.

Engineering Design and Analysis Group and Prototype Facilities

The Department of Biomedical Engineering houses an integrated team focused on engineering design, analysis, and prototype fabrication. The team, under the direction of Mark Goodin, M.S., combines the skill sets of the Engineering Design and Analysis Group with the fabrication capabilities of the Mechanical, Electrical, and Polymer Prototype Facilities. Over the course of the entire award period, these groups have made significant contributions in the design and fabrication of devices furthering our tissue engineering research efforts.

Mark VI Magnetic Flow Sorter

The initial work involving the Mark VI flow chamber, described in the 2000 Annual Report, focused on the design and fabrication of a "clinical", full-scale disposable prototype device. This cell separation flow chamber was designed to separate and selectively concentrate bone precursor cells in support of Dr. Maciej Zborowski's research efforts (Figs. 51, 52, ***Project 7***). During the 2001 reporting period, the Engineering Design and Analysis Group refined the initial Mark VI design. To further improve the flow uniformity within the device, a second inlet port was added for the carrier fluid. The inlet and outlet connections were also modified to accommodate the same size tubing. The Mechanical Prototype and Polymer Prototype Facilities fabricated four second-generation Mark VI flow chambers. The most recent experimental results from the second-generation flow chambers show further performance improvement in the reduction of unwanted, non-magnetic cell crossover. Dr. Zborowski's lab, in collaboration with the Electronic Prototype Facility, continues to refine the electrical fields to further improve the selectivity of the system.

Tendon Tissue Cyclic Loading Device

A test unit was designed and fabricated to perform cyclic loading of canine flexor tendon samples while suspended in culture medium. This device was built to support Dr. Kathleen Derwin's research studying the effect of mechanical loading on tendon fibroblasts (Fig. 30, ***Project 5***). The Engineering Design and Analysis Group and the Mechanical and Electrical Prototyping Facilities collaborated on this project. The entire test setup can be placed in an incubator to maintain physiologic conditions. The design of the test unit allows for minimum amount of culture medium (2 – 3 ml), small overall tendon displacements (1 – 2 mm) and a gripping mechanism to prevent tissue slippage or failure. The test unit is easily disassembled for cleaning and sterilization. A stopcock and septum allows for routine exchange of culture medium, without compromising sterility or removing the tendon sample from the gripping mechanism. Software programming using LabVIEW™ (v6.0.2, National Instruments, Austin, TX) to control the test system and to acquire the test data has been completed. The existing version has been tested with both native tendon and SIS grafts in load control. Currently, a second-generation version is being worked on to allow the investigators to also run the system in displacement control. The next step in this program is to replicate the test chamber and make the necessary modifications to the system to provide the capability to test up to eight individual specimens simultaneously. The current system allows for loading of a single specimen and requires manual exchange of test chambers in order to test more than one specimen. A newer system that allows for the simultaneous loading of up to 8 specimens, as well as continuous flow-through of medium to improve nutrient delivery, is currently in development.

In Vitro Articular Cartilage / Synovium (IVACS) Chamber

The IVACS chamber is a flow chamber designed to provide consistent, uniform, laminar flow of nutrients to cultured cartilage tumor cells at a rate that is similar to the flow rates experienced by articular cartilage cells *in vivo*. The concept of the IVACS chamber was conceived by Anthony Calabro, Ph.D., to provide a uniform nutrient concentration to different articular cartilage specimens. The IVACS flow chamber is shown in Figure 69. In this image, the fluid carrying the nutrients for the cartilage cells is shown in blue. The design has two inlet ports, 180° apart, with an outlet in the center of the device with fluid exiting at the top. The fluid rich in nutrients flows in from the sides, through the stainless steel outer housing, around the stainless steel center piece, across the flat bottom which is in contact with the upper surface of the specimens (not shown in this image) and then upwards out the center exit. A cut-away view of the flow chamber showing velocity vectors, static pressure distribution, and streamlines colored by speed is presented in Figure 70.

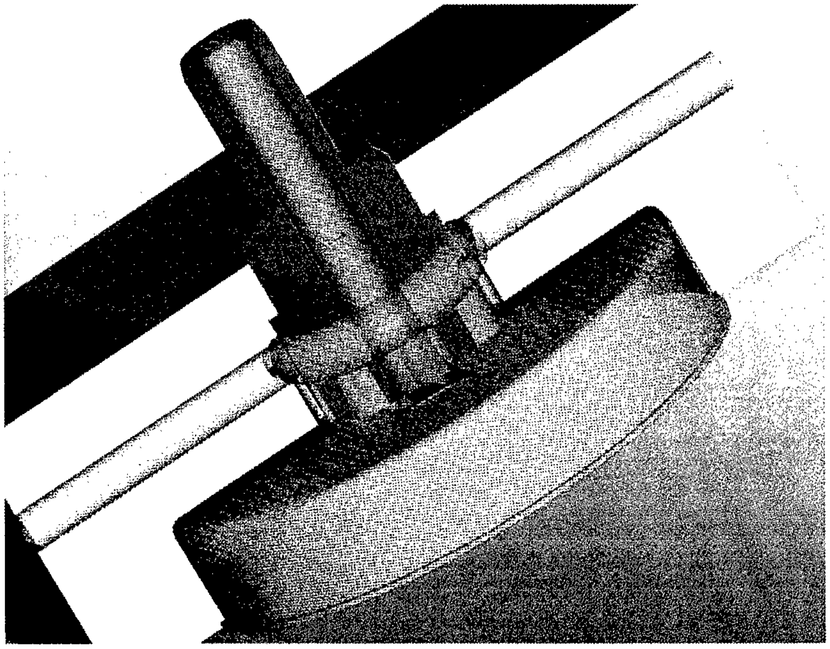

Figure 69. *In Vitro* Articular Cartilage/Synovium (IVACS) Chamber.

Three dimensional solid modeling software (Pro/Engineer, Parametric Technology Corporation, Waltham, MA) and Computational Fluid Dynamics (CFD) software (CFX5, AEA Technology

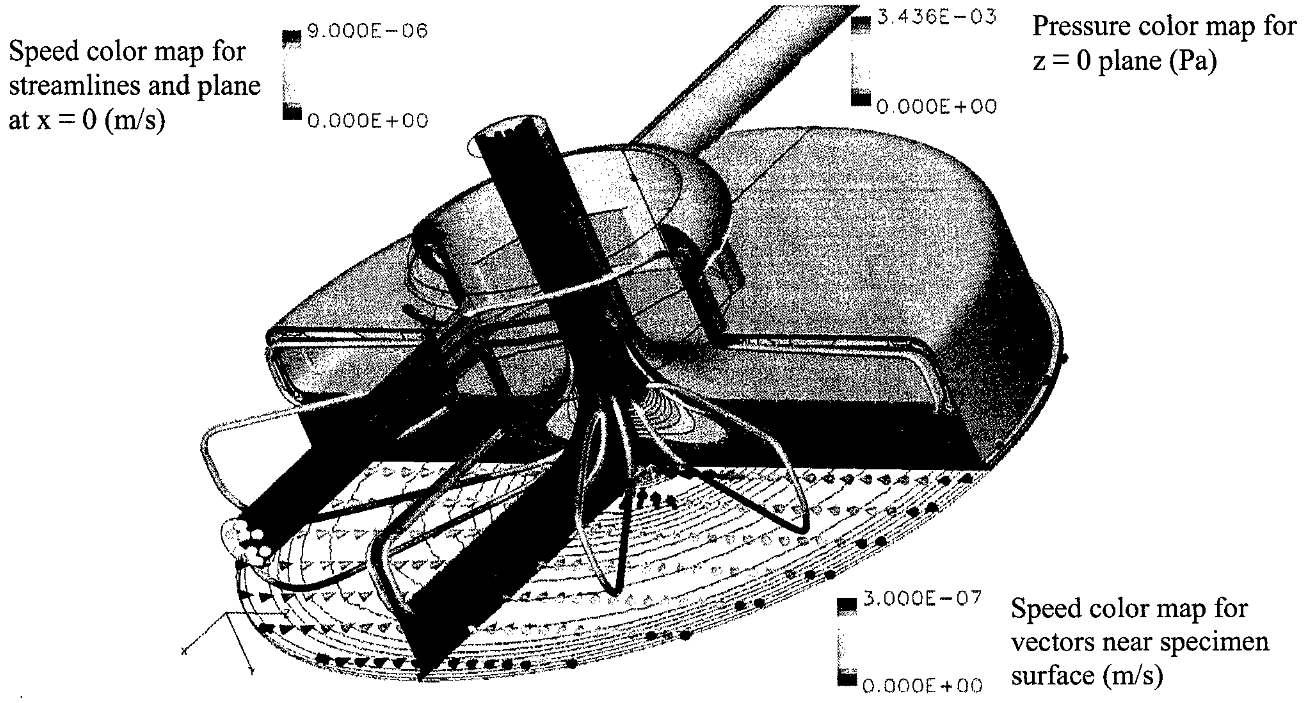
Speed color map for streamlines and plane at x = 0 (m/s)
9.000E-06
0.000E+00
3.436E-03
0.000E+00
Pressure color map for z = 0 plane (Pa)
3.000E-07
0.000E+00
Speed color map for vectors near specimen surface (m/s)

Figure 70. IVACS cut-away view to show velocity, pressure, and streamline distributions.

Engineering Software Inc., Bethel Park, PA) were used to design the device and simulate the fluid flow patterns in the flow chamber. Design iterations were accomplished rapidly using Pro/Engineer to make design changes and then using CFX5 to determine the resulting impact on the chamber flow field. This approach allowed us to optimize the chamber design and provide a uniform flow field across the cartilage cell specimens. For example, the number of inlet ports needed to provide uniform flow across the specimen area was determined using this iteration process. The addition of a second inlet port, 180° opposed to the initial single inlet, greatly improved the flow uniformity across the cartilage cells. This is demonstrated in Figure 71 that presents fluid speed versus distance circumferentially around the flow chamber at an axial location near the specimen surface. In this figure, the lines show the CFD predicted speed of the fluid at three radial locations from the centerline of the chamber. A linear regression is shown for each set of data. At a radial location of 0.015 m, which is near the center points for the cell specimens, the total variation in speed around the device is 14%. Adding a second inlet reduces this total variation in speed to 3%. A four-inlet version was also designed and analyzed but the improvement in terms of uniform flow was extremely small and therefore did not warrant the further complication of the design.

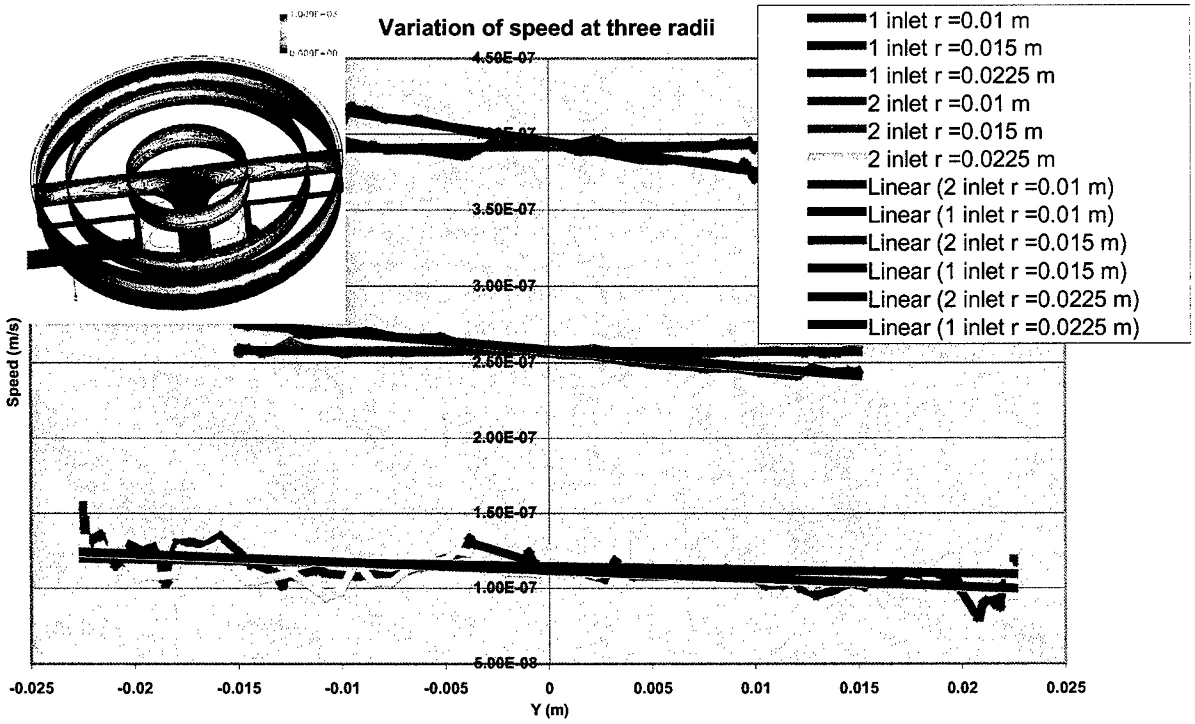

Figure 71. Demonstration of improved flow uniformity after addition of the second inlet port.

Micro CT Scanner

The design, development, and fabrication of the Micro CT scanner, for microimaging of small animals and specimens such as biopsies, was accomplished by the Mechanical and Electronic Prototyping Facilities. This new equipment, developed under the direction of Kim Powell, Ph.D., is available for use by all investigators in the Department of Biomedical Engineering. The Micro CT scanner is capable of high-resolution 3D imaging on the order of ~ 20 μm. The specific contributions for this large project from each group are outlined below:

Electronic Prototyping Facility

- System design, assembly, drawings, room modifications
- Design and build camera/shutter controller
- Install camera, frame grabber, software, drawings for sample riser, source mount
- Modified camera/shutter controller timing circuits
- Mounted source, new camera interface, x-ray survey, tested intensifier
- Enclosure design, phantom designs, planer test images
- Cable management design and implementation, 3D phantom imaging
- Modified camera controller to also control intensifier field, install interlock switches

Mechanical *Prototyping Facility*

- Built lead room enclosure (6’ x 14’ x 7’ high) including construction of plywood inner framing, outer lead walls & lead doors, and interior white liners
- Designed and constructed translation frame for x-ray source
- Designed and fabricated brackets for holding indexing table and a frame for the image intensifier
- Designed and built four phantoms for system calibration
- Designed and built specimen holders

Other contributions

In addition to these large scale contributions, the Mechanical, Electronic, and Polymer Prototyping Facilities have contributed in the design and fabrication of many custom fixtures that are integral parts of the various Tissue Engineering Initiative research projects. While too numerous to list completely, many of these fixtures can be seen within the context of the individual PIs’ summaries, for example:

- The silicone mold for branched collagen constructs (Fig. 22, ***Project 4***)
- Custom grips for mechanical loading of tendon explant and bioartificial graft evaluation (Fig. 26A, ***Project 5***)
- Custom rotational device for evaluation of cross-sectional area in tendon explants and bioartificial grafts (Fig. 26B, ***Project 5***)
- Static loading jigs for the culture of tendon explants under physiologic loads (Fig. 28, ***Project 5***)
- Custom jig for the positioning and stabilization of diabetic foot specimens while undergoing mechanical testing (Fig. 36, ***Project 6***)
- *In vivo* oxygen tension telemetry probes for use in the femoral bone defect model (Fig. 66, ***Project 9***)
- Multi-axial extensometer for *in vivo* measurement of bone strain (Fig. 68, ***Project 10***)

KEY RESEARCH ACCOMPLISHMENTS

---

1. Established in-house development of hylan gels. These efforts yielded elastic gels with improved mechanical integrity that are much better suited to our purposes than those previously investigated (***Project 1***). Efforts to further refine these gels are ongoing.

2. Identified multiple factors that provide evidence for a direct role of hyaluronan synthesis in epidermal regeneration during wound repair, using the organotypic rat epidermal keratinocyte (REK) model (***Project 2***).

3. Implemented a well-defined investigation into the benefits of surface modification and UV-irradiation of the hylan gel formulations to enhance cell attachment and proliferation (***Project 4***).

4. Began investigations into the strengthening of hylan gel substrates through the deposition of collagen and elastin matrices laid down by cells cultured on and within these gels (***Project 4***).

5. Established baseline biochemical and mechanical properties of native flexor tendon tissue for comparison to future tissue engineered tendon constructs (***Project 5***).

6. Initiated development of a small intestine submucosa-based (SIS) tissue engineered tendon construct (***Project 5***).

7. Designed a dynamic loading device for investigation of the impact of load on the mechanical properties of tendon matrix. This device can also be used to condition tissue engineered tendon constructs (***Project 5***).

8. Developed a biaxial skin measurement system (BSMS) for assessing the mechanical properties of skin (***Project 6***).

9. Developed methods for assessing the mechanical properties of skin that are likely to affect stress at the skin-fat interface (***Project 6***).

10. Refined a second-generation prototype magnetic cell deposition system for the selective isolation and concentration of bone precursor cells (***Project 7***).

11. Developed methods for the assessment of bone precursor cell attachment, proliferation, and mineralization on hylan substrates (***Project 8***).

12. Developed a technique for isotropic, hylan coated tissue culture inserts for the *in vitro* investigation of hyaluronan's role in the differentiation of bone precursor cells (***Project 8***).

13. Refined cell-loading protocol to allow for the use of hylan beads as a substrate for use in a previously developed *in vivo* canine femoral defect model. This reverses claims made previously that this matrix was not suitable for use in this model (***Project 9***).

14. Conducted in vivo assessments of hylan beads as a potential matrix for loading of connective tissue progenitor cells (CTPs) in the canine femoral defect model (***Project 9***).

15. Developed a novel multiaxial strain gauge for the in vivo assessment of bone strain, in addition to the methods for implantation of such a gauge (***Project 10***).

16. Incorporated several new imaging and image analysis systems into the Department of Biomedical Engineering's Image Processing Group.

17. Developed and fabricated many prototype devices to facilitate the various tissue engineering projects through collaborations between the investigators, the Department of Biomedical Engineering's Engineering Design and Analysis Group and the Mechanical, Electronic, and Polymer Prototype Support Facilities.

REPORTABLE OUTCOMES

---

1. A 2-year postdoctoral fellowship was awarded to Anand Ramamurthi, Ph.D., a post-doctoral research associate by the American Heart Association (Ohio Valley Affiliate) (AHA ID# 0020393B, awarded 7/1/00 – 6/30/02).

2. A technical abstract based on the study of smooth muscle cell attachment on UV-irradiated hylans was presented at the Biomedical Engineering Society (BMES) Annual Meeting in Durham, NC (October 2001).

   Ramamurthi, A. and Vesely, I., Surface Treatment of Hylan Gels for Induction of Cell Attachment (2001 Annual Report)

3. A technical abstract based on the study of smooth muscle cell attachment on UV-irradiated hylans was presented at the Biomedical Engineering Society (BMES) Annual Meeting in Durham, NC (October 2001).

   Ramamurthi, A. and Vesely, I., Effects of UV-Irradiation on Cell-Adhering Properties of Crosslinked Hyaluronan Gels (2001 Annual Report).

4. A technical abstract based on the study of cell attachment on hylans was presented as a poster at the *NIH BECON Symposium on Tissue Engineering*, Bethesda, M.D., (June 2001).

   Ramamurthi, A., and Vesely, I., Crosslinked Hyaluronan as Scaffolds for Engineering Soft Tissues (2001 Annual Report).

5. A technical abstract based on the study of smooth muscle cell attachment on hylans was presented at the Midwestern Tissue Engineering Consortium (MTEC) in Cleveland, OH (April 2001).

   Ramamurthi, A. and Vesely, I., Smooth Muscle Cell Adhesion on Crosslinked Hyaluronan Gels (2001 Annual Report).

6. A technical abstract based on the study of cell attachment on hylans was presented as a poster at the Cleveland Clinic Foundation Annual Research Symposium in Cleveland, OH (October 2000).

   Ramamurthi, A. and Vesely, I., Cell Attachment on Surface-Treated Hylan Gels (2001 Annual Report).

7. A technical abstract based on the study of cell attachment on hylans was presented at the Biomedical Engineering Society (BMES) Annual Meeting in Seattle, WA (October 2000).

   Ramamurthi, A. and Vesely, I., Cell Attachment on Surface-Treated Hylan Gels (2000 Annual Report).

8. A technical abstract based on the study of cell attachment on hylans was presented as a poster at the Hyaluronan 2000 meeting in Wrexham, Wales, UK (September 2000).

   Ramamurthi, A. and Vesely, I., Cell Attachment on Surface-Treated Hylan Gels (2000 Annual Report).

9. A technical abstract based on the study of tendon organ culture was submitted for presentation at the Orthopaedic Research Society (ORS) Annual Meeting in New Orleans, LA (February 2003).
   Abreu, E., Baker, A., and Derwin K., The Mechanical Properties of Tendons Cultured Under No Load in Variable Serum Concentrations.

10. A technical abstract based on the homotypic variation of canine flexor tendons was presented at the Midwest Tissue Engineering Consortium (MTEC) Annual Meeting in Ann Arbor, MI (April 2002).
    Abreu, E., Baker, A., and Derwin K., Effects of Mechanical Load on Tendon Cells Resident in an "Ideal" Scaffold.

11. A technical abstract based on the homotypic variation of canine flexor tendons was submitted for presentation at the Orthopaedic Research Society (ORS) Annual Meeting in New Orleans, LA (February 2003).
    Abreu, E., Baker, A., and Derwin K., Homotypic Variation of Canine Flexor Tendons.

12. A technical abstract based on the in vivo animal model of SIS as a replacement for canine flexor tendons was submitted for presentation at the 4th Annual SIS Symposium in Phoenix, AZ (December 2002).
    Androjna, C., Spencer, E., Orban, J.M., Caplan, A.I., Iannotti J.P., and Derwin K., Evaluation of Porcine Small Intestine Submucosa (SIS) for the Repair and Regeneration of Flexor Tendon.

13. A manuscript summarizing the underlying work upon which ***Project 2*** is based has been accepted for publication and will be sent for addition to this report once it is published.
    Rilla, K., Lammi M.J., Sironen R., Törrönen K., Luukkonen M., Hascall V.C., Midura R.J., Hyttinen M., Pelkonen J., Tammi M.I., and Tammi R. Changed lamellipodial extension, adhesion plaques and migration in epidermal keratinocytes containing constitutively expressed sense and antisense hyaluronan synthase 2 (HAS2) genes. *Journal of Cell Sciences* (in press), 2002.

14. A manuscript summarizing the underlying work upon which ***Project 2*** is based was published.
    Tammi, R.H., Rilla, K., Pienimäki, J.P., MacCallum, D.K., Hogg, M., Luukkonen, M., Hascall, V.C., and Tammi, M.I.. Hyaluronan enters keratinocytes by a novel endocytic route for catabolism. *The Journal of Biological Chemistry* **276**: 35111-35122, 2001.

15. A manuscript summarizing the underlying work upon which ***Project 2*** is based was published.
    Pienimäki, J.P., Rilla, K., Fülöp, C., Sironen, R.K., Karvinen, S., Pasonen, S., Lammi M.J., Tammi, R.H., Hascall, V.C., and Tammi, M.I. Epidermal growth factor activates hyaluronan synthase 2 in epidermal keratinocytes and increases pericellular and intracellular hyaluronan. *The Journal of Biological Chemistry* **276**: 20428-20435, 2001 (2001 Annual Report).

16. The thesis "The effect of the degree of crosslinking on the modulus of hylan" was completed by Ms. Maida Ann Ludwig, Department of Biomedical Engineering, Case Western Reserve

University, as a research requirement for the granting of an M.S. degree in Biomedical Engineering in August 2000 (2000 Annual Report).

17. The thesis "Design and test of an extensometer for global measurement of bone strain suitable for use *in vivo* in humans" was completed by Ms. Gail Patricia Perusek, Department of Mechanical and Aerospace Engineering, Case Western Reserve University, as a research requirement for the granting of an M.S. degree in Mechanical Engineering in May 2000 (2000 Annual Report).

18. A manuscript summarizing the underlying work upon which ***Project 2*** is based was published.
    Tammi, R.H., Tammi, M.I., Hascall, V.C., Hogg, M., Pasonen, S., and MacCallum, D.K. A preformed basal lamina alters the metabolism and distribution of hyaluronan in epidermal keratinocyte "organotypic" cultures grown on collagen matrices. *Histochemistry and Cell Biology* **113**: 265-277, 2000 (2000 Annual Report).

19. A manuscript summarizing the development work detailed in ***Project 4*** was published.
    Ramamurthi, A. and Vesely, I. Smooth Muscle Cell Adhesion on Crosslinked Hyaluronan Gels. *Journal of Biomedical Materials Research* **60**: 196-205, 2002.

20. A technical abstract based on the study of cell attachment on hylans has been submitted and accepted for presentation at the 2nd Joint EMBS-BMES Conference in Houston, TX (October 2002).
    Ramamurthi, A. and Vesely, I. In Vitro Synthesis of Elastin Sheets on Crosslinked Hyaluronan Gels for Tissue Engineering of Aortic Valves.

21. A technical abstract based on the study of cell attachment on hylans was presented at the IV World Congress of Biomechanics in Calgary, Alberta, Canada (August 2002).
    Vesely, I., Shi, Y., and Ramamurthi, A. Developing a Composite, Tissue Engineered Aortic Valve.

22. A technical abstract based on the study of cell attachment on hylans was presented at the 2nd European Conference on Elastin at the University of Basilicata in Acquafredda di Mantratea, Campania, Italy (April 2002).
    Ramamurthi, A. and Vesely, I. Elastin-Hyaluronan Composite Materials for Tissue Engineering of the Aortic Valve.

23. A technical manuscript based on the study of cell attachment on hylans was presented at, and was published in the proceedings of, the 39th Annual Rocky Mountain Bioengineering Symposium in Copper Mountain, CO (April 2002).
    Shi, Y., Ramamurthi, A., and Vesely, I. Towards Tissue Engineering of a Composite Aortic Valve. *Biomedical Sciences Instrumentation* **38**: 35-40, 2002.

24. A technical abstract based on the study of cell attachment on hylans has been submitted for presentation at the Biosurfaces 2002 Conference in Scottsdale, AZ (November 2002).
    Ramamurthi, A. and Vesely, I. Surface Modification of Hyaluronan Gels to Enhance Cell Adhesion.

25. A technical abstract based on the study of cell attachment on hylans was presented at the Society for Biomaterials Annual Conference in Tampa, FL (April 2002).
    Ramamurthi, A. and Vesely, I. Evaluation of UV-Treated Hyaluronan Gels as Biomaterials for Cardiovascular Tissue Engineering.

26. A technical abstract based on the study of cell attachment on hylans was presented at the International Society for Applied Cardiovascular Biology and Medicine Meeting (ISACB) in St. Gallen, Switzerland (February 2002).
    Ramamurthi, A. and Vesely, I. Ultraviolet Irradiation Enhances the Performance of Hylan Gels as Scaffolds for Cardiovascular Tissue Engineering. *Cardiovascular Pathology* **11**(1): 55, 2002.

27. A technical abstract based on the study of cell attachment on hylans was presented at the TE 2002: International Workshop in Tissue Engineering in St. Gallen, Switzerland (February 2002).
    Vesely, I., Shi, Y., and Ramamurthi, A. Towards a Composite, Tissue-Engineered Aortic Valve.

28. A manuscript summarizing the development work detailed in ***Project 4*** has been provisionally accepted for publication and will be sent for addition to this report once it is published.
    Ramamurthi, A. and Vesely, I. Ultraviolet Light-Induced Modification of Crosslinked Hyaluronan Gels. *Journal of Biomedical Materials Research* (submitted 2002).

29. A manuscript summarizing the development work detailed in ***Project 4*** has been accepted for publication and will be sent for addition to this report once it is published.
    Ramamurthi, A. and Vesely, I. In Vitro Synthesis of Elastin Sheets on Crosslinked Hyaluronan Gels for Tissue Engineering of Aortic Heart Valves. *IEEE Transactions on Biomedical Engineering* (in press).

30. A technical abstract based on the study of cell attachment on hylans has been accepted for presentation at the International Smith and Nephew International Symposium on Tissue Engineering in Atlanta, Georgia (October 2002).
    Ramamurthi, A., and Vesely, I. Elastin-Hyaluronan Composites for Tissue Engineering of the Aortic Valve.

31. A technical abstract based on the study of cell attachment on hylans has been accepted for presentation at the International Smith and Nephew International Symposium on Tissue Engineering in Atlanta, Georgia (October 2002).
    Shi, Y., and Vesely, I. *In-Vitro* Synthesis of Elastin Sheets on Collagen Fiber Bundles.

32. A technical abstract based on the study of the mechanical properties of diabetic skin was presented at, and was published in the proceedings of, the IEEE 28th Annual Northeast Bioengineering Conference at Drexel University in Philadelphia, Pennsylvania (April 2002).
    Chen, Y., Davis, B., and Valdevit, A. Regional Differences In Strength At The Plantar Skin-Fat Interface.

33. A poster presentation and technical abstract based on the study of the mechanical properties of diabetic skin were presented at the IV World Congress of Biomechanics in Calgary, Alberta, Canada (August 2002).

    Chen, Y., Davis, B., and Valdevit, A. Effects Of Diabetes On The Strength Of The Plantar Skin-Fat Interface.

All publications listed above are included in their entirety in the Appendices that follow, except where otherwise noted.

CONCLUSIONS

It has been shown that cells attach and proliferate (neonatal rat aortic smooth muscle cells, ***Project 4***) actively on hylan gels treated with cell adhesion proteins (best results with collagen I). These cells can also migrate and proliferate into UV-irradiated gels. Additionally, cells that bind to hyaluronan via CD44 receptors are able to adhere without surface modification (TFX 3224.17.14 cells, ***Project 8***). The efforts of Dr. Hascall's and Dr. Midura's labs continue to further define the role of hyaluronan in the development of both soft tissues as well as bone (***Projects 2*** and ***8*** respectively). Furthermore, *in vitro* studies have shown that hylan gel beads can serve as an effective substrate for attachment of connective tissue progenitor cells (CTPs, ***Project 9***). *In vivo* experiments, where control of influencing factors is much less predictable, have been completed in this realm. However, the full analyses of these specimens are not yet complete.

Our work in the three-year granting period of the project has shown that hylan gels are suitable materials for development of biological implants. Chemical and structural modifications made over the past year and a half have significantly improved the strength and elasticity of these gels (*i.e.* increased salt content and alcohol/salt wash to reduce swelling). These changes have allowed for the mechanical testing in tension that had previously been unattainable. It is believed that gel reinforcement via synthesis of collagen-rich and elastin-rich matrices by attached cells will contribute to further improvement in gel strength and elasticity. Experiments to verify the validity of this claim to date have been encouraging. The improvements in these matrices coupled with the many testing techniques and prototypes developed in this initiative give great hope to the continued efforts in these realms of tissue engineering.

REFERENCES

1. Balazs EA and Denlinger JL. Clinical uses of hyaluronan. In *The Biology of Hyaluronan* (Ciba Foundation Symposium #143). (Eds. Evered D and Whelan J). John Wiley & Sons, Chichester and New York: 265-280, 1989.

2. Larsen NE, Leshchiner E, Balazs EA, Belmonte C. Biocompatibility of hylan polymers in various tissue compartments. In Polymers in Medicine and Pharmacy (Proceedings of the Materials Research Society, Spring Meeting, April 17-21, 1995, San Francisco, CA). (Eds. Mikos AG, Leong KW, Radomsky ML, Tamada JA, Yaszemski MJ). Materials Research Society, Pittsburgh, PA: 149-153.

3. Rilla K, Lammi MJ, Sironen R, Törrönen K, Luukkonen M, Hascall VC, Midura RJ, Hyttinen M, Pelkonen J, Tammi MI, Tammi R. Changed lamellipodial extension, adhesion plaques and migration in epidermal keratinocytes containing constitutively expressed sense and antisense hyaluronan sythase 2 (HAS2) genes. *Journal of Cell Sciences* (in press), 2002.

4. Pienimäki JP, Rilla K, Fülöp C, Sironen RK, Karvinen S, Pasonen S, Lammi MJ, Tammi R, Hascall VC, Tammi MI. Epidermal Growth Factor Activates Hyaluronan Synthase 2 in Epidermal Keratinocytes and Increases Pericellular and Intracellular Hyaluronan. *The Journal of Biological Chemistry* **276**: 20428-20435, 2001.

5. Tammi R, Rilla K, Pienimäki JP, MacCallum DK, Hogg M, Luukkonen M, Hascall VC, Tammi MI. Hyaluronan enters keratinocytes by a novel endocytic route for catabolism. *The Journal of Biological Chemistry* **276**: 35111-35122, 2001.

6. Tammi R, Tammi MI, Hascall VC, Hogg M, Pasonen S, MacCallum DK. A preformed basal lamina alters the metabolism and distribution of hyaluronan in epidermal keratinocyte "organotypic" cultures grown on collagen matrices. *Histochemistry and Cell Biology* **113**: 265-277, 2000.

7. Kader KN, Akella R, Ziats NP, Lakey LA, Harasaki H, Ranieri J, Bellamkonda RV). ENOS over-expressing endothelial cells inhibit platelet aggregation smooth muscle cell proliferation in vitro. *Tissue Engineering* **6**[3]: 241-251, 2000.

8. Mulholland DS, Gotleib AI. Cell biology of vascular interstitial cells. *Canadian Journal of Cardiology* **12**(3): 231-236, 1996.

9. Oakes BW, Batty AC, Handley CJ, Sandberg LB. The synthesis of elastin, collagen, and glycosaminoglycans by high density primary cultures of neonatal rat aortic smooth muscle. An ultrastructural and biochemical study. *European Journal of Cell Biology* **27**: 34-46, 1982.

10. Andreopoulos FM, Beckman EJ, Russell AJ. Light-induced tailoring of PEG-hydrogel properties. *Biomaterials* **19**(15): 1343-52, 1998.

11. Balazs EA, Leshchiner A. Crosslinked gels of hyaluronic acid and products containing such gels. U.S. Patent No. 4,582,865, 1986.

12. Ramamurthi A and Vesely I. Smooth Muscle Cell Adhesion on Crosslinked Hyaluronan Gels. *Journal of Biomedical Materials Research* **60**: 196-205, 2002.

13. Rehakova M, Bakos D, Soldan M, Vizarova K. Depolymerization reactions of hyaluronic acid in solution. *International Journal of Biological Macromolecules* **16**(3): 121-124, 1994.

14. Orlidge A, D'Amore PA. Cell specific effects of glycosaminoglycans on the attachment and proliferation of vascular wall components. *Microvascular Research* **31**(1): 41-53, 1986.

15. Termeer CC, Hennies J, Voith U, Ahrens T, Weiss JM, Prehm P, Simon JC. Oligosaccharides of hyaluronan are potent activators of dendritic cells. *Journal of Immunology* **165**(4): 1863-1870, 2000.

16. Ludwig MA. The effect of the degree of crosslinking on the modulus of hylan. *Case Western Reserve University Thesis*, August 2000. (Included in Appendix of 2000 Annual Report).

17. Butler DL, Awad HA. Perspectives on cell and collagen composites for tendon repair. *Clinical Orthopaedics* **367**(Supplement): S324-S332, 1999.

18. Barocas VH, Tranquillo RT. An isotropic biphasic theory of tissue-equivalent mechanics: the interplay among cell traction, fibrillar network deformation, fibril alignment, and cell contact guidance. *Journal of Biomechanical Engineering* **119**(2): 137-145, 1997.

19. Guidry C, Grinnell F. Studies on the mechanism of hydrated collagen gel reorganization by human skin fibroblasts. *Journal of Cell Science* **79**: 67-81, 1985.

20. Tranquillo RT, Durrani MA, Moon AG. Tissue engineering science: consequences of cell traction force. *Cytotechnology* **10**(3): 225-250, 1992.

21. Young PK, Grinnell F. Metalloproteinase activation cascade after burn injury: a longitudinal analysis of the human wound environment. *Journal of Investigative Dermatology* **103**(5): 660-664, 1994.

22. Grinnell F. Fibroblast-collagen-matrix contraction: growth-factor signaling and mechanical loading. *Trends in Cell Biology* **10**(9): 362-365, 2000.

23. Seliktar D, Black RA, Vito RP, Nerem RM. Dynamic mechanical conditioning of collagen-gel blood vessel constructs induces remodeling in vitro. *Annals of Biomedical Engineering* **28**(4): 351-362, 2000.

24. Schuind F, Ventura M, Pasteels JL. Idiopathic carpal tunnel syndrome: histologic study of flexor tendon synovium. *Journal of Hand Surgery - American* **15**: 497-503, 1990.

25. Masear VR, Hayes JM, Hyde AG. An industrial cause of carpal tunnel syndrome. *Journal of Hand Surgery - American* **11**: 222-227, 1986.

26. Hannafin JA, Arnoczky SP, Hoonjan A, Torzilli PA. Effect of stress deprivation and cyclic tensile loading on the material and morphologic properties of canine flexor digitorum profundus tendon: an in vitro study. *Journal of Orthopaedic Research* **13**: 907-914, 1995.

27. Evanko SP, Vogel KG. Proteoglycan synthesis in fetal tendon is differentially regulated by cyclic compression in vitro. *Archives of Biochemistry and Biophysics* **307**: 153-164, 1993.

28. Abrahamsson SO, Lundborg G, Lohmander LS. Segmental variation in microstructure, matrix synthesis and cell proliferation in rabbit flexor tendon. *Scandinavian Journal of Plastic & Reconstructive Surgery & Hand Surgery* **23**: 191-198, 1989.

29. Calabro A, Benavides M, Tammi M, Hascall VC, Midura RJ. Microanalysis of enzyme digests of hyaluronan and chondroitin/dermatan sulfate by fluorophore-assisted carbohydrate electrophoreses (FACE). *Glycobiology* **10**(3): 273-281, 2000.

30. Calabro A, Hascall VC, Midura RJ. Adaptation of FACE methodology for microanalysis of total hyaluronan and chondroitin sulfate composition from cartilage. *Glycobiology* **10**(3): 283-293, 2000.

31. Levene H. *Contribution to Probability and Statistics.* Stanford University Press, Palo Alto, CA: 278-292, 1960.

32. Turner CH, Owan I, Takano Y. Mechanotransduction in bone: role of strain rate. *American Journal of Physiology* **269**: E438-E442, 1995.

33. Korvick DL, Cummings JF, Grood ES, Holden JP, Feder SM, Butler DL. The use of an implantable force transducer to measure patellar tendon forces in goats. *Journal of Biomechanics* **29**: 557-561, 1996.

34. Malaviya P, Butler DL, Korvick DL, Proch FS. In vivo tendon forces correlate with activity level and remain bounded: evidence in a rabbit flexor tendon model. *Journal of Biomechanics* **31**: 1043-1049, 1998.

35. Androjna C, Spencer E, Orban JM, Caplan AI, Iannotti JP, Derwin KA. Evaluation of porcine small intestinal submucosa (SIS) for the repair and regeneration of flexor tendon. Submitted to 4th SIS-ECM Symposium, 2002.

36. Gelberman RH, Chu CR, Williams CS, Seiler JG III, Amiel D. Angiogenesis in healing autogenous flexor-tendon grafts. *Journal of Bone and Joint Surgery - American* **74**(8): 1207-1216, 1992.

37. Monnier VM, Vishwanath V, Frank KE, Elmets CA, Dauchot P, Kohn RR. Relation between complications of type I diabetes mellitus and collagen-linked fluorescence. *New England Journal of Medicine* **314**(7): 403-408, Feb. 13, 1986.

38. Pierard GE, Nikkels-Toussoudji N, Pierard-Franchimont C. Influence of the test area on the mechanical properties of skin. *Dermatology* **19**: 9-15, 1995.

39. Reihsner R, Menzel EJ. Two-dimensional stress-relaxation behavior of human skin as influenced by non-enzymatic glycation and the inhibitory agent aminoguanidine. *Journal of Biomechanics* **31**(11): 985-993, 1998.

40. Stokes IAF, Faris IB, Hutton WC. The neuropathic ulcer and loads on the foot in diabetic patients. *ACTA Orthopaedica Scandinivica* **46**: 839-847, 1975.

41. Ctercteko GC, Dhanendran M, Hutton WC, Le Quesne LP. Vertical forces acting on the feet of diabetic patients with neuropathic ulceration. *British Journal of Surgery* **68**: 608-614, 1981.

42. Sims DS, Cavanagh PR, Ulbrect JS. Risk factors in the diabetic foot: recognition and management. *Physical Therapy* **68**(12): 1887-1902, 1988.

43. Pollard JP, Le Quesne, Tappin JW. Forces under the foot. *Journal of Biomedical Engineering* **5**: 37-40, 1983.

44. Landsman AS, Meaney DF, Cargill RS 2nd, Macarak EJ, Thibault LE. 1995 William J. Stickel Gold Award. High strain rate tissue deformation. A theory on the mechanical etiology of diabetic foot ulcerations. *Journal of the American Podiatric Medical Association* **85**(10): 519-527, Oct. 1995.

45. Delbridge L, Ctercteko GC, Fowler C, Reeve TS, Le Quesne LP. The aetiology of diabetic neuropathic ulceration of the foot. *British Journal of Surgery* **72**: 1-6, 1985.

46. Thompson DL, Davis BL, Cao D. Effects of diabetic-induced soft tissue changes on stress distribution in the calcaneal soft tissue. 1999 International Society of Biomechanics, Calgery, Alberta, Canada.

47. Fung YC. Elasticity of soft tissues in simple elongation. *American Journal of Physiology* **13**(6): 1532-1544, Dec. 1967.

48. Kunnel JG, Stern PH, Gilbert JL. Role of hysteresis energy in bone response to cyclic loading. 80th IADR/AADR/CADR Conference.

49. Laurent TC, Laurent UBG, Fraser JRE. The structure and function of hyaluronan: an overview. *Immunology & Cell Biology* **74**(2): A1-7, 1996.

50. Laurent TC, Laurent UBG, Fraser JRE. Functions of hyaluronan. *Annals of Rheumatic Diseases* **53**: 429-432, 1995.

51. Toole BP, Hay ED, (eds.). Cell biology of the extracellular matrix, 2nd ed. Plenum Press, New York: 305-341, 1991.

52. Noonan KJ, Stevens JW, Tammi R, Tammi M, Hernandez JA, Midura RJ. Spatial distribution of CD44 and HA in the proximal tibia of the growing rat. *Journal of Orthopaedic Research* **14**: 573-581, 1996.

53. Genever PG, Dickson IR. Influence of vitamin D status on HA localization in Bone. *Bone* **18**: 429-435, 1996.

54. Yamazaki M, Nakajima F, Ogasawara A, Moriya H, Majeska RJ, Einhorn TA. Spatial and temporal distribution of CD44 and osteopontin in fracture callus. *Journal of Bone and Joint Surgery* **81-B**: 508-515, 1999.

55. Luben RA, Wong GL, Cohn DV. Biochemical characterization with parathormone: effects on isolated bone cells: provisional identification of osteoclasts and osteoblasts. *Endocrinology* **99**: 526-534, 1976.

56. Wong GL, Luben RA, Cohn DV. 1,25-Dihydroxycholecalciferol and parathormone: effects on isolated osteoclast-like and osteoblast-like cells. *Science* **197**: 663-665, 1977.

57. Whitfield JF, Morley P, Willick GE. The bone-building action of the parathyroid hormone: implications for the treatment of osteoporosis. *Drugs & Aging* **15**: 117-129, 1999.

58. Weigel PH, Hascall VC, Tammi M. HA synthases. *Journal of Biological Chemistry* **272**(22): 13997-14000, 1997.

59. Lesley J, He Q, Miyake K, Hamann A, Hyman R, Kincade P. Requirements for hyaluronic acid binding by CD44: a role for the cytoplasmic domain and activation by antibody. *J Exp Med* **175**: 257-266, 1992.

60. Lesley J, Hascall VC, Tammi M, Hyman R. Hyaluronan binding by cell surface CD44. *J Biol Chem* **275**: 26967-26975, 2000.

61. Perusek, GP. Design and test of an extensometer for global measurement of bone strain suitable for use *in vivo* in humans. *Case Western Reserve University Thesis*, May 2000. (Included in Appendix of 2000 Annual Report).

APPENDICIES

The Mechanical Properties of Tendons Cultured Under No Load in Variable Serum Concentrations (Abstract) 121

Homotypic Variation of Canine Flexor Tendons (Abstract) 122

Evaluation of Porcine Small Intestine Submucosa (SIS) for the Repair and Regeneration of Flexor Tendon (Abstract) 123

Hyaluronan Enters Keratinocytes by a Novel Endocytic Route for Catabolism (Manuscript) 125

Smooth Muscle Cell Adhesion on Crosslinked Hyaluronan Gels (Manuscript) 137

In Vitro Synthesis of elastin Sheets on Crosslinked Hyaluronan Gels for Tissue Engineering of Aortic Valves (Abstract) 147

Developing a Composite, Tissue Engineered Aortic Valve (Abstract) 149

Elastin-Hyaluronan Composite Materials for Tissue Engineering of the Aortic Valve (Abstract) 150

Towards Tissue Engineering of a Composite Aortic Valve (Abstract) 151

Surface modification of Hyaluronan Gels to Enhance Cell Adhesion (Abstract) 157

Evaluation of UV-Treated Hyaluronan Gels as Biomaterials for Cardiovascular Tissue Engineering (Abstract) 158

Ultraviolet Irradiation Enhances the Performance of Hylan Gels as Scaffolds for Cardiovascular Tissue Engineering (Abstract) 159

Towards a Composite, Tissue-Engineered Aortic Valve (Abstract) 160

Elastin-Hyaluronan Composites for Tissue Engineering of the Aortic Valve (Abstract) 161

In-Vitro Synthesis of Elastin Sheets on Collagen Fiber Bundles (Abstract) 162

Regional Differences In Strength At The Plantar Skin-Fat Interface (Abstract) 163

Effects Of Diabetes On The Strength Of The Plantar Skin-Fat Interface (Abstract) 164

Effects Of Diabetes On The Strength Of The Plantar Skin-Fat Interface (Poster) 165

Evaluation of Hyaluronic Acid Based Matrices for Bone Healing Applications (Report) 166

THE MECHANICAL PROPERTIES OF TENDONS CULTURED UNDER NO LOAD IN VARIABLE SERUM CONCENTRATIONS

*Abreu, EL; *Baker, AR; +*Derwin KA
+*The Departments of Biomedical Engineering and Orthopaedic Surgery and the Orthopaedic Research Center,
The Cleveland Clinic Foundation, Cleveland, OH

Introduction: Although immobilization is required for the treatment of some musculoskeletal injuries, the concurrent stress deprivation has been shown to be detrimental to the functional properties of associated tissues. For example, a dramatic decrease in the mechanical properties of tendon was shown in response to even short-term immobilization [1]. To investigate the mechanisms underlying this significant response to reduced loads, *in vitro* organ culture models have been developed [2]. These models allow tendons to be isolated from their *in vivo* environment such that the effects of mechanical load on intrinsic cells can be directly studied. For example, Hanaffin *et al* demonstrated a large decrease in mechanical properties in canine flexor tendons cultured under no load for several weeks *in vitro* [2]. However, mimicking the tendon's *in vivo* environment remains a challenge. In particular, the influence of the medium conditions on the results of *in vitro* studies has not been carefully evaluated. Therefore, the purpose of this study is to investigate the effect of fetal bovine serum (FBS) concentration (0.5, 1, and 2%) on the mechanical properties of tendons cultured under no load for 4 weeks. These serum concentrations were chosen based on our pilot study showing that 10% FBS over-stimulated the cells in our organ culture model. We hypothesize that the mechanical properties of unloaded tendons will decrease in a dose dependent manner with serum concentration.

Methods: FDS tendons were aseptically harvested from the hind paws of eight mature, male and female, mongrel dogs (24–28 kg). From each hind paw, two explants of 4.5 cm were harvested from the extrasynovial portion of the FDS tendon that extends to the 3rd and 4th digits (four per dog, n=32). The dogs were part of an institutionally approved, unrelated study. Three groups of eight tendons were cultured in the absence of mechanical load for four weeks, in medium M199 supplemented with either 0.5, 1 or 2% FBS, at 37°C, in 5% CO_2. The complete medium was changed every 48hrs. At the end of the culture period, explants were frozen at -20°C until tested. Eight tendons were frozen immediately at harvest and served as fresh controls.

At the time of testing, tendon explants were thawed and clamped in custom grips leaving a grip-to-grip gauge length of 20 mm. Gripped tendons were mounted in a custom device, nominally tensioned and rotated 360° while viewed under a stereomicroscope. Cross-sectional area was estimated from optical analysis of images captured during rotation. Optical markers were placed on the surface of the tendons, prior to mounting them in a testing tank containing physiologic saline at 37°C. An optical system, synchronized with the load system (Instron 1321), allowed the markers' position to be monitored throughout the test. Tendons were preconditioned 10X to loads corresponding to 30MPa, and immediately ramped to 30MPa at 10mm/min. Load vs. local displacement curves were readily generated and normalized by initial gauge length and cross-sectional area to produce stress-strain curves. Elastic moduli were estimated from the linear portion of the stress-strain curves. After the elastic test, the tendons were allowed to rest for 40min prior to viscoelastic testing. Tendons were then ramped to 1.45mm (corresponding to stresses $\geq$ 30MPa) at a rate of 100mm/sec and held for 1200sec. A stress relaxation ratio was computed from the ratio of final to "peak" load. To avoid errors associated with overshoot, the "peak" load was defined as the load when the loading ramp first reached 1.45mm. Differences between the elastic moduli and stress relaxation ratios of each group were tested using ANOVA ($p>0.05$).

Essential results: The average elastic moduli and stress relaxation ratios for each group are shown in Table 1. There were no significant differences between any groups in terms of either elastic moduli ($p=0.22$) or stress relaxation ratio ($p=0.63$). In other words, culturing FDS tendons for four weeks under no load resulted in no change in mechanical properties under any of the serum conditions investigated.

Table 1: Elastic and viscoelastic parameters of FDS tendons cultured under no load for 4 weeks

Groups (n=8)	Elastic Moduli ± SD (MPa)	Stress Relaxation Ratio ± SD
Fresh	1183.6 ± 128.5	0.675 ± 0.021
0.5% FBS	1328.9 ± 246.3	0.682 ± 0.058
1% FBS	1149.8 ± 183.1	0.666 ± 0.028
2% FBS	1230.1 ± 114.2	0.648 ± 0.082

We also assessed the magnitude of the gripping artifact by comparing the mechanical parameters computed using local vs. grip-to-grip strains. The elastic moduli would have been on average 34 ± 10% lower if grip-to-grip strains had been used. In the viscoelastic test, a step displacement of 1.45mm corresponded to 7.25% grip-to-grip strain, while the averaged local strain across all groups was actually 3.9 ± 0.8%. These results demonstrate the importance of determining strains using a local measurement technique.

Discussion: In our study there was no decrease in the mechanical properties of tendons cultured under no load for 4 weeks. These results are in contrast to the significant decrease in mechanical properties of tendons deprived of stress for 3-4 weeks *in vivo* [1] and *in vitro* [2]. One explanation for the discrepancy between our results and previous work is that serum concentrations $\leq$ 2% were not sufficient to maintain cell viability for 4 weeks in our model system. A loss of cell viability would reduce the number of cells able to respond to the absence of load and facilitate remodeling. We are currently evaluating the viability of the experimental explants from this study to explore this hypothesis. We are also evaluating the effect of 5% FBS on the mechanical properties and viability of FDS tendon explants cultured under no load for 4 weeks.

A second explanation for the discrepancy between our results and previous studies could be the tendon model chosen. The intrasynovial region of the FDP tendon has been previously used in organ culture [2]. It is avascular and nurtured by diffusion, which makes it an attractive model for *in vitro* culture studies. Further, the FDP has two fibrocartilage regions that facilitate gripping for mechanical testing. However, histological evidence demonstrates features that are characteristic of fibrocartilage throughout the FDP tendon (unpublished observation). Therefore, in our model system we chose FDS tendons because they are purely tendinous along their length. When FDS tendons are explanted, however, their intrinsic micro-vasculature is disrupted. This may limit the nourishment of the tendon cells, resulting in arrested remodeling or even cell death. We are currently investigating the importance of the tendon model by comparing the viability and change in mechanical properties of FDP and FDS tendon explants cultured under no load and similar serum conditions.

References: **[1]** Loitz, et al: *COOR* (244):265-71, 1989. **[2]** Hannafin, et al: *J Orthop Res* 13(6): 907-14, 1995.

Acknowledgements: U.S. Department of Defense, DAMD17-99-1-9475; Emily Bohnlein for her valuable assistance.

HOMOTYPIC VARIATION OF CANINE FLEXOR TENDONS

+*Derwin, KA; *Baker, AR; *Abreu, EA
+*The Cleveland Clinic Foundation, Cleveland, OH

Introduction The design of experimental studies in animal models has operated under the assumption that the variation in tissue properties within an animal is less than the variation between animals. For example, the contralateral limb is assumed to be the best control for musculoskeletal investigations. Further, this assumption suggests that organ culture studies should utilize a paired, within-animal control for every experimental sample. However, such experimental designs have distinct limitations. Particularly, contralateral limbs are not "normal" because of compensation for the treated limb [1]. And a paired design may be impractical (greatly increasing the number of samples for analysis), if not unattainable, in organ culture studies.

The apparent necessity of choosing a within-animal control is based on the above stated assumption that the variation in tissue properties is smaller within- than between- animals. However, to our knowledge this assumption has not been rigorously evaluated across multiple biologic and mechanical parameters. Therefore, the objective of this work is to investigate the within- and between- animal variability of mature, canine, flexor digitorum superficialis (FDS) tendons. We hypothesize that tendon "material" properties do not vary more between- than within-dogs, where "material" properties are those that are normalized by tendon mass or geometry. A random source, mongrel dog model should provide a "worst case" assessment of between-animal variability. A flexor tendon model will allow the contribution of both right-left (leg) and medial-lateral (tendons within the same paw) variance to the total within-animal variance to be evaluated.

Methods FDS tendons were retrieved at sacrifice from 24, adult (24-30 kg), male, random source, mongrel dogs. The FDS tendon branches associated with the 3rd and 4th digits in both hind paws were utilized (4 per dog, n=96). Within each paw, we refer to these as the medial (3rd digit) and lateral (4th digit) tendons. The dogs were part of an institutionally approved, unrelated study our institution. Tendons were frozen until analysis (–20°C).

Forty-eight tendons were analyzed for biochemical variability with respect to water, collagen and chondroitin/dermatan sulfate glycosaminoglycan content (CSDS GAG). A 7-8 mm segment from each was weighed before and after drying at 60°C for 72hrs. Water content was determined by calculating the percent decrease in mass. Dried samples were rehydrated in 100mM ammonium acetate, pH 7.0, for 48hrs at 4°C and then digested with proteinase K at 60°C for 24hrs. An aliquot of the supernatant was used for collagen and the remainder for GAG analysis. Aliquots for collagen analysis were lyophilized to dry and hydrolyzed in 6N HCl at 110°C for 16hrs. Hydrolyzed samples were dried under nitrogen and resuspended in water. Hydroxyproline content was determined using a spectrophotometric technique [2]. Collagen content was estimated assuming hydroxyproline is derived solely from collagen, and that it represents 13% of collagen by weight [3].

Aliquots for GAG analysis were analyzed with fluorophore-assisted carbohydrate electrophoresis (FACE) [4]. Samples were precipitated in 77% ethanol at -20°C for 18hrs, and centrifuged to pellet macromolecular material. The pellets were resuspended in 100mM ammonium acetate, pH 7.0, and digested for 3hr at 37°C with 100mU/ml chondroitinase ABC (Seikagaku). Samples were lyophilized until dry. Finally, samples were fluorotagged by addition of 40μl of 12.5 mM 2-aminoacridone (AMAC) (500 nmoles) in 85% DMSO/15% acetic acid and 40μl of 1.25M sodium cyanoborohydride (50,000 nmoles) in ultrapure water, followed by incubation for 16hrs at 37°C. After fluorotagging, samples were mixed with glycerol (20μl) then mixed 1:1 with an AMAC-derivatized trisaccharide standard (maltotriose). Samples were electrophoresed on a Glyco monosaccharide gel using Glyco buffer (80min, 500 V). Gels were imaged under UV light (365nm), and peak areas for the various saccharide derivatives present were quantitated (ΔDi0S, ΔDi4S, ΔDi6S). The total CSDS GAG content was computed as ΔDi0S+ΔDi4S+ΔDi6S per mg dry wt.

Forty-eight tendons were analyzed for geometric and biomechanical variability with respect to cross-sectional area, stiffness and elastic modulus. Tendons were clamped in custom grips and cleaned of superficial sheath material. Tendons were then mounted in a custom device, nominally tensioned and rotated 360° while viewed under a stereomicroscope. Cross-sectional area was estimated from optical analysis of images captured during rotation. Gripped tendons were then mounted in a testing tank containing physiologic saline at 37°C. Optical (surface) markers were placed on the tendons and tracked with a video system during the test. The optical system was synchronized with an Instron 5543 load system, such that load vs. local displacement curves were readily generated. Tendons were preconditioned 10x to loads representing 15MPa, then tested at 10mm/min to failure. Load and optical (local) displacement data were either plotted directly or normalized by cross-sectional area and initial gauge length to generate load-displacement or stress-strain curves. Stiffness was estimated from the linear portion of the load-displacement curve. Elastic modulus was estimated similarly from the stress-strain curve.

Within- and between-dog variance in parameters was compared using the modified (median) Levene's test (5). Within-dog variance includes both right-left (leg) and medial-lateral (tendon) variability.

Essential results The results are shown in Table 1. The variance of parameters normalized by tissue mass (i.e., water, collagen, GAG contents) or tissue geometry (i.e., modulus) was not statistically larger between-dogs than within-dogs. However, the variance of the non-normalized parameters (i.e., cross-sectional area and stiffness) was significantly greater between- than within-dogs. In all cases, the within-dog variance was mostly from right-left leg comparisons.

Table 1: Variability of canine FDS tendons (n = 48, each parameter)

Parameter	Mean±SD	Within-dog variance[1]	Between-dog variance[2]	P-value[3]
Water (%)	68.4±1.7	1.04	1.30	0.19
Collagen (%)	80.9±6.6	4.5	5.2	0.41
CSDS GAG ($\mu g/mg_{dw}$)	0.84±0.24	0.14	0.18	0.15
XS area (mm^2)	3.38±0.68	0.31	0.55	0.005
Stiffness (N/mm)	885±167	88.2	132.0	0.03
Modulus (MPa)	1319±256	154.9	200.9	0.16

[1] Avg. absolute deviation from median of dog. [2] Avg. absolute deviation from overall median. [3] Levene's test for variances around median

Discussion These results demonstrate the variability of mature, flexor tendon from random source mongrel dogs. The variance in cross-sectional area and stiffness of tendons was significantly greater between dog than within the same animal. However, when biochemical or mechanical properties were normalized by tissue mass or geometry, the between-dog variance is not larger than within-dog. The results demonstrate that canine flexor tendons can vary appreciably in terms of mass or size between dogs, resulting in functional differences in tendon stiffness. However, the normalized, "material" properties of canine flexor tendon are as similar between- as within-dog.

We note that the within-dog variance includes both right-left (leg) and medial-lateral (tendon) variability, and that the within-dog variance was mostly from right-left leg comparisons. This result suggests that a paired, within-leg or within-tendon experimental design would give optimal statistical power since variability between dogs and between legs within-dog would be removed. However, because this type of design may be impractical or unattainable for some investigations, these data also suggest that it is appropriate to utilize tissue from another group of animals as controls as long as one evaluates "material" properties, i.e., parameters normalized by tissue mass or geometry.

References **[1]** Frank et al: *J Bone Joint Surg Am* 76(3):403-12, 1994. **[2]** Stegeman and Stalder: *Cin Chim Acta* 18:267-273, 1967. **[3]** Cetta et al: *Biochem J* 204:61-67, 1982. **[4]** Calabro et al: *Glycobiology* 10:273-281, 2000. **[5]** Levene H: *Contribution to Probability and Statistics*, pp 278-292. Palo Alto, CA, Stanford University Press, 1960.

Acknowledgements We thank Ed Mascha, M.S. from the Dept. of Biostatistics at The Cleveland Clinic for assistance with data analysis.

EVALUATION OF PORCINE SMALL INTESTINE SUBMUCOSA (SIS) FOR THE REPAIR AND REGENERATION OF FLEXOR TENDON

Androjna C[1], Spencer E[1], Orban JM[2], Caplan AI[1], Iannotti JP[1], Derwin KA[1]

[1]Departments of Biomedical Engineering and Orthopaedic Surgery and the Orthopaedic Research Center,
The Cleveland Clinic Foundation, Cleveland, OH
[2]Depuy Orthopaedics, Warsaw, IN

INTRODUCTORY REMARKS: Tendon injuries and conditions such as tendonitis, tendinosis, tendon tears and complete tendon ruptures pose a significant health problem. Tendon injuries requiring repair are treated by grafting, when a primary repair is not indicated. Current sources of grafts include autograft, allograft, xenograft or synthetic prosthesis. While these approaches have worked reasonably well in the clinical setting, there are limitations and disadvantages of each. Some of these limitations may include donor site morbidity, significant loss of function due to scarring, disease transmission, or immunologic rejection. In almost all cases, the graft remodels into a tissue that is inferior to the native tendon. In recent years there has been a trend in research to engineer a tendon replacement that will provide appropriate long-term biological and mechanical function. Since tendons possess some intrinsic healing properties, an engineered graft should provide a temporary scaffold that will promote healing as well as regeneration of new tendon tissue. An attractive solution from the standpoint of tissue engineering is the use of biological scaffolds. These scaffolds can provide temporary functional support, inherent biological properties that influence cell behavior and tissue development, and are biocompatible, bioresorbable and immunologically safe. One such scaffold material that has shown promise in musculoskeletal applications is porcine-derived small intestinal submucosa (SIS).

The purpose of the present study is to evaluate the feasibility of SIS as a biological scaffold for use in flexor tendon repair/regeneration.

MATERIALS AND METHODS: Sterilized porcine-derived SIS grafts were used for flexor digitorum profundus (FDP) tendon replacement in a canine model. The SIS grafts consisted of a 25-layer, vacuum-dried inner core that was subsequently wrapped with a piece of hydrated SIS and lyophilized (fabricated by DePuy Orthopaedics, Inc.). The graft dimensions were approximately 2.5mm wide by 1mm thick. A 7-8cm length of graft was used to replace the native FDP tendon in the intrasynovial region of the second and fifth digits of the left forepaw. The graft was sutured proximally to the native FDP tendon and distally to the base of the distal phalanx. After surgery, the forelimb was immobilized in a shoulder spica cast (1). The volar aspect of the cast at the paw was removable for rehabilitation purposes. Postoperative rehabilitation consisted of passive flexion of the wrist and digits at a rate of 0.5 Hz, twice daily for 5min intervals, 6days/week, starting on the first postoperative day. The animals were sacrificed three weeks postoperatively and the grafts were assessed by gross observation for adhesions/scarring, functionality, and healing. The grafted digits were then excised *en bloc* for histological evaluation (hematoxylin and eosin stained).

RESULTS: To date we have completed two animals in our study (n=4 grafts at 3 weeks). Gross observation showed minimal to extensive scarring of the graft to adjacent tendons and tissues at the proximal repair site in all four digits. After removal of the scar tissue, however, the FDP/SIS could be readily differentiated from the adjacent flexor digitorum superficialis (FDS) tendon. To evaluate functionality, the FDP/SIS and FDS were independently pulled to determine the degree of distal interphalangeal (DIP) joint motion contributed by each. In three digits the distal phalanx moved similarly whether pulling on the FDP/SIS or the FDS tendon. This suggests some scarring/adhesions between the tendons in these digits. Histologically, a mononuclear cell infiltrate was observed throughout the length and width of all grafts. All grafts appeared to be well vascularized along their lengths. In some regions, the SIS appeared integrated with the adjacent FDS tendon, in others the SIS appeared to be distinct from the FDS. In all digits the proximal repair demonstrated direct apposition and integration between the native tendon and SIS. At the distal repair, the SIS appeared to be integrated with the surrounding tissue and the bony phalanx.

DISCUSSION: Our initial results on the use of SIS as biological scaffold for flexor tendon repair are encouraging. We chose SIS for this application based on its well-documented ability to promote site-specific matrix deposition and tissue regeneration (e.g. 2-5). In this study, the graft was well infiltrated by cells, vascularized throughout its length and well integrated at the proximal and distal repair sites by three weeks. The SIS grafts were sufficiently strong to withstand isometric muscle loads and loads introduced during passive motion rehabilitation. In our ongoing studies, we will evaluate the SIS graft at six weeks post-operatively for resorption of the SIS and neo-tendinous matrix deposition and organization. An intrasynovial autograft and contralateral FDP tendon will be used as controls.

PRESENTED BY:

Kathleen A. Derwin, PhD
Department of Biomedical Engineering – ND20
Cleveland Clinic Foundation
9500 Euclid Avenue
Cleveland, OH 44195

Phone: (216) 445-5982
Fax: (216) 445-4383
Email: derwink@bme.ri.ccf.org

REFERENCES:

1. Gelberman RH, Chu CR, Williams CS, Seiler JG, III, Amiel D. Angiogenesis in healing autogenous flexor-tendon grafts. J Bone Joint Surg Am 1992; 74(8):1207-1216.
2. Kropp BP, Eppley BL, Prevel CD, Rippy MK, Harruff RC, Badylak SF et al. Experimental assessment of small intestinal submucosa as a bladder wall substitute. Urology 1995; 46(3):396-400.
3. Badylak SF, Tullius R, Kokini K, Shelbourne KD, Klootwyk T, Voytik SL et al. The use of xenogeneic small intestinal submucosa as a biomaterial for Achilles tendon repair in a dog model. J Biomed Mater Res 1995; 29(8):977-985.
4. Badylak SF, Lantz GC, Coffey A, Geddes LA. Small intestinal submucosa as a large diameter vascular graft in the dog. J Surg Res 1989; 47(1):74-80.
5. Dejardin LM, Arnoczky SP, Ewers BJ, Haut RC, Clarke RB. Tissue-engineered rotator cuff tendon using porcine small intestine submucosa. Histologic and mechanical evaluation in dogs. Am J Sports Med 2001; 29(2):175-184.

This project is funded by Depuy Orthopaedics, Inc.

THE JOURNAL OF BIOLOGICAL CHEMISTRY
© 2001 by The American Society for Biochemistry and Molecular Biology, Inc.

Vol. 276, No. 37, Issue of September 14, pp. 35111–35122, 2001
Printed in U.S.A.

Hyaluronan Enters Keratinocytes by a Novel Endocytic Route for Catabolism*

Received for publication, April 19, 2001, and in revised form, July 10, 2001
Published, JBC Papers in Press, July 12, 2001, DOI 10.1074/jbc.M103481200

Raija Tammi[‡§‖], Kirsi Rilla[‡], Juha-Pekka Pienimäki[‡], Donald K. MacCallum[¶], Michael Hogg[‖], Merja Luukkonen[‡], Vincent C. Hascall[‖], and Markku Tammi[‡‖]

From the ‡Department of Anatomy, University of Kuopio, P. O. Box 1627, FIN-70211 Kuopio, Finland, the ‖Department of Biomedical Engineering/ND20, Lerner Research Institute, The Cleveland Clinic Foundation, Cleveland, Ohio 44195, and the ¶Department of Anatomy and Cell Biology, University of Michigan, Ann Arbor, Michigan 48109

Hyaluronan synthesized in the epidermis has an exceptionally short half-life, indicative of its catabolism by epidermal keratinocytes. An intracellular pool of endogenously synthesized hyaluronan, from 1 to 20 fg/cell, inversely related to cell density, was observed in cultured rat epidermal keratinocytes. More than 80% of the intracellular hyaluronan was small (<90 kDa). Approximately 25% of newly synthesized hyaluronan was endocytosed by the keratinocytes and had a half-life of 2–3 h. A biotinylated aggrecan G_1 domain/link protein probe demonstrated hyaluronan in small vesicles of ~100 nm diameter close to the plasma membrane, and in large vesicles and multivesicular bodies up to 1300 nm diameter around the nucleus. Hyaluronan did not co-localize with markers of lysosomes. However, inhibition of lysosomal acidification with NH_4Cl or chloroquine, or treating the cells with the hyaluronidase inhibitor apigenin increased intracellular hyaluronan staining, suggesting that it resided in prelysosomal endosomes. Competitive displacement of hyaluronan from surface receptors using hyaluronan decasaccharides, resulted in a rapid disappearance of this endosomal hyaluronan ($t_{1/2}$ ~5 min), indicating its transitory nature. The ultrastructure of the hyaluronan-containing vesicles, co-localization with marker proteins for different vesicle types, and application of specific uptake inhibitors demonstrated that the formation of hyaluronan-containing vesicles did not involve clathrin-coated pits or caveolae. Treatment of rat epidermal keratinocytes with the OX50 monoclonal antibody against the hyaluronan receptor CD44 increased endosomal hyaluronan. However, no CD44-hyaluronan co-localization was observed intracellularly unless endosomal trafficking was retarded by monensin, or cultivation at 20 °C, suggesting CD44 recycling. Rat epidermal keratinocytes thus internalize a large proportion of their newly synthesized hyaluronan into non-clathrin-coated endosomes in a receptor mediated way, and rapidly transport it to slower degradation in the endosomal/lysosomal system.

Hyaluronan is produced by the hyaluronan synthase family of enzymes (1), which directly extrude the growing glycosaminoglycan chain through the plasma membrane into the extracellular matrix or onto the cell surface. Most of the hyaluronan synthesized in tissues eventually diffuses into lymph, and is subsequently catabolized by lymph nodes (2), or the liver (3, 4). However, partial degradation of radiolabeled hyaluronan injected into joints (5) and skin (6) occurs, indicating that there are also local catabolic systems. Furthermore, cultured chondrocytes (7, 8), fibroblasts, smooth muscle cells (9), macrophages (10–12), and some breast cancer cell lines (13) internalize and degrade labeled exogenous hyaluronan.

A protein (HARE) associated with the endocytosis of hyaluronan in liver endothelial cells and lymph nodes has been recently cloned (14), and another (LYVE) may be involved in hyaluronan uptake by lymph vessel endothelium (15). In peripheral tissues, the ubiquitous plasma membrane protein CD44 is known to bind hyaluronan, and is also thought to contribute to hyaluronan internalization (8, 12, 16). Details of the molecular mechanisms of endocytosis by any of the hyaluronan receptors are largely unknown. However, it is likely that specific uptake processes are required for this macromolecule, that can exceed a molecular mass of 6 × 10^6 Da and have a 300-nm radius of gyration in solution (17), a size clearly beyond the ~100 nm diameter of a regular primary endosome.

Human epidermal keratinocytes actively synthesize hyaluronan (18), and pulse-chase experiments in skin organ cultures demonstrate a short half-life (~1 day) for epidermal hyaluronan (19, 20). Similar metabolic labeling experiments in rat epidermal keratinocytes (REKs)[1] in organotypic cultures also indicate rapid hyaluronan catabolism (21). Partial degradation of epidermal hyaluronan in organ cultures is also indicated by the decrease in the molecular mass of newly synthesized hyaluronan molecules from >4 × 10^6 Da to 1 × 10^6 and 0.5 × 10^6 Da after 24- and 48-h chases, respectively (20). Keratinocytes express a high level of CD44 (22), a receptor thought to be responsible for hyaluronan uptake in other cells (7, 13). Accordingly, mice with blocked epidermal CD44 expression accumulate hyaluronan in skin (16), suggesting impaired hyaluronan uptake by keratinocytes.

We found earlier that REKs contain a pool of hyaluronan resistant to trypsin and *Streptomyces* hyaluronidase treatments (23), suggesting an intracellular location. The present

---

* This work was supported by the Academy of Finland, Cleveland Clinic Foundation, Biotechnology Funds from the University of Kuopio, EVO Funds from Kuopio University Hospital, and The Finnish Cancer Foundation. The costs of publication of this article were defrayed in part by the payment of page charges. This article must therefore be hereby marked "*advertisement*" in accordance with 18 U.S.C. Section 1734 solely to indicate this fact.

§ To whom correspondence should be addressed: Dept. of Anatomy, University of Kuopio, P. O. Box 1627, FIN-70211 Kuopio, Finland. Tel.: 358-17-163009; Fax: 358-17-163032; E-mail: raija.tammi@uku.fi.

[1] The abbreviations used are: REK, rat epidermal keratinocyte; HBSS, Hank's balanced salt solution; bHABC, biotinylated hyaluronan binding complex; TRU, turbidity reducing unit(s); PB, phosphate buffer; DAB, 3,3-diaminobenzidine; FL-HA, fluorescein-labeled hyaluronan; mAb, monoclonal antibody; DAMP, [*N*-(3-(2,4-dinitrophenyl)amino)propyl]-*N*-(3-aminopropyl)methylamine dihydrochloride; FM 1-43, *N*-(3-triethylammoniumpropyl)-4-(4-(dibutylamino)styryl)pyridinium dibromide; AMAC, 2-aminoacridone; FITC, fluorescein isothiocyanate; CHAPS, 3-[(3-cholamidopropyl) dimethylammonio]-1-propanesulfonic acid.

This paper is available on line at http://www.jbc.org

study characterizes the size, location, turnover, molecular weight, and regulation of this hyaluronan pool in more detail, particularly because it has been recently suggested that intracellular hyaluronan may be involved in cell signaling, mitosis, and cell cycle regulation (24, 25). Our experiments show that even in open monolayer cultures, where hyaluronan can easily escape into the culture medium, REKs actively internalize and rapidly metabolize newly synthesized hyaluronan in a receptor-mediated fashion through an endocytic route which is not dependent on coated pits or caveolae, but which involves CD44.

EXPERIMENTAL PROCEDURES

Cell Culture—The REK cell line was developed by MacCallum and Lillie (26) from neonatal rat epidermal cells originally isolated by Baden and Kubilus (27). REKs were cultured in Dulbecco's minimal essential medium (low glucose, Life Technologies, Paisley, United Kingdom) with 10% fetal bovine serum (HyClone, Logan, UT), 4 mM L-glutamine, and penicillin and streptomycin (50 milliunits/ml and 50 μg/ml, respectively, Sigma) at 37 °C in a humidified atmosphere containing 5% CO$_2$ in air. Cells were passaged when confluent using 0.05% trypsin (w/v), 0.02% EDTA (w/v) (Biochrom, Berlin, Germany) in phosphate-buffered saline. For biochemical assays and radiolabeling, the cells were seeded at 100,000/ml and grown to near confluency in 6-well plates (Costar Corp., Cambridge, MA). For microscopic studies, the cells were plated at 20,000 cells/well in 8-well chamber slides (Lab-Tek, Nalge Nunc Int. Corp., Naperville, IL) precoated with fetal bovine serum for 30 min at 37 °C.

Manipulation of Hyaluronan Uptake and Degradation—To study the receptor mediated uptake of hyaluronan, we treated recently confluent or nearly confluent REK cultures with hyaluronan oligosaccharides consisting of 4, 6, 10, 12, and 14 monosaccharide units in length (HA4, HA6, HA10, HA12, and HA14, respectively) (23, 28) at final concentrations of 0.2–0.5 mg/ml (23) or with 0.3 mg/ml chondroitin, chondroitin sulfate A (mainly chondroitin 4-sulfate), chondroitin sulfate C (mainly chondroitin 6-sulfate), or heparan sulfate (all from Seikagaku Kogyo Co., Tokyo, Japan). Other cultures were incubated with the anti-CD44 mAbs Ox 50 (BIOSOURCE Int., Camarillo, CA), Hermes 3 (a gift from Dr. Sirpa Jalkanen, Turku), or with non-immune mouse IgG (Sigma).

To block hyaluronan uptake through clathrin-coated pits, we: 1) added 2.5–10.0 μg/ml chlorpromazine (Sigma) for 0.5–4 h in the culture medium, or 2) used serum-free hypertonic medium with 0.4 M sucrose and 0.15% bovine serum albumin for 60 min as described (29). Control cells were kept in the same medium without sucrose.

To block uptake through caveolae, we added: 1) filipin III (Sigma) to final concentrations of 0.4–23 μM for 0.5–6 h, or 2) nystatin (Sigma) (1–10 μM) for 0.5–1 h (30). To block macropinocytosis, we treated cells either with 2–3 mM amiloride (Sigma,) or 0.05–0.5 mM 5-(*N,N*-dimethyl)-amiloride (Sigma) (31, 32).

The function of lysosomes was perturbed by using either 2–10 mM ammonium chloride or 0.5–2.5 mM chloroquine (Sigma), for 0.5–6.0 h (33). Receptor recycling was inhibited by 2–32 μM monensin (Sigma) for 0.5 to 4 h (34).

Isolation of Intracellular Hyaluronan—The REK cultures were radiolabeled with 20 and 100 μCi/ml [^{3}H]glucosamine and [^{35}S]sulfate (Amersham, Little Chalfont, UK), respectively, for different times in 6-well plates (9.6 cm^2/well), and washed with 2 × 250 μl of Hank's balanced salt solution (HBSS, Euroclone, Milano, Italy). The medium and washes were combined and designated as "medium." To remove cell surface-associated hyaluronan, the cells were usually incubated for 10 min at 37 °C with the trypsin-EDTA as above, pelleted, and washed with HBSS. The trypsin solution and combined washes were designated as "trypsinate" and the pellet as "intracellular" fraction.

In some experiments, incubation was done with 0.2% trypsin (Sigma type XI, 6000–9000 BAEE units/mg) and 0.1% EDTA in Ca^{2+},Mg^{2+}-free HBSS at 4 °C for 1 h, the cells were pelleted by low speed centrifugation in the cold, washed with cold HBSS containing 10% fetal bovine serum, and washed 4 times with HBSS. Thereafter, the cells were digested with *Streptomyces* hyaluronidase (15 turbidity reducing units (TRU)/ml in HBSS) for 4–12 h at 4 °C, washed 4 times with cold HBSS, and suspended in 200 μl of HBSS. The cells were boiled for 15 min to inactivate any exogenous or endogenous hyaluronidase. Alternatively, the cultures were directly digested with *Streptomyces* hyaluronidase at 4 °C, washed, and incubated with proteinase K as described below.

After adding carrier hyaluronan (Healon^{TM}, Amersham Pharmacia Biotech, Uppsala, Sweden) (4 μg in 40 μl) to each, the medium, trypsinate, and intracellular samples were digested with 50 μg of proteinase K at 60 °C for 4 h, then heated at 100 °C for 10 min, and centrifuged at 13,000 × *g* for 15 min. Hyaluronan and other glycosaminoglycans in the supernatants were precipitated with 4 volumes of ethanol for 2 h at −20 °C, and collected by centrifugation at 13,000 × *g* for 15 min. Each precipitate was analyzed for specific disaccharides as described below.

To estimate the proportion of intracellular hyaluronan originating from the cell surface and culture medium, cells were radiolabeled as above for 6 h in medium with 1–5 units/ml of *Streptomyces* hyaluronidase. The half-life of intracellular hyaluronan was determined by overnight labeling of the cultures as described above, then washing the cultures with unlabeled medium and analyzing intracellular hyaluronan after 1–6 h chase in the presence of 1 TRU/ml *Streptomyces* hyaluronidase.

Assay of Hyaluronan Disaccharides—Samples were dialyzed in minidialysis units (Slide-A-Lyzer, molecular mass cut-off 3500, Pierce, Rockford, IL) against distilled water containing 20% ethanol, and then evaporated to dryness under vacuum centrifugation. Each sample was then dissolved in 40 μl of 0.5 M sodium acetate, pH 6.2, and digested for 3 h at 37 °C with 1 milliunit of *Streptococcus* hyaluronidase, followed by 2 h incubation with 25 milliunits of chondroitinase ABC (both enzymes from Seikagaku). Aliquots of 10–45 μl were injected onto a 1 × 30-cm Superdex Peptide column eluted at 0.5 ml/min with 0.012 M NH$_4$HCO$_3$. The eluent was monitored at 232 nm, and for ^{3}H and ^{35}S activities to quantitate chondroitin sulfate and hyaluronan disaccharides, as described in detail before (21, 23, 35).

Hyaluronan Size Assays—The samples were chromatographed on 1 × 30-cm columns of Sephacryl S-400 and S-1000 (Amersham Pharmacia Biotech), eluted at 24 ml/h with 0.15 M sodium acetate, 0.1% CHAPS, pH 6.8. Fractions of 0.5 ml were collected. Healon^{TM} (4 μg) was added as a carrier in each fraction containing radioactivity, followed by precipitation with 4 volumes of ethanol for 2 h at −20 °C and pelleting by centrifugation at 13,000 × *g* for 15 min. The precipitates of two consecutive fractions were redissolved in 20 μl of 0.5 M sodium acetate, pH 6.2, pooled, and incubated with 1 milliunit of *Streptococcus* hyaluronidase (Seikagaku) for 3 h at 37 °C. 200 μl of ethanol was added, and the precipitate centrifuged as above. The supernatants were dried in a centrifugal evaporator, dissolved in 40 μl of 0.012 M NH$_4$HCO$_3$ and analyzed for hyaluronan disaccharides as described above.

Hyaluronan Oligosaccharide Analysis—Medium and intracellular samples were digested with proteinase K (250 μg/ml) at 60 °C for 4 h, boiled for 10 min, and evaporated until the volume of the sample was about 100 μl. The specimens were run on a Superdex Peptide column (Amersham Pharmacia Biotech), eluted at 0.5 ml/min with 0.012 M NH$_4$HCO$_3$, and 100-μl aliquots from 250-μl fractions were counted for radioactivity. The included fractions were combined in three pools (fractions 27–29, 30–32, and 33–35), and 4 μg of Healon was added as a carrier. Each pool was then evaporated to dryness, redissolved in 20 μl of 0.5 M sodium acetate, pH 6.2, digested with *Streptococcus* hyaluronidase, and analyzed for hyaluronan disaccharides as described above.

Fluorescent Hyaluronan—Fluorescein-labeled hyaluronan preparations (FL-HA, gifts from Drs. Ronald Midura, Cleveland Clinic Foundation, Cleveland, OH, and Jayne Lesley, Salk Institute, La Jolla, CA) were made as described (36). The molecular mass of the intact FL-HA showed a wide distribution between 200 and 2000 kDa on Sephacryl S-1000 gel filtration and was completely susceptible to *Streptomyces* hyaluronidase digestion, demonstrated by the shift of all UV absorbing and fluorescent material from the excluded volume to positions corresponding to tetra- to tetradecasaccharides on Superdex Peptide gel filtration. Hyaluronan oligosaccharides were labeled at their reducing ends by 2-aminoacridone (37).

Staining for Endogenous Intracellular Hyaluronan—The basic staining protocol was essentially as decribed before (23, 38). The cells were washed once with HBSS and fixed for 20 min in 2% paraformaldehyde in 0.1 M sodium phosphate buffer, pH 7.4 (PB), at room temperature. After fixation, the cells were washed 5 × 2 min with PB, and digested with *Streptomyces* hyaluronidase, 5–10 TRU/ml PB for 10 min at 37 °C. After washes in PB, the cells were permeabilized for 10 min in 1% bovine serum albumin containing 0.1% Triton X-100. Thereafter, a biotinylated complex of hyaluronan-binding region of bovine articular cartilage aggrecan G$_1$ domain and link protein (bHABC) (38), diluted to 3–5 μg/ml in 1% bovine serum albumin, was applied to the cells, and incubated overnight at 4 °C, followed by 1 h in avidin-biotin peroxidase (ABC-standard kit, Vector Laboratories, Inc., Burlingame, CA) at room temperature. The color was developed with 0.05% 3,3′-diaminobenzidine (DAB, Sigma) and 0.03% H$_2$O$_2$. Specimens for photography were counterstained with hematoxylin for 2 min, and embedded in Supermount (Biogenex, San Ramon, CA). Specimens for densitometry were embedded in Supermount without counterstaining. For fluorescence microscopy, the procedure was modified as follows. Either Texas Red streptavidin or FITC-avidin D (Vector, 1:1000 and 1:500 dilutions, respectively, in PB) was used instead of the ABC kit. The cells were coverslipped using Vectashield (Vector) mounting medium.

Microscopy of Uptake Markers—The endocytic compartment was visualized by incubating the cells for 5 min to 4 h with a fluorescent lipid derivative (*N*-(3-triethylammoniumpropyl)-4-(4-(dibutylamino)styryl)-pyridinium dibromide (FM 1-43, Molecular Probes, Eugene, OR; 1 μM), which incorporates into the outer leaflet of the plasma membrane and a part of which is subsequently transported to endocytic vesicles (39). The cells were washed to remove the compound from the plasma membrane, fixed, and stained for endogenous intracellular hyaluronan using Alexa Fluor 633-labeled streptavidin as a reporter (Molecular Probes).

Monoclonal antibodies for transferrin receptor (Chemicon International Inc., Temecula, CA), anti-caveolin 1 (Transduction Laboratories, Lexington, KY), β-COP (Sigma), and anti-CD44 mAb (OX50, BIOSOURCE, Camarillo, CA) were used at a dilution of 1:100, and the mAb against cathepsin D (Transduction Laboratories) was used at a 1:50 dilution. Texas Red-labeled anti-mouse antibody (Vector) at 1:100 dilution was used as the secondary step. In the double staining protocols the primary mAb was added together with the bHABC, and the secondary antibody simultaneously with FITC-avidin.

Acidic compartments in keratinocytes were visualized by feeding the cells with 30 μM DAMP (*N*-(3-(2,4-dinitrophenyl)amino)propyl)-*N*-(3-aminopropyl)methylamine dihydrochloride) (Molecular Probes) for 30 min (40). The cells were then washed with PB, fixed, permeabilized as described above, and allowed to react overnight at 4 °C with a polyclonal antibody (FITC-labeled anti-DAMP, Molecular Probes, dilution 1:100). After incubation, the cells were washed and mounted in Vectashield. For hyaluronan double stainings, the anti-DAMP mAb was added to the bHABC solution; otherwise the staining was done as described above for bHABC.

Fluid phase uptake and coated pit pathways were visualized by incubating REKs in the presence of lysine fixable, Texas Red-labeled dextran (M_r 10,000, Sigma, 10 μg/ml) (41) and Texas Red-labeled human transferrin (Molecular Probes, 4 μg/ml) for 10–120 min (42). The cells were then fixed and processed for microscopy as above. For dual staining of dextran or transferrin, and endogenous hyaluronan, cells were first fed with Texas Red-labeled dextran or transferrin for 10–60 min, and then fixed and stained for hyaluronan as described above.

Confocal Microscopy—Laser scanning confocal microscopy was done using an Ultraview confocal scanner, built on a Nikon TE300 microscope with a 100 × NA 1.3 oil immersion objective, and equipped with an UltraPix CCD camera as a detector (PE-Wallac-LSR, Oxford, UK). Recordings consisted of 5–10 optical sections from the top to the bottom of the cell layer. Images were processed with Scanware image analysis system for Microsoft Windows. Further contrast enhancement was done with Photoshop software (Adobe, Mountain View, CA).

Electron Microscopy—After fixation *in situ* with 2% paraformaldehyde and 0.5% glutaraldehyde for 20 min and blocking with 3% bovine serum albumin in 0.1% Triton X-100 for 10 min, the cells were incubated with bHABC (5 μg/ml) overnight at 4 °C, washed with PB, and visualized with DAB as described above. The cells were postfixed with reduced osmium tetroxide by adding potassium ferrocyanide (2.5 mg/ml final concentration) into aqueous 1% OsO_4 (43). The cells were dehydrated in graded ethanol and embedded in Spurr's resin. Thin sections were mounted on formvar-coated copper grids, stained with uranyl acetate, and viewed using a JEOL 1200 EX microscope.

For dual staining of hyaluronan and CD44, the OX50 anti-CD44 antibody was added to the bHABC solution at a 1:50 final dilution. The anti-mouse secondary antibody, conjugated to 5-nm gold particles (Amersham Pharmacia Biotech, Little Chalfont, UK) and diluted 1:40, was applied together with the streptavidin-peroxidase (1:500, Vector) solution. The peroxidase activity was visualized as described above.

Internalization of Exogenous Hyaluronan—The experiments were done in minimal essential medium supplemented with 1% bovine serum albumin (binding medium). The cells were first washed three times with cold binding medium, then incubated in binding medium containing 10 μg/ml FL-HA at 4 °C for 1–2 h. The cells were washed 3 × 2 min with cold binding medium, and fixed after incubation at 37 °C or at room temperature for 0, 30, 60, 90, or 120 min. Fixation was done in 2% paraformaldehyde for 20 min at room temperature, and the cell layer then washed with PB and mounted in Vectashield.

In preliminary experiments, cells were digested with testicular hyaluronidase in culture prior to the incubation with FL-HA. However, no obvious difference in the binding was observed following hyaluronidase digestion, which was omitted from later experiments.

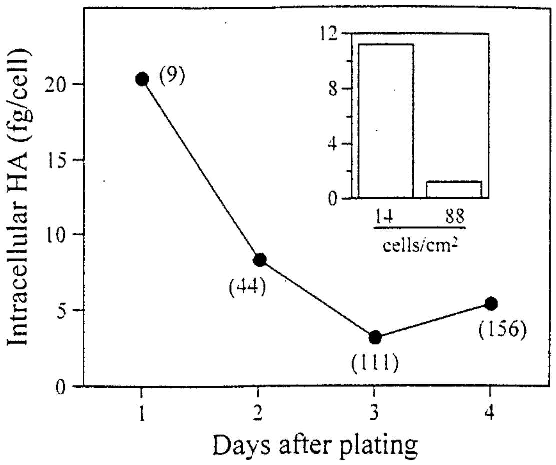

FIG. 1. **The influence of cell density on intracellular hyaluronan content.** REKs were plated at 10,000 cells/cm², metabolically labeled with [^{3}H]glucosamine and [^{35}S]sulfate for 20 h (*bars*) after 0, 1, 2, or 3 days of culture. The intracellular hyaluronan was recovered after removal of the pericellular hyaluronan with trypsin and quantitated as described under "Experimental Procedures." The density of the cultures (cells per cm² × 10^{-3}) at the end of labeling is shown in *parentheses* for each time point. The *inset* shows the data from another experiment where cells were seeded at low and high densities, and labeled 24 h later. The number of cells per cm² (× 10^{-3}) at the end of labeling is given on the *x* axis.

The specificity of the binding was tested in parallel cultures incubated in: 1) FL-HA digested by *Streptomyces* hyaluronidase; 2) FL-HA together with hyaluronan oligosaccharides (HA14, 0.3–1.0 mg/ml); and 3) FL-HA together with 1 mg/ml commercially available chondroitin sulfate or heparan sulfate (Seikagaku).

For quantitative measurements of FL-HA binding, cells were seeded onto 6-well plates at 20,000 cells/cm², grown to near confluency, and incubated with FL-HA with and without the competing substances described above. Each cell layer was washed 2 × 2 min with phosphate-buffered saline and stripped of surface hyaluronan by 0.025% trypsin and 0.02% EDTA for 10 min at 37 °C. The cells were then pelleted and washed with phosphate-buffered saline before lysis in distilled water. The amount of FL-HA was determined using a fluorescence plate reader (SpectraFluor, Tecan, Salzburg, Austria) calibrated with known amounts of FL-HA.

RESULTS

Content of Intracellular Hyaluronan—Our previous biochemical studies demonstrated that REKs contain a pool of hyaluronan which is resistant to trypsin digestion, a treatment that removes virtually all hyaluronan from the cell surfaces, and which comprised about 3% of the total hyaluronan recovered after a 24-h radiolabeling period in confluent cultures (23). The present study shows that the size of this trypsin-resistant hyaluronan pool is larger in low cell density cultures, as demonstrated by analysis of consecutive 24-h synthesis periods on a set of REK cultures, allowed to grow from an initial density of 9 × 10^4 to a final density of 156 × 10^4 cells/cm² during 4 days (Fig. 1). In another experiment, parallel cultures were seeded at different densities and metabolically labeled the next day. This resulted in a 10-fold higher intracellular hyaluronan content in cells seeded at 14 × 10^4 *versus* 88 × 10^4 cells/cm² (Fig. 1, *inset*).

In order to minimize internalization of hyaluronan during enzymatic treatment, we conducted sequential trypsin and *Streptomyces* hyaluronidase digestion at 4 °C. This cold, sequential enzymatic treatment reduced the amount of intracellular hyaluronan to 2–4 fg/cell, 30–50% less than the amount determined when digestions were carried out at 37 °C, reflecting the high rate of hyaluronan uptake. Despite the relatively small quantity of hyaluronan in the REKs, metabolic studies suggest that ~25% of the total hyaluronan synthesized is ulti-

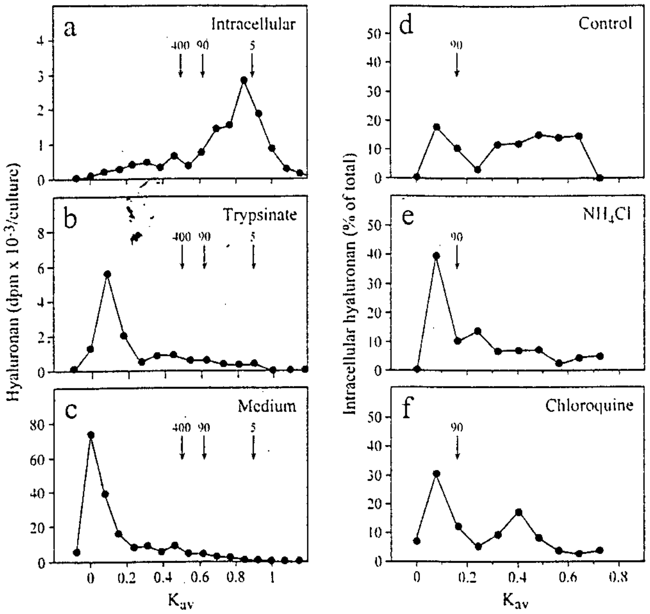

FIG. 2. **Molecular mass distributions of hyaluronan.** *a-c*, hyaluronan was metabolically labeled with [^{3}H]glucosamine, recovered from the medium, pericellular and intracellular compartments, and fractionated with Sephacryl S-1000 gel filtration as described under "Experimental Procedures." *a*, intracellular compartment; *b*, trypsinate; *c*, medium. *d-f*, REK cultures were treated with 5 mM NH_4Cl and 1 mM chloroquine while metabolically labeled with [^{3}H]glucosamine for 6 h. Hyaluronan was recovered from the intracellular compartment at 4 °C as described under "Experimental Procedures" and fractionated with Sephacryl S-400 gel filtration. The *arrows* indicate the elution positions of 400- and 90-kDa hyaluronan determined with the calibration curves supplied by the manufacturer of the chromatographic resin, and the position of hyaluronan oligosaccharides of about 5 kDa, prepared in our laboratory.

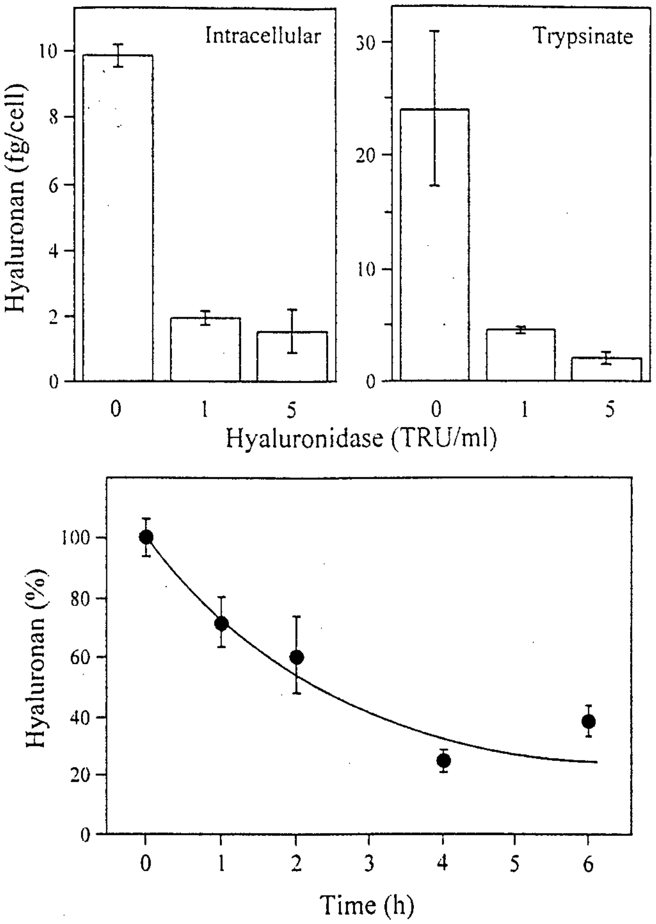

FIG. 3. **Effect of extracellular hyaluronidase treatment on intracellular hyaluronan.** *Upper panels*, nearly confluent cultures were metabolically labeled with [^{3}H]glucosamine and [^{35}S]sulfate for 6 h in the presence of 1 and 5 units/ml *Streptomyces* hyaluronidase in order to demonstrate the cell surface or extracellular source of intracellular hyaluronan. Intracellular and cell surface (trypsinate) hyaluronan were quantitated after separation of the compartments with trypsin at 37 °C as described under "Experimental Procedures." *Lower panel*, nearly confluent cultures were metabolically labeled with [^{3}H]glucosamine and [^{35}S]sulfate for 18 h, washed with unlabeled medium, and chased for 0–6 h in the presence of 1 unit/ml *Streptomyces* hyaluronidase before the assay of intracellular hyaluronan to estimate the half-life of the intracellular hyaluronan. The *bar* shows the range of duplicate cultures.

mately catabolized intracellularly (see "Discussion," Hyaluronan Turnover in Keratinocytes).

Molecular Mass Distribution of Intracellular Hyaluronan—For analysis of the size distribution of the intracellular hyaluronan, pericellular hyaluronan was first removed by treating the 20-h radiolabeled cultures with *Streptomyces* hyaluronidase in the cold, and then solubilizing intracellular hyaluronan with proteinase K as described under "Experimental Procedures." For comparison, pericellular hyaluronan was isolated by regular trypsinization in parallel cultures. Aliquots of each sample were eluted on Sephacryl S-1000. In the fractions collected, hyaluronan was distinguished from other ^{3}H-labeled macromolecules as described under "Experimental Procedures." Most of the intracellular hyaluronan eluted after K_{av} 0.5, indicating a molecular mass below 400 kDa (Fig. 2*a*), with the most abundant hyaluronan eluting at K_{av} 0.67, a molecular mass of ~30 kDa. In contrast, hyaluronan in the medium and that released from the cell surface by trypsin treatment, both eluted close to the excluded volume, indicating a molecular mass greater than 2000 kDa (Fig. 2, *b* and *c*). Although hyaluronan of <400 kDa size formed a minor proportion of the total hyaluronan in the extracellular compartments, the total amount in this size range was somewhat higher than that within the cell (Fig. 2, *b* and *c*). Superdex Peptide column chromatography demonstrated negligible amounts of hyaluronan oligosaccharides less than 5 kDa in any of the cell compartments (data not shown).

Origin and Turnover of Intracellular Hyaluronan—An experiment was designed to show that the intracellular hyaluronan is derived from the cell surface or the culture medium. REK cultures were incubated with a radiolabeled precursor of hyaluronan while *Streptomyces* hyaluronidase was present in the culture medium. At a concentration (5 units/ml) that removed >90% of the cell surface hyaluronan, there was a concomitant 85% decrease of the intracellular hyaluronan (Fig. 3, *top*), indicating that hyaluronan that is present within the cell had its origin at the cell surface and/or from the culture medium, compartments accessible to hyaluronidase. An almost equal reduction in the amount of intracellular hyaluronan was obtained by using a lower enzyme concentration (1 TRU/ml) (Fig. 3, *top*). Therefore, most of the intracellular hyaluronan in the untreated cultures was probably endocytosed after its biosynthesis and extrusion across the plasma membrane.

The turnover time of the intracellular hyaluronan was studied by steady state radiolabeling the REK cultures, then chasing in a precursor-free medium containing *Streptomyces* hyaluronidase to prevent the entry of cell surface hyaluronan and that subsequently synthesized from the labeled precursor pool still remaining in the cell. The amount of intracellular radiolabeled hyaluronan was 70% of the starting value after 1 h chase and 60% after 2 h (Fig. 3, *bottom*). A plateau (~30% of the starting value) in the intracellular hyaluronan was reached in 4 h. The chase experiment thus showed that the half-life of

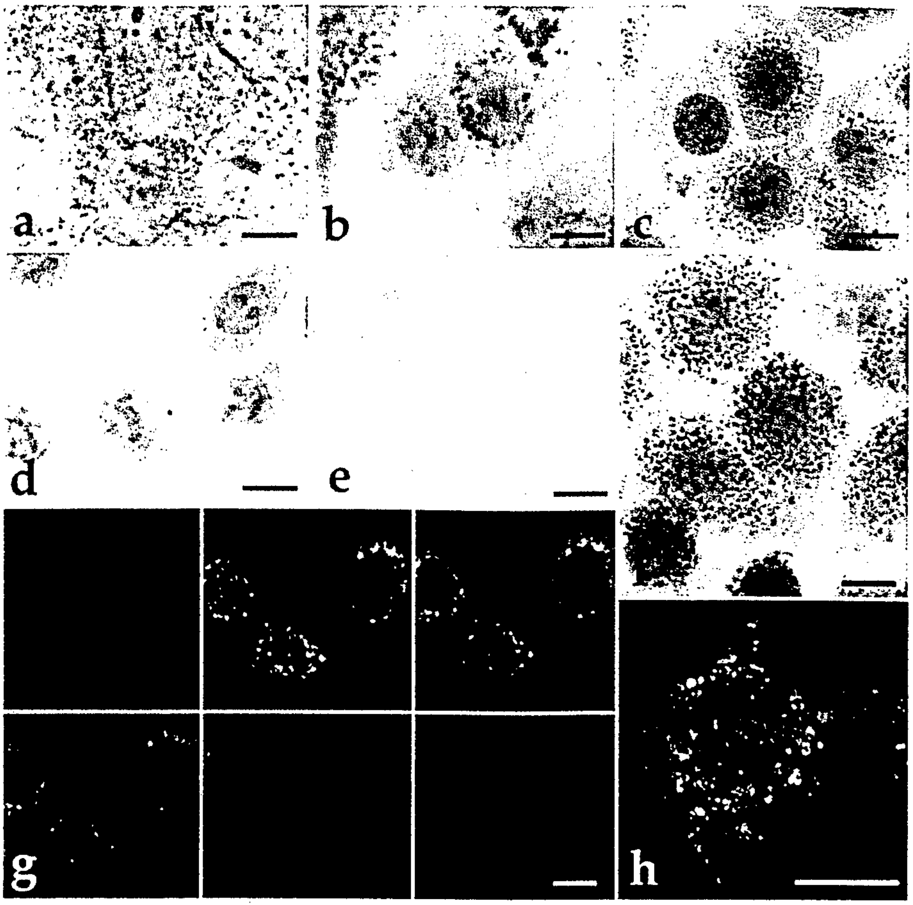

FIG. 4. **Localization of intracellular hyaluronan.** Subconfluent REK cultures were stained with bHABC for intracellular hyaluronan using the avidin-biotin-peroxidase technique and DAB (*a-f*) or with FITC-avidin (*g*), or Texas Red-streptavidin (*h*). *a*, an untreated REK culture permeabilized with Triton X-100 and stained. *b*, a culture treated with *Streptomyces* hyaluronidase prior to fixation, permeabilization, and staining. *c* and *e-h*, cultures fixed, first digested with hyaluronidase, then permeabilized and stained. *d*, a culture fixed, first permeabilized, then digested with hyaluronidase and stained. Staining with the appearance of intracellular vesicles is present whether hyaluronidase digestion is performed on live (*b*) or fixed (*c*) cultures, but not in cultures treated with the enzyme after permeabilization (*d*) which allows access to intracellular compartments, and abolishes the vesicular hyaluronan. *e*, a REK culture treated with HA_{10}-oligosaccharides for 4 h prior to fixation, permeabilization, and staining. *f*, a culture treated with 10 mM ammonium chloride for 4 h to block lysosomal activity. *g*, a series of optical sections through the cell layer confirming the intracellular localization of the endogenous hyaluronan vesicles around the nucleus. The *left image* in the *top row*, and the *right image* in the *lower row* represent the *upper* and *lower* surfaces of the cell layer, respectively. *h*, localization of endogenous hyaluronan with bHABC (*red*) and exogenous FITC-labeled hyaluronan (*green*). *Magnification bars*, 10 µm.

most of the intracellular hyaluronan is 2–3 h (See Fig. 3, *lower panel*).

Hyaluronan in Cytoplasmic Vesicles—The cytochemical hyaluronan probe (bHABC) showed that most of the cell-associated hyaluronan was distributed in patches on plasma membrane (23) (Fig. 4*a*). However, some was also located in vesicle-like structures, often close to the nucleus, suggesting an intracellular location. This was confirmed by short treatment of live REK cultures with *Streptomyces* hyaluronidase before staining for hyaluronan. The perinuclear signal was retained, while plasma membrane staining was removed by the enzyme (Fig. 4*b*). To avoid possible translocation of hyaluronan in live cells in response to the enzyme, we treated fixed cells with hyaluronidase prior to permeabilization of the cell membranes. This resulted in the same vesicular staining pattern as that seen with an enzyme digestion prior to the fixation (Fig. 4*c*). Confocal microscopy of cells pretreated with hyaluronidase after fixation also exhibited vesicle-like hyaluronan signals distributed in a perinuclear position (Fig. 4*g*). Cultures incubated with the bHABC probe preblocked with hyaluronan oligosaccharides (Ref. 44, and data not shown), or digested with *Streptomyces* hyaluronidase after permeabilization (Fig. 4*d*), were completely negative, demonstrating the specificity of the staining.

Transmission electron microscopy unequivocally confirmed the vesicular residence of the hyaluronan (Figs. 5, *a-f*). Fig. 5*a* shows the hyaluronan-positive intracellular structures using gold-labeled streptavidin and silver enhancement. Fig. 5, *b-f*, show sections from cultures stained with streptavidin peroxidase for hyaluronan and with gold-labeled secondary antibody for CD44. The hyaluronan-positive vesicles varied from 60 to 600 nm in diameter, with a few even larger (800–1300 nm). The small diameter vesicles (~100 nm) were typically found close to the plasma membrane and were often elongated, forming tube-like structures (Fig. 5, *b* and *d*). Larger vesicles were distributed around the nucleus with some appearing to be multivesicular bodies (Fig. 5, *a* and *e*). Cells pretreated with *Streptomyces* hyaluronidase prior to permeabilization lost the fuzzy surface coat visible in Fig. 5*b*, while both small (Fig. 5*c*) and large (Fig. 5*e*) vesicles remained hyaluronan positive. This finding excluded the possibility that the hyaluronan-positive vesicles represented deep invaginations of the plasma membrane. Interestingly, hyaluronan found in liver endothelial cells by Fraser *et al.* (3) was found mainly in large 0.3 to 1.2-µm vesicles resembling the perinuclear hyaluronan-positive structures seen in the REKs.

Co-localization of Intracellular Hyaluronan with a Membrane Endocytic Tracer, but Not with Markers of Lysosomes and Golgi Vesicles—The endocytic compartment was visualized using a fluorescent lipid derivative (FM 1-43) which incorporates into the outer leaflet of the plasma membrane, and translocates to endocytic vesicles as a part of the plasma membrane (39). After a few minutes treatment, FM 1-43 positive vesicles appeared in REKs. The post-staining with bHABC reduced the signal of FM 1-43. However, enough was retained to confirm a co-localization with intracellular hyaluronan (Fig. 6*a*). The data suggest that intracellular hyaluronan is derived from pericellular/extracellular locations, although the intracellular origin is not totally ruled out because of possible intracellular vesicle fusion events.

Most of the lysosomes, visualized with anti-cathepsin D staining (Fig. 6*c*), were hyaluronan negative, and most of the hyaluronan positive structures were negative for cathepsin D (Fig. 6*c*), indicating that the demonstrable intracellular hyaluronan in REKs was not localized in lysosomes. Likewise, REKs fed with DAMP, a tracer that seeks its way into acidic compartments of the cell (40), showed only rare co-localization with intracellular hyaluronan (Fig. 6*b*). The data suggest that most

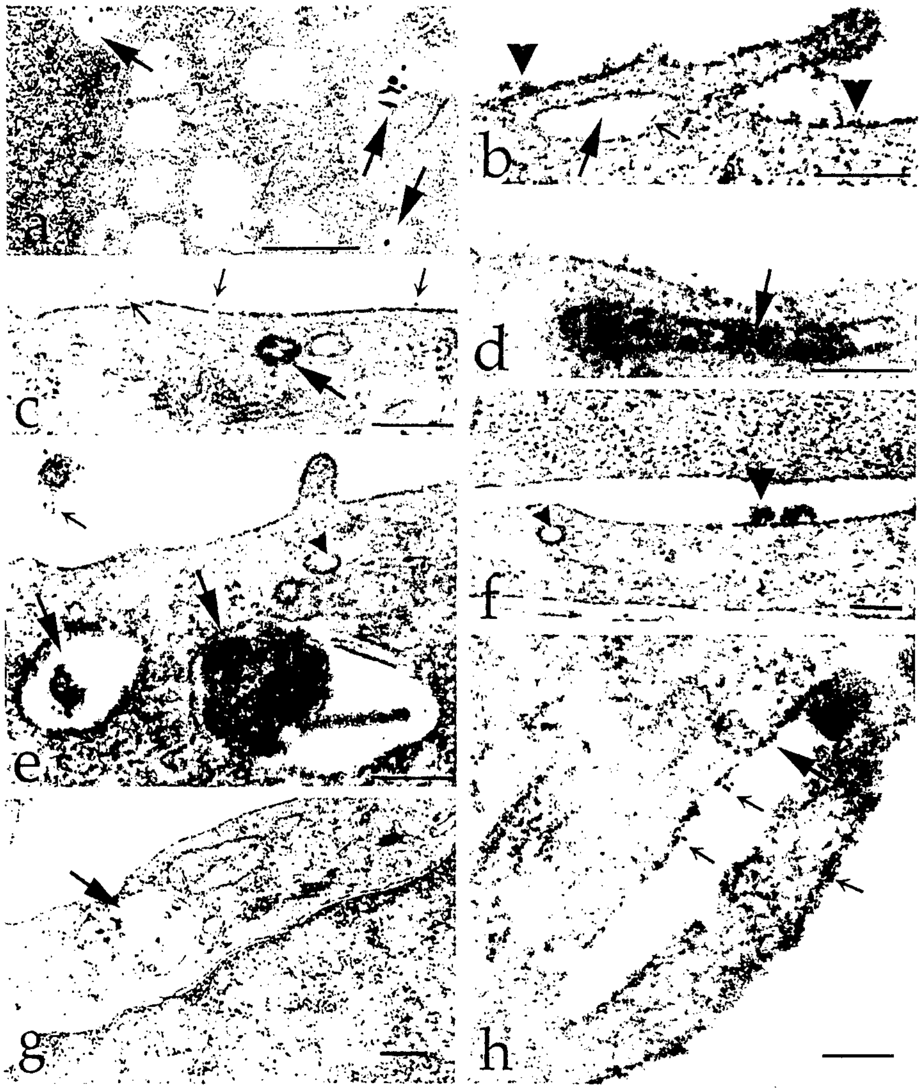

FIG. 5. **Electron microscopic localization of hyaluronan and CD44.** *a,* subconfluent REKs stained for hyaluronan with bHABC using gold-labeled streptavidin and silver enhancement prior to embedding in plastic. *b-h,* double staining for hyaluronan with bHABC-avidin-biotin-peroxidase-DAB technique, and CD44 with a gold-labeled secondary antibody. *c, e,* and *g,* cells treated with *Streptomyces* hyaluronidase prior to permeabilization to specifically remove pericellular hyaluronan. Note the strong, fuzzy, pericellular hyaluronan signal (*b, d, f,* and *h, large arrowheads* in *b* and *f*), and the CD44 staining (*small arrows*), especially abundant on cell processes (*e*). Intracellular vesicles containing hyaluronan (*large arrows*) are seen both with the silver enhancement technique (*a*) and DAB visualization (*b-h*). The hyaluronan vesicles close to the plasma membrane are often elongated (*b, d,* and *h*). CD44 is also found in some of the vesicles close to the plasma membrane (*b* and *h*). Coated vesicles appear to be hyaluronan-negative (*e* and *f, small arrowheads*). A culture treated with 5 mM ammonium chloride for 4 h (*g*) contains a large (diameter 600 nm) hyaluronan-positive vesicle. *Magnification bars*: 500 nm in *a*, 200 nm in *b-g*, and 100 nm in *h*.

of the hyaluronan-containing vesicles had close to neutral pH, and probably represented early endosomes.

Golgi compartments were localized using an anti-COP mAb (45) (Fig. 6*d, red*). While the COP-positive structures were grouped around the nucleus, like most of the vesicles positive for hyaluronan, they did not co-localize (Fig. 6*d*).

Intracellular Hyaluronan Accumulation following Lysosome Inhibition—Lysosomal functions of the REKs were inhibited by ammonium chloride or chloroquine treatment, followed by staining for intracellular hyaluronan. Optical density (OD) of the intracellular hyaluronan signal was also measured, and the mean OD per area as well as the relative area of intracellular hyaluronan-positive structures were determined. Both reagents increased the OD and the hyaluronan positive area ~3–4 times over that of controls (Table I). Ammonium chloride and chloroquine gave their maximum responses at 5 and 1 mM concentrations, respectively (data not shown). Accumulation of intracellular hyaluronan was increased by 30 min, and more pronounced after 2 h, reaching a maximum at 4 h after which it declined (data not shown). An image of the intracellular hyaluronan in a REK culture treated with 10 mM ammonium chloride for 4 h is shown in Fig. 4*f*. Most cells showed both an increased number and size of hyaluronan-positive vesicles. Fig. 5*g* shows a TEM image of a REK culture treated with 5 mM ammonium chloride for 4 h with a very large hyaluronan-positive intracellular vesicle. Monensin, an ionophore which has been reported to inhibit lysosomal activity and receptor recycling (34), also caused an increase in the intracellular hyaluronan staining (Figs. 6*g* and 7*e*). The hyaluronan-positive structures in monensin-treated cultures often showed a ring-like morphology (Fig. 7*e*).

The molecular mass distribution of metabolically labeled intracellular hyaluronan was also analyzed in ammonium chloride and chloroquine-treated cultures using S-400 gel filtration (Fig. 2, *d-f*). In control cultures about 23% of the intracellular hyaluronan had the apparent molecular mass larger than 90 kDa, while the corresponding figures for chloroquine- and ammonium chloride-treated cultures were 50 and 53%, respectively, indicating a shift toward higher molecular mass.

Apigenin reportedly inhibits hyaluronidase *in vitro* (46), in sperm penetration assays (47), and in mammary and cervix tumors (48). When added to the REK culture medium, apigenin caused a rapid and dose-dependent increase in intracellular hyaluronan staining although the accumulation was less pronounced than with ammonium chloride (Table I). Taken together, these data in which lysosomal function was perturbed suggest that the intracellular hyaluronan demonstrated by the bHABC probe resides in vesicles targeted to lysosomes.

Reduction of Vesicular Hyaluronan by Hyaluronan Oligosaccharides—Subconfluent REK cultures were incubated with hyaluronan oligosaccharides of different sizes at 0.2–0.5 mg/ml concentrations. The OD measurement of the hyaluronan staining showed that oligosaccharides with 8 monosaccharide units (HA_8) or smaller had no effect, while HA_{10} or greater decreased

FIG. 6. **Characterization of the hyaluronan vesicles.** Confocal optical sections are shown, each with two fluorescent markers, that when co-localized yield a *yellow* color. *a*, cells incubated with a fluorescent lipid to specifically demonstrate the vesicles derived from plasma membrane (*green*) and those containing endogenous hyaluronan (*red*). *b*, cells incubated with DAMP to visualize acidic compartments (*green*) and endogenous hyaluronan (*red*). *c*, lysosomes indicated by staining for cathepsin D (*red*) and endogenous hyaluronan (*green*). *d*, Golgi vesicles localized by staining for COP (*red*) and endogenous hyaluronan (*green*). *e*, coated pit derived endosomes after 30 min incubation at 37 °C with Texas Red-labeled transferrin (*red*) and endogenous hyaluronan (*green*). *f*, coated pit derived endosomes and hyaluronan as in *e*, but incubated at 20 °C. *g*, coated pit derived endosomes and hyaluronan as in *e* but incubated with monensin to inhibit receptor recycling. *h*, Texas Red-labeled 10-kDa dextran (10 μg/ml) incubated for 30 min at 37 °C to demonstrate bulk phase endocytosis vesicles (*red*), and endogenous hyaluronan (*green*). *i*, Texas Red-labeled dextran (*red*) and 10 μg/ml FITC-labeled exogenous hyaluronan (*green*) incubated together for 30 min at 37 °C. *j*, Texas Red-labeled dextran (*red*) and ~6 kDa AMAC-labeled hyaluronan oligosaccharides (*green*) incubated for 30 min at 37 °C. *k*, Texas Red-labeled dextran (*red*) and AMAC-oligosaccharides (*green*) incubated as in *j* with an excess of unlabeled oligosaccharides. *l*, caveolin containing vesicles (*red*) and endogenous hyaluronan (*green*).

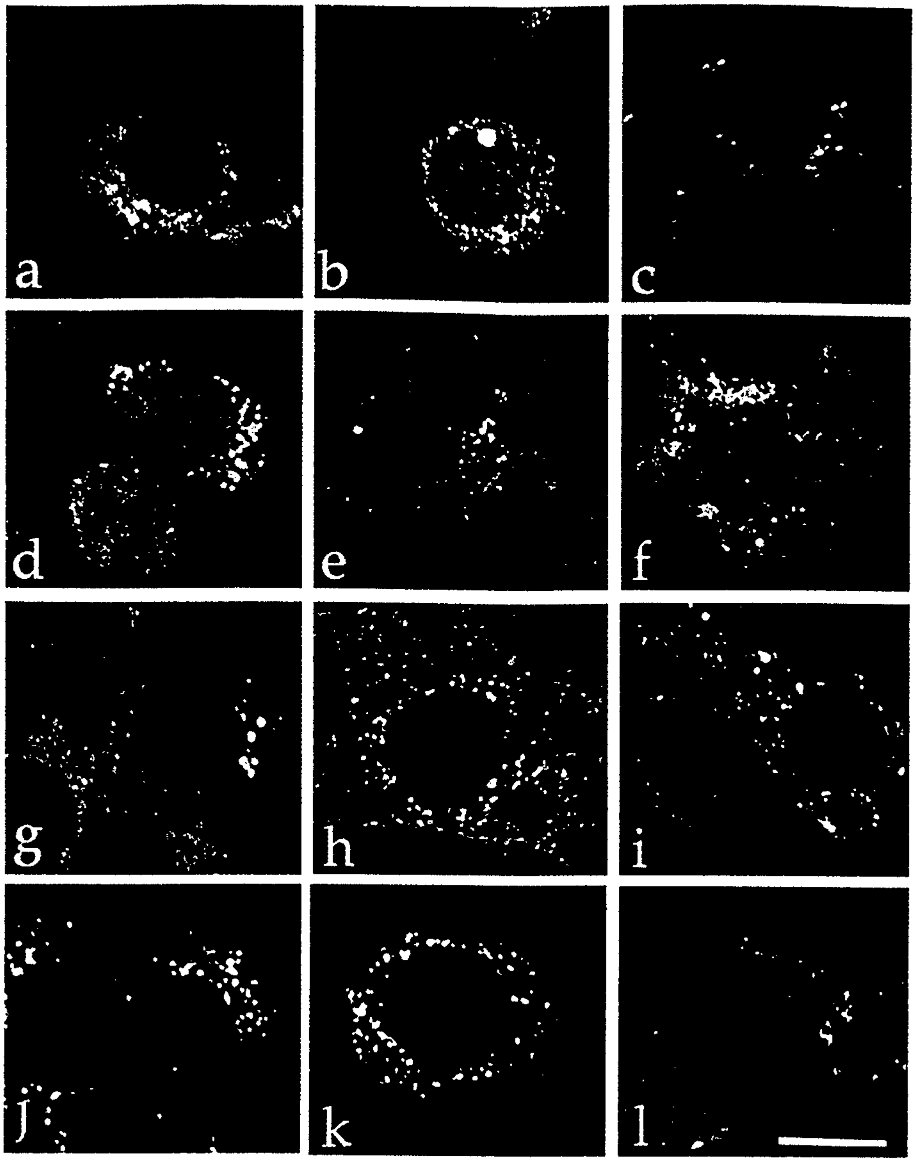

intracellular hyaluronan staining (Fig. 8*a*). The area of DAB positivity was reduced with HA_{14} to 20% of the control cultures. The structurally related glycosaminoglycans chondroitin sulfate and heparan sulfate had no effect (Fig. 8*a*). Fig. 4*e* shows histological staining for intracellular hyaluronan of a culture treated with HA_{10} for 4 h, exhibiting virtually no hyaluronan signal. These findings suggest that there is an uptake receptor in REKs specific for hyaluronan which requires a minimum length of HA_{10} for effective binding.

The kinetics of clearance of the intracellular hyaluronan signal following addition of HA_{12} into growth medium, visualized with bHABC, is shown in Fig. 8*b*. The OD of the DAB color was reduced to 60% of the starting value in 5 min and reached a stable basal level, ~20% of control, in 10 min. The half-life of the intracellular hyaluronan detected with bHABC was thus considerably shorter than the total hyaluronan assayed by radiolabeling (Fig. 3). This observation is consistent with the hypothesis that the bHABC probe specifically demonstrates recently endocytosed hyaluronan molecules that are rapidly shifted to another pool that cannot be detected with the bHABC probe.

Intracellular Hyaluronan and CD44—REKs reacted with the mAb OX50 against the hyaluronan receptor CD44 showed a strong plasma membrane signal, especially concentrated at areas of cell-cell contact and in patches on the apical surface, a distribution similar to that of hyaluronan (Fig. 7*a*, and Ref. 23). Very little CD44 was detected intracellularly by confocal microscopy, and dual staining of CD44 and intracellular hyaluronan exhibited only rare co-localizations close to the plasma membrane (Fig. 7, *a-c*). Immunoelectron microscopy demonstrated CD44 enrichment on plasma membrane projections (Fig. 5*b*). CD44-positive, small diameter vesicles or tubules close to plasma membrane were occasionally ultrastructurally seen (Fig. 5, *b* and *h*). These structures were also hyaluronan-positive (Fig. 5, *b* and *h*). CD44 was not found in coated pits or coated vesicles (Fig. 5, *e* and *f*).

Perturbation of lysosomal activity with ammonium chloride or chloroquine, which markedly increased the amount of vesicular hyaluronan, caused a minor increase in the intracellular CD44 staining (data not shown). However, treatments which have been shown to slow down receptor recycling, *e.g.* monensin (34) (Fig. 7, *d-f*), or incubation at room temperature (49) (Fig. 7, *g-l*), caused accumulation of intracellular CD44 in addition to hyaluronan. Monensin-treated cultures frequently exhibited large circular structures with CD44 on the perimeter and hyaluronan inside (Fig. 7, *d-f*). Confocal analyses confirmed that these structures with a ring-like distribution of CD44 were within the cells. REKs incubated at room temper-

TABLE I
Influence of perturbation of lysosomal activity on intracellular hyaluronan

REK cultures were incubated with ammonium chloride, chloroquine, or apigenin for 4 h prior to staining for intracellular hyaluronan. The optical densities (OD) were measured and the area of DAB-positive (above the threshold value) intracellular structures was compared to that in control cultures. Medians and ranges of three experiments are shown.

Effector	% of OD in controls
Ammonium chloride (10 mM)	494 (216–2045)
Chloroquine (2 mM)	345 (340–345)
Apigenin (25 μM)	203 (131–264)

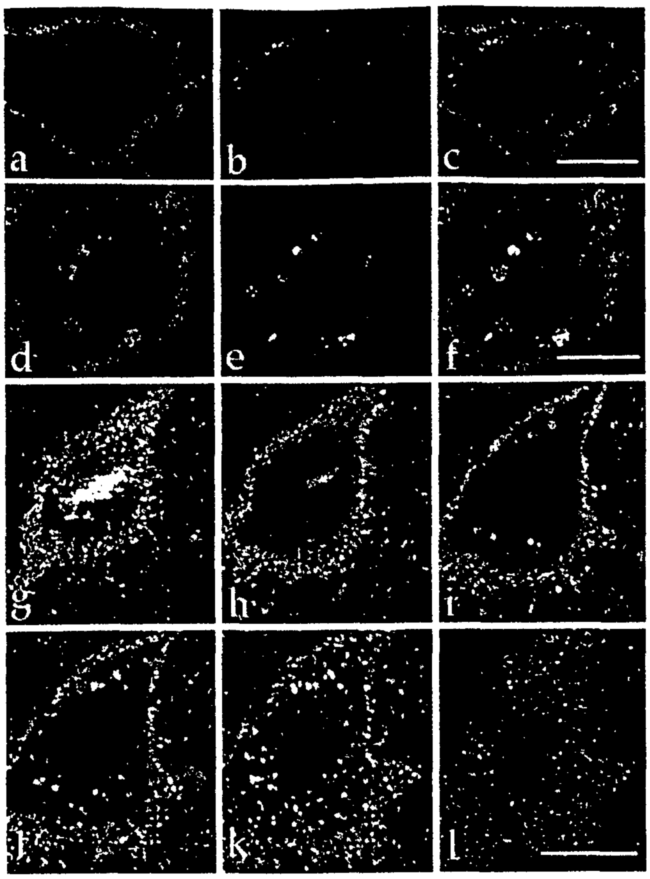

FIG. 7. **Localization of CD44 in REKs.** Dual staining for CD44 (*red*) and endogenous intracellular hyaluronan (*green*), using Texas Red-labeled secondary antibody and FITC-labeled avidin as reporters, respectively. Confocal optical sections through the cell layer are shown. *a-c*, untreated cells, with the signal of CD44 (*a*), hyaluronan (*b*), and both (*c*). *d-f*, cells treated with 2 μM monensin for 2 h at 37 °C, showing CD44 (*d*), hyaluronan (*e*), and both (*f*). *g-l*, a series of consecutive optical sections through a cell incubated for 1 h at room temperature, with the *top most* section in *g* and *lower most* in *l*. Note the strong CD44 signal from the plasma membrane, but little intracellular staining in untreated cells (*a*). Incubation with monensin induced large intracellular structures positive for hyaluronan (*e*) and CD44 (*d*) that were often co-localized (*f*). Intracellular CD44 and its co-localization with hyaluronan was also markedly increased by incubation at room temperature (*g-l*). *Magnification bars,* 10 μm.

ature also showed a co-localized signal for CD44 and hyaluronan, typically close to the plasma membrane (Fig. 7, *g-l*), in addition to vesicles farther removed from the surface (Fig. 7, *i* and *j*, 4 and 2 μm from the bottom, respectively).

It was previously shown that OX50, a monoclonal anti-CD44 antibody increases pericellular hyaluronan staining on REKs (23). The consequences of this pericellular accumulation were studied by an OD assay of intracellular hyaluronan after a 4-h incubation with OX50. This antibody caused a consistent, dose-dependent increase in the intracellular hyaluronan-positive area (Fig. 9). A normal, isotypically matched mouse IgG (data not shown) and Hermes 3, an anti-CD44 antibody against human CD44, which does not recognize rat CD44, had little or no effect on the level of intracellular hyaluronan (Fig. 9).

Endogenous Hyaluronan Uptake and Coated Pits, Caveolae, and Pinocytosis—Two established mechanisms of receptor-mediated endocytosis, utilizing clathrin-coated pits and caveolae, were studied. The avid internalization of transferrin, a widely used marker of the coated pit pathway (42), confirmed that this endocytosis pathway operated in REKs (Fig. 6, *e-g*). The formation of coated pits is selectively inhibited by chlorpromazine and hyperosmotic medium (50). Both of these inhibitors significantly reduced the uptake of Texas Red- or FITC-labeled transferrin (data not shown), indicating that the treatments perturb the coated pit pathway in REKs. However, neither of these treatments decreased the amount of intracellular endogenous hyaluronan in REK cultures (Table II). In fact, chlorpromazine caused an increase in the intracellular hyaluronan staining in all experiments (Table II). Higher chlorpromazine concentrations and shorter and longer treatment times (30 min to 4 h) also caused a consistent increase in the intracellular hyaluronan staining (data not shown).

Cells with very active transferrin uptake usually exhibited low intracellular hyaluronan content. The converse was also true with cells exhibiting abundant intracellular hyaluronan demonstrating reduced transferrin uptake (Fig. 6*e*). Incubation of cells at room temperature permits endocytosis, but slows receptor recycling and transport to lysosomes (49). REKs incubated at room temperature for 1 h (Fig. 6*f*) contained more intracellular hyaluronan-positive vesicles than cells taken directly from 37 °C (Fig. 6*e*), and also accumulated more Texas Red-transferrin. Most of the intracellular hyaluronan and transferrin resided in separate compartments (Fig. 6*f*). REKs treated with monensin to reduce receptor recycling (34) showed accumulation of both transferrin and intracellular hyaluronan, again mainly in distinct compartments (Fig. 6*g*). Staining for the receptor of transferrin also confirmed separate uptake vesicles for hyaluronan and transferrin (data not shown). Furthermore, electron microscopy did not reveal coats on hyaluronan vesicles (Fig. 5, *e* and *f*). These data indicate that hyaluronan did not enter REKs through coated pits.

REKs showed active pinocytosis of Texas Red-labeled dextran, a commonly used fluid-phase endocytosis marker (41). Cells with the most active dextran uptake usually had more endogenous intracellular hyaluronan. An example of such a cell is shown in Fig. 6*h*. Despite this association of intracellular hyaluronan with the fluid-phase endocytosis, most of the endogenous hyaluronan vesicles were dextran-negative (Fig. 6*h*).

The large size of the endogenous hyaluronan-positive vesicles and their responsiveness to growth factor stimulation (51) and the fact that large polysaccharides like dextrans, are preferentially taken into macropinosomes rather than micropinosomes (41), suggested that hyaluronan-positive vesicles might be formed via macropinocytosis. The possibility that hyaluronan bound to cell surface receptors is recruited into these macropinocytotic vesicles was probed with amiloride, an inhibitor of macropinocytosis (31, 32). However, amiloride was unable to influence the content of intracellular hyaluronan in REKs (Table II). A more potent derivative of amiloride, *N,N*-dimethylamiloride, also had a negligible influence on the amount of intracellular hyaluronan positivity (data not shown).

Basal cells in the epidermis have caveolae on their basolateral surfaces (52), and immunostaining with anti-caveolin 1 antibody demonstrated a positive reaction in the same area (53). REKs stained with a monoclonal antibody against caveo-

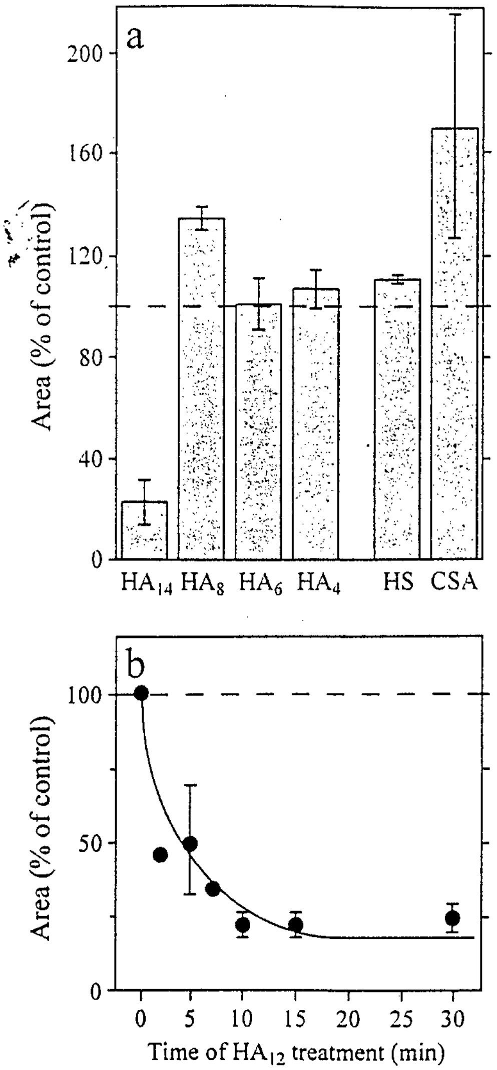

FIG. 8. **Influence of hyaluronan oligosaccharides and related GAGs on intracellular hyaluronan.** *a*, REK cultures were incubated with 0.3 mg/ml sized hyaluronan-oligosaccharides (HA_4-HA_{14}), heparan sulfate (*HS*) and chondroitin sulfate (*CSA*) for 4 h prior to fixation and staining for endogenous intracellular hyaluronan. *b*, REKs were incubated with 0.2 mg/ml HA_{14} for 0–30 min before fixation and staining. The optical densities of the cultures were measured, and the areas of the DAB-positive intracellular structures were compared with that in control cultures. The data represent mean ± S.E. from two independent experiments for hyaluronan oligosaccharides and three for heparan sulfate and chondroitin sulfate.

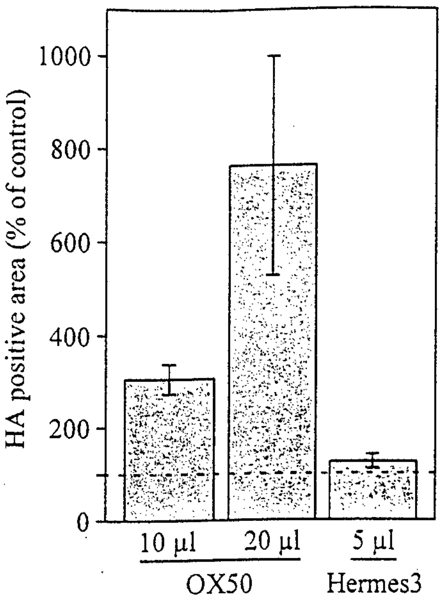

FIG. 9. **Influence of anti-CD44 monoclonal antibodies on intracellular hyaluronan.** REK cultures were incubated with either the OX50 antibody or the Hermes 3 antibody for 4 h prior to the staining for endogenous intracellular hyaluronan. The optical densities were measured, and the area of DAB-positive intracellular structures were compared with that in control cultures. The data represent mean ± S.E. from three different experiments.

lin 1 showed a diffuse plasma membrane and cytoplasmic signal (Fig. 6*l*). Occasional cells with more intense punctate caveolin 1 staining were seen (Fig. 6*l*). The distribution patterns of caveolin 1 and hyaluronan were clearly different (Fig. 6*l*). Filipin and nystatin, reported to inhibit the formation of caveolae in endothelial cells (30), failed to cause any reduction in the intracellular hyaluronan staining (Table II). In contrast, both increased intracellular hyaluronan positivity (Table II). Lower and higher concentrations of inhibitors, and longer and shorter treatment times, were also tested, and they gave similar results (data not shown).

Receptor-mediated and Bulk Phase Uptake of Exogenous Hyaluronan—Exogenous FITC-labeled macromolecular hyaluronan (size > 100 kDa) given to the REKs, was internalized into vesicular structures (Figs. 4*h* and 6*i*). Cells showing efficient uptake of exogenous hyaluronan often had high endogenous intracellular hyaluronan content, and the two signals showed partial co-localization (Fig. 4*h*). To distinguish between receptor-mediated *versus* bulk phase endodocytosis of exogenous hyaluronan, hyaluronan oligosaccharides were added to inhibit the binding and uptake of FITC-labeled hyaluronan. The amount of FITC-hyaluronan bound to the cell surface at 4 °C, and that associated with the cells after 30 min chase at 37 °C, are shown in Fig. 10. The oligosaccharides partially inhibited FITC-hyaluronan binding on the cell surface, while sulfated glycosaminoglycans at the same concentration were less effective as competitors (Fig. 10). The HA_{14} oligosaccharide also reduced the internalization of high molecular weight hyaluronan by ~70%, while the other glycosaminoglycans were less effective (Fig. 10). The uptake of exogenous hyaluronan in the presence of competing oligosaccharides and the fact that exogenous hyaluronan showed partial co-localization with dextran (Fig. 6*i*) suggest that exogenous hyaluronan can be endocytosed both via receptor-mediated (HA_{14} affected) and nonspecific mechanisms.

Short hyaluronan oligosaccharides ($HA_{\geq 10}$) can displace hyaluronan from its receptors on REKs (23). To study whether they were also internalized, oligosaccharides were labeled with the fluorescent AMAC group at their reducing end to avoid possible interference of receptor binding along the relatively short chain. The biological properties of the tagged oligosaccharides were similar to those of unlabeled oligosaccharides in that they were equally effective in displacing intact hyaluronan from the cell surface (data not shown). Throughout the HA_4-HA_{40} size range examined, the labeled oligosaccharides were avidly internalized by REKs when incubated at 37 °C (Fig. 6*j*). However, this internalization was not inhibited by unlabeled oligosaccharides (Fig. 6*k*). Unlike macromolecular hyaluronan, the labeled oligosaccharides were not bound to the cells when incubated at 4 °C, or internalized upon subsequent chase at 37 °C (data not shown). This suggests that these small hyaluronan oligosaccharides have a low affinity for the hyaluronan receptor, and that their uptake is not receptor mediated. The labeled oligosaccharides were taken up into the same vesicles as the Texas Red-labeled dextran (Fig. 6, *j* and *k*), supporting the idea of bulk phase endocytosis as their primary route for internalization.

TABLE II

Influence of perturbation of coated pits, caveolae and macropinosomes on endogenous intracellular hyaluronan

REK cultures were incubated with chlorpromazine, sucrose, nystatin, filipin, or amiloride for 1 h prior to the fixation and staining for intracellular hyaluronan. The optical densities (OD) were measured and the area of DAB-positive (above the threshold value) intracellular structures was compared to that in control cultures. Medians and ranges of three experiments for chlorpromazine, filipin, and nystatin, and two experiments for amiloride and sucrose are shown.

Effector	% of OD in controls
Chlorpromazine (2 mM)	339 (199–2088)
Sucrose (0.4 M)	151 (87–214)
Filipin (4 μM)	165 (88–442)
Nystatin (2 mM)	224 (121–296)
Amiloride (2 mM)	91 (70–111)

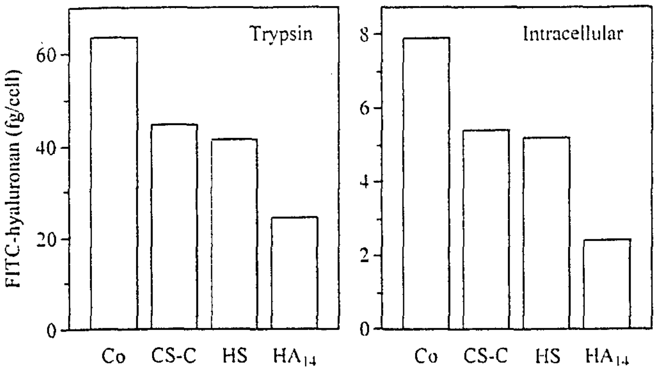

FIG. 10. **Uptake of exogenous hyaluronan.** REK cultures were incubated with FITC-labeled hyaluronan for 120 min at 37 °C alone (*Co*) or with 1 mg/ml of chondroitin sulfate (*CS-C*), heparan sulfate (*HS*), or hyaluronan-oligosaccharides (HA_{14}), and the fluorescence released from the cells with trypsin (*left panel*) and that recovered from lysed cells (*right panel*) were measured. One of two experiments with similar results is shown.

DISCUSSION

Origin of Intracellular Hyaluronan—The present data demonstrate that intracellular vesicles in rat epidermal keratinocytes contain hyaluronan derived from either endogenous or exogenous sources. Most of the endogenous intracellular hyaluronan originates from the cell surface via receptor-mediated endocytosis and is destined for lysosomal degradation since: 1) intracellular hyaluronan co-localized with a plasma membrane endocytic tracer; 2) the content of intracellular hyaluronan decreased by competition with $HA_{\geq 10}$ oligosaccharides which block binding of hyaluronan to cell-surface receptors; 3) continuous hyaluronidase digestion of extracellular hyaluronan reduced intracellular hyaluronan; and 4) the inhibition of endogenous hyaluronidase and lysosomal functions lead to accumulation of intracellular hyaluronan and a shift of the size toward higher molecular mass (see diagram in Fig. 11). Exogenous hyaluronan is partly taken up via receptor mediated uptake, and partly via bulk phase endocytosis, because: 1) its uptake was only partially reduced with hyaluronan oligosaccharides; and 2) it showed a marked co-localization with bulk fluid phase endocytosis markers.

Properties of the Hyaluronan Uptake Receptor—The hyaluronan uptake receptor in keratinocytes is distinct in that it is not sensitive to sulfated glycosaminoglycans, unlike those in chondrocytes and liver endothelial cells (17, 54, 55). Likewise, HA_6 or HA_8 oligosaccharides compete for hyaluronan uptake in chondrocytes (8) and liver endothelial cells, but not in REKs, which require HA_{10}.

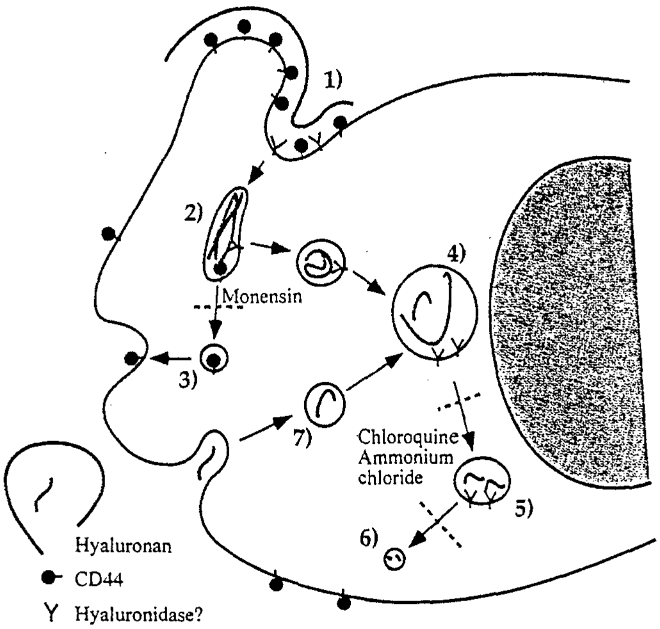

FIG. 11. **Suggested hyaluronan endocytosis and degradation process in keratinocytes.** *1*) hyaluronan binds to clustered CD44 and possibly other unknown cell surface receptors. *2*) Hyaluronan and the receptors are internalized and detected in elongated vesicles close to plasma membrane, a step possibly involving limited cleavage by a hyaluronidase. *3*) CD44 is released and recycled back to cell surface. *4*) Hyaluronan is found in larger, perinuclear, non-acidic vesicles. The half-life of steps 2–4 combined is ~5 min. *5*) Fragmentation, perhaps by a hyaluronidase, into a weakly bHABC positive <90 kDa size pool with 2–3 h half-life. *6*) Degradation in lysosomes. *7*) Hyaluronan and particularly hyaluronan oligosaccharides can also enter cells via non-receptor mediated pathway. The *dashed lines* indicate steps inhibited by the lysosomal inhibitors ammonium chloride and chloroquine, and the endosome recycling inhibitor monensin.

While an excess of end-labeled fluorescent oligosaccharides in the size range HA_{10} to ~HA_{40} competed for the binding and internalization of hyaluronan, they were not bound to the receptors tightly enough to be demonstrated on the cell surface by fluorescence microscopy. Furthermore, they were mainly endocytosed through bulk phase pinocytosis as indicated by the lack of competition with unlabeled oligosaccharides. This suggests that the uptake of intact hyaluronan involves multivalent binding to several receptor molecules (28), probably clustered at defined sites on the plasma membrane (23, 56). Coalescence of such cholesterol-enriched (56) and detergent-resistant (57) receptor clusters is compatible with the patchy distribution of hyaluronan and CD44 on keratinocytes (23). The patching of CD44 may enhance its affinity for hyaluronan, and may also be required for receptor-mediated uptake. It has been shown by several studies that the proximity of CD44 molecules, spontaneous or induced by cross-linking in the membrane spanning domain or by antibodies, enhance hyaluronan binding (57–59).

Role of CD44 in Hyaluronan Uptake of Keratinocytes—While the increase of endogenous intracellular hyaluronan by the anti-CD44 antibody OX50 suggested that CD44 is involved in hyaluronan endocytosis in REKs, the mechanism remains incompletely understood. Immunostaining of REKs with a mAb against CD44 showed only occasional intracellular signal, similar to that observed in human keratinocytes *in vivo* (22). The absence of intracellular CD44 staining may indicate that CD44 does not act alone in the uptake of hyaluronan. The fact that decasaccharides are required to compete for the binding and uptake in keratinocytes, while hexasaccharide size is large enough to compete for CD44 binding in many other cells and tissues, can be taken to support this alternative. On the other hand, incubation of REKs with monensin or at room temperature to interfere with receptor recycling, increased the number and size of CD44-positive intracellular vesicles, the number of hyaluronan-positive vesicles, and co-localization of intracellular CD44 and hyaluronan. These experiments suggest that the low number of CD44-positive vesicles and the lack of co-localization with hyaluronan reflect recycling of CD44 back to the cell surface from early endosomes (Fig. 11).

Routes of Hyaluronan Endocytosis—It is puzzling that clathrin-coated pits, a common vehicle for wrapping and detaching receptor bound cargo into endosomal vesicles, and also shown to be active in REKs, seems not to operate in hyaluronan uptake. This is suggested by: 1) the lack of transferrin and transferrin receptor co-localizations with hyaluronan; 2) the inability of the inhibitors of coated pit formation to reduce intracellular hyaluronan although they effectively reduced the uptake of transferrin; and 3) the lack of electron microscopically detectable coats around hyaluronan-containing vesicles. There is previous evidence for the involvement of coated pits with the hyaluronan uptake mediated by the receptor HARE on liver endothelial cells (60) although non-saturable, fluid-phase endocytosis has also been reported in these cells (4). Coated pits were not associated with the CD44-associated hyaluronan endocytosis in chondrocytes (7, 61), nor was CD44 found in the coated pits of the present keratinocytes. Keratinocytes are known to use unusual mechanisms not corresponding to the classical endocytic routes to internalize subdomains of their plasma membrane. Thus, hemidesmosomal and desmosomal plaques are internalized by a pathway not involving clathrin-coated pits (62, 63). A similar mechanism might operate in the uptake of membrane bound hyaluronan.

Caveolae, the other common mechanism of receptor mediated endocytosis, were also excluded as the hyaluronan-uptake route because: 1) inhibitors of caveola formation did not reduce intracellular hyaluronan content; and 2) immunostaining for caveolae showed no co-localization with hyaluronan. The fact that inhibitors of endocytosis through coated pits and caveolae actually lead to accumulation of intracellular hyaluronan may reflect the pleiotropic effects of the inhibitors, or activation of alternate uptake systems when one route is blocked (64).

While the hyaluronan endocytosed by specific receptors, and labeled dextran taken up by bulk phase endocytosis, resided in separate vesicles, both were often abundant in the same cells, suggesting that the two processes are somehow linked. Both uptake systems may correlate with the rate of membrane turnover. High molecular mass hyaluronan when present in the forming endosome may sterically exclude other macromolecules like dextran, thereby explaining the lack of co-localization of hyaluronan and dextran in most vesicles.

Degradation of Hyaluronan following Endocytosis—The molecular mass of the intracellular hyaluronan was strongly skewed toward the lower end, with most of the material below 400 kDa and a peak at ~20 kDa, in contrast to that on the cell surface and in the medium, mostly exceeding 2000 kDa. This suggests that either: 1) the intracellular material has already undergone degradation after endocytosis; or 2) there is selective uptake of low molecular mass hyaluronan from the cell surface. The fact that perturbation of lysosomal activity caused a shift toward higher molecular mass species of intracellular hyaluronan supports the idea that the intracellular hyaluronan detected in control samples was partly degraded inside the cells; quite likely by hyaluronidases in the early endosomal compartment. Interestingly, one of the recently described hyaluronidases (Hyal 2) was reported to produce ~20-kDa hyaluronan fragments as its end product (65). The rapid clearance of the bHABC-positive vesicles by the receptor competing oligosaccharides also fits with the hypothesis that these endosomes represent dynamic, transitory vehicles in which hyaluronan is moved toward lysosomes and in which its initial fragmentation takes place. The 20–90-kDa hyaluronan probably does not give a signal in contrast to the high molecular mass hyaluronan, since it may not fix well enough to be retained throughout the staining procedure. The relatively long 2–3-h half-life of the total intracellular hyaluronan is best explained by gradual endoglycosidase action in the prelysosomal endosomes (Fig. 11), a process similar to that in heparan sulfate catabolism (66). The final degradation in lysosomes may be rapid, since no oligosaccharide size intermediates were detected.

Hyaluronan Size and Endocytosis—The alternative that there was preferential uptake of low molecular mass hyaluronan cannot be completely excluded, however, since there was sufficient low molecular mass material in the medium, despite its low proportion of the total, to supply the intracellular pool. Selective endocytosis of relatively low molecular mass material is also in agreement with a study on cultured endothelial cells, fibroblasts, and vascular smooth muscle cells, showing the highest internalization rate in the molecular mass range ≤30 kDa (9). Interestingly, the present study showed efficient non-receptor mediated internalization of 0.8–8-kDa hyaluronan oligosaccharides (HA_4-HA_{40}).

The size of pericellular hyaluronan may also influence the probability of its engulfment into a vesicle, since a long chain of hyaluronan simultaneously bound to distant cell surface sites would be expected to resist vesicle budding and detachment. Extracellular and intracellular hyaluronan showed a molecular mass up to 6000 kDa and less than 400 kDa, respectively, corresponding to 300 and 65 nm radius of gyration (17). It has been shown that high molecular mass dextran (150 kDa) is taken up by macropinocytosis, *i.e.* vesicles larger than 200 nm in diameter, while small dextran molecules (4–10 kDa) can enter both in macropinosomes and micropinosomes. Therefore, accommodation of the large hyaluronan species in the micropinosomes of ~120-nm diameter vesicles (41) seems difficult, and fragmentation of cell surface-attached hyaluronan could facilitate its uptake. In chondrocytes, the increased content of hyaluronan, and its liberation from other matrix molecules enhances CD44 turnover and internalization (7). Our previous organ culture experiments suggest that epidermal hyaluronan is fragmented into intermediate sizes before final clearance (20), perhaps mediated by reactive oxygen species (19).

Hyaluronan Turnover in Keratinocytes—The present and earlier data (23) suggest that a considerable proportion of newly synthesized hyaluronan is internalized and degraded. In continuous labeling of REK cultures, a steady state in cell surface, and intracellular hyaluronan prevails between 12 and 24 h after label introduction (23). It can be calculated that hyaluronan in the medium increases by ~32 fg/cell during that time (23) and that ~11 fg/cell is degraded in a similar time period in the present experiments, suggesting that 25% of all hyaluronan is endocytosed shortly after synthesis. It is highly likely that this fast hyaluronan synthesis/endocytosis traffic on the cell surface has a biological importance of which little is currently known.

Acknowledgments—Expert technical help from Arja Venäläinen, Eija Rahunen, Päivi Perttula, Virpi Miettinen, and Riikka Tiihonen is gratefully acknowledged. We thank Alpo Peltari for the opportunity to use the facilities of the Department of Electron Microscopy.

REFERENCES

1. Weigel, P. H., Hascall, V. C., and Tammi, M. (1997) *J. Biol. Chem.* **272,** 13997–14000
2. Fraser, J. R., Kimpton, W. G., Laurent, T. C., Cahill, R. N., and Vakakis, N. (1988) *Biochem. J.* **256,** 153–158
3. Fraser, J. R., Alcorn, D., Laurent, T. C., Robinson, A. D., and Ryan, G. B. (1985) *Cell Tissue Res.* **242,** 505–510
4. Smedsrød, B., Pertoft, H., Eriksson, S., Fraser, J. R., and Laurent, T. C. (1984) *Biochem. J.* **223,** 617–626
5. Laurent, U. B., Fraser, J. R., Engström-Laurent, A., Reed, R. K., Dahl, L. B., and Laurent, T. C. (1992) *Matrix* **12,** 130–136
6. Laurent, U. B., Dahl, L. B., and Reed, R. K. (1991) *Exp. Physiol.* **76,** 695–703

7. Aguiar, D. J., Knudson, W., and Knudson, C. B. (1999) *Exp. Cell Res.* **252,** 292–302
8. Hua, Q., Knudson, C. B., and Knudson, W. (1993) *J. Cell Sci.* **106,** 365–375
9. McGuire, P. G., Castellot, J. J., Jr., and Orkin, R. W. (1987) *J. Cell. Physiol.* **133,** 267–276
10. Culty, M., O'Mara, T. E., Underhill, C. B., Yeager, H., Jr., and Swartz, R. P. (1994) *J. Leukoc. Biol.* **56,** 605–611
11. Underhill, C. B., Nguyen, H. A., Shizari, M., and Culty, M. (1993) *Dev. Biol.* **155,** 324–336
12. Culty, M., Nguyen, H. A., and Underhill, C. B. (1992) *J. Cell Biol.* **116,** 1055–1062
13. Culty, M., Shizari, M., Thompson, E. W., and Underhill, C. B. (1994) *J. Cell. Physiol.* **160,** 275–286
14. Zhou, B., Weigel, J. A., Fauss, L., and Weigel, P. H. (2000) *J. Biol. Chem.* **275,** 37733–37741
15. Banerji, S., Ni, J., Wang, S. X., Clasper, S., Su, J., Tammi, R., Jones, M., and Jackson, D. G. (1999) *J. Cell Biol.* **144,** 789–801
16. Kaya, G., Rodriguez, I., Jorcano, J. L., Vassalli, P., and Stamenkovic, I. (1997) *Genes Dev.* **11,** 996–1007
17. Laurent, T. C., Fraser, J. R., Pertoft, H., and Smedsrød, B. (1986) *Biochem. J.* **234,** 653–658
18. Tammi, R., and Tammi, M. (1986) *J. Cell. Physiol.* **126,** 389–398
19. Ågren, U. M., Tammi, M., and Tammi, R. (1995) *J. Cell. Physiol.* **164,** 240–248
20. Tammi, R., Säämänen, A. M., Maibach, H. I., and Tammi, M. (1991) *J. Invest. Dermatol.* **97,** 126–130
21. Tammi, R. H., Tammi, M. I., Hascall, V. C., Hogg, M., Pasonen, S., and MacCallum, D. K. (2000) *Histochem. Cell Biol.* **113,** 265–277
22. Tuhkanen, A. L., Tammi, M., and Tammi, R. (1997) *J. Invest. Dermatol.* **109,** 213–218
23. Tammi, R., MacCallum, D., Hascall, V. C., Pienimäki, J. P., Hyttinen, M., and Tammi, M. (1998) *J. Biol. Chem.* **273,** 28878–28888
24. Evanko, S. P., and Wight, T. N. (1999) *J. Histochem. Cytochem.* **47,** 1331–1342
25. Collis, L., Hall, C., Lange, L., Ziebell, M., Prestwich, R., and Turley, E. A. (1998) *FEBS Lett.* **440,** 444–449
26. MacCallum, D. K., and Lillie, J. H. (1990) *Skin Pharmacol.* **3,** 86–96
27. Baden, H. P., and Kubilus, J. (1983) *J. Invest. Dermatol.* **80,** 124–130
28. Lesley, J., Hascall, V. C., Tammi, M., and Hyman, R. (2000) *J. Biol. Chem.* **275,** 26967–26975
29. Oka, J. A., Christensen, M. D., and Weigel, P. H. (1989) *J. Biol. Chem.* **264,** 12016–12024
30. Schnitzer, J. E., Oh, P., Pinney, E., and Allard, J. (1994) *J. Cell Biol.* **127,** 1217–1232
31. West, M. A., Bretscher, M. S., and West, C. (1989) *J. Cell Biol.* **109,** 2731–2739
32. Dowrick, P., Kenworthy, P., McCann, B., and Warn, R. (1993) *Eur J. Cell Biol.* **61,** 44–53
33. Mellman, I., Fuchs, R., and Helenius, A. (1986) *Annu. Rev. Biochem.* **55,** 663–700
34. Cupers, P., Veithen, A., Hoeckstra, D., Baudhuin, P., and Courtoy, P. J. (1997) *Biochem. Biophys. Res. Commun.* **236,** 661–664
35. Yanagishita, M., Salustri, A., and Hascall, V. C. (1989) *Methods Enzymol.* **179,** 435–445
36. de Belder, A. N., and Wik, K. O. (1975) *Carbohydr. Res.* **44,** 251–257
37. Calabro, A., Benavides, M., Tammi, M., Hascall, V. C., and Midura, R. J. (2000) *Glycobiology* **10,** 273–281
38. Tammi, R., Ågren, U. M., Tuhkanen, A. L., and Tammi, M. (1994) *Prog. Histochem. Cytochem.* **29,** 1–81
39. Raucher, D., and Sheetz, M. P. (1999) *J. Cell Biol.* **144,** 497–506
40. Berger, M., Wetzler, E., August, J. T., and Tartakoff, A. M. (1994) *J. Clin. Invest.* **94,** 1113–1125
41. Araki, N., Johnson, M. T., and Swanson, J. A. (1996) *J. Cell Biol.* **135,** 1249–1260
42. Hopkins, C. R. (1983) *Cell* **35,** 321–330
43. Stenberg, P. E., Shuman, M. A., Levine, S. P., and Bainton, D. F. (1984) *Histochem. J.* **16,** 983–1001
44. Ripellino, J. A., Klinger, M. M., Margolis, R. U., and Margolis, R. K. (1985) *J. Histochem. Cytochem.* **33,** 1060–1066
45. Duden, R., Griffiths, G., Frank, R., Argos, P., and Kreis, T. (1991) *Cell* **64,** 649–665
46. Kuppusamy, U. R., Khoo, H. E., and Das, N. P. (1990) *Biochem. Pharmacol* **40,** 397–401
47. Meyers, S. A., Yudin, A. I., Cherr, G. N., Van deVoort, C. A., Myles, D. G., Primakoff, P., and Overstreet, J. W. (1997) *Mol. Reprod. Dev.* **46,** 392–400
48. Podyma, K. A., Yamagata, S., Sakata, K., and Yamagata, T. (1997) *Biochem. Biophys. Res. Commun.* **241,** 446–452
49. Dunn, W. A., Hubbard, A. L., and Aronson, N. N., Jr. (1980) *J. Biol. Chem.* **255,** 5971–5978
50. Yannariello-Brown, J., and Weigel, P. H. (1992) *Biochemistry* **31,** 576–584
51. Pienimäki, J.-P., Rilla, K., Fülöp, C., Sironen, R., Karvinen, S., Pasonen, S., Lammi, M. J., Tammi, R., Hascall, V. C., and Tammi, M. I. (2000) *J. Biol. Chem.* **276,** 20428–20435
52. Fujimoto, T., Nakade, S., Miyawaki, A., Mikoshiba, K., and Ogawa, K. (1992) *J. Cell Biol.* **119,** 1507–1513
53. Gassmann, M. G., and Werner, S. (2000) *Exp. Cell Res.* **258,** 23–32
54. Knudson, C. B. (1993) *J. Cell Biol.* **120,** 825–834
55. Underhill, C. B., Chi-Rosso, G., and Toole, B. P. (1983) *J. Biol. Chem.* **258,** 8086–8091
56. Oliferenko, S., Paiha, K., Harder, T., Gerke, V., Schwarzler, C., Schwarz, H., Beug, H., Günthert, U., and Huber, L. A. (1999) *J. Cell Biol.* **146,** 843–854
57. Perschl, A., Lesley, J., English, N., Trowbridge, I., and Hyman, R. (1995) *Eur. J. Immunol.* **25,** 495–501
58. Lesley, J., Kincade, P. W., and Hyman, R. (1993) *Eur. J. Immunol.* **23,** 1902–1909
59. Sleeman, J., Rudy, W., Hofmann, M., Moll, J., Herrlich, P., and Ponta, H. (1996) *J. Cell Biol.* **135,** 1139–1150
60. McGary, C. T., Raja, R. H., and Weigel, P. H. (1989) *Biochem. J.* **257,** 875–884
61. Knudson, W., Aguiar, D. J., Hua, Q., and Knudson, C. B. (1996) *Exp. Cell. Res.* **228,** 216–228
62. Poumay, Y., Leclercq-Smekens, M., Grailly, S., Degen, A., and Leloup, R. (1993) *Eur J. Cell Biol.* **60,** 12–20
63. Holm, P. K., Hansen, S. H., Sandvig, K. K., and vanDeurs, B. (1993) *Eur. J. Cell Biol.* **62,** 362–371
64. Watts, C., and Marsh, M. (1992) *J. Cell Sci.* **103,** 1–8
65. Lepperdinger, G., Strobl, B., and Kreil, G. (1998) *J. Biol. Chem.* **273,** 22466–22470
66. Yanagishita, M. (1992) *J. Biol. Chem.* **267,** 9505–9511

Smooth muscle cell adhesion on crosslinked hyaluronan gels

Anand Ramamurthi, Ivan Vesely
Department of Biomedical Engineering, ND20, Lerner Research Institute, The Cleveland Clinic Foundation,
9500 Euclid Avenue, Cleveland, Ohio 44120

Received 18 May 2001; revised 22 August 2001; accepted 30 August 2001
Published online 23 January 2002

Abstract: Hyaluronic acid (HA)-based polymers (hylans) are highly biocompatible and can be structurally modified to obtain desired mechanical properties. This study evaluated divinyl sulfone-crosslinked solid and particulate hylans as cellular scaffolds. These two hylan types differ in surface characteristics, mode of preparation, HA content, and extent of crosslinking. Neonatal rat aortic smooth muscle cells were cultured on hylan gels coated with matrix factors including collagen I, ECM gel, laminin, and fibronectin and on uncoated controls for ≤4 weeks. Cell attachment was sparse on uncoated controls but significantly enhanced on coated gels. Cell morphology was influenced by the identity of the matrix factors coated and the surface topography of the hylan gels. Cells attached to coated particulate gels appeared either highly spread (collagen, fibronectin) or irregularly shaped (ECM gel, laminin). Cells on laminin and fibronectin-coated solid gels were rounded and nonproliferative. Cells proliferated most rapidly on ECM gel-coated gels. The uneven surface of particulate gels induced more protein deposition and the subsequent attachment and active proliferation of cells. This study shows that surface texturizing and subsequent surface treatment with matrix factors enhances cell attachment and proliferation of hylans. These results are useful toward developing bioengineered materials based on cell-hylan composites. © 2002 John Wiley & Sons, Inc. J Biomed Mater Res 60: 196–205, 2002

Key words: hylan; hyaluronan; divinyl sulfone; cell attachment and growth; hydrogels

INTRODUCTION

The principles of tissue engineering have been demonstrated in applications such as skin,[1] blood vessels,[2] and heart valve leaflets.[3] Depending on the application, the selection criteria for an appropriate scaffold may include biocompatibility, mechanical properties such as stiffness, elasticity, failure strength, durability, and biodegradability. To become populated with cells and integrate into the underlying tissue, the scaffold must stimulate cell attachment, proliferation, and migration. The cellular response may be modulated by coating the scaffold with extracellular matrix proteins or by immobilizing adhesion factors or cell receptor peptide sequences on the scaffold surface.[4]

One of the many candidate materials considered for tissue engineering applications has been hyaluronan.[5] Hyaluronan has been shown to have excellent potential as a biomaterial since it can be chemically and structurally modified to suit the desired application. Hylan, the crosslinked form of hyaluronan, is highly biocompatible and does not elicit a foreign-body reaction.[6–8] Several methods for derivatizing and crosslinking hyaluronan have been documented previously.[9,10] Weakly crosslinked hylans are used widely as viscoelastic supplements in the vitreous of the eye[11] and more highly crosslinked varieties are used as tissue spacers to reduce adhesions following surgery.[12] A number of different crosslinking reagents involving hydrazides,[13] carbodiimides,[14] and esters[15] have been documented. Balazs et al.[16] used and documented a novel technology for crosslinking hyaluronan using divinyl sulfone (DVS). DVS and its degradation products are nontoxic when fully reacted with hyaluronan.[17] Crosslinking imparts structural strength and greater permanency to the hyaluronan gel and is necessary for its use as a cellular scaffold for tissue engineering applications, particularly at sites of limited remodeling, such as the aortic valve cusp. Although biodegradable hyaluronan sponges seeded

---

Correspondence to: I. Vesely; e-mail: vesely@bme.ri.ccf.org

Contract grant sponsor: United States Department of Defense; contract grant number: DAMD17-99-1-9475.

Contract grant sponsor: postdoctoral fellowship from the American Heart Association; contract grant number: 0020393B.

© 2002 John Wiley & Sons, Inc.
DOI 10.1002/jbm.10061

with mesenchymal progenitor cells have been used for tissue-engineered repair of bone and cartilage,[18] very little information is available regarding the attachment and subsequent viability of cells cultured on highly crosslinked hylan gels.[19]

Our long-term goal is to develop a cell-hylan composite material, wherein the hylan scaffold is structurally reinforced by collagen and elastin synthesized by attached cells. The objectives of the current study were to investigate the parameters necessary for the attachment of neonatal rat aortic smooth muscle cells to the surface of DVS-crosslinked hylan gels of different formulations and surface properties. Cell seeding is necessary to enable complete integration of the scaffold material with native tissue upon implantation. The information obtained through this study will help in the selection of surface topography, gel formulation, and possible surface modification that would maximize cell attachment to hylan gels.

MATERIALS AND METHODS

Neonatal rat aortic smooth muscle cells were selected for this study because they synthesize the structural extracellular matrix proteins collagen and elastin[20] in much larger quantities than most cell types and even adult rat aortic smooth muscle cells.[21] Smooth muscle cells were seeded onto hylan gels of two different formulations, which were either uncoated (controls) or coated with cell-binding matrix factors. The proliferation of attached cells on hylan gels was estimated weekly over a 4-week period using a colorimetric cell attachment assay. Cellular DNA was also quantified to further corroborate results of the above assay. Immunofluorescence microscopy was used to determine if cell attachment on different hylan types was influenced by differences in the amount of adhesion factors actually bound to the substrate surface. The Biological Resources Unit at the Cleveland Clinic Foundation approved all animal procedures used in this study. NIH guidelines for the care and use of laboratory animals have been observed.

Materials

The hylan gels used in this study were obtained from Biomatrix, Inc. (Ridgefield, NJ) and consisted of long-chain hyaluronic acid crosslinked with DVS. All gels were prepared from high-molecular-weight (>2 × 10^6) hyaluronan isolated from rooster combs. In all crosslinked gels, the ratio of hyaluronan to DVS was approximately 4:1 by weight. To investigate the effects of surface texture, two different gel formulations were tested. One was prepared originally as an optically clear, smooth, and highly hydrated solid gel; the other was a particulate film. Particulate gels were prepared by pulverizing the solid gel, beating it into a sheet, hydrating the sample, and then dehydrating it yet again. The gels were prepared crosslinked with DVS in 1*M* NaOH (pH 12.0) at 4°C and allowed to gel for 2 h. Gels were equilibrated in physiologic saline to remove DVS before use. The particulate gels had crosslinked hyaluronan microparticles with a diameter between 460 and 920 μm. The films were hydrated before use and swelled roughly 12-fold in volume. The final water content of the solid gels was greater than that of the particulate gels. Hydrated solid and particulate gels contained 4 and 6.7% (w/w) of HA, respectively. The hydrated gels varied from 2 to 7 mm in thickness. The optical characteristics of the two formulations indicated that the surface of solid gels is much smoother than that of particulate gels. Gels were steam sterilized at 120°C for 15 min before their use for cell culture. Steam sterilization did not have any impact on the handling properties of the hylan gels.

Preparation and coating of cell adhesion (matrix) factors

To determine if surface modification enhanced cell attachment, hylan gels were either precoated with cell-binding matrix factors such as collagen (type I, from rat tail), extracellular matrix (ECM) gel (from mouse sarcoma), laminin, and fibronectin from bovine plasma) or were left uncoated (controls). All matrix factors, except collagen, were purchased from Sigma Chemicals (St. Louis, MO). Acid-soluble collagen (3.63 mg/ml in 0.2*M* acetic acid) was procured from Collaborative Biomedical Products (Bedford, MA). Stock solutions were diluted with either 1% (v/v) PBS (collagen and fibronectin) or with serum-free culture medium (ECM gel). For each surface treatment, three different concentrations of factors were used to prepare coating suspensions. Collagen and fibronectin suspensions contained 30, 50, or 100 μg of matrix factor, whereas laminin and ECM gel suspensions contained 10, 30, or 50 μg of matrix factor. Coating suspensions were overlaid on circular disks of hylan (area = 1.9 cm^2) and incubated in a humid atmosphere at 37°C for 5 h. The hylans were subsequently rinsed with PBS for 5 min to remove unbound factors.

Cell isolation and culture

Neonatal rat smooth muscle cells were isolated from the aortas of 1- to 3-day-old rat pups using methods adapted from Oakes et al.[22] Briefly, aortas from 20 Sprague-Dawley rat pups were excised under sterile conditions. The aortas were opened longitudinally in sterile PBS (with 2 m*M* Ca^{2+}, 4°C) and digested with 2 ml of type II collagenase (2 mg/mL in serum-free medium; Worthington Chemical Corporation, Lakewood, NJ) for 10 min at 37°C. Three milliliters of Dulbecco's modified Eagle's medium with F-12 supplement (DMEM-F12; Life Technologies, Grand Island, NY), pH 7.3, containing 10% fetal bovine serum (FBS), was added to the digested segments. Segments of aorta were stripped of surface endothelium by shearing, minced into 0.5-mm-long pieces, and then transferred to a petri dish prewetted with sterile culture medium. After 1 week, explants were removed, and the primary cells were cultured to confluence in 5 mL of medium per 100-mm dish.

Primary cells were trypsinized (0.25% trypsin/0.1% EDTA; Life Technologies) centrifuged at 500 × *g* for 10 min, and the pellet was resuspended in 2 mL of culture medium to disperse cells for counting. Cells were seeded at a count of 1 × 10^6 cells per 75-cm^2 flask (passage 1). Subsequent passages were typically made at 1-week intervals. The culture medium was replaced twice weekly. Passage 6 cells were seeded on to the hylan gels. In preparation for cell culture, solid and particulate hylan gels were equilibrated overnight with serum-free culture medium.

Neonatal rat aortic smooth muscle cells were seeded onto coated and uncoated hylan gel samples that occupied the entire area of wells in a 24-well tissue culture plate (1.9 cm^2). Each well was seeded with 2 × 10^5 cells and initially incubated with a minimal volume (200 μL) of DMEM-F12 (containing 10% FBS and 1% penicillin-streptomycin) per well, to facilitate cell attachment. Two hours after seeding, the volume of the medium was increased to 1000 μL per well. Cells were cultured on the hylans for 7 to 28 days. All experimental trials were performed in triplicate. The culture medium was changed twice weekly for up to 3 weeks of culture and more often thereafter.

Cell attachment and proliferation

MTT assay

Cell attachment and subsequent proliferation on hylans was assessed quantitatively using the colorimetric MTT assay, described previously by Denizot and Lang.[23] The MTT reagent is reduced by the mitochondria of live attached cells to yield a blue formazan product, which can be measured. The number of live, attached cells on each set of samples was quantified at 7, 14, 21, and 28 days, respectively, after seeding. At the end of the culture period, medium was aspirated from the wells, and the hylans with adherent cells were transferred to fresh wells. Hylans were briefly rinsed with 1% (v/v) PBS to remove unattached cells. One milliliter of 2-(4,5-dimethylthiazol-2-yl)-2,5-diphenyl tetrazolium bromide (MTT) reagent (1 mg/mL in phenol red-free DMEM-F12) was added to each well containing hylan. Samples were incubated for 3 h at 37°C, and all the dye was aspirated. Each sample was overlaid with 1 mm of *n*-propanol and mixed for 1 h on a rotary shaker (Labline Instruments, Inc., Melrose Park, IL). The formazan product produced by cells was extracted by the propanol, 100 μL of the extract was pipetted into micro-well plates, and the absorbance was measured at

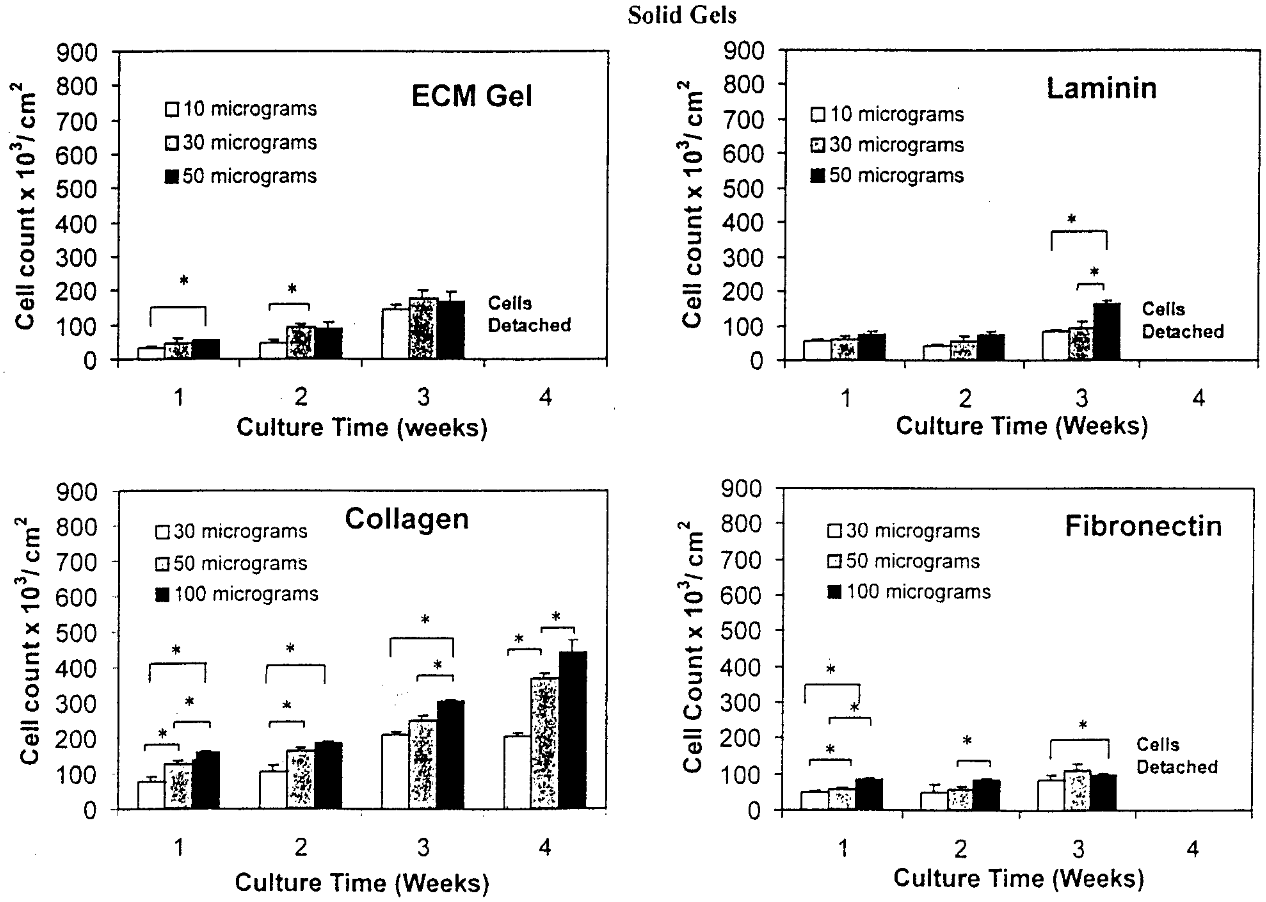

Figure 1. Cell attachment on solid hylan gels, quantified by the MTT Assay. Gels were precoated with matrix factors to facilitate cell attachment. Results indicate mean ± standard deviation of the attached cell count on 1.9 cm^2 of gel surface (n = 3; $^*p < 0.05$).

$\lambda = 550$ nm. Background absorbance from control wells containing no cells was subtracted from other absorbance measurements. A calibration was also performed simultaneously with the assay at each time point to determine the absorbance units per cell. For calibrations, between 1×10^4 and 3×10^5 cells were seeded per well. Wells were previously coated with 1 mg/ml of collagen type I in order to maximize the number of seeded cells that would attach to the substratum. Cells were allowed to attach overnight before they were assayed.

DNA assay

The MTT assay is a standardized method for quantifying cell attachment but can be biased by errors in calibration and in reagent composition. Thus, a quantitative assay of the total DNA content of the culture was performed to confirm the results of the above assay. This biochemical quantification of DNA was based on the assumption that for this cell type, the amount of cellular DNA would not change during the culture period.

Hylans with adherent cell layers were transferred carefully to fresh wells, gently rinsed with 1% (v/v) PBS, overlaid with 1 mL of 0.25% trypsin/0.1% EDTA per well, and incubated at 37°C for 10 min. Cells on collagen-coated gels were disrupted with trypsin-EDTA containing collagenase at a concentration of 2 mg/mL and 2 m*M* of Ca^{2+} as $CaCl_2$ over 10 min at 37°C and scraped off the gels. The wash was centrifuged, and the cell pellet resuspended in Pi buffer [50 m*M* Na_2HPO_4, 2 m*M* EDTA, 0.02% Na azide, pH 7.4]. The cell count in a 50-μL aliquot of the suspension was determined using a hemocytometer. The remaining suspension was sonicated for 6 min in ice, and DNA in the homogenate was measured by the fluorescent DNA assay described by Labarca and Paigen.[24]

Immunochemistry

Immunofluorescence microscopy was used to determine if collagen and fibronectin coated similarly on both solid and particulate hylans. Hylan samples in a 24-well plate were overlaid with 100 μL of PBS containing 100 μg of matrix factor, allowed to incubate overnight at 37°C, and then rinsed twice with PBS (1×) at room temperature. Nonspecific labeling by the primary antibody was blocked by incubating with a limited volume of PBS containing 5% (v/v) goat serum (Sigma Chemicals), for 20 min at 37°C. The samples were then incubated with 200 μL of PBS containing 5% (v/v) goat serum and polyclonal rabbit anti-(bovine fibronectin)

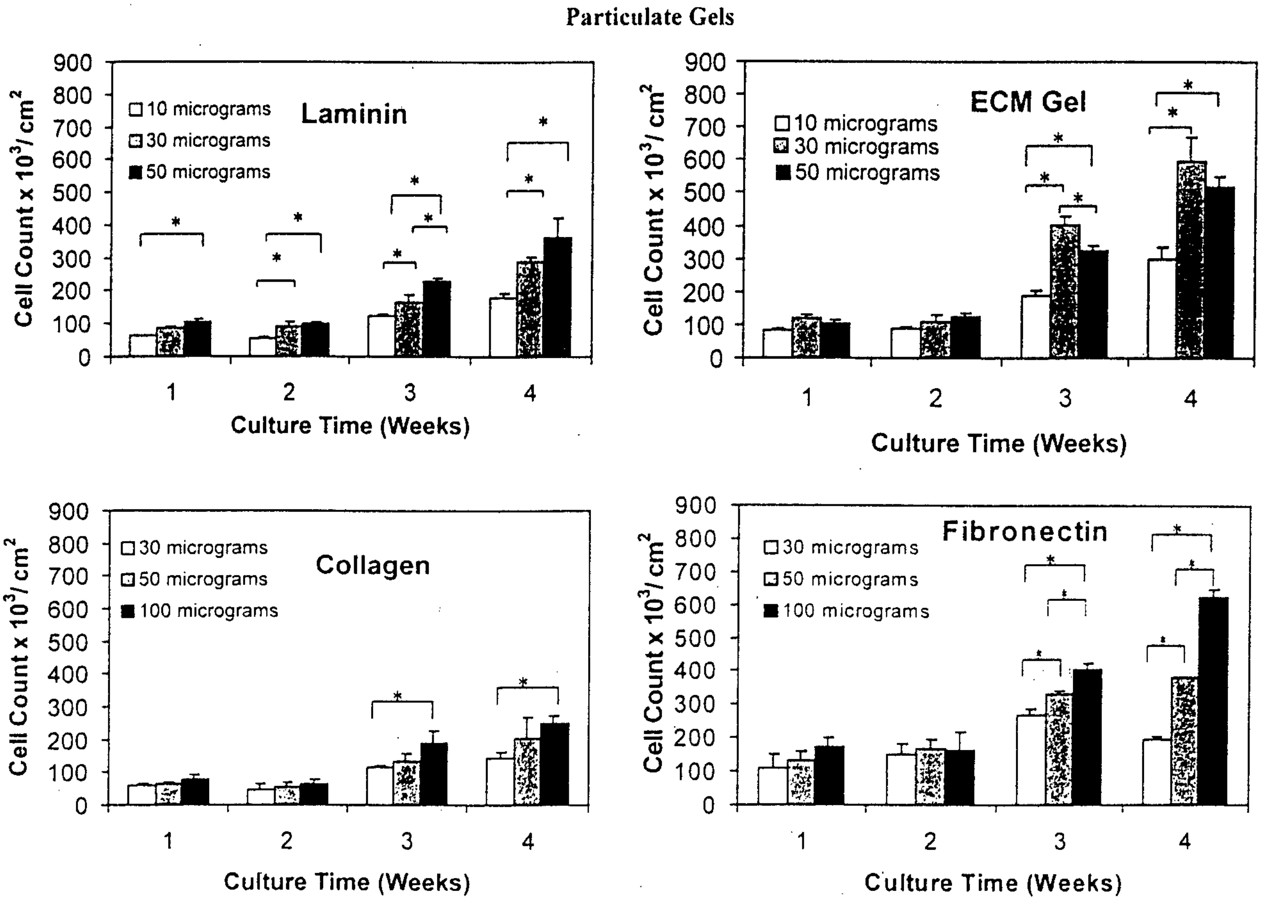

Figure 2. Cell attachment on particulate hylans, quantified by the MTT Assay. Gels were precoated with matrix factors to facilitate cell attachment. Results indicate mean ± standard deviation of the attached cell count on 1.9 cm^2 of gel surface ($n = 3$; $^*p < 0.05$).

TABLE I
Effect of Coated Amounts of Attachment Factors on Cell Attachment on Hylan Gels[a]

Attachment Factor	A Minimum Coated Weight (μg)	B Coated weight (μg)	Attached Cells$_B$/ Attached Cells$_A$	
			Solids	Particulates
Collagen I	30	30	1.0	1.0
		50	1.6 ± 0.3	1.2 ± 0.2
		100	1.9 ± 0.3	1.7 ± 0.4
Matrigel	10	10	1.0	1.0
		30	1.8 ± 0.6	1.7 ± 0.4
		50	1.5 ± 0.3	1.5 ± 0.2
Laminin	10	10	1.0	1.0
		30	1.2 ± 0.1	1.5 ± 0.2
		50	1.7 ± 0.3	1.9 ± 0.1
Fibronectin	30	30	1.0	1.0
		50	1.2 ± 0.1	1.4 ± 0.4
		100	1.5 ± 0.3	1.8 ± 0.9

[a] Weights indicated refer to amounts in the bulk coating suspension. Shown are the mean ± standard deviation of attached cell counts expressed relative to the number of cells attached on gels coated from the least concentrated suspensions (n = 3). Values were averaged over 3 weeks for solid gels and 4 weeks for particulate gels. The area of test samples was 1.9 cm^2.

antibody or polyclonal rabbit anti-(rat collagen I) antibody (Chemicon International, Inc., Temecula, CA), as applicable. Primary antibodies were diluted 100:1 in PBS. Labeling was carried out for 1 h in the dark at room temperature. Control samples were not treated with the primary antibody. The hylans were then rinsed gently with PBS three times and labeled in the dark with Alexa-594 goat anti-rabbit secondary antibody (Molecular Probes, Eugene, OR), diluted 500:1 in a PBS containing 5% (v/v) goat serum. After gentle rinsing with PBS, the samples were transferred to a slide and observed using a fluorescence microscope (Model DMR; Leica Microsystems, Inc., Bannockburn, IL).

Statistical analysis

To determine the significance of the observed differences in cell attachment on hylans, the Student's *t* test was employed using Microsoft Excel's statistical function for *t* tests, assuming unequal variance and two-tailed distribution. All results were reported as mean ± standard deviation. Differences were considered statistically significant at $p < 0.05$.

RESULTS

Cell attachment on uncoated control solid or particulate hylans was sparse. Significant cell attachment occurred only when the hylans were coated with matrix factors. Once attached, the cells proliferated over 4-week period. However, cells cultured on solid hylan gels coated with ECM gel, laminin, or fibronectin were not analyzed beyond 3 weeks because of detachment of confluent cell layers during routine feeding. Very few cells were left attached on the surface.

Cell attachment

MTT assay

Initial cell attachment on hylan gels and their subsequent proliferation depended on the types and amounts of coated matrix factors and on culture time. Collagen was most appropriate as a coating agent, because cells attached on both solid and particulate collagen-coated hylans and maintained their normal proliferative phenotype. At 1 week, cell attachment was similar for both solid and particulate hylans for each type of treatment (Figs. 1 and 2). The different stimuli that the various matrix factors produced were more apparent after 1 week of culture. ECM gel coatings stimulated cell proliferation the most, on both solid and particulate gels. Cell attachment on solid and particulate hylans was 3.7 and 4.5 times greater at 3 and 4 weeks, respectively, than it was at 1 week. On solid gels, cell attachment was greatest on gels coated with collagen, regardless of culture duration. On particulate gels, ECM gel coatings stimulated the greatest cell attachment.

Generally, a greater amount of matrix factor used produced greater cell attachment at each time point,

TABLE II
Agreement of Attached Cell Counts Determined via the MTT Assay and by Hemocytometry[a]

Adhesion Factor	Culture Time (weeks)	Cell Count × 10^5/cm^2	
		MTT	Hemocytometer
Collagen I	1	1.59 ± 0.04	1.44 ± 0.00
	2	1.85 ± 0.05	1.80 ± 0.00
	3	3.05 ± 0.02	1.93 ± 0.10
	4	4.38 ± 0.03	3.11 ± 0.19
Matrigel	1	0.54 ± 0.03	0.58 ± 0.00
	2	0.90 ± 0.17	0.93 ± 0.00
	3	1.67 ± 0.31	1.42 ± 0.00
Laminin	1	0.74± 0.11	0.33 ± 0.00
	2	0.75 ± 0.08	0.82 ± 0.10
	3	1.63 ± 0.09	0.81 ± 0.10
Fibronectin	1	0.84 ± 0.06	0.47 ± 0.00
	2	0.84 ± 0.11	1.10 ± 0.04
	3	0.98 ± 0.07	1.01 ± 0.09

[a] Results show the mean ± standard deviation of the number of attached cells on solid gels overlaid with 100 μg of collagen or fibronectin and 50 μg of ECM gel or laminin (n = 3). The culture area was 1.9 cm^2

although this trend was more pronounced after 3 weeks of culture (Fig. 2; Table I). The amount of adhesion factor used did not influence the rate at which cell number increased over time. Cell attachment on the ECM gel-coated particulate hylans was greatest for an intermediate coating weight of ECM gel (30 μg) and did not increase further for coatings deposited from more concentrated suspensions.

DNA assay

The hemocytometer cell count and the biochemical assay for cellular DNA content were performed to confirm the trends described above. In general, cell counts measured at each time point were similar via the MTT assay and hemocytometry (Table II). Cell counts obtained using hemocytometry were used to determine the average DNA per cell, and our value of 7.8 ± 1.2 pg of DNA per cell is in agreement with the accepted value of ~6 pg/cell.[24]

Active proliferation of the attached cell population was confirmed by an increase in DNA levels over time (Fig. 3). Cells attached on solid gels appear to have a short lag phase and then enter into the exponential growth phase within 2–3 days of seeding. Relative to 1 day of culture, cell counts after 1 week were 3.7 times greater for collagen, ECM gel, and laminin and 5.7 times greater for fibronectin. Cell counts and DNA levels reached a plateau at 7 and 14 days of culture, respectively. Cells cultured on laminin- and fibronectin-coated gels were not analyzed beyond 3 weeks because detachment of cell layers during routine medium change. Fibronectin coated on particulate gels induced a rapid increase in cell number and DNA levels after seeding, whereas all other coatings had a lag period of almost 7 days. Cell counts increased exponentially for a further 10–14 days before reaching a plateau. In the case of laminin- and fibronectin-coated

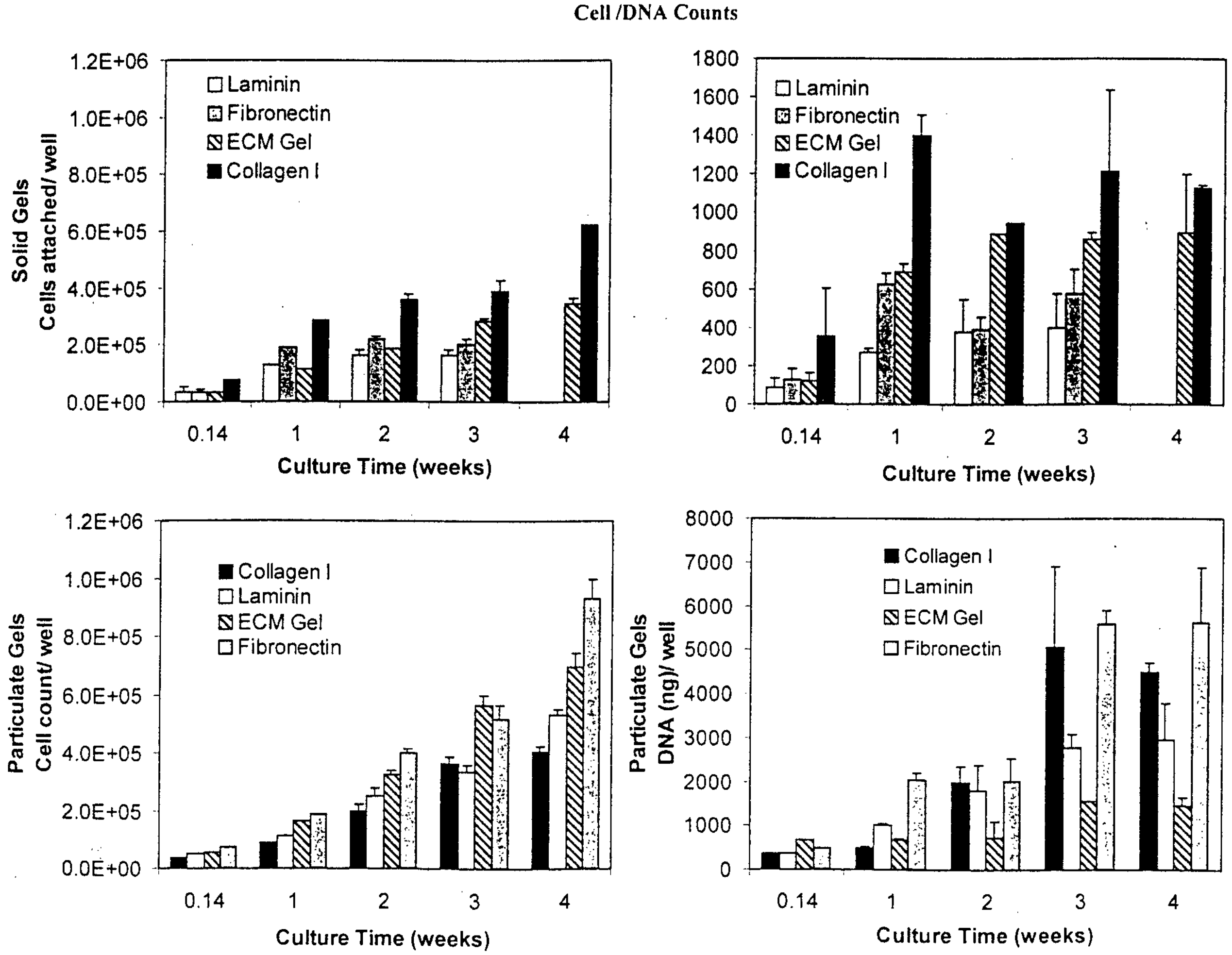

Figure 3. Proliferation on neonatal rat aortic smooth muscle cells on solid and particulate hylan gels expressed in terms of the total number of cells and cellular DNA. Cell counts were performed using a hemocytometer. Cells were cultured on gels (1.9 cm^2) coated with collagen I, ECM gel, laminin, or fibronectin. Values shown are mean ± standard deviation of three trials. The average DNA per cell was 7.8 ± 1.2 pg.

gels, cell number continued to increase over time, although DNA content leveled off around day 21.

Cell morphology

Cell morphology appeared to be influenced by both the identity of the matrix factors coated and the hylan type (Fig. 4). Cells attached on collagen-coated solid or particulate gels were highly elongated and were aligned along the direction of the collagen fibers. Cells attached on fibronectin-coated particulate gels were similarly greatly extended. Laminin and ECM gel coatings on particulate hylan gels induced the formation of dense cell clusters. Cells were irregularly shaped, similar to cells cultured on plastic petri dishes. Smooth muscle cells became attached to fibronectin- and laminin-coated solid gels but appeared mostly rounded, with a sparse distribution of spindle-shaped cells. This trend was maintained for up to 3 weeks of culture. In all cases, cells attached to the coated gels within a few hours of seeding. Particulate gels, regardless of their treatment, and collagen- and ECM gel-coated solid gels were confluent with cells within 2 weeks of seeding (Fig. 4).

The sparse attachment and the rounded morphology of cells of fibronectin- and laminin-coated solid gels contrasted sharply with irregularly shaped cells cultured to confluence on similarly treated particulate gels. Immunolabeling methods were used to explain this phenomenon. Collagen and fibronectin were coated on both solid and particulate gels and visualized using immunolabeling techniques. Collagen I deposited uniformly on both solid and particulate gels forming extensive surface sheets that were folded up on themselves at the edges [Fig. 5(A,B)]. Fibronectin, however, adsorbed sparsely to solid hylan gels but coated particulate gels uniformly [Fig. 5(C,D)]. These results explain why fibronectin-coated solid gels supported fewer cells than similarly treated particulate gels, whereas collagen coating stimulated cell attachment and proliferation well on both solid and particulate hylans.

DISCUSSION

This study has therefore demonstrated that cells attach and proliferate well on particulate hylan gels irrespective of the surface treatment, but do so on solid

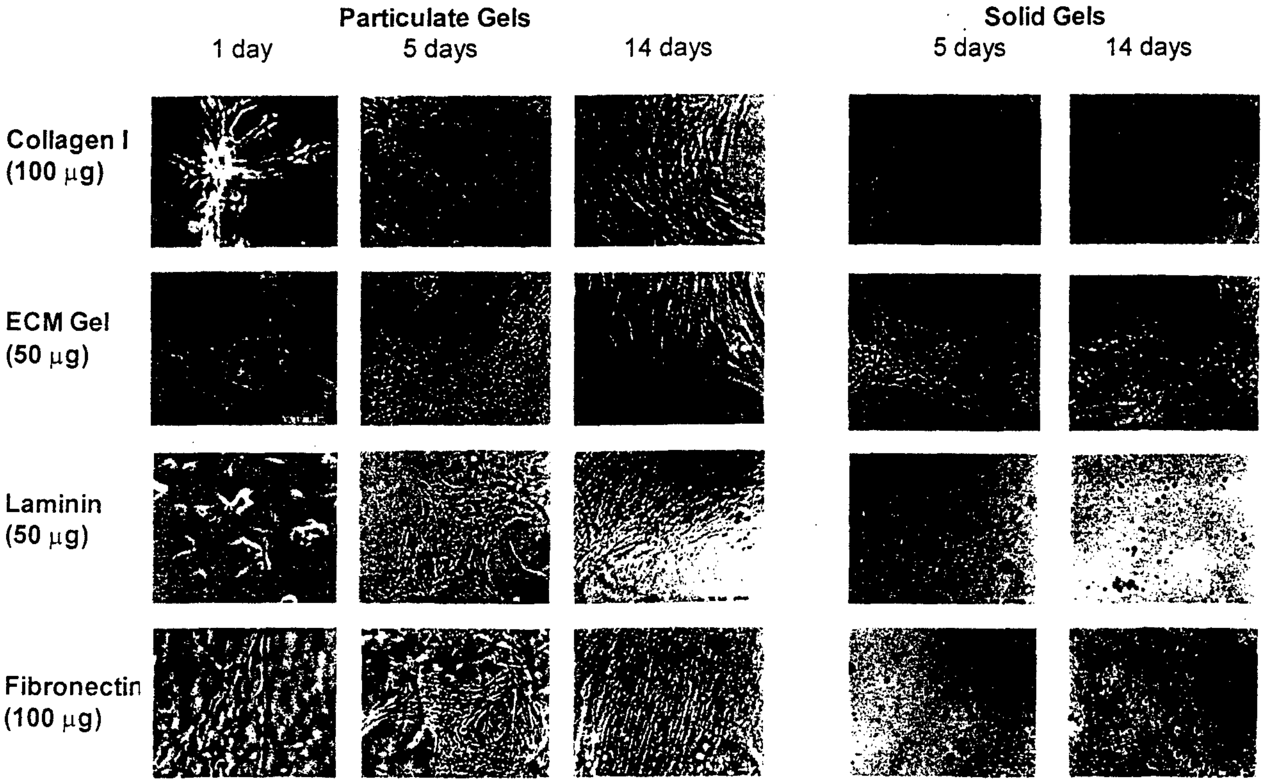

Figure 4. Neonatal rat aortic smooth muscle cells (NRASMC) cultured on particulate hylan gels, shown at 1, 5, and 14 days after seeding. Gel surfaces were coated with adhesion proteins to facilitate cell attachment. Note the spreading and proliferation of cells on particulate gels. Also shown are cells on solid gels at 5 and 14 days after seeding (right panels). Note the presence of rounded and nonproliferative cells on laminin- and fibronectin-coated solid gels. Culture area was 1.9 cm^2. Magnification, ×40.

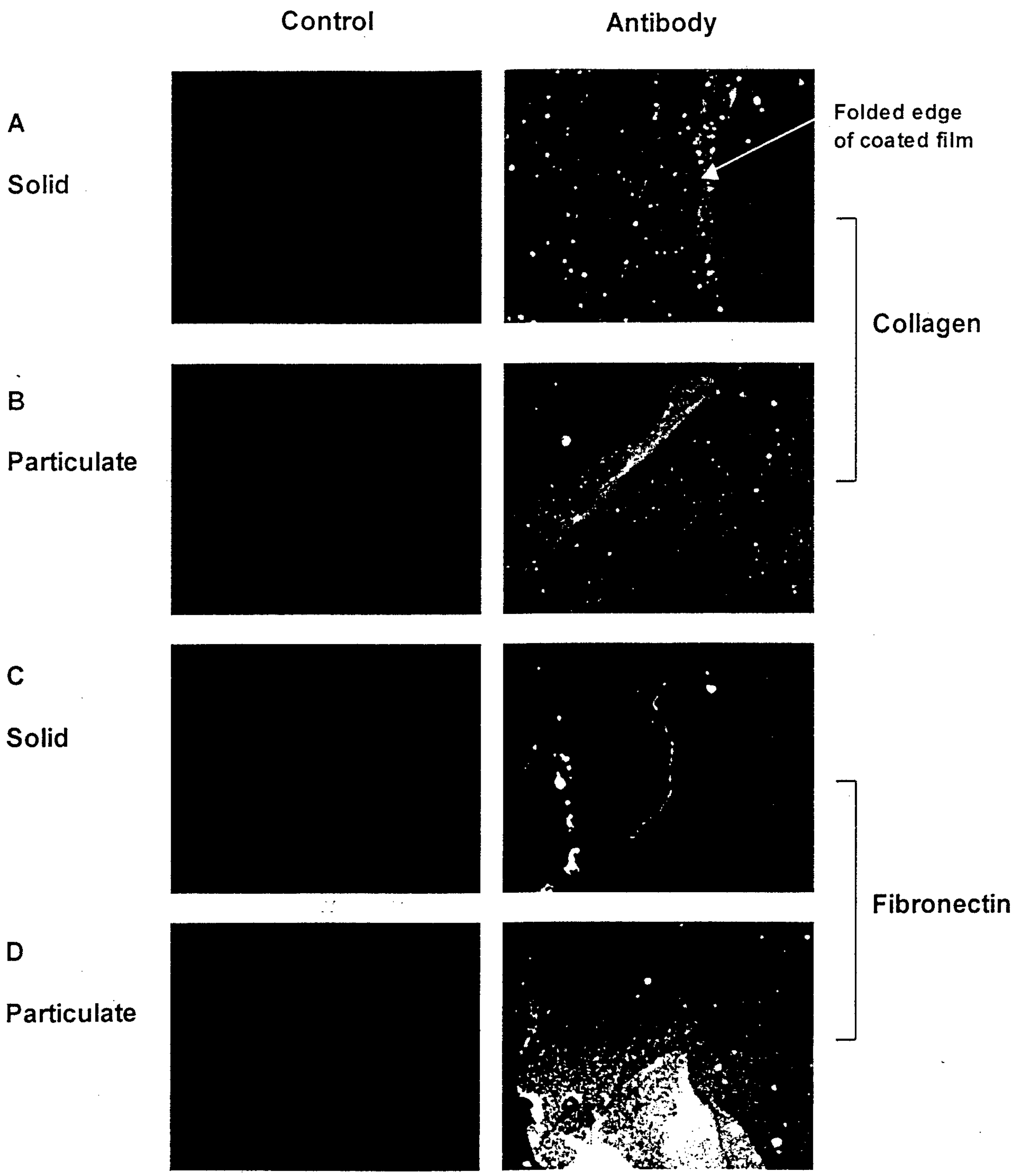

Figure 5. Coating of cell adhesion factors on solid (A,C) and particulate (B,D) hylan gels. Gels were overlaid with 100 μg of collagen type I (rat tail; A,B) or fibronectin (from bovine plasma; C,D). Noncontrols were treated with rabbit polyclonal primary antibodies against bovine fibronectin and rat collagen I, respectively. Adhesion proteins were visualized with a second antibody conjugated with Texas-red fluorophore ($\lambda = 594$ nm). Untreated control gels were not treated with primary antibodies. Note the uniform coating of collagen on both solid (A) and particulate (B) gels and the sparse coating of fibronectin on the solid gel (C). This may explain the poor adherence of cells to fibronectin-coated solid gels. Gels were imaged at their edge to clearly distinguish between background fluorescence (if any) and fluorescence from the protein coat.

gels only if the gels are coated with collagen or ECM gel. This study has also shown that solid and particulate hylan gels coated from identical coating suspensions induced significantly different levels of cell attachment. These results suggest that the bulk and surface properties of hylans influence the deposition of matrix factors and hence the subsequent attachment of cells. One factor that could influence cell attachment is surface charge and hydrophilicity. Negatively charged cells adhere far less strongly to substrates containing acidic or neutral groups than to those with basic (positively charged) groups.[25] In addition, the DVS-crosslinked hylan gels are very hydrophilic in nature. Previous studies have shown that extremely hydrophilic surfaces are thermodynamically unfavorable for cell attachment and protein deposition.[26] This explains why cells do not attach to untreated hylan gels.

A second factor likely to influence both cell attachment and phenotype is gel surface topography. Previous studies[27] showed that surface roughness, both at the level of cell adhesion (1 μm) and the level of protein adsorption (50 nm), can stimulate cell attachment. A detailed investigation into the surface features of the hylan gels is too extensive to be included in this study. However, even at the macroscopic level, solid gel surfaces appear much smoother and more uniform than particulate hylans.

The sparse cell attachment to uncoated controls (both particulate and solid gels) suggests that cell interaction with the highly anionic hylan surface is too weak to be influenced by microscale surface texturing. However, surface roughness may enhance the deposition of matrix factors, which will in turn induce greater cell attachment and proliferation. The particulate gels were clearly rougher than the solid gels, when examined optically.

The significance of this work is that we have determined that appropriately modified hydrogels based on DVS-crosslinked hyaluronan (hylans) can be used as cellular scaffolds for tissue engineering applications. This study has also shown that hylan gels with similar compositions, but different preparation, can elicit very different responses to protein deposition and cell attachment. Our results suggest that surface texturizing of gels could be adopted as a means of modulating the cellular response to the material by influencing protein deposition. Since physically adsorbed protein layers can potentially be detached by shear, a logical solution would be to chemically attach the cell-binding peptides to the gel. The results of the study are therefore important in the selection of the most appropriate amino acid sequences for enhancing cell attachment and enabling the formation of a permanent cell layer on the gel surface.

The authors thank Dr. Endre Balazs formerly of Biomatrix, Inc., and currently at the Matrix Biology Institute, Ridgefield, NJ, for providing hylan gels used in this study and Dr. Vincent C. Hascall, The Cleveland Clinic Foundation, for his valuable input to this study.

References

1. Yamada N, Uchinuma E, Kuroyanagi Y. Clinical evaluation of an allogeneic cultured dermal substitute composed of fibroblasts within a spongy collagen matrix. Scand J Plast Reconstr Surg Hand Surg 1999;33:147–154.
2. Stock UA, Nagashima M, Khalil PN, Nollert GD, Herden T, Sperling JS, Moran A, Lien J, Martin DP, Schoen FJ, Vacanti JP, Mayer JE Jr. Tissue-engineered valved conduits in the pulmonary circulation. J Thorac Cardiovasc Surg 2000;119(4 Pt 1): 732–740.
3. Sodian R, Sperling JS, Martin DP, Egozy A, Stock U, Mayer JE Jr, Vacanti JP. Fabrication of a trileaflet heart valve scaffold from a polyhydroxyalkanoate biopolyester for use in tissue engineering. Tissue Eng 2000;6:183–188.
4. Quirk RA, Chan WC, Davies MC, Tendler SJ, Shakesheff KM. Poly(L-lysine)-GRGDS as a biomimetic surface modifier for poly(lactic acid). Biomaterials 2001;22:865–872.
5. Angele P, Kujat R, Nerlich M, Yoo J, Goldberg V, Johnstone B. Engineering of osteochondral tissue with bone marrow mesenchymal progenitor cells in a derivatized hyaluronan-gelatin composite sponge. Tissue Eng 1999;5:545–554.
6. Larsen NE, Pollak CT, Reiner K, Leshchiner E, Balazs EA. Hylan gel biomaterial: Dermal and immunologic compatibility. J Biomed Mater Res 1993;27:1129–1134.
7. Larsen NE, Leshchiner E, Balazs EA, Belmonte C. Biocompatibility of hylan polymers in various tissue compartments. In: Mikos AG, Leong KW, Yaszemski MJ, Tamada JA, Radomsky ML, editors. Polymers in medicine and pharmacy. Warrendale, PA: Materials Research Society; 1995. p 149–153.
8. Denlinger JL, Balazs EA. Replacement of liquid vitreous with sodium hyaluronate in monkeys. Short-term evaluation. Exp Eye Res 1980;3:81–99.
9. Bulpitt P, Aeschlimann D. New strategy for chemical modification of hyaluronic acid: Preparation of functionalized derivatives and their use in the formation of novel biocompatible hydrogels. J Biomed Mater Res 1999;47:152–169.
10. Tomihata K, Ikada Y. Preparation of cross-linked hyaluronic acid films of low water content. Biomaterials 1997;18:189–195.
11. Balazs EA, Denlinger JL. Clinical uses of hyaluronan. In: Evered D, Whelan J, editors. The biology of hyaluronan. CIBA Foundation Symposium 143. Chichester and New York: Wiley; 1989. p 265–280.
12. Piacquadio D, Jarcho M, Goltz R. Evaluation of hylan b gel as a soft-tissue augmentation implant material. J Am Acad Dermatol 1997;36:544–549.
13. Vercruysse KP, Marecak DM, Marecek JF, Prestwich GD. Synthesis and in vitro degradation of new polyvalent hydrazide cross-linked hydrogels of hyaluronic acid. Bioconjug Chem 1997;8:686–694.
14. Tomihata K, Ikada Y. Crosslinking of hyaluronic acid with water-soluble carbodiimide. J Biomed Mater Res 1997;37:243–251.
15. Mälson T, Lindqvist B. Crosslinked hyaluronate gels their use and method for producing them. U.S. Patent No. 5,783,691 (July 21, 1998).
16. Balazs EA, Leshchiner A. Crosslinked gels of hyaluronic acid and products containing such gels. U.S. Patent No. 4,582,865 (April 15, 1986).
17. Balazs EA, Leshchiner E, Larsen N, Band P. Hyaluronan biomaterials: medical applications. In: Wise et al., editors. Handbook of biomaterials and applications. New York: Marcel Dekker; 1995. p 2719–2741.
18. Solchaga LA, Dennis JE, Goldberg VM, Caplan AI. Hyaluronic acid-based polymers as cell carriers for tissue-engineered repair of bone and cartilage. J Orthop Res 1999;17:205–213.
19. Larsen NE, Lombard KM, Parent EG, Balazs EA. Effect of hylan on cartilage and chondrocyte cultures. J Orthoped Res 1992;10:23–32.

20. Oakes BW, Batty AC, Handley CJ. Biochemical and ultrastructural studies of the synthesis of elastin, proteoglycans, and collagen by neonatal rat aortic smooth muscle cells in tissue culture. Uppsala J Med Sci 1977;82:147–156.
21. Jones PA, Scott-Burden T, Gevers W. Glycoprotein, elastin, and collagen secretion by rat smooth muscle cells. Proc Natl Acad Sci USA 1979;76:353–357.
22. Oakes BW, Batty AC, Handley CJ, Sandberg LB. The synthesis of elastin, collagen, and glycosaminoglycans by high-density primary cultures of neonatal rat aortic smooth muscle. An ultrastructural and biochemical study. Eur J Cell Biol 1982;27:34–46.
23. Denizot F, Lang R. Rapid colorimetric assay for cell growth and survival. Modifications to the tetrazolium dye procedure giving improved sensitivity and reliability. J Immunol Methods 1986;89:271–277.
24. Labarca C, Paigen K. A simple, rapid, and sensitive DNA assay procedure. Anal Biochem 1980;102:344–352.
25. Koyano T, Minoura N, Nagura M, Kobayashi K. Attachment and growth of cultured fibroblast cells on PVA/chitosan-blended hydrogels. J Biomed Mater Res 1998;39:486–490.
26. Rowley JA, Madlambayan G, Mooney DJ. Alginate hydrogels as synthetic extracellular matrix materials. Biomaterials 1999; 20:45–53.
27. Zingg W, Neumann AW, Strong AB, Hum OS, Absolom DR. Effect of surface roughness on platelet adhesion under static and under flow conditions. Can J Surg 1982;25:16–19.

Ramamurthi A., and Vesely, I. "In vitro synthesis of elastin sheets on crosslinked hyaluronan gels for tissue engineering of aortic valves" 2nd Joint EMBS-BMES Conference, Houston, Texas, October 2002 (Accepted)

IN-VITRO SYNTHESIS OF ELASTIN SHEETS ON CROSSLINKED HYALURONAN GELS FOR TISSUE ENGINEERING OF AORTIC VALVES

A. Ramamurthi, I. Vesely

Department of Biomedical Engineering, The Cleveland Clinic Foundation, Cleveland, Ohio, USA

Abstract- **The complex triple-layered structure of aortic valve cusps is organized from the matrix components collagen, glycosaminoglycans, and elastin. Our approach to tissue engineering the aortic valve is to fabricate a functional composite tissue from each layer grown separately *in vitro*. The current work summarizes our efforts to fabricate, two of these layers namely, the viscoelastic spongiosa, and elastin-rich ventricularis.**

Keywords- **Aortic Valve, matrix, elastin, hyaluronan, hylan, cardiovascular, tissue engineering**

I. INTRODUCTION

Tissue-engineering (TE) of heart valves is a promising approach to overcome the deficiencies of currently available mechanical and bioprosthetic replacement devices. The rigidity of mechanical valves, their requirement for chronic anticoagulant therapy and the risk of sudden failure, are some of their undesirable characteristics. Bioprosthetic valves on the other hand have poor long-term durability due to tissue calcification and mechanical damage. Tissue-engineered aortic valves are not expected to have any of these problems. The TE of the aortic valve however presents its own set of challenges. Due to this limited remodeling in the aortic position, the conventional TE approach of culturing cells on a biodegradable scaffold *in vitro*, and subsequently regenerating a functional tissue *in vivo* is not expected to be appropriate for aortic valves. A more promising approach would be to fabricate the entire leaflet microstructure *in vitro* using matrix molecules and cells, so that the tissue might be functional immediately upon implantation.

The unique mechanical characteristics of native aortic valve cusps are a result of their complex multilayered morphology (Fig. 1). The fibrosa, composed mainly of collagen bundles, is the primary load-bearing layer of the tissue. The ventricularis contains elastin sheets and fibers [1] that keep the fibrosa in a compressed state. The central spongiosa layer contains glycosaminoglycans (GAGs) that keep the cusp hydrated, and permits shear between the fibrosa and ventricularis during tissue loading and unloading.

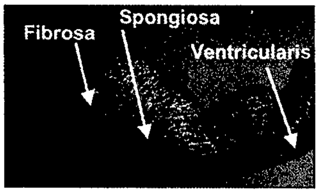

Figure1. Multilayered morphology of the aortic valve cusp.

Our approach to engineering of the aortic valve is to integrate the above essential components into a composite cusp, once each has been fabricated separately *in vitro*. The immediate goals of this project are to fabricate a spongiosa-like layer using hyaluronan, a GAG, and then stimulate cells seeded atop this layer to synthesize elastin sheets and fibers in a morphology similar to that of the ventricularis (Fig. 2).

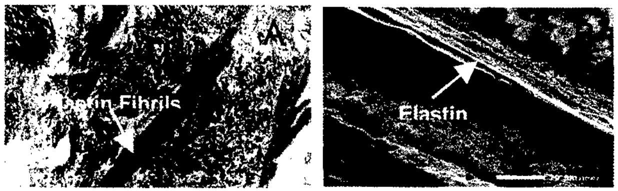

Figure 2. TEM (A) and SEM (B) images showing elastin organized into either fibers or sheets.

Hylauronan (HA), the material selected for replacing the spongiosa, is a major component of all connective tissues. It is a long chain GAG containing up to 25,000 alternating units of β-(1→4) 2-acetamido-2-deoxy-D-glucose and β-(1→3) D-glucuronic acid. The high purity of hyaluronan and its common structural identity across species contribute to its extremely low immunogenicity and antigenicity. Divinyl sulfone (DVS)-cross-linked derivatives of hyaluronan (hylans) are exceptional implant materials because they are highly biocompatible, non-antigenic and non-inflammatory [2]. The crosslinking chemistry of HA can be controlled to yield hylans with predictable mechanical properties. The biological activity of HA molecules in hylan gels are retained because the biologically active carboxyl groups are not involved in crosslinking [2].

The only limitation to the use of hylans as cell scaffolds are the highly anionic nature of the HA molecule and the very smooth gel surface, which are not conducive to cell attachment. However, in a previous study, we developed a method to enhance cell attachment and proliferation atop and within hylan gels. Irradiation of hylan gels with low-wavelength UV light for 48 hours was shown to texturize the gel surface with a ridged honeycomb pattern that provides sites of anchorage to the cells. When dehydrated prior to irradiation, the UV light also creates cracks through which cells can migrate into the gel. The enhanced cellular response to UV-modified gels could also be due to stimuli provided by the newly created HA fragments of various lengths. As a next step, we intend to use these novel, UV-altered hylan gels as scaffolds upon which cells can be made to synthesize elastin in the sheets and fibers observed in native valves. With this approach, we expect to develop a composite material that can replace both the spongiosa and ventricularis of the aortic valve cusp.

II. METHODOLOGY

Formulation and Modification of Hylan Gels

The hylan films used in this study were prepared using a method based on one previously patented by Balazs et al [2]. Briefly, 230 mg of NaHA (MW> 1.5×10^6) was mixed with 0.2 M NaOH, pH 13.0, at 4°C, crosslinked with 44 μl of DVS, cast as thin films, and allowed to gel for 2 hours. The HA film was rinsed overnight with distilled

Ramamurthi A., **and Vesely, I. "In vitro synthesis of elastin sheets on crosslinked hyaluronan gels for tissue engineering of aortic valves" 2nd Joint EMBS-BMES Conference, Houston, Texas, October 2002 (Accepted)**

water to remove unreacted DVS. For cell culture, the films were equilibrated with serum-free Dulbecco's Modified Eagle's Medium with an F-12 supplement (DMEM: F12) and then exposed to UV light (λ = 254 nm) for 48 hours in a biological hood. The films were kept hydrated at all times.

Cell Culture

Neonatal rat aortic smooth muscle cells were selected for study due to their demonstrated ability to prolifically synthesize elastin [3]. Cells (passages 6-8) suspended in DMEM: F12 (containing 10% FBS and 1% penicillin-streptomycin) were seeded atop the hylan films at a count of 4×10^6-cells/ gel (Culture area= 100 mm^2; n= 3) and cultured for up to 6 weeks.

Biochemical Assay for Elastin Synthesis

Cell layers atop hylan films were harvested and assayed for elastin at 2, 4, and 6 weeks of culture. Cell layers were trypsinized with 0.25% Trypsin-EDTA for 15 minutes, at 37°C, scraped off the films, and then centrifuged with culture medium to isolate a pellet containing hylan and cells. The pellet was dried in an oven at 110°C, weighed, and then re-hydrated with distilled water. After another cycle of centrifugation and drying, the pellet was digested with 0.1 M NaOH (98°C, 48 h). The long period of digestion was necessary to breakdown the large amount of crosslinked hylan. Matrix elastin alone survived digestion, and was pelleted, weighed, solubilized with oxalic acid (0.25 N, 95°C, 1 h, 3 cycles) and finally quantified using a dye-binding Fastin Assay (Accurate Scientific and Chemical, Westbury, NY). The digestate was also assayed to quantify any matrix elastin that was leached out during digestion.

Microscopy

Segments of hylan films (< 100 μm thin) with adherent cell layers (at 4 weeks) were immobilized on a steel holder and digested in 0.1 M NaOH (20 minutes, 75°C). Elastin surviving the digestion were frozen in a –80°C freezer overnight and then rapidly quenched in a bath of liquid N_2. Samples were lyophilized and then sputter-coated with gold for 90 s. Cell-free hylan films and detached 4 week-old cell layers from petri-dishes were also digested similarly and processed for SEM. For TEM, the cell layers were fixed in paraformaldehyde, post-fixed, dehydrated, embedded in a resin, and then cut longitudinally and stained. Cell-free irradiated hylan films and cell-seeded and non-irradiated hylan films were used as controls.

III. RESULTS

Elastin synthesized by cells atop irradiated hylan gels was incorporated into the extracellular matrix in increasing amounts over the period of culture (Figure 3). At, 2 weeks, all the elastin was retained in the matrix. However, 17 ± 10% and 20 ± 1% of the matrix elastin in the 4- and 6-week old cell layers respectively, were soluble in alkali. SEM of alkali-digested cell layers from petridishes, or atop hylan films both showed the presence of fenestrated sheets (likely elastin) and of fibrillar elastin networks (Fig. 4). TEM images show multiple layers of cells atop hylan films.

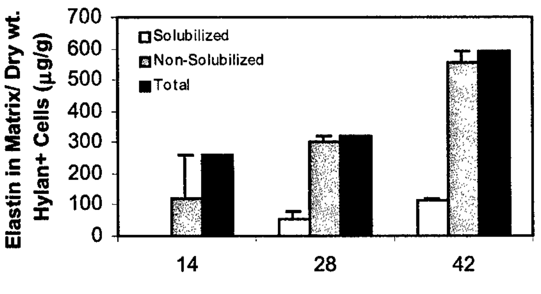

Figure 3. Elastin synthesis atop UV-irradiated hylan films

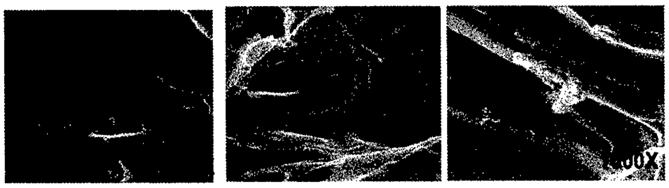

Figure 4. SEM images of elastin structures isolated by alkali-digestion of cell layers from petri-dishes (A) or hylan films (B, C). Fibrils, likely fibrillar elastin, were also seen (C).

At 2 weeks, small clumps of amorphous elastin were deposited between cells. Also, the beginnings of thin basal layer of matrix (likely elastin) were visible at the cell-hylan interface (Fig. 5A). At 4 weeks, a much greater amount of elastin was found distributed between cells. A thick, well-defined basal matrix layer was also laid down (Fig. 5B). Cell attachment and matrix was not observed on control hylan films.

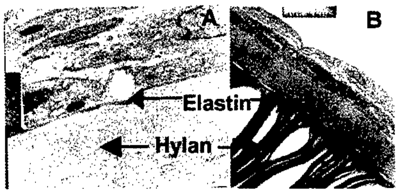

Figure 5. TEM images of elastin synthesized atop hylan films for (A) 2 wks, and (B) 6 wks of culture. Magnification: ×3000(A), ×8000 (B).

IV. DISCUSSION AND CONCLUSION

Our studies indicate that neonatal rat aortic smooth muscle cells synthesize a large amount of elastin within 2 weeks, when cultured atop irradiated hylan films. Although most of the elastin is present as sheets, some elastin fibrils were also seen. In future work, biochemical and mechanical stimuli will be provided to enhance elastin synthesis and obtain the desired ultrastructure. The study is promising towards the development of a TE aortic valve cusp.

REFERENCES

1. Scott M.J., and I. Vesely, *Morphology of porcine aortic valve cusp elastin.* J Heart Val Dis, 1996. 5(5): p464-71.
2. Balazs EA, Leshchiner A. *Crosslinked gels of hyaluronic acid and products containing such gels.* U.S. Patent No. 4,582,865 (April 15, 1986).
3. Oakes, B.E. et al., *The synthesis of elastin, collagen, and glycosaminoglycans by high density primary cultures of neonatal rat aortic smooth muscle. An ultrastructural and biochemical study.* Eur J Cell Biol, 1982. 27: p34-46.

DEVELOPING A COMPOSITE, TISSUE-ENGINEERED AORTIC VALVE

Ivan Vesely, Ph.D., Yaling Shi, M.S., Anand Ramamurthi, Ph.D.

Department of Biomedical Engineering, The Cleveland Clinic Foundation, Cleveland, Ohio, USA
vesely@bme.ri.ccf.org

INTRODUCTION

A tissue-engineered valve will need to incorporate the complex microstructure of the aortic valve if it is expected to offer durability comparable to that of conventional bioprosthetic valves. Native aortic valve cusps contain three layers of morphologically distinct tissue: fibrosa, spongiosa, and ventricularis. The fibrosa contains large, bifurcating collagen fiber bundles; the ventricularis consists of multiple sheets of elastin; and the spongiosa consists of collagen, elastin, and glycosaminoglycans (GAGs). Collagen fiber bundles are surrounded by tubular sheaths of elastin, which are linked together by elastin struts. Given the complexity of native aortic valve cusps, our approach to tissue engineering the aortic valve has been to fabricate cusps from the basic building blocks: (i) branching collagen fiber bundles; (ii) elastin sheets and tubes; and (iii) a highly hydrated GAG matrix.

METHODS

We have developed the following building blocks:
Collagen fiber bundles were fabricated using the principle of directed collagen gel shrinkage. Fibroblasts were mixed with acid-solubilized rat tail collagen and cast into silicon rubber wells with microporous holders to entrap the gel. Since the gel is constrained in the longitudinal direction, it contracts only laterally forming well-aligned collagen fiber bundles.
The viscoelastic matrix that integrates these components together has been fabricated from divinyl sulfone-crosslinked high molecular weight hyaluronan (hylan) [1], texturized by UV irradiation to enhance cell attachment.
Elastin sheets were grown atop the hylan gels and around the collagen fiber constructs by way of long-term cultures of neonatal rat aortic smooth muscle cells.

RESULTS AND DISCUSSION

Collagen gel contraction increased with higher cell seeding density, the optimal value being 1 million cells/ml. The optimal collagen concentration was 2 mg/ml, producing a failure strength as high as 2 MPa. Branched bundles were formed using appropriately shaped wells (Fig 1).
UV-irradiated gels had highly extended cells throughout their thickness. The confocal studies indicate that cells atop and within the gels actively proliferate. The hylan matrices had stiffness values as high as 40 kPa, and strain to failure in excess of 150%.
Transmission electron microscopy showed the presence of a uniform elastic membrane at the surface of UV-exposed gels. We also found that an elastin sheath developed around the collagen core after 6 weeks of culture (Fig 2).

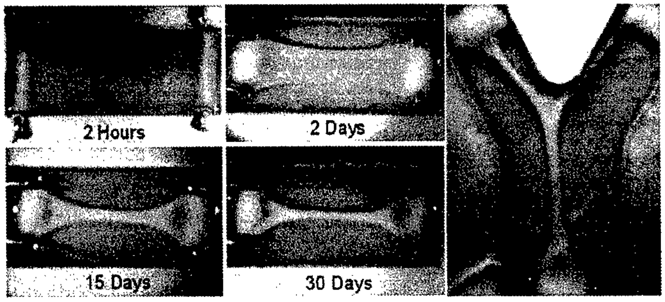

Figure 1: Examples of collagen gel shrinkage and a branched constructs (right)

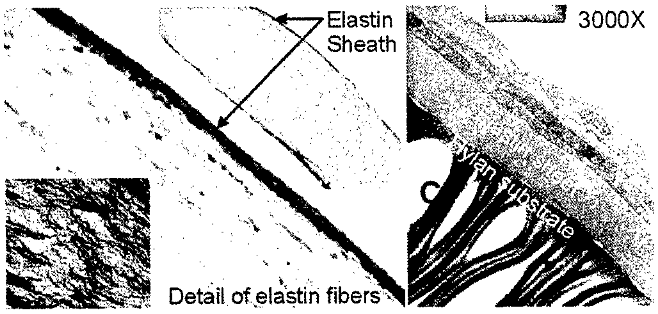

Figure 2: Examples of elastin sheath surrounding a collagen fiber bundle (left), and a flat sheet of elastin bound to the texturized hylan gel (right)

CONCLUSIONS

We have therefore fabricated the basic building blocks of the structure of the native aortic valve using tissue engineering principles. These are: (i) strong collagen fiber bundles that branch, (ii) sheets of elastin adherent to an underlying matrix, (iii) tubes of elastin that surround collagen fiber bundles, and (iv) a highly biocompatible, elastic matrix that can integrate all of these components. We are enhancing the mechanical properties of these components further through dynamic tissue culture. Entire leaflets can thus be fabricated from these constructs by growing each of individually, and assembling them together to make the composite tissue-engineering aortic valve cusp.

REFERENCES

[1] Ramamurthi A., Vesely I., Smooth muscle cell adhesion on crosslinked hyaluronan gels. J. Biomed.Mater.Res., (in press)

Ramamurthi,A, and Vesely, I. "Elastin-Hyaluronan Composite Materials for Soft Tissue Engineering" 2nd European Conference on Elastin. University of Basilicata, Acquafredda di Matratea, Campania, Italy, April 2002.

ELASTIN-HYALURONAN COMPOSITE MATERIALS FOR TISSUE ENGINEERING OF THE AORTIC VALVE

A. Ramamurthi, I. Vesely
Department of Biomedical Engineering, The Cleveland Clinic Foundation, Cleveland, OH, USA, vesely@bme.ri.ccf.org

Tissue-engineering (TE) is a promising approach to overcome the deficiencies of currently available mechanical and bioprosthetic heart valve replacement devices. Due to the limited remodeling potential of heart valve tissues, the conventional TE approach of culturing cells on a biodegradable scaffold *in vitro,* and subsequently regenerating a functional tissue *in vivo,* is not expected to be appropriate for aortic valves. A more promising approach would be to fabricate the entire leaflet microstructure *in vitro* using matrix molecules and cells, so that the tissue could be functional immediately upon implantation. The complex triple-layered structure of aortic valve cusps is organized from collagen, glycosamino-glycans (GAGs), and elastin. Our approach to tissue engineering the aortic valve is to fabricate a functional composite tissue from each layer grown separately in vitro. The immediate goals of this project are to fabricate the GAG-rich spongiosa layer using hyaluronan, and then stimulate cells seeded atop this layer to synthesize elastin sheets and fibers in a morphology similar to that of the elastin-rich ventricularis layer.

Methods. To replace the spongiosa, films based on divinyl sulfone-crosslinked high molecular weight ($> 1.5 \times 10^6$) hyaluronan (hylan) were prepared using a method based on one previously patented by Balazs et al [1]. For cell culture, the films were equilibrated with serum-free DMEM: F12 culture medium and then exposed to UV light ($\lambda = 254$ nm) for 48 hours in a biological hood. This treatment was previously shown to texture the film surface and thus enhance cell attachment. Neonatal rat aortic smooth muscle cells (passages 6-8) suspended in DMEM: F12 (containing 10% FBS and 1% penicillin-streptomycin) were seeded atop the hylan films at a count of 4×10^6-cells/ gel (Culture area= 79 cm^2; $n = 3$) and cultured for up to 6 weeks. Elastin synthesized by these cells was quantified using a dye- binding Fastin Elastin Assay (Accurate Scientific and Chemical, Westbury, NY) at 2, 4, and 6 weeks of culture. At each assay time point, cell layers atop hylan films were harvested using 0.25% Trypsin-EDTA (15 min, 37°C), scraped off, and then centrifuged with culture medium to isolate a pellet containing hylan and cells. The pellet was dried in an oven at 110°C, weighed, and then re-hydrated with distilled water. After another cycle of centrifugation and drying, the pellet was digested with 0.1 M NaOH (98°C, 48 h). Matrix elastin alone survived digestion, and was pelleted, weighed, solubilized with oxalic acid (0.25 N, 95°C, 1 h, 3 cycles) and finally assayed. The digestate was also assayed to quantify any matrix elastin that was leached out during digestion. For SEM, segments of thin hylan films (< 100 μm) with adherent cell layers (at 4 weeks) were immobilized on a steel holder and digested in 0.1 M NaOH (20 minutes, 75°C). Elastin surviving the digestion was cryofrozen, lyophilized and then sputter-coated. Cell-free hylan films, and detached 4 week-old cell layers from petri dishes, were also digested similarly and processed for SEM. For TEM, the cell layers were fixed in paraformaldehyde, post-fixed, dehydrated, embedded in a resin, and then cut longitudinally and stained. Cell-free irradiated hylan films and cell-seeded and non-irradiated hylan films were used as controls.

Results. Elastin was incorporated into the extracellular matrix in increasing amounts over the period of culture. At 2 weeks, almost all the matrix elastin was insoluble in NaOH. At 4 and 6-weeks of culture respectively, 17 ± 10% and 20 ± 1% of the matrix elastin was solubilized by the alkali. SEM of alkali-digested cell layers from petridishes, or atop hylan films both showed the presence of fenestrated elastin sheets and of fibrillar elastin networks typical of that seen in native heart valves and aorta. TEM images showed multiple layers of cells atop hylan films. At 2 weeks, small clumps of amorphous elastin were deposited between cells. Also, the beginnings of thin basal layer of matrix (likely elastin) were visible at the cell-hylan interface. At 4 weeks, a much greater amount of elastin was found distributed between cells. A thick, well-defined layer of matrix was also laid down at the interface between the cells and the hylan. Cell attachment and matrix were not observed on control hylan films.

Conclusions. Our studies indicate that neonatal rat aortic smooth muscle cells synthesize a large amount of elastin within 2 weeks, when cultured atop irradiated hylan films. Although most of the elastin is present as sheets, some elastin fibrils were also seen. In future work, biochemical and mechanical stimuli will be provided to enhance elastin synthesis and obtain the desired ultrastructure. The study is promising towards the development of a composite tissue engineered aortic valve cusp.

[1] **Balazs EA, Leshchiner A.** *Crosslinked gels of hyaluronic acid and products containing such gels.* U.S. Patent No. 4,582,865 (April 15, 1986).

TOWARDS TISSUE ENGINEERING OF A COMPOSITE AORTIC VALVE

Yaling Shi, M.S., Anand Ramamurthi, Ph.D., Ivan Vesely, Ph.D.
Department of Biomedical Engineering / ND20
Lerner Research Institute, The Cleveland Clinic Foundation
Cleveland, Ohio 44121

ABSTRACT

e-engineered valve needs to incorporate the complex microstructure of the native aortic valve if it be as durable as existing bioprosthetic valves. Native aortic valve cusps contain large collagen fiber ues surrounded by tubes of elastin, linked together by elastin sheets and struts. They also contain saminoglycans (GAGs) that bind water and give the valve cusp a gelatinous consistency. Our oach to tissue engineering the aortic valve is to fabricate the cusp from the building blocks ibed above. We have developed collagen fiber bundles using the principle of directed collagen gel nkage, a GAG matrix by crosslinking high molecular weight hyaluronan with divinyl sulfone, and in sheets and tubes by culturing neonatal aortic fibroblasts on the appropriate substrates. To make agen fiber bundles, cells are mixed with solubilized fibrillar collagen and cast into silicon rubber lds fitted with microporous holders to entrap the gel and hold it in place. As the cells interact with the llagen fibrils, they contract and compact the gel. Since the gel is constrained in the longitudinal ection, it can contract only laterally, forming well-aligned, strong (>1 MPa) collagen fiber bundles. in sheaths form naturally around the collagen fiber bundles and atop the hyaluronan gel when the natal aortic fibroblasts are cultured for more than 4 weeks. The individual building blocks of the nic valve cusp, designed and fabricated according to patterns dictated by the microstructure of the ive aortic valve, will be stacked together to make the final composite, tissue-engineered aortic valve

words: Tissue engineering, cardiac valve, bioprosthesis, collagen, elastin, hyaluronan, composite

1. INTRODUCTION

Tissue engineering technologies promise the creation of a nearly limitless supply of organs and tissues to treat a wide variety of injuries and diseases. Like all new technologies, however, tissue engineering has promised more than it has delivered. In the cardiovascular field in particular, tissue engineering has not made great inroads into product lines occupied by conventional synthetic devices. Part of the problems has been that cardiovascular tissues are far more complex than initially envisioned, and have a capacity to repair far less effective than tissue engineering principles demand.

The conventional approach to tissue engineering involves the seeding of cells on a biodegradable matrix, such as polylactic or polyglycolic acid (PLA/PGA). These polymers have been very successful in engineering skin substitutes where remodeling and renewal are the normal physiologic process. However, inducing cardiovascular tissue-engineered organs to regrow has not been successful. For heart valves, the conventional approach to tissue engineering is unlikely to be successful since these tissues do not naturally remodel *in vivo*. Our approach to engineering heart valve tissues has been to fabricate the entire leaflet microstructure *in vitro* using the appropriate matrix molecules and cells, rathe than implanting a scaffold which cells are expected to remodel and turn into a functional valve. Th approach that has shown considerable promise.

2. METHODS AND RESULTS

Collagen Fiber Bundles:

Our approach to fabricating collagen fiber bundles is based on the principle of directed collagen ge shrinkage [1-4]. The principle involves first mixing soluble, fibrillar collagen with cells, neutralizing th mixture to induce gelation, and maintaining the system in culture. When the collagen gels, cells becom entrapped within and begin to interact with the collagen fibrils. These cells reorganize the surroundin collagen matrix, contracting it and excluding water. In many ways, this *in vitro* contraction mimic wound healing *in vivo* [5]. When the gel is mechanically constrained from shrinking in one direction, th collagen fibrils align in the direction of constraint [6, 7]. Highly aligned, compacted collageno constructs can thus be fabricated.

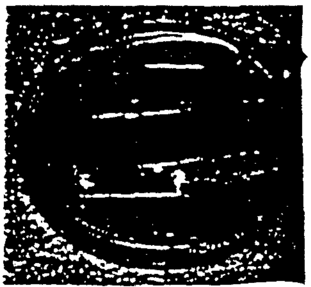

Figure 1: Picture of tissue culture dis with silicone rubber wells and wire holders.

We constructed a rectangular chamber (36 × 18 × 18 mm) from silicone rubber in a 100-mm-diameter petri dish (Fig. 1). Strips of glass fiber were wrapped around a stainless steel wire and placed at the ends of well to act as anchors for the collagen gel [8, 9]. Neonatal rat aortic smooth muscle cells (NRASMC) were isolated by a method outlined by Oakes et al. [10]. In brief, segments of aorta were incubated with 2 ml of type II collagenase (2 mg/ml in DMEM/F12 (1:1) medium; Washington Biomedical) for 10 minutes at 37 °C to remove the endothelium. The explants were then washed with PBS several times, minced into small pieces, transferred onto a sterile petri dish and incubated in limited volumes of equal ratio of DMEM and F12, supplemented with 10% fetal bovine serum (Life Technologies, Grand Island, NY) at 37 °C for one week to establish the primary culture. Prior to use, cells were detache from the culture dishes by trypsinization, counted, centrifuged and added to the collagen suspension at a cell-seeding concentration of 1.0 million cells/ml.

Sterile acid-soluble type I collagen (3D Biosciences, Rat tail: 3.94 mg/ml, 0.02 N acetic acid) was added to medium (5×DMEM/F12) to get an initial concentration of 2.0 mg/ml. The suspension was brought to physiological pH by the addition of 0.1 N NaOH and the cells were added. All mixing was done over ice. This collagen-cell suspension was then pipetted into the wells and incubated at 37°C. Within several hours, the collagen gel formed and attached to the microporous holders at the ends of the wells. These anchors prevented longitudinal contraction and allowed shrinkage to occur only transverse to the long axis of the wells. The constructs were cultured for 8 weeks, and culture medium was changed every 2 days.

Within several hours, the collagen gel detached from the walls of the well and began to contract. Contraction was initially rapid and eventually slowed down, continuing for up to 8 weeks. The original translucent gel became a dense, cylindrical construct with well-aligned collagen fibrils (Fig. 2). The rate of initial collagen gel contraction depended on cell type, cell seeding density, initial collagen ntration and serum concentration. All of these parameters were ized through exhaustive experiments [11] (Shi. Y. and I. Vesely. cation of Mitral Valve Chordae Using Directed Collagen Gel kage. Tissue Engineering, submitted) The final constructs had the non-linear stress/strain curve of tendonous materials, an ibility of 14%, a stiffness of 5 MPa and failure strength of 1.1 Although the stiffness and strength are still an order of itude lower than what is required, our constructs are already 10 to times stronger than similar collagen-based materials fabricated viously [12, 13]. Ultrastructural analyses have shown that the main on for the good strength of our constructs is the very high collagen ll density resulting from the high contraction ratio. Because the structs are relatively simple, one-dimensional collagen bundles, they mpacted in two directions producing an area shrinkage ratio that is ter than 99% (from an area of 324 mm^2 to less than 1 mm^2).

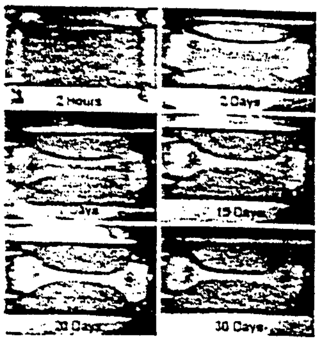

Figure 2: Images showing how the collagen gells attached to the holders and shrank over time to form thin, dense collagen fiber bundles.

nce collagen fiber bundles in heart valves are branched, we have also empted to fabricate branched structures, with good results (Fig. 3). e key to these geometries is to ensure that tension is properly ntrolled during the shrinkage process so that the constructs do not r away from the holders during the early stages. As the images monstrate, different branching angles and parent/daughter ratios can engineered with the use of appropriate molds.

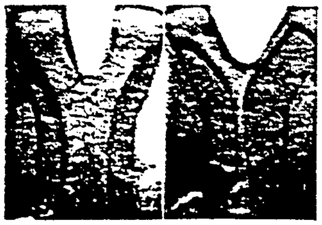

Figure 3: Images showing branched constructs at 1 day and at 3 weeks.

yaluronan Matrix:

yaluronan is a glycosaminoglycan polymer with a repeating disaccharide structure (glucuronic acid-13-N-acetylgalactosamine-β1,4-)$_n$, where n can reach 25,000 or more. In solution, hyaluronan forms rge, random coil structures, which occupy large solvent volumes. When constrained within a matrix uch as a collagen network, hyaluronan exerts a swelling pressure on the matrix which traps water, gives issues compressive resistance and imparts viscoelastic properties. Hyaluronan is exceptionally iocompatible [14-16]. Unlike collagen that has both tissue- and species-specific markers, hyaluronan is identical across species. For example, hyaluronan made by bacteria shows remarkable homology with hyaluronan made by man [17]. Because of its interesting viscoelastic properties and its broad biocompatibility, hyaluronan has been used in a number of clinical applications. Perhaps the greatest contribution to bringing hyaluronan to commercial use has been made by Dr. Endre Balazs, the founder of Biomatrix Inc. (Ridgefield, N.J.), now owned by Genzyme. Dr. Balazs pioneered the crosslinking of hyaluronan with divinyl sulfone and began using it for "viscosurgery" of the eye [18]. One important advantage of divinyl sulfone is that it utilizes the hydroxyl groups on the glycosaminoglycan chains, thereby leaving the more specific groups (carboxylate and N-acetyl groups) unaltered. The crosslinked molecules therefore have high biocompatibility and unaltered biological activity. In the long term, divinyl sulfone-crosslinked hyaluronan persists in the body unaltered. It does not elicit a foreign-body reaction, and does not calcify. These are features very desirable for engineering cardiac valves.

Crosslinked hyaluronan can be manipulated to have properties suitable for its use as a structural material. We have been able to produce hylan gels with a modulus of 40 kPa, a failure strength of 20 kPa and a strain to failure of over 150%. Given that the modulus of the elastin matrix of aortic valve is only 10 kPa [19], we are satisfied with our progress.

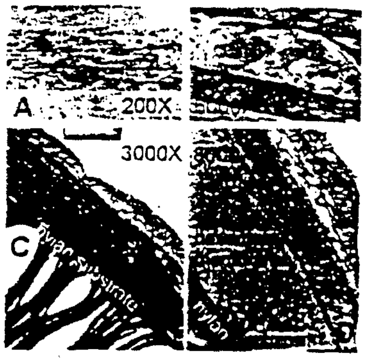

Figure 4: TEM Images of cultured cell layers with elastin lamellae (A), amorphous elastin grown without the addition of copper (B), and basement membrane-like sheets synthesized atop UV-irradiated hylan gels with copper added to the culture (C,D)

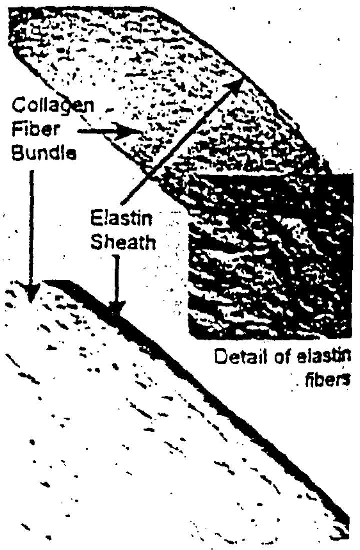

Figure 5: Histologic sections of a collagen fiber bundle construct at low (top) and high (bottom) magnification, showing the presence of an elastin sheath that has formed around the bundle in culture. On the interior, elastin fibers form between crimpled collagen (inset image).

Elastin Sheets:

Neonatal rat aortic smooth muscle cells were selected since they were previously reported to prolifically synthesize elastin in culture [10, 20]. Our initial studies indeed confirmed that these cells start synthesizing both soluble tropoelastin and insoluble elastin within 1 week of seeding, whereas collagen was deposited into the matrix in measurable amounts only after 2 weeks of culture. Based on the above studies, we coated hylan gels with collagen and fibronectin and cultured the neonatal rat aortic smooth muscle cells. Cell layers on hylans were treated with primary antibodies against rat elastin, which was visualized using a Texas Red fluorophore conjugated to a secondary antibody that bound to the elastin. Cellular actin was labeled with Alexa 488 phalloidin and nuclei were labeled with DAPI. Quantitative studies were performed using a Fastin™ Elastin Assay [21]. Control cultures produced approximately 0.5 ng of insoluble elastin per cell over a period of 3 weeks. The production of soluble tropoelastin during the same period ranged between 1.3 and 3 mg/ml. In an attempt to drive elastin synthesis towards generation of insoluble elastin, we have added a number of growth factors to the culture medium (TGF-β, retinoic acid, and copper as Cu^{2+}). TGF-β and retinoic acid have been shown previously to enhance elastin synthesis, primarily upregulating transcription of the elastin mRNA [22-24]. Our previous studies showed that the presence of Cu^{2+} ions (2.5-5 μM) promoted crosslinking of soluble elastin. Over 3 weeks, cell cultures with 5 μM Cu^{2+} generated 2.8 times more insoluble elastin than control cultures, and TEM images confirmed the increased deposition of insoluble elastin, although most of it was in the amorphous rather than the fibrillar form. Interestingly, a uniform basement membrane-type matrix formed at the interface between the cell layers and the gel surface, roughly 10-12 μm thick (Fig. 4).

As mentioned previously, the second major elastin structure is a tube that envelops large collagen fiber bundles. Working with the neonatal rat aortic smooth muscle cells, we have also been able to replicate such structures. When these cells were cultured on the collagen fiber bundle constructs for more than 5 weeks, an elastin sheath formed naturally around the bundle (Fig. 5). Movat's stain clearly shows the presence of elastin fibers between the crimped collagen fibers, becoming denser towards the outside. On the r of the collagen construct, the elastin sheath is relatively thick and continuous. Although we ly do not know why such an elastin sheath would form around these collagen constructs *in vitro*, cess is certainly reproducible.

ave therefore established that neonatal rat aortic cells synthesize significant amounts of insoluble ellular elastin. Elastin synthesis can be enhanced further through the use of a culture medium that ified with copper ions. We can culture cells to produce elastin on collagen fiber constructs and on ylan sheets. We can therefore obtain both elastin tubes and elastin sheets. The presence of the n sheath around the collagen fiber bundles is particularly convenient, since that is exactly where should be, if these collagen bundles are to be integrated into an aortic valve cusp. Our ability to the elastin sheets on the hylan is also very convenient since the central hyaluronan-rich spongiosa n elastin-rich ventricularis on one surface. Having these technologies at our disposal places us in a position to assemble these components and integrate them into a complete, composite aortic valve (Fig. 6).

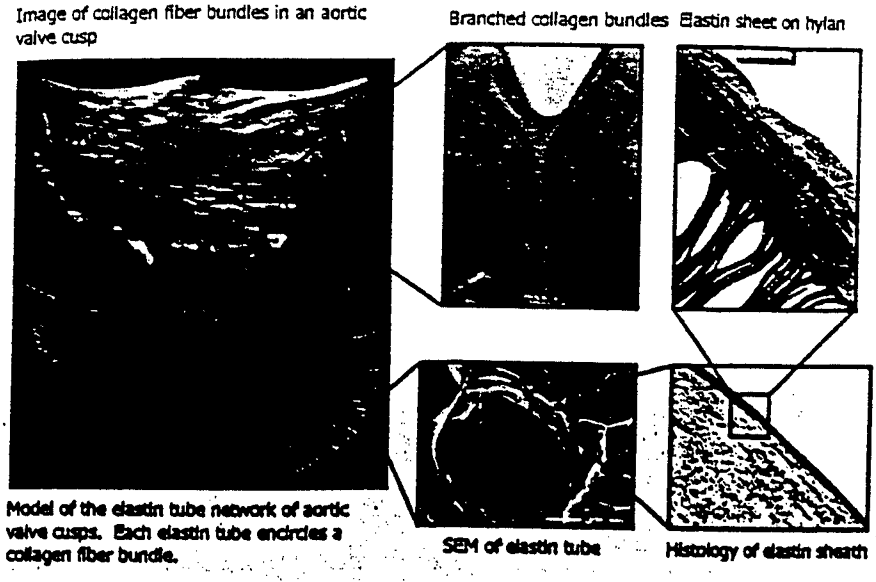
Image of collagen fiber bundles in an aortic valve cusp
Branched collagen bundles
Elastin sheet on hylan
Model of the elastin tube network of aortic valve cusps. Each elastin tube encircles a collagen fiber bundle.
SEM of elastin tube
Histology of elastin sheath

Fig. 6. Flow chart and images showing how the various components of an aortic valve can be fabricated using conventional tissue engineering techniques.

3. DISCUSSION

The assembly of a composite aortic valve cusp involves the fabrication of the individual components in he appropriate size, shape and number. These are the current objectives of our work. We have estimated hat a typical aortic valve will require about ten sets of branched constructs, with perhaps 3 levels of branching. The central portion of the fibrosa will require a network of several dozen parallel fiber bundles, joined together by elastin sheets and struts. This will be done by sandwiching the collagen structures between sheets of crosslinked hyaluronan. We expect that cellular ingrowth into these

composite structures, and new matrix synthesis under static and dynamic culture conditions, will provide the necessary bonding of the components together.

REFERENCES

1. Bell, E., *et al.*, *Living tissue formed in vitro and accepted as skin-equivalent tissue of full thickness.* Science, 1981. 211(4486): p. 1052-4.
2. Huang, D., *et al.*, *Mechanisms and dynamics of mechanical strengthening in ligament- equivalent fibroblast-populated collagen matrices.* Ann Biomed Eng, 1993. 21(3): p. 289-305.
3. Butler, D.L. and H.A. Awad, *Perspectives on cell and collagen composites for tendon repair.* Clin Orthop, 1999(367 Suppl): p. S324-32.
4. Barocas, V.H. and R.T. Tranquillo, *An anisotropic biphasic theory of tissue-equivalent mechanics: the interplay amon cell traction, fibrillar network deformation, fibril alignment, and cell contact guidance.* J Biomech Eng, 1997. 119(2): p 137-45.
5. Grinnell, F., *Fibroblasts, myofibroblasts, and wound contraction.* J Cell Biol, 1994. 124(4): p. 401-4.
6. Grinnell, F., *Fibroblast-collagen-matrix contraction: growth-factor signalling and mechanical loading.* Trends Cel Biol, 2000. 10(9): p. 362-5.
7. Tranquillo, R.T., M.A. Durrani, and A.G. Moon, *Tissue engineering science: consequences of cell traction force.* Cytotechnology, 1992. 10(3): p. 225-50.
8. Valle, C.A.L., *et al.*, *Peripheral anchorage of dermal equivalents.* Brit. J. Derm., 1992. 127: p. 365-371.
9. Auger, F.A., *et al.*, *Tissue-engineered human skin substitutes developed from collagen- populated hydrated gels: clinical and fundamental applications.* Med Biol Eng Comput, 1998. 36(6): p. 801-12.
10. Oakes, B.W., *et al.*, *The synthesis of elastin, collagen, and glycosaminoglycans by high density primary cultures of neonatal rat aortic smooth muscle. An ultrastructural and biochemical study.* Eur J Cell Biol, 1982. 27: p. 34-46.
11. Shi, Y. and I. Vesely. *The use of directed collagen gel shrinkage in the development of tissue engineered mitral valve chordae.* in *1st Biennial Meeting of the Society for Heart Valve Disease.* 2001. London, England.
12. Girton, T.S., T.R. Oegema, and R.T. Tranquillo, *Exploiting glycation to stiffen and strengthen tissue equivalents for tissue engineering.* J Biomed Mater Res, 1999. 46(1): p. 87-92.
13. Seliktar, D., *et al.*, *Dynamic mechanical conditioning of collagen-gel blood vessel constructs induces remodeling in vitro.* Ann Biomed Eng, 2000. 28(4): p. 351-62.
14. Larsen, N.E., *et al.*, *Hylan gel biomaterial: Dermal and immunologic compatibility.* J Biomed Mater Res, 1993. 27: p. 1129-1134.
15. Larsen, N.E., *et al.*, *Biocompatibility of hylan polymers in various tissue compartments*, in *Polymers in medicine and pharmacy*, A.G. Mikos, *et al.*, Editors. 1995, Materials Research Society.: Pittsburgh. p. 149-153.
16. Denlinger, J.L., A.A. El-Mofty, and E.A. Balazs, *Replacement of the liquid vitreus with sodium hyaluronate in monkeys. II. Long-term evaluation.* Exp Eye Res, 1980. 31(1): p. 101-17.
17. Laurent, T.C., *Biochemistry of hyaluronan.* Acta Otolaryngol Suppl, 1987. 442: p. 7-24.
18. Balazs, E.A. and J.L. Denlinger, *Clinical uses of hyaluronan.* Ciba Foundation Symposium, 1989. 143: p. 265-75; discussion 275-80.
19. Vesely, I., *The role of elastin in aortic valve mechanics.* J Biomech, 1998. 31(2): p. 115-23.
20. Jones, P.A., T. Scott-Burden, and W. Gevers, *Glycoprotein, elastin, and collagen secretion by rat smooth muscle cells* Proc Natl Acad Sci U S A, 1979. 76(1): p. 353-7.
21. Kim, B.S., *et al.*, *Optimizing seeding and culture methods to engineer smooth muscle tissue on biodegradable polyme matrices.* Biotechnol Bioeng, 1998. 57(1): p. 46-54.
22. Liu, B., C.S. Harvey, and S.E. McGowan, *Retinoic acid increases elastin in neonatal rat lung fibroblast cultures.* Am Physiol, 1993. 265(5 Pt 1): p. L430-7.
23. McGowan, S.E., *Influences of endogenous and exogenous TGF-beta on elastin in rat lung fibroblasts and aortic smoot muscle cells.* Am J Physiol, 1992. 263(2 Pt 1): p. L257-63.
24. Quaglino, D., *et al.*, *Extracellular matrix modifications in rat tissues of different ages. Correlations between elastin an collagen type I mRNA expression and lysyl-oxidase activity.* Matrix, 1993. 13(6): p. 481-90.

Ramamurthi A., and Vesely, I. "Surface Modification of Hyaluronan Gels to Enhance Cell Adhesion" Biosurfaces 2002 Conference, Scottsdale, AZ, November 2002 (Accepted)

Surface Modification of Hyaluronan Gels to Enhance Cell Adhesion

Anand Ramamurthi, Ivan Vesely
Department of Biomedical Engineering, The Cleveland Clinic Foundation, Cleveland, OH 44195

Abstract Summary: We have explored the use of crosslinked hyaluronan gels as scaffolds for engineering cardiac valves. We found that irradiation with ultraviolet (UV) light enhances cell attachment, most likely by producing physical and chemical links to which the cells can adhere.

Background: The conventional tissue engineering approach of seeding cells on a biodegradable matrix, such as polylactic acid (PLA), as used in skin substitutes, is unlikely to be successful for heart valves since the extracellular matrix does not rapidly remodel in vivo. We propose to develop tissue-engineered heart valves based on biological molecules that do not require remodeling in vivo and are relatively stable in the long term.

We have identified crosslinked hyaluronan (hylan) as an appropriate molecule for our application. Hyaluronan is a glycosaminoglycan polymer with a repeating disaccharide structure (glucuronic acid-β1,3-N-acetylgalactosamine-β1,4-)n, where n can reach 25,000 or more. In solution, hyaluronan forms large, random coil structures, which occupy large solvent volumes. Hyaluronan is also exceptionally biocompatible [1, 2]. Unlike collagen that has both tissue- and species-specific markers, hyaluronan is identical across species. For example, hyaluronan made by bacteria shows remarkable homology with hyaluronan made by man [3]. Because of its interesting viscoelastic properties and its broad biocompatibility, hyaluronan has been used in a number of clinical applications, particularly when crosslinked with divinyl sulfone (DVS). We have been able to produce hylan gels with a modulus of 40 kPa, a failure strength of 20 kPa and a strain to failure of over 150%. Divinyl sulfone crosslinking utilizes the hydroxyl groups on the glycosaminoglycan chains, thereby leaving the more specific groups (carboxylate and N-acetyl groups) unaltered. Because of its highly negatively charged, hydrated state, crosslinked hyaluronan is not conducive to cell attachment and growth. Hylan gels needed to be pre-coated with adhesion proteins to enable cell attachment [4]. Our previous studies have also shown, however, that hylan gels prepared with a rough surface stimulated greater protein deposition and were more conducive to cell attachment and spreading. We therefore sought to investigate methods for texturing the surface of hylan gels and modifying their bulk properties to enable cell infiltration.

Methods: We exposed dehydrated, DVS-crosslinked hyaluronan gels to ultraviolet (UV) light to modify the gel surface, and investigated the relative growth and proliferation of smooth muscle cells atop these textured gels. Gels were also imaged using light and Scanning Electron Microscopy (SEM) to visualize the textured surface. Gels were also analyzed using carbohydrate electrophoresis to determine if UV irradiation produced any new chemical species.

Results and Discussion: Cell attachment was sparse on both non-irradiated and dehydrated gels. Significantly higher levels of cell attachment were observed on the surface of irradiated and dehydrated-irradiated gels, likely due to texturing of the gel surface by UV light. SEM imaging revealed the presence of a honeycomb-like texturing of the surface, to which cells attached (Fig. 1), as well as cracks or fissures, into which cells were observed to migrate. Carbohydrate electrophoresis assays demonstrated that UV-irradiation alters the chemistry of HA, causing some minor breakdown of HA chains and divinyl sulfone crosslinks, and possibly creating new crosslinks that have not yet been identified. Since the hylan gels are altered structurally and chemically, binding of cells to the material is likely to be more permanent than possible by other approaches, such as coating of cell-adhesive matrix factors on the gel surface, described previously.

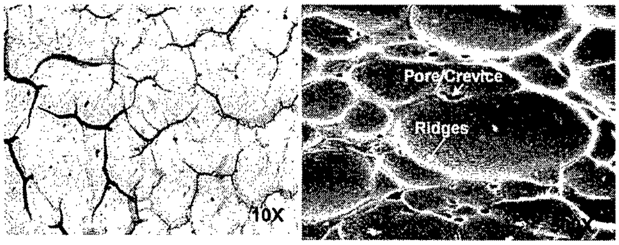

Fig. 1: Low magnification light microscopy image (left) showing patterns of ridges and cracks. Higher magnification SEM image (right) showing pattern of ridges and pores.

Conclusion: The significance of this work is that we have developed a technique for the modification of hyaluronan gels to enhance their performance as a cellular scaffold for tissue engineering applications.

References:

1. Larsen, N.E., *et al.*, *Hylan gel biomaterial: Dermal and immunologic compatibility.* J Biomed Mater Res, 1993. 27: p. 1129-1134.
2. Larsen, N.E., et al., Biocompatibility of hylan polymers in various tissue compartments, in Polymers in medicine and pharmacy, A.G. Mikos, et al., Editors. 1995, Materials Research Society.: Pittsburgh. p. 149-153.
3. Laurent, T.C., *Biochemistry of hyaluronan.* Acta Otolaryngol Suppl, 1987. 442: p. 7-24.
4. Ramamurthi A, Vesely I. Smooth muscle cell adhesion on crosslinked hylauronan gels. J Biomed Mater Res, 2002; 60(1); 196-205.

Ramamurthi, A., and Vesely, I., "Evaluation of UV-Treated Hyaluronan Gels as Biomaterials for Cardiovascular Tissue Engineering" Society for Biomaterials Annual Conference 2002, Tampa Bay, FL, April 24-27, 2002.

Evaluation of UV-Treated Hyaluronan Gels as Biomaterials for Cardiovascular Tissue Engineering

Anand Ramamurthi and Ivan Vesely
Department of Biomedical Engineering, The Cleveland Clinic Foundation /ND20, 9500 Euclid Avenue,
Cleveland, OH 44195, USA

Background: The high biocompatibility of divinyl sulfone (DVS)-crosslinked hyaluronan gels (hylans) makes them excellent candidates for tissue engineering applications. In addition, a large number of gel formulations are possible, which can impart very different structural characteristics to the material. The gels can also be formulated to be permanent. Our interest is to use such permanent hylan gels as materials to replace diseased cuspal tissue of the aortic valve, a site of limited remodeling. A drawback of the material is that the highly anionic nature of the hyaluronan chains limits cell attachment. In this study, we modified the physical and chemical properties of hylan gels via exposure to ultraviolet (UV) light and evaluated attachment and proliferation.

Methods: Sterile hylan gels were prepared containing 4% by weight of high molecular weight sodium hyaluronate (HA; MW> 1.5 x 10^6; Genzyme, Cambridge, MA) and a HA to crosslinker weight ratio of 4:1. All gels were equilibrated overnight with serum-free culture medium. Thereafter, one group of gels was exposed to low intensity UV light for 48 hours, a second group was dehydrated in an oven at 32 °C for 36 hours, and a third group was first dehydrated and then UV-exposed. Unmodified gels were used as controls. After the respective treatments, the gels were re-hydrated with serum-free medium, cut into circular disks to fit into wells of a 24-well plate (Area = 1.9 cm^2). The gels were seeded with neonatal rat aortic smooth muscle cells (passage 3) at a count of 4 $\times 10^5$ cells per well, and cultured for up to 8 weeks. Cell proliferation atop and within gels was measured using a DNA assay using the fluorescent dye, Hoechst 33258. Cell attachment and migration were monitored by confocal microscopy. We investigated possible UV-induced texturing of gel surfaces using scanning electron microscopy (SEM) techniques. Immuno-histochemical and transmission electron microscopy (TEM) methods were used to evaluate extracellular matrix synthesis by the cells. Fluorophore-Assisted Carbohydrate Electrophoresis (FACE) was used to investigate UV-induced changes to the gel chemistry. Briefly, uncrosslinked HA samples (0.1 mg) and crosslinked hylan gels (containing 0.1 mg HA) were solubilized in 100 µl of ammonium acetate buffer (pH 7.0), and exposed to UV-light for periods ranging from 0 to 120 hours. Samples were digested with hyaluronidase SD (10 mU) for 4 hours at 37 °C and lyophilized. Free reducing groups on the digested HA chains were labeled with a fluorescent dye (2-aminoacridone; Molecular Probes, Eugene, OR) and the samples were run on a gel. Band intensities were then measured.

Results: Cells did not attach to unmodified hylan gels. Cell attachment was sparse on dehydrated gels but was enhanced on all UV-exposed gels. Dehydration of gels prior to UV-irradiation enabled the migration of highly extended cells into their interior. Cells both atop and within gels proliferated. Cell attachment at 3 weeks of culture was 4.9 ± 0.9 times the cell attachment at 1 day. A reconstruction of the gel using confocal microscopy showed the presence of dividing nuclei within the gel. Only cells cultured on UV-exposed gels formed a basement membrane-like layer between the cell layers and the gel surface. Further study is ongoing to characterize extracellular matrix synthesis within the gel. A comparison of irradiated and non-irradiated but dehydrated hylan gels using SEM showed that UV-light texturizes the gel surface and forms cracks through which cells can penetrate into the interior. Hylan gels exposed to UV-light were less easily digested by hyaluronidase SD, suggesting crosslinking by UV, or other changes to the gel chemistry. Gels exposed to UV for longer periods of time were digested less easily, as suggested by decreased intensity of the bands containing HA disaccharides (sample data in Table 1). The simultaneous decrease in the intensity of bands containing DVS-crosslinked HA fragments suggests possible changes to the vinyl sulfone crosslinks as well.

Band	Un-X-linked HA	Gel No UV	Gel UV (22 h)	Gel UV (60h)
Other			1.83E+04	
X-linked HA		8.40E+05	3.63E+04	9.12E+02
ΔDi HA	1.48E+07	2.42E+06	2.34E+05	5.14E+04
Crosslink : ΔDi HA	-	0.35	0.16	0.02

Table 1. Reduced digestibility of hylan gels upon UV exposure. Shown are representative data from one of three trials, corrected to an exposure of 350 ms (intensities were measured at different exposures for each trial).

FACE performed on uncrosslinked HA showed that HA-disaccharide band intensities decreased by roughly 50% over the first 12 hours of UV-exposure, and very marginally for longer exposures. These experiments suggest that UV light crosslinks the HA chains mostly within the first 12 hours of exposure. Although these results need to be confirmed with further experiments, the study suggests that UV-light primarily alters the chemistry of the DVS-crosslinks within hylan gels.

Discussion: This study shows that we can modify the surface and bulk properties of hylan gels by exposure to UV light, and thus enhance cell attachment and proliferation. Cells anchor readily, and proliferate atop UV-exposed hylan gels, mainly due to texturing of the surface by UV, and the creation of fissures. Dehydration of gels prior to UV-exposure reduces the gel thickness upon reconstitution, and thus enables UV light to alter bulk gel properties in addition to altering the surface characteristics. Our study has demonstrated that cells actively synthesize structural extracellular matrix atop UV-modified gels. Further experiments need to be performed to confirm similar matrix synthesis by cells within the gel as well. Such matrix synthesis is expected to structurally reinforce the hylan gels and impart it mechanical characteristics more similar to native valve cusps. The significance of this study is that we can now tailor hylan gel properties to enhance their use as cellular scaffolds for engineering valvular and other cardiovascular tissues.

This work is funded by the US Department of Defense (# DAMD 17-99-1-9475).

ULTRAVIOLET IRRADIATION ENHANCES THE PERFORMANCE OF HYLAN GELS AS SCAFFOLDS FOR CARDIOVASCULAR TISSUE ENGINEERING

Anand Ramamurthi, Ph.D. and Ivan Vesely, Ph.D.
Department of Biomedical Engineering, The Cleveland Clinic Foundation, Cleveland, USA

Because of their high biocompatibility, divinyl sulfone-crosslinked hyaluronan (HA) gels, called hylans, may be useful as tissue-engineering scaffolds. Our objectives were to determine (i) if ultraviolet (UV) irradiation enhances cell attachment and penetration into gels, and (ii) if the material could be mechanically reinforced with extracellular matrix synthesized by the cultured cells.

Sterile hylan gels (4% HA by weight; HA to crosslinker ratio of 4:1) were equilibrated with serum-free culture medium. One group of gels was exposed to UV irradiation for 48 hours, a second group was dehydrated, and a third group was subjected to both treatments. All gels were then rehydrated. The attachment and proliferation of smooth muscle cells on modified gels relative to unmodified controls was measured at four weeks. Gels were imaged using confocal microscopy and cells were counted using Image Pro® software. Possible UV-induced changes in gel chemistry and structure were investigated via flurophore-assisted carbohydrate electrophoresis (FACE) and using SEM techniques. Immunohistochemical and transmission electron microscopy techniques were used to characterize the nature of the extracellular matrix atop and within the gels.

Cells did not attach to unmodified gels. UV-irradiated gels supported multilayered cell growth for up to 8 weeks. Dehydrated, UV-irradiated gels had highly extended cells throughout their thickness, while non-UV irradiated gels had few spindle-shaped cells on their surface. Irradiated gels were also less easily digested using *streptococcal* hyaluronidase, suggesting either increased crosslinking induced by UV, or a change in HA chemistry. SEM studies suggest that UV-irradiation induces pore formation in gels enabling cell infiltration. The confocal studies indicate that cells atop and within the gels actively proliferate. Transmission electron microscopy showed the formation of a uniform basement membrane at the interface between the cell layers and the surface of the UV-exposed gel.

These studies show that we can texturize the surface and alter the bulk properties of hylan gels by exposure to UV light and enhance cell attachment and proliferation. Hylan gel properties can thus be tailored to suit specific requirements for use in different tissue- engineering applications.

CYTOKINE EXPRESSION IN PATIENTS UNDERGOING CAROTID ENDARTERECTOMY FOR ATHEROSCLEROSIS

Elisabetta Profumo*, Elena Ortona*, Paola Margutti*, Bruno Salvati#,
Raffaele Capoano# & **Rachele Riganò***
** Laboratorio di Immunologia, Istituto Superiore di Sanità and # Istituto di III Clinica Chirurgica,*
Università "La Sapienza", Rome, ITALY.

Recent findings suggest that inflammation and cytokine regulation play a role in the pathogenesis of atherosclerosis. The immune response is mediated by circulating and resident leukocytes and by the cells with which they interact. Whether immune responses modulate the atherosclerotic process remains unknown. The aim of this study was to determine whether cytokine expression in whole blood of patients undergoing surgery for carotid-artery atherosclerosis can be used as an endogenous marker of restenosis or of a contralateral carotid lesion. For this purpose, we evaluated the expression of antigenic surface markers (CD4, CD8, CD45RO, CD45RA, TCR α/β, and TCR γ/δ) in T lymphocytes isolated from patients' atherosclerotic plaques and peripheral blood. In both subpopulations (CD4+ and CD8+) of circulating and resident T lymphocytes we determined the intracellular expression of IFN-γ, IL-4 and TNF-α. Blood samples were taken from patients before surgery and at regular intervals during the postoperative clinical follow-up (1, 3, 6, and 12 months) and from healthy donors. Patients were divided into three groups according to the intraoperative morphological classification of atherosclerotic plaques (smooth, rough and ulcerated). Expression of phenotypic markers of lymphocytes and of intracellular cytokines was determined by a three color cytofluorimetric analysis. Th1 and Th2 cytokine expression changed appreciably during follow-up. Our preliminary findings indicate that cytokines may be useful as immunological markers in the postoperative surveillance of patients with carotid-artery atherosclerosis.

Final Prgram Abstracts TE 2002: International Workshop of Tissue Engineering; St. Gallen Switzerland,
February 24-27, 2002

Towards a Composite, Tissue-Engineered Aortic Valve

Ivan Vesely, Yaling Shi and Anand Ramamurthi
Department of Biomedical Engineering, Lerner Research Institute, The Cleveland Clinic Foundation, 9500 Euclid Avenue, Cleveland, Ohio, 44195, USA (vesely@bme.ri.ccf.org)

INTRODUCTION

The complex microstructure of the aortic valve is important to its long-term function and durability. A tissue-engineered valve will need to incorporate this microstructure if it is expected to offer durability comparable to that of conventional bioprosthetic valves. Native aortic valve cusps contain three layers of morphologically distinct tissue: fibrosa, spongiosa, and ventricularis. In the fibrosa, large collagen fiber bundles begin near the edges of the cusps and bifurcate many times towards the belly of the cusp. The ventricularis consists of multiple sheets of elastin. Separating the fibrosa and ventricularis is a very loosely organized spongiosa, consisting of collagen, elastin, and glycosaminoglycans (GAGs). The GAGs bind water readily and give the spongiosa a gelatinous, watery consistency. Collagen fiber bundles are surrounded by tubular sheaths of elastin, which are linked together by elastin struts. Given the complexity of native aortic valve cusps, our approach to tissue engineering the aortic valve is not to rely on remodeling of a degrading scaffold, but rather to fabricate the cusp from its basic building blocks: (i) branching collagen fiber bundles; (ii) elastin sheets and tubes; and (iii) a highly hydrated GAG matrix.

MATERIALS AND METHODS

We have developed each of these structures as follows:

(i) Collagen fiber bundles were fabricated using the principle of directed collagen gel shrinkage. Fibroblasts are mixed with acid-solubilized rat tail collagen and cast into silicon rubber wells. Microporous holders are used at the ends to entrap the gel and hold it in place. As the cells interact with the collagen fibrils, they contract and compact the gel, excluding water. Since the gel is constrained in the longitudinal direction, it contracts only laterally, forming well-aligned, collagen fiber bundles.

(ii) The viscoelastic matrix that integrates these components together has been fabricated from divinyl sulfone-crosslinked high molecular weight hyaluronan (hylan). Although hylans are highly biocompatible, they have relatively low cell adherence [1] We therefore investigated cell attachment and penetration into gels could be enhanced by texturizing the surface of the gel though exposure to ultraviolet (UV) irradiation. Sterile hylan gels (4% HA by weight; HA to crosslinker ratio of 4:1) were either dehydrated, exposed to UV irradiation for 48 hours, or subjected to both treatments. The attachment and proliferation of smooth muscle cells on modified gels relative to unmodified controls was measured for up to four weeks.

(iii) Attempts were made to grow elastin sheets atop of texturized hylan gels as well as collagen fiber constructs by way of long-term cultures of neonatal rat aortic smooth muscle cells. These cells are known to prolifically synthesize elastin in culture [2]. Constructs were examined with light, confocal, scanning and transmission electron microscopy at 7 weeks of culture, and subjected to mechanical testing.

RESULTS AND DISCUSSION

(i) Collagen gel contraction increased with higher cell seeding density, the optimal value being 1 million cells/ml. Increasing the initial collagen concentration and culture time had a positive effect on the strength of the constructs. The optimal collagen concentration was 2 mg/ml, producing failure strengths as high as 1.1 MPa. The strength of our constructs was at least an order of magnitude greater than previously published results with other collagen-based constructs. Branched bundles were formed using appropriately shaped wells (Fig 1).

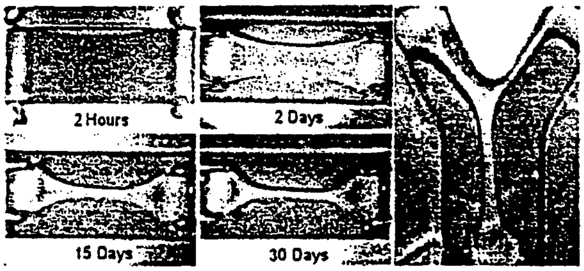

Figure 1: Examples of collagen gel shrinkage and a branched constructs (right)

(ii) Dehydrated, UV-irradiated gels had highly extended cells throughout their thickness, while non-UV irradiated gels had few spindle-shaped cells on their surface. SEM studies suggest that UV-irradiation produces pores in gels enabling cell infiltration. The confocal studies indicate that cells atop and within the gels actively proliferate. The hylan matrices had stiffness values as high as 40 kPa, and strain to failure in excess of 150%. These studies show that we can modify the surface and bulk properties of hylan gels by exposure to UV light and enhance cell attachment and proliferation.

(iii) Transmission electron microscopy showed the presence of a uniform elastic membrane at the surface of UV-exposed gels. We also found that an elastin sheath developed around the collagen core after 6 weeks of culture (Fig 2).

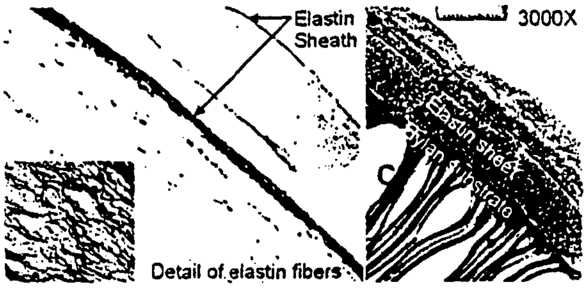

Figure 2: Examples of elastin sheath surrounding a collagen fiber bundle (left), and a flat sheet of elastin bound to the texturized hylan gel (right)

CONCLUSIONS

We have therefore fabricated the basic building blocks of the structure of the native aortic valve using tissue engineering principles. These are: (i) strong collagen fiber bundles that branch, (ii) sheets of elastin adherent to an underlying matrix, (iii) tubes of elastin that surround collagen fiber bundles, and (iv) a highly biocompatible, elastic matrix that can integrate all of these components. We are now fabricating entire leaflets by growing each of the necessary structural components in culture individually, and assembling them together to make the composite tissue-engineering aortic valve cusp.

REFERENCES

1) Ramamurthi A., Vesely I., Smooth muscle cell adhesion on crosslinked hyaluronan gels. J. Biomed.Mater.Res., (in press)
2) Oakes, B.W., et al., The synthesis of elastin, collagen, and glycosaminoglycans by high density primary cultures of neonatal rat aortic smooth muscle. Eur J Cell Biol, 1982. 27: p. 34-46.

Ramamurthi A., and Vesely, I. International Smith and Nephew International Symposium on Tissue Engineering, Atlanta, Georgia, Oct 2002 (Accepted)

Elastin-Hyaluronan Composites for Tissue Engineering of the Aortic Valve

A. Ramamurthi, I. Vesely

Department of Biomedical Engineering, Lerner Research Institute, The Cleveland Clinic Foundation, Cleveland, Ohio, U.S.A., vesely@bme.ri.ccf.org FAX: (216) 444-9198

We have been working on developing a tissue-engineered aortic valve by fabricating the entire leaflet microstructure in vitro, so that the device could be functional immediately upon implantation. The complex triple-layered structure of aortic valve cusps is organized from collagen, glycosaminoglycans (GAGs), and elastin. One objective is to fabricate the GAG-rich spongiosa layer from hyaluronan, and then use tissue culture techniques to synthesize elastin sheets and fibers atop this layer to fabricate the elastin-rich ventricularis layer.

We first fabricated films from divinyl sulfone-crosslinked high molecular weight ($> 1.5 \times 10^6$) hyaluronan (hylan) and exposed them to UV light for 48 hours to texturize the film surface and enhance cell attachment. Neonatal rat aortic smooth muscle cells (passages 6-8) suspended in DMEM: F12 (containing 10% FBS and 1% penicillin-streptomycin) were seeded atop the hylan films at a count of 4×10^6-cells/ gel and cultured for up to 8 weeks. Elastin synthesized by these cells was quantified using a commercial dye-binding Fastin Elastin Assay (Accurate Scientific and Chemical, Westbury, NY) at 2, 4, and 6 weeks of culture. For SEM, segments of the hylan films with adherent cell layers were immobilized on a steel holder and digested in 0.1 M NaOH to isolate the elastin. The isolated elastin was cryofrozen, lyophilized and then sputter-coated. Cell-free hylan films were also digested similarly and processed for SEM. For TEM, the cell layers were fixed in 4% paraformaldehyde, post-fixed, dehydrated, embedded in a resin, and then cut longitudinally and stained.

Elastin was incorporated into the extracellular matrix in increasing amounts over the period of culture. At 4 and 6-weeks of culture respectively, 17 ± 10% and 20 ± 1% of the matrix elastin was solubilized by the alkali. SEM of alkali-digested cell layers atop hylan films showed the presence of fenestrated elastin sheets and of fibrillar elastin networks typical of that seen in native heart valves and aorta. TEM images showed multiple layers of cells atop hylan films. At 2 and 4 weeks of culture, clumps of amorphous elastin were deposited between cells and a basal layer of matrix was visible at the cell-hylan interface.

Our studies indicate that neonatal rat aortic smooth muscle cells synthesize a large amount of sheet elastin within 2 weeks, when cultured atop irradiated hylan films, thus forming a composite similar to the ventricularis and spongiosa layers. The study shows promise towards the development of a composite tissue engineered aortic valve cusp.

Shi, Y., and Vesely, I. International Smith and Nephew International Symposium on Tissue Engineering, Atlanta, Georgia, Oct 2002 (Accepted)

In-vitro Synthesis of Elastin Sheets on Collagen Fiber Bundles.

Y. Shi, I. Vesely

Department of Biomedical Engineering, Lerner Research Institute, The Cleveland Clinic Foundation, Cleveland, Ohio, U.S.A., vesely@bme.ri.ccf.org. FAX: (216) 444-9198

We have been using the principle of directed collagen gel shrinkage to fabricate highly aligned tendonous structures for artificial mitral valve chordae tendineae. Fibrillar collagen is mixed with cells and cast as a gel into rectangular wells. The entrapped cells interact with the collagen fibrils and contract it, excluding water. When the gel is mechanically constrained from shrinking in one direction, the collagen fibrils align in the direction of constraint. Highly aligned, compacted collagenous constructs can thus be fabricated. Since native chordae also contain an elastin sheath that surrounds the collagen core, we were interested in investigating the growth of elastin sheets on the collagen bundles *in vitro.*

Neonatal rat aortic smooth muscle cells (NRASMC) were isolated by incubating segments of rat aorta with 2 mg/ml of type II collagenase for 10 minutes at 37°C to remove the endothelium, washed with PBS several times, minced into small pieces, transferred onto a sterile petri dish and incubated for one week to establish the primary cell line. The gels consisted of sterile, acid-soluble type I collagen at a concentration of 2.0 mg/ml, mixed with cells at a concentration of 1.0 million cells/ml. Once the suspension was neutralized, a gel formed and the constructs began to shrink in a few hours. Constructs were cultured for 4 to 8 weeks to enable a new matrix to be synthesized and subjected to histologic and SEM exam to investigate the morphology of the elastin sheath.

Histologic sections showed that elastin sheets surrounded the dense collagen core after 5 weeks of culture. Movat's-stained sections and Electron Microscopy clearly showed the presence of elastin on the surface of the collagen constructs, as well as between the crimped collagen fibers. On the exterior of the collagen construct, the elastin sheath was thick and continuous. We used digestion in NaOH to isolate the elastin sheets in their morphologically intact state, and then imaged them using Scanning Electron Microscopy (SEM). A Fastin Elastin Assay was used to verify that the elastin structures that remained after NaOH digestion contained only elastin, and no residual collagen. These elastin structures were continuous, thick and had a surface topography similar to that observed on porcine mitral valve chordae.

We therefore conclude that NRASMCs can be used to synthesize significant amounts of elastin in culture. Elastin may preferentially form at the outer surface of collagen constructs because of nutrition of physical/mechanical cues that may be analogous to those present in developing artery or mitral valve chordae.

Proceedings of the IEEE 28th Annual Northeast Bioengineering Conference; Drexel University, Philadelphia, PA
April 20-21, 2002. Editors Karen Moxon, Ph.D., Dalia El-Sherif, Saravan Kanakasabi

Regional Differences In Strength At The Plantar Skin-Fat Interface

Yan Chen, Brian Davis, Antonio Valdevit
Department of Biomedical Engineering,
Cleveland Clinic Foundation, Cleveland, OH

Abstract: Mechanical factors are now widely recognized as important in the understanding of diabetic foot disease. Previous finite element modeling research suggested that the skin-fat interface might be the site for initial ulcer formation since peak first principal stresses at this location are dramatically increased by changes in material properties and boundary conditions. No study to date has investigated the effects of the disease process on the bonding between skin and underlying fat tissue on the plantar surface of the human foot. In total, 38 feet (70.9±2.2 years) have been studied. The plantar surface of the foot sample was divided into 18 areas. For each area the skin was peeled off the underlying fat tissue at a rate of 1 mm/sec by a materials testing (MTS) machine. There was no difference between medial and lateral strips (p=0.603). The strength of the skin-fat interface was significantly higher in strips from the metatarsal head region and heel region than in mid-arch region of the foot. The strength of the skin-fat interface increased with the thickness of the skin at that site.

INTRODUCTION

Foot ulceration is one of the most common complications of diabetes mellitus and a major cause of disability and morbidity. 15% of all diabetic patients will have a foot ulcer during their lifetime and 20% of all hospital admissions of diabetic patients are for foot problems [1]. Foot ulceration is estimated to result in some eight hundred million dollars in medical expenses per year in the United States alone [2]. Diabetic neuropathy, susceptibility to infection, circulation problems, and mechanical trauma are the major factors that contribute to the diabetic foot ulceration. Although the mechanical factors are now widely recognized as important in the treatment of diabetic foot ulceration, the effects of mechanical factors on the formation of ulceration are not fully understood. Many studies have focused on the identification of a threshold plantar pressure that leads to tissue damage [3]. Recent studies have suggested that peak barefoot pressure may be only 65% for the development of ulceration [3]. There have been clinical reports that diabetic ulcers may originate internally [4]. Thompson [5] built a two-dimensional plane strain finite element model that included skin, aponeurosis, and fat pads and simulated the heel-strike phase of walking. He found high stress at the skin-fat interface and suggested that the skin–fat interface might be the site for initial ulcer formation since peak first principal stresses at this location were dramatically increased by the changes in material properties and boundary condition [5]. Currently, there is no data about the strength of the skin and underlying fat tissue interface. The goal of this study was to investigate the strength of the skin-fat interface at the plantar surface of the human foot and regional differences in the strength.

METHODS

38 feet specimens (70.9±2.2 years) were studied. The foot specimens were stored at -20°C until needed for the test. Before testing, the specimens were thawed for 18 hours in a refrigerator. A custom designed jig was used to hold the foot specimen in the supine position (Figure 1). The jig was placed on top of a transitional unit which can move in both x and y directions to keep the peeling force vertical to the peeling site. The transitional unit was then mounted on a universal material testing machine (MTS). The plantar surface of the foot specimen was cut into a 9x2 array from the first metatarsal head (row 1) to the anterior heel (row 9) and divided down the medial/lateral axis. Each strip of skin was 1 cm wide and 2 mm deep. The skin strip was clamped to a load cell and tension was applied at a rate of 1 mm/sec as the skin was peeled off the underlying fat tissue. After the skin strip was peeled off the underlying fat

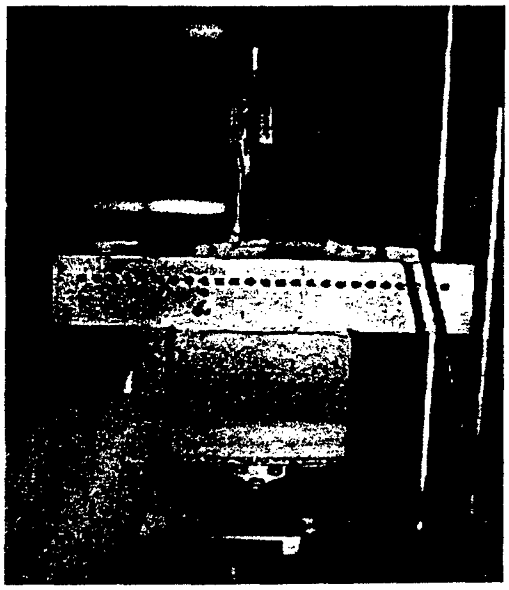

Figure 1. Test setup (The MTS machine is pulling a skin strip of the plantar surface of the foot. The calf is shown on the lower left).

0-7803-7419-3/02/$17.00 ©2002 IEEE.

EFFECTS OF DIABETES ON THE STRENGTH OF THE PLANTAR SKIN-FAT INTERFACE

Yan Chen, Brian Davis, Antonio Valdevit
Department of Biomedical Engineering, Cleveland Clinic Foundation, Cleveland, USA
cheny@bme.ri.ccf.org

INTRODUCTION

Foot ulceration is one of the most common complications of diabetes mellitus. Research has suggested that the plantar skin–fat interface may be the site for initial ulcer formation since peak first principal stresses at this location dramatically increase with changes in material properties and boundary conditions (Thompson, 1997). The goal of this study was to compare the skin-fat interface strength in diabetic and non-diabetic feet.

METHODS

For 21 diabetic (68±2.4 years) and 17 non-diabetic (74.6±3.8 years) foot specimens, the plantar skin surface was cut into a 9x2 array from the first metatarsal head (row 1) to the anterior heel (row 9) and divided down the medial/lateral axis. Each strip of skin was 1 cm wide and 2 mm deep. The skin was clamped to a load cell and tension was applied at a rate of 1 mm/sec as the skin was peeled off the underlying fat tissue. During testing the foot specimen was held in a supine position in a custom designed jig that was placed on top of a transitional unit that could move in both x and y directions to keep the peeling force vertical to the peeling site. This unit was then mounted on a universal MTS machine. The mean peeling force over the entire removal process was calculated and normalized to the width of the skin strip (i.e. F=N/cm).

RESULTS

The strength of the skin-fat interface was significantly different ($p<0.05$) with the diabetic strips requiring greater skin removal force (Table 1). There was no significant difference between medial and lateral strips within both groups. The skin-fat strength decreased with age in the non-diabetic group ($p<0.00$, Fig 1), but this trend did not exist in the diabetic group.

	Diabetic group (n=21)		Non-diabetic group(n=17)	
	Medial	Lateral	Medial	Lateral
Row 1	32.2±6.7	38.2±10.6	31.9±13.6	30.8±9.6
Row 2	33.2±9.2	36.1±12.7	29.0±9.4	30.4±7.9
Row 3	30.7±8.7	31.2±11.4	26.0±8.5	25.1±9.3
Row 4	28.1±8.0	28.7±9.1	24.7±8.6	24.4±10.5
Row 5	26.1±7.5	26.4±7.1	22.5±7.7	24.4±10.5
Row 6	28.3±9.5	29.6±7.8	22.7±7.9	24.4±9.5
Row 7	32.7±10.0	31.9±9.0	24.5±8.7	26.5±9.8
Row 8	34.4±9.9	34.2±10.7	29.3±8.9	27.7±10.2
Row 9	46.7±16.5	42.5±15.3	35.9±14.4	34.7±13.9

Table 1. The mean and standard deviation for the mean skin-fat strength (N/cm) at different regions across the plantar surface of the foot.

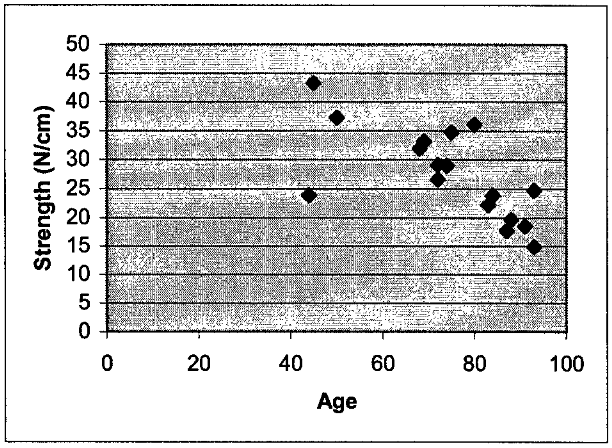

Fig 1. Skin-fat interface strength vs age in the non-diabetic group.

DISCUSSION

This experiment demonstrated that the strength of the skin-fat interface in the diabetic group was higher than in the non-diabetic group. Due to tissue property changes and bone deformity, diabetic patients usually experience elevated vertical stress at the foot-ground interface. The strength of the skin-fat interface might be an adaptive response to this elevated vertical stress. The trend with age in the non-diabetic group might also be explained by this assumption. In general, people become less active with age, which implies less stress under the foot, and thus lower skin-fat interface strength. In the diabetic group, as age increases, the stress concentration might be greater because of changes taking place in the foot due to diabetes, thus the decreasing trend with age did not exist in the diabetic group.

REFERENCES

Thompson, D.L (1997). *Finite Element Modeling of the Diabetic Foot.* Unpublished Master's Dissertation, Ohio State University.

EFFECTS OF DIABETES ON THE STRENGTH OF THE PLANTAR SKIN-FAT INTERFACE

Yan Chen*+, Brian L. Davis+, Antonio Valdevit+
*Cleveland State University and +The Cleveland Clinic Foundation, Cleveland, Ohio

INTRODUCTION

Foot ulceration is one of the most common complications of diabetes mellitus. Research has suggested that the plantar skin–fat interface may be the site for initial ulcer formation since peak first principal stresses (Figure 1) at this location dramatically increase with changes in material properties and boundary conditions (Thompson, 1997). What is not clear, however, is whether patients with diabetes have a skin-fat interface that is (i) less capable of withstanding elevated stresses, or (ii) has adapted to higher stresses and is more capable of withstanding these stresses.

The goal of this study was to compare the skin-fat interface strength in diabetic and non-diabetic feet.

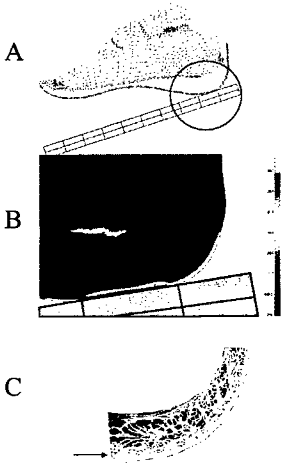

Figure 1. Previous finite element modeling has suggested that plantar skin stiffening leads to elevated stresses at the skin-fat interface. This "interface" comprises strands of connective tissue that, if stiffer, could make the skin more tightly adherent to the subcutaneous layers but, if damaged, could more easily lead to "skin delamination"

HYPOTHESIS

Due to either non-enzymatic glycation or adaptation to higher plantar pressures, it was hypothesized that skin samples taken from cadaveric diabetic donors would have a skin-fat interface that would be more difficult to disrupt with mechanical forces.

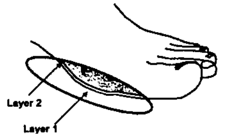

Figure 2. Since most diabetic ulcers occur in the forefoot and midfoot regions, these areas were the focus of the current investigation.

PROCEDURE

•21 diabetic (68±2.4 years) and 17 non-diabetic (74.6±3.8 years) foot specimens were studied.

•For each specimen, the plantar skin surface was cut into a 9x2 array from the first metatarsal head (row 1) to the anterior heel (row 9) and divided down the medial/lateral axis (Figure 3).

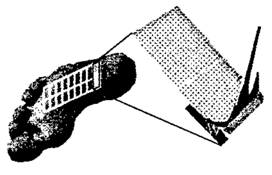

Figure 3. The plantar surface on each foot was cut into 18 strips, in a 2 x 9 array. The medial edge of each strip was attached to a claw grip which was connected to the actuator of an MTS testing machine.

- Each strip of skin was 1 cm wide and 2 mm deep. The skin was clamped to a load cell and tension was applied at a rate of 1 mm/sec as the skin was peeled off the underlying fat tissue.

•During testing the foot specimen was held in a supine position in a custom designed jig.

- The jig was placed on top of a transitional unit that could move in both x and y directions to keep the peeling force vertical to the peeling site (Figure 4). This unit was then mounted on a universal MTS machine.

•The mean peeling force (Figure 5) over the entire removal process was calculated and normalized to the width of the skin strip (i.e. F=N/cm).

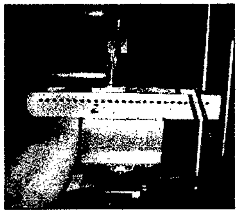

Figure 4. A jig was used to rigidly attach the foot to the MTS machine. Note the dovetail mortice beneath the jig that allowed each foot to be positioned directly under the MTS actuator for each strip that was tested.

•A two-way ANOVA model was utilized (diabetic versus control and medial versus lateral) with age as a covariate for the statistical analyses.

RESULTS

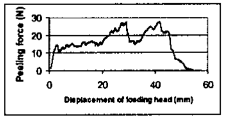

Figure 5. Representative force-displacement data for one peeling test.

- The strength of the skin-fat interface was significantly different (p<0.05) with the diabetic strips requiring greater skin removal force (Table 1).
- There was no significant difference between medial and lateral strips within both groups (Figure 6).
- The skin-fat strength decreased with age in the non-diabetic group (p=0.016, Figure 7), but this trend did not exist in the diabetic group.
- The strength of the skin-fat interface was significantly higher in forefoot and heel region and lower in the mid-arch region (p < 0.01)
- There was a positive correlation between the strength of the skin-fat interface and the thickness of the skin at the site (p<0.0001)

Table 1. The mean and standard deviation for the mean skin-fat strength (N/cm) at different regions across the plantar surface of the foot.

	Diabetic group (n=21)		Non-diabetic group (n=17)	
Row	Medial	Lateral	Medial	Lateral
1	32.2±6.7	38.2±10.6	31.9±13.6	30.8±9.6
2	33.2±9.2	36.1±12.7	29.0±9.4	30.4±7.9
3	30.7±8.7	31.2±11.4	26.0±8.5	25.1±9.3
4	28.1±8.0	28.7±9.1	24.7±8.6	24.4±10.5
5	26.1±7.5	26.4±7.1	22.5±7.7	24.4±10.5
6	28.3±9.5	29.6±7.8	22.7±7.9	24.4±9.5
7	32.7±10.0	31.9±9.0	24.5±8.7	26.5±9.8
8	34.4±9.9	34.2±10.7	29.3±8.9	27.7±10.2
9	46.7±16.5	42.5±15.3	35.9±14.4	34.7±13.9

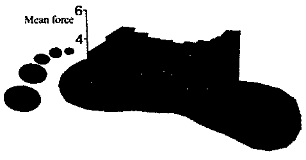

Figure 6. Combined (diabetic and control) data for all foot regions.

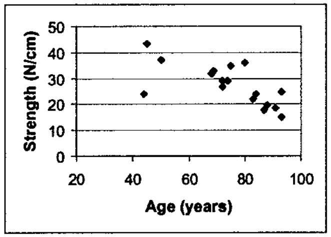

Figure 7. Skin-fat interface strength vs age in the non-diabetic group

DISCUSSION

- While it is known diabetes results in an accumulation of advanced glycation endproducts (AGEs) in skin (Kohn, Cerami, Monnier, 1984), and that these lead to tissue stiffening (Reihsner and Menzel, 1998), it is unclear what effect diabetes has on the skin-fat interface.
- In this study, the variable of interest was the mean force required to peel the dermis off of the underlying subcutaneous tissue. This variable is less susceptible to the influence of a few collagenous strands (Figure 1c) that result in localized peaks (Figure 5) in the data.

•The skin-fat interface strength in the forefoot and heel regions was higher than in the mid-arch region of foot. This finding suggests a "skin equivalent" to Wolff's Law for bone, i.e., higher stresses lead to stronger tissue.

•The high strength areas are of clinical importance since in diabetic patients these areas are prone to ulceration.

•The fact that, for non-diabetic specimens, age was negatively associated with the force required to peel off the skin is likely due these older individuals being less active and therefore placing less stress on their skin. It is noteworthy that this age dependency did not hold for diabetic tissue, and this could be due to the fact that patients with diabetes tend to place higher loads on their plantar skin surface (Cavanagh, Ulbrecht and Caputo, 2000).

- It is important to note that the data collected in this study were obtained from regions of the foot where the skin surface was intact. Thus, if the skin-fat interface was compromised by the presence of an ulcer, that region was not tested.

CONCLUSIONS

- This study has demonstrated that patients with diabetes have a skin-fat interface that is more difficult to disrupt in peeling tests.

•Furthermore, in these patients the age-dependent decline in interface strength is likely offset by higher stresses at the foot-ground interface.

REFERENCES

- Cavanagh PR, Ulbrecht JS, Caputo GM. (2000). New developments in the biomechanics of the diabetic foot. Diabetes Metab Res Rev;16 Suppl 1:S6-S10.

•Kohn RR, Cerami A, Monnier VM. (1984). Collagen aging in vitro by nonenzymatic glycosylation and browning. Diabetes, 33(1): 57-9.

- Reihsner R, Menzel EJ. (1998). Two-dimensional stress-relaxation behavior of human skin as influenced by non-enzymatic glycation and the inhibitory agent aminoguanidine. Journal of Biomechanics, 1(11): 985-93
- Thompson, D.L (1997). Finite element modeling of the diabetic foot. Unpublished master's dissertation, Ohio State University

ACKNOWLEDGEMENTS

•The authors acknowledge funding provided by the United States Department of Defense. Assistance in specimen preparation was provided by S. Solomon Praveen.

ORTHOPEDIC PATHOLOGY AND BIOMATERIALS LABORATORY

DEPARTMENT OF ANATOMIC PATHOLOGY
THE CLEVELAND CLINIC FOUNDATION
CLEVELAND, OHIO

CCF Reference Numbers: R01-917, 974

EVALUATION OF HYALURONIC ACID BASED MATRICES FOR BONE HEALING APPLICATIONS

Daisuke Togawa, MD, PhD
Thomas W. Bauer, MD, PhD

Departments of Orthopaedic Surgery and Pathology, L-25
The Cleveland Clinic Foundation
Cleveland, Ohio

George F. Muschler, MD
Hidetake Takigami, MD, PhD

Department of Biomedical Engineering, ND-
The Cleveland Clinic Foundation
Cleveland, Ohio

Technical Assistance: Ms. Diane Mahovlic

The Cleveland Clinic Foundation
Cleveland, Ohio

Draft of August 23, 2002

PURPOSE: The purpose of this study is to evaluate the extent of bone graft incorporation of cross-linked hyaluronic acid based matrix using a canine femoral defect model.

METHODS:

Graft Material Preparation

A cross-linked hyaluronic acid based matrix produced by BioMatrix (Ridgefield, NJ) was used as a preparation of beads with a mean diameter of 1,000 um. This graft material was approximately 0.95 cm in diameter X 1.0 cm long.

Graft Implantation

Two canines were used in this experiment. Four identical 1.0 cm diameter and 1.5 cm long cylindrical defects were created in the canine proximal femur using a template fixed with proximal and distal screw. Each defect was separated by 1.5 cm of normal marrow. These 4 defects were designated A, B, C, and D, respectively, from proximal to distal. Graft material prepared with dimensions of 0.95 cm diameter and 1.0 cm in height were placed in 2 defects in each femur. No graft material was implanted in the other 2 defects in the same femur (Table 1).

Table 1 Graft Preparation for Each Defect

CCF #	Dog #	Duration	Defect			
			A	B	C	D
R01-917	01D-271	1W	HA	Empty	HA	Empty
R01-974	01D-331	2W	Empty	HA	Empty	HA

Histological Preparation

The specimens were cut sagittaly at the middle of the defect cylinder (cut axially against the defect cylinder), and fixed in formalin. Half of each specimen was dehydrated in alcohols and embedded in Spurr's plastic without decalcification. The reminder of each specimen was dehydrated in a graded series of alcohols, decalcified, and embedded in paraffin. Sections were stained with Giemsa (undecalcified) or hematoxylin and eosin (decalcified).

Histological Evaluation

The sections were reviewed qualitatively, and the approximate areas occupied by HA remnant, voids, fibrosis, hematoma, and bone in the defect were visually estimated.

RESULTS:

Post Op. 1W (R01-917)

Macro Images

Giemsa

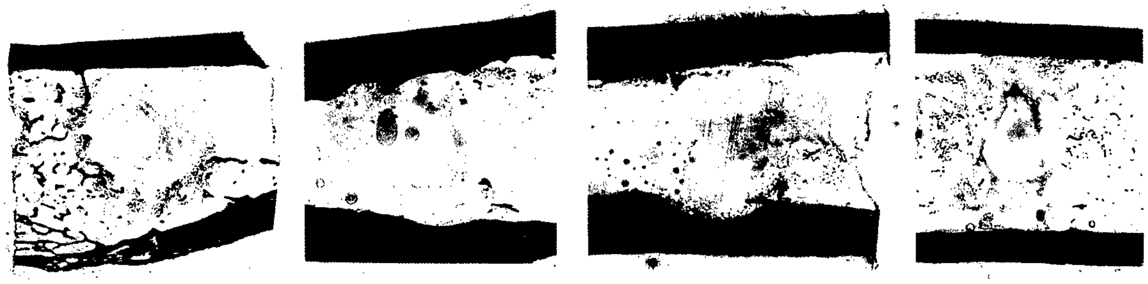

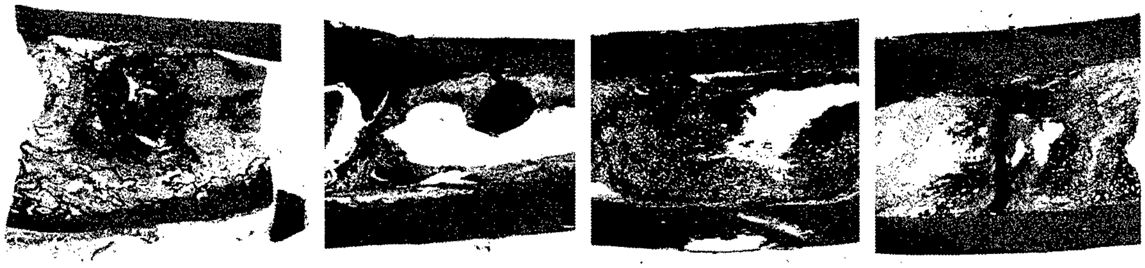

H & E

Figs 1~8. Low magnification photos showing axial sections of the 4 defects. Tissue processing with decalcification made the sections shrink, and most of the hyaluronic acid based matrices (HA) were lost. The areas occupied by HA appear as either a void or were replaced by adjacent tissue. The approximate area occupied by HA remnant, voids, fibrosis, hematoma, and bone in the each defect was mostly evaluated in the un-decal sections (above; Giemsa stain (undecal), below; H & E stain (decal)).

Microscopic Images

Hylan B Group (A and C)

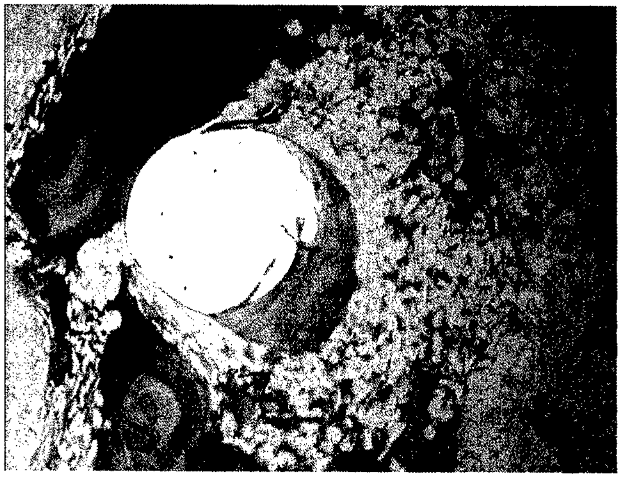

Fig 9. Low magnification showing the center hole of defect A, suggesting the position of oxygen tension sensor. The adjacent area was occupied by either hematoma or HA beads.

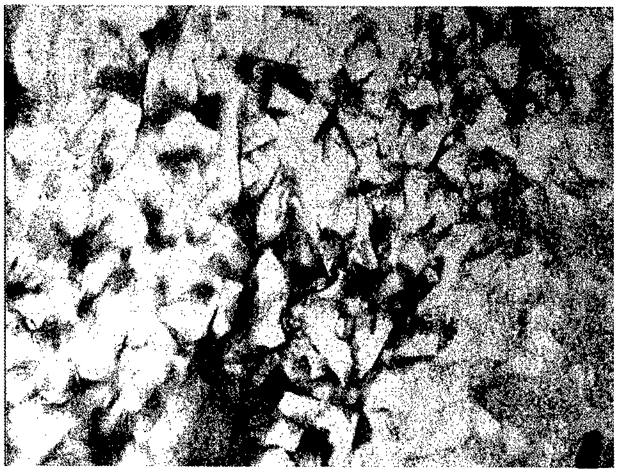

Fig 10. Higher magnification of HA beads adjacent to the canter hole. These HA beads occupied approximately 65 % of the defect area. Hematoma was present among these HA beads.

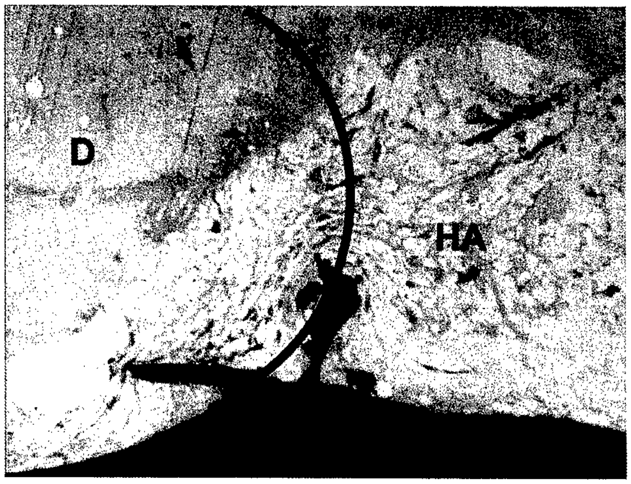

Fig 11. Low magnification of the section of the defect C. The cortical defect (below) suggests the margin of the original defect (D)(red line). The HA beads (HA) were located both inside and outside of the defect.

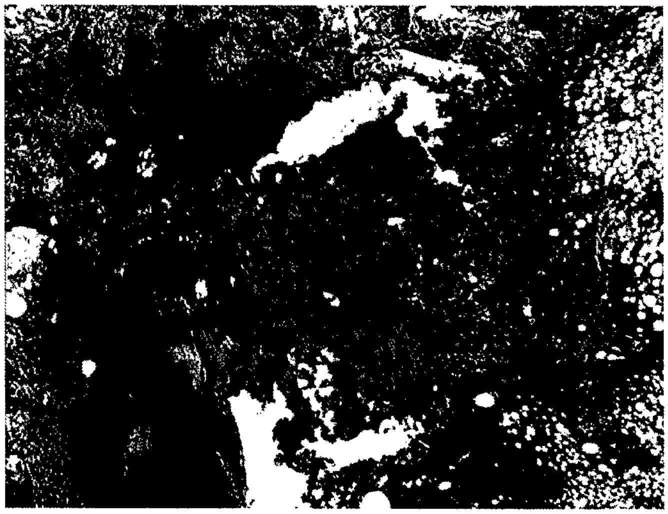

Fig 12. Low magnification showing the areas of HA remnant, hematoma, void, and fibrous marrow in the defect. Some of the HA beads observed in the un-decal section were lost, presumably due to the process of decalcification.

Fig 13. Higher magnification showing each piece of HA beads remnant in the hematoma area of the defect A.

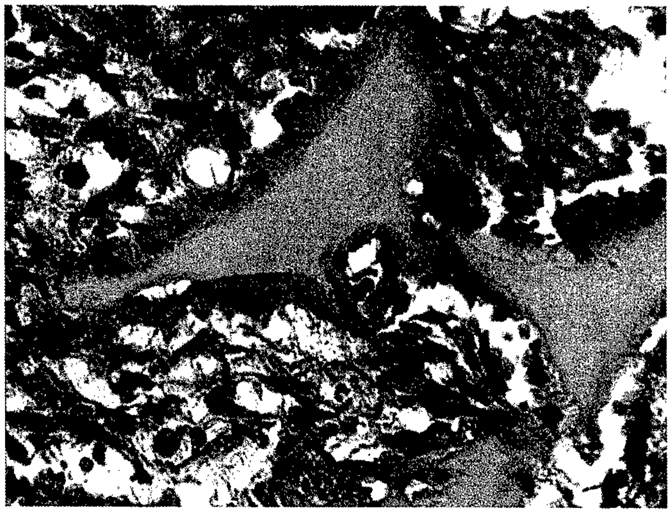

Fig 14. Very high magnification showing pieces of HA beads. A lot of macrophages were present associated with HA beads, suggesting the process of HA beads resorption.

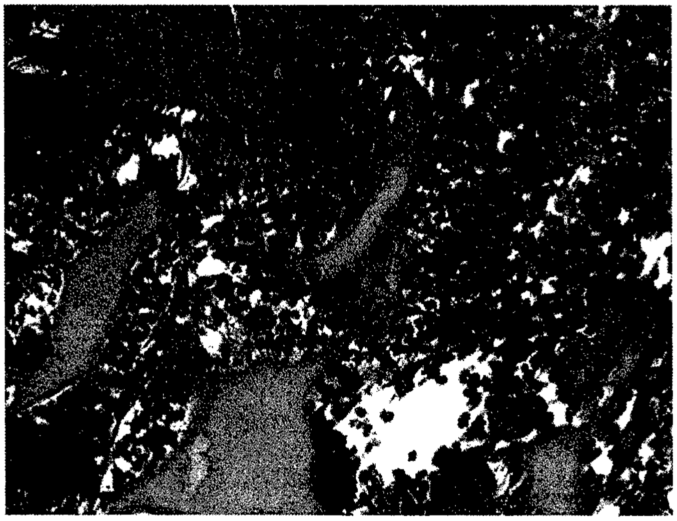

Fig 15. In a few areas acute inflammatory cells were present associated with HA beads.

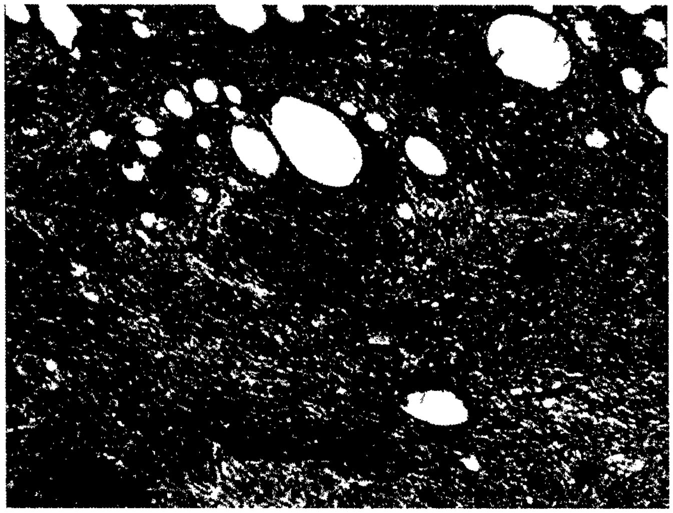

Fig 16. The site also contained fibrosis, with fibrous tissue occupying approximately 50% of defect C, and 10% of defect A.

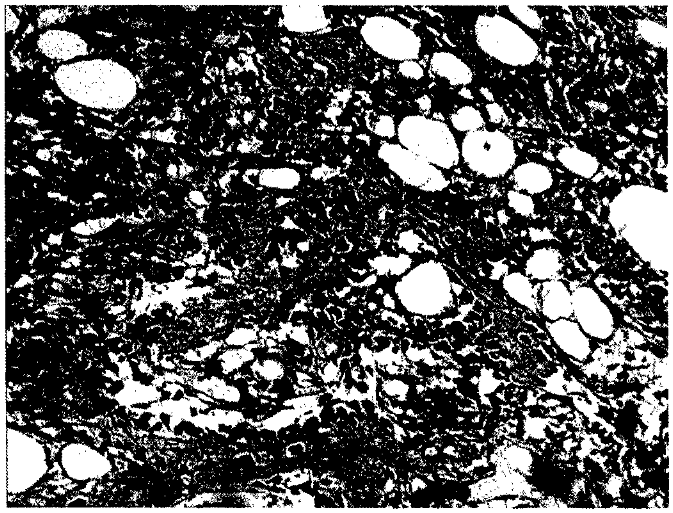

Fig 17. The area outside of the fibrosis showed new bone formation, with osteoblasts and woven bone in the area immediately outside of the defect.

Empty Defect Group (B and D)

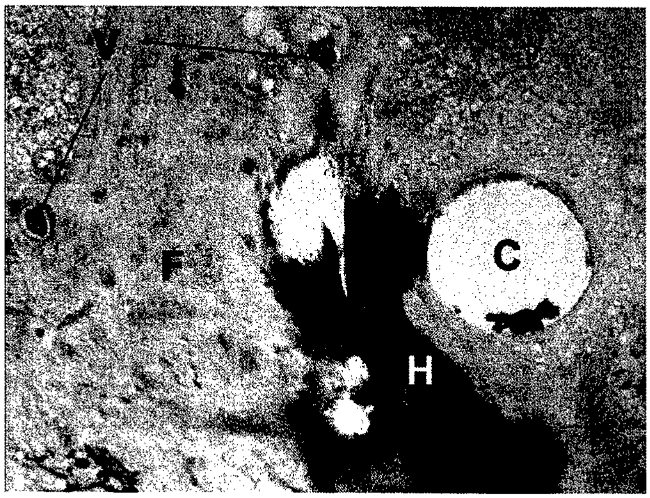

Fig 18. Low magnification showing the center hole (C) of the defect B. Hematoma (H) and fibrosis (F) occupied most of the defect area. Small vascular spaces (V) were also present outside of the defect.

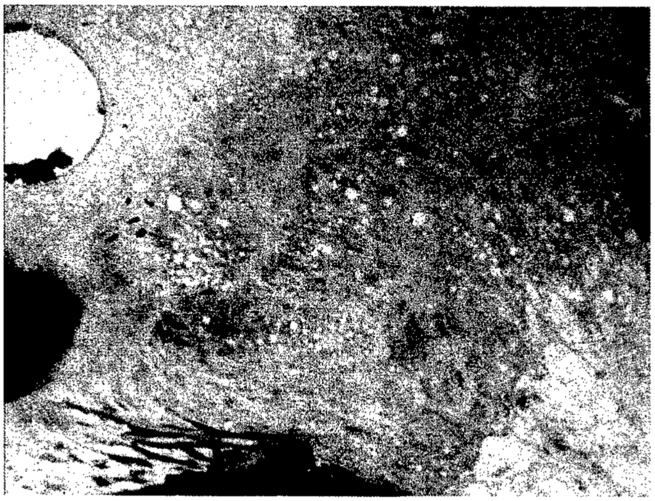

Fig 19. Extensive fibrous tissue formation was present adjacent to the center hole of the defect.

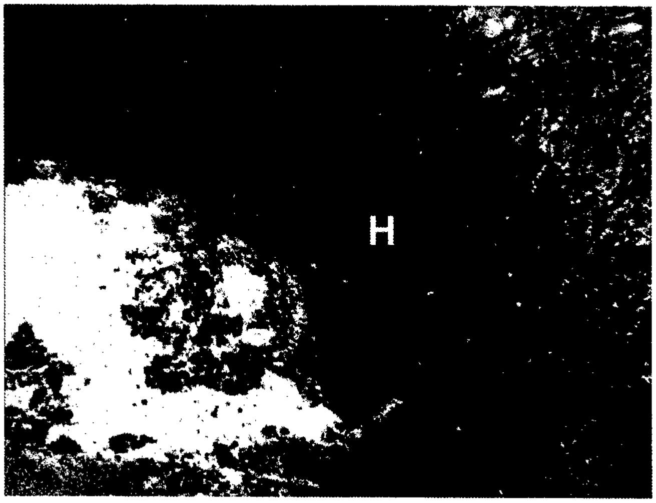

Fig 20. Large area of the hematoma (H) was present in this section of defect B.

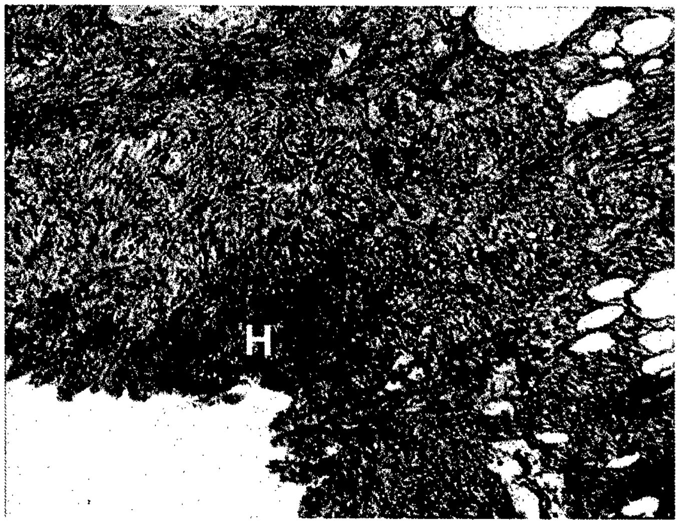

Fig 21. Extensive fibrous tissue (FT) was present close to the center of the defect. Hematoma (H) was surrounded by fibrous tissue, suggesting that the hematoma was partially resorbed and re-organized.

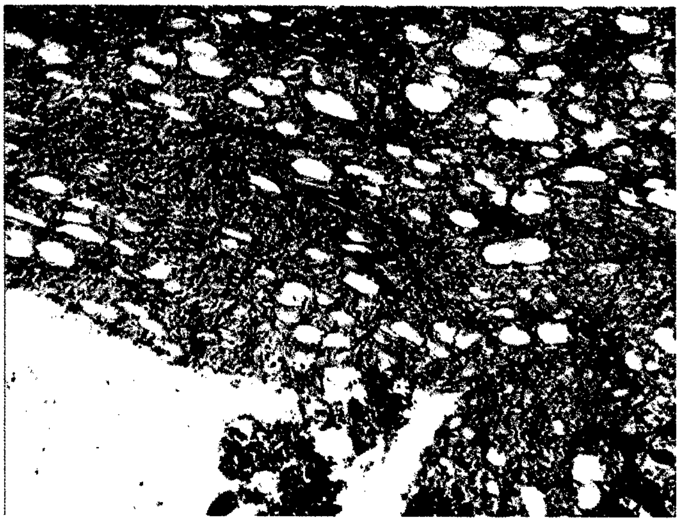

Fig 22. Fibrous marrow was present adjacent to the void in the defect. There was no acute inflammation in any of the empty defects.

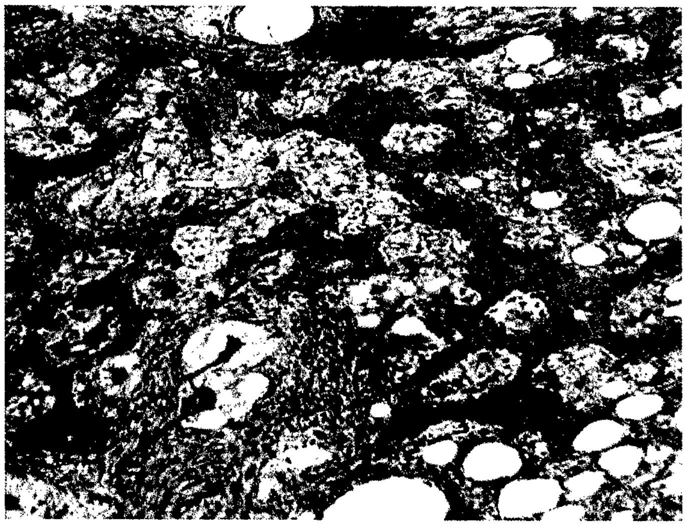

Fig 23. Outside of the area of fibrosis, extensive new bone formation was present,

Post Op. 2W (R01-974)

Macro Images

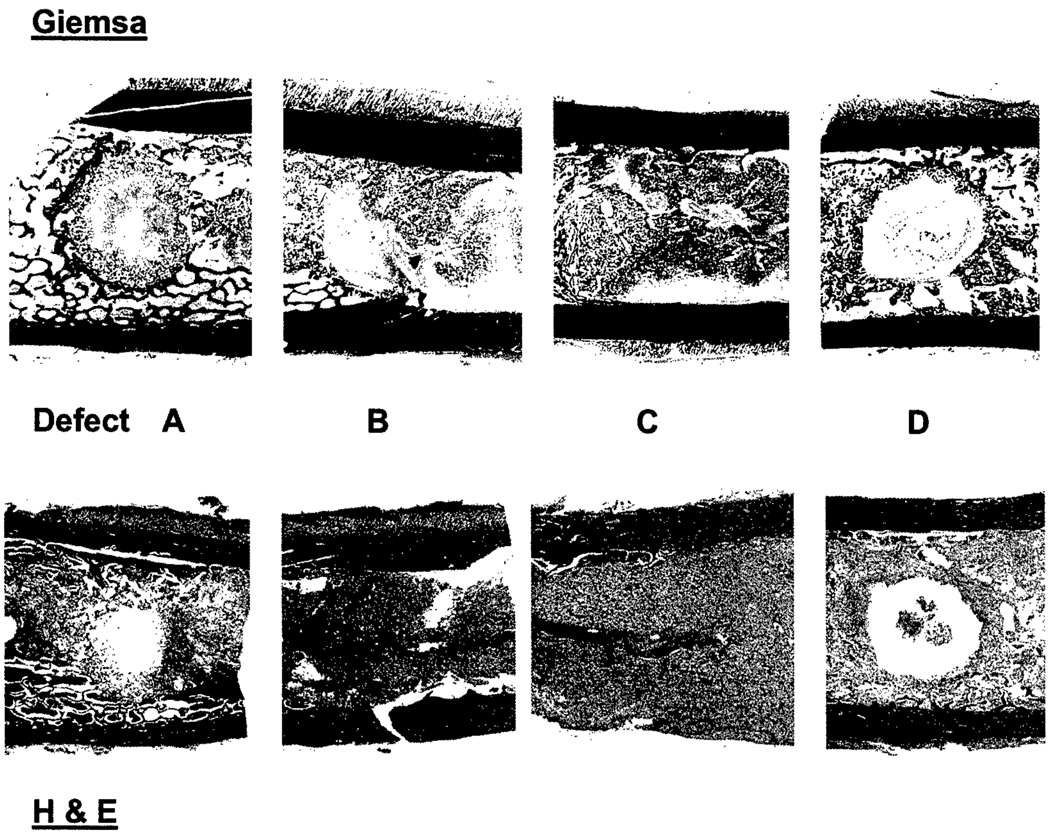

Fig 24~31. Photomicrographs of axial sections of the specimens retrieved at 2 weeks after surgery. The margins of defects A and D were relatively easily to recognize. The areas of cancellous bone were more prominent in these 2-week specimens than those in the 1 week specimens. Hematoma occupied less area in each defect than at 1 week.

Microscopic Images

Hylan B Group (B and D)

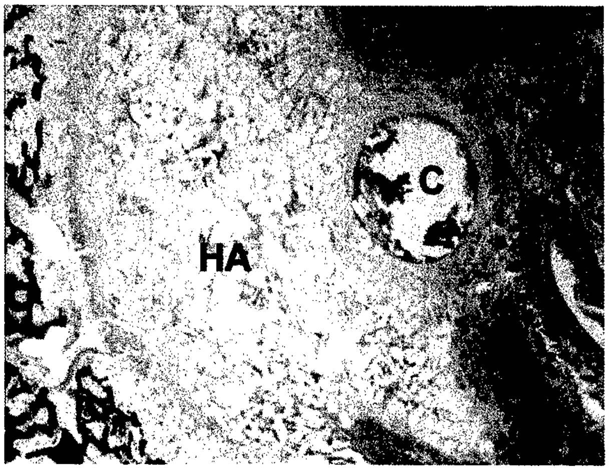

Fig 32. Low magnification showing the center hole (C) of defect B. Although this section was 2 weeks after surgery, about half of the area (left, lower) of the defect was still occupied by mostly HA remnant (HA).

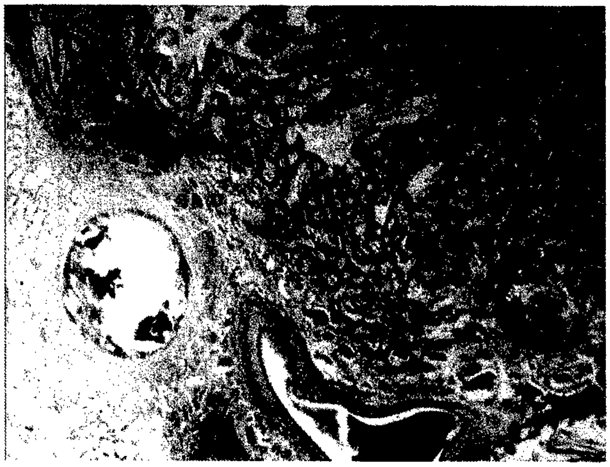

Fig 33. Other half area was occupied mostly by new bone, formed centripetally towards the center hole. Fibrous tissue was present between the new bone and the center hole.

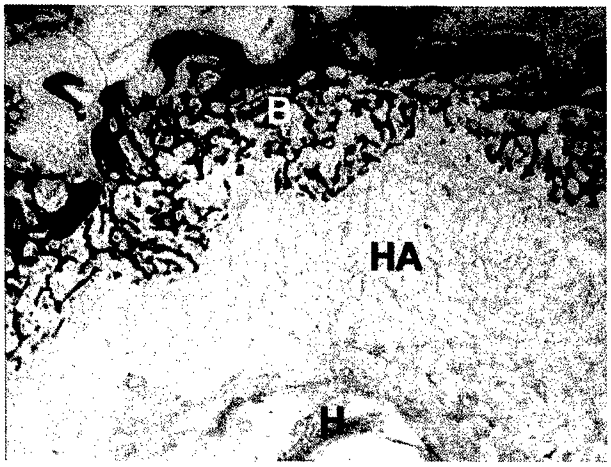

Fig 34. The area of HA remnant (HA) occupied approximately 40% of the defect area. New bone formation (B) was present along the margin of the defect. Only a small area was occupied by hematoma (H) close to the center hole.

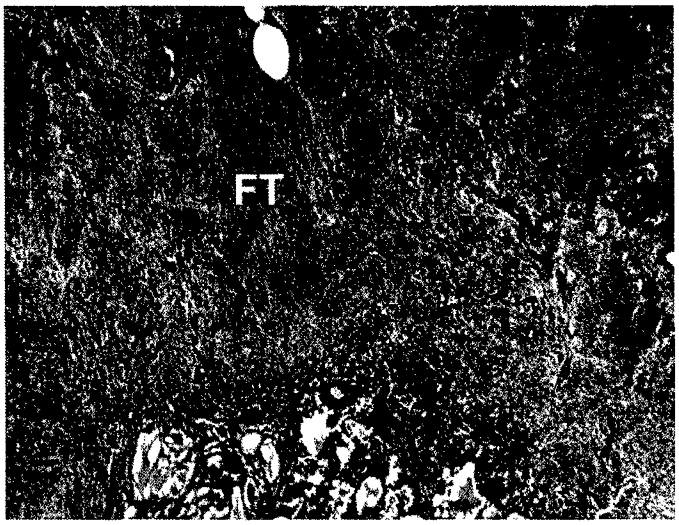

Fig 35. Fibrosis (FT) occupied approximately 15% of the defect area.

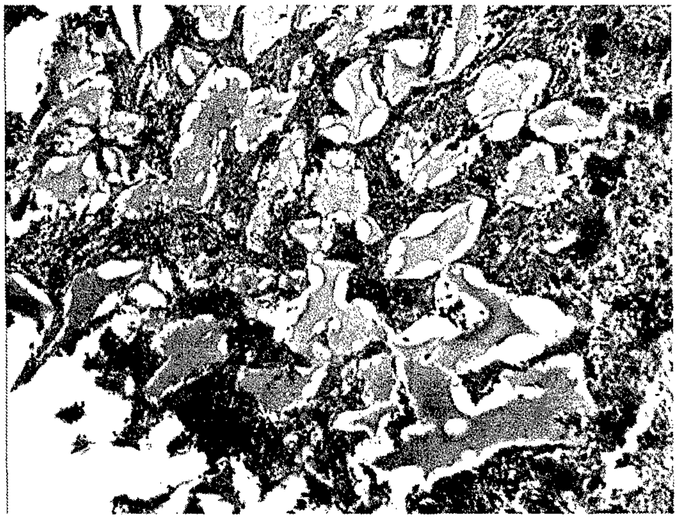

Fig 36. HA remnant was still present, but not in a distinctive bead form. Each piece of HA was surrounded by fibrous bone marrow, giant cells, and macrophages (see below, Figs 37 and 38).

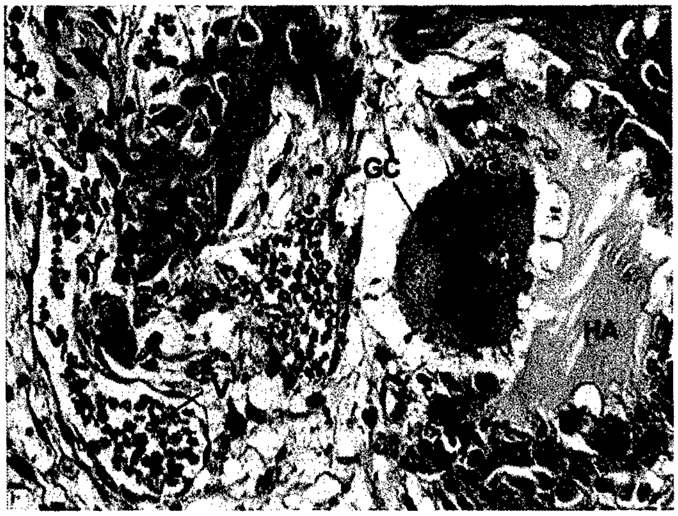

Fig 37. High magnification showing giant cell (GC) associated with HA remnant (HA). A lot of small vessels (V) were also present in the area adjacent to new bone formation.

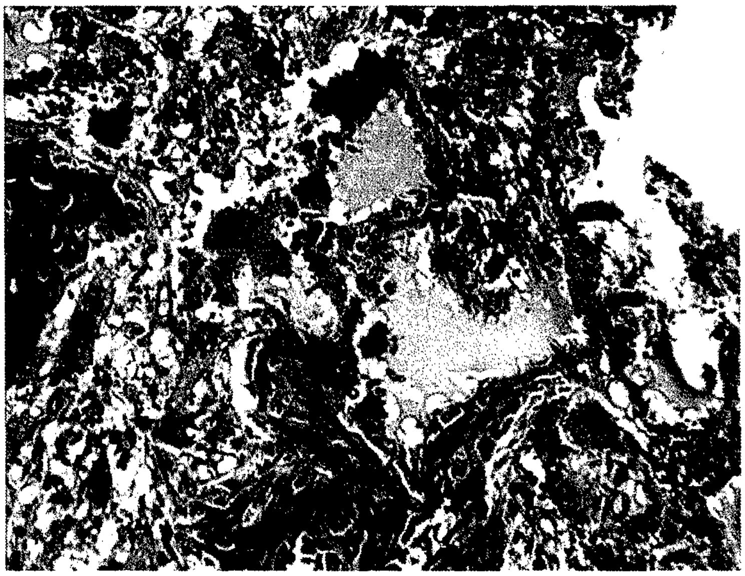

Fig 38. A number of macrophages and giant cells were associated with HA pieces. New bone formation was present even adjacent to the giant cells.

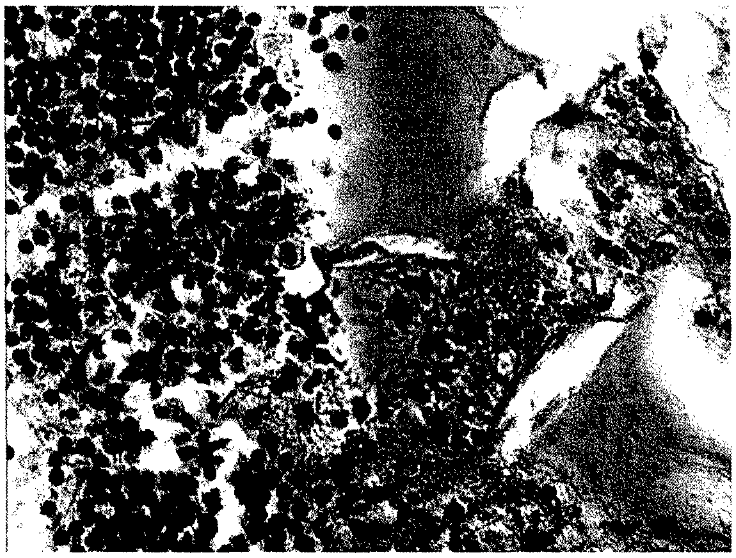

Fig 39. In a few areas neutrophils were associated with HA remnants.

Empty Defect Group (A and C)

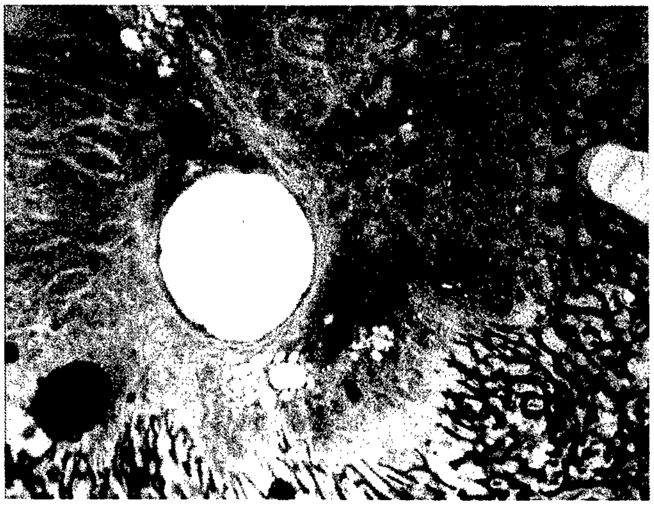

Fig 40. Photomicrograph showing the center hole of defect A at 2 weeks after surgery. The hole was surrounded mostly by fibrous tissue. New bone formation was present from the margin of the defect towards to the center.

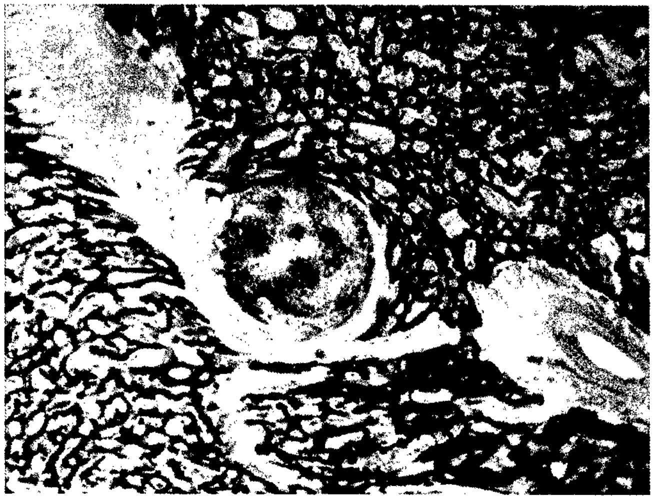

Fig 41. Low magnification showing the center hole of defect C. Most of this defect was occupied by bone. The approximate area occupied by bone in this defect was 70%.

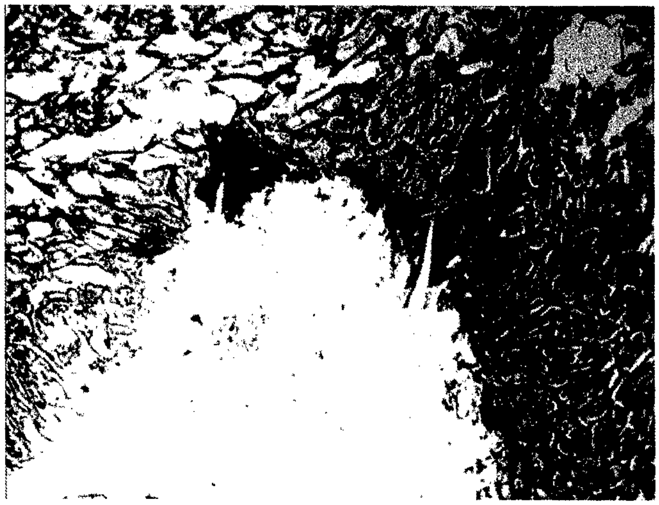

Fig 42. Low magnification of defect A. The tissue adjacent to the center hole was lost. Extensive new bone formation was present outside of the defect.

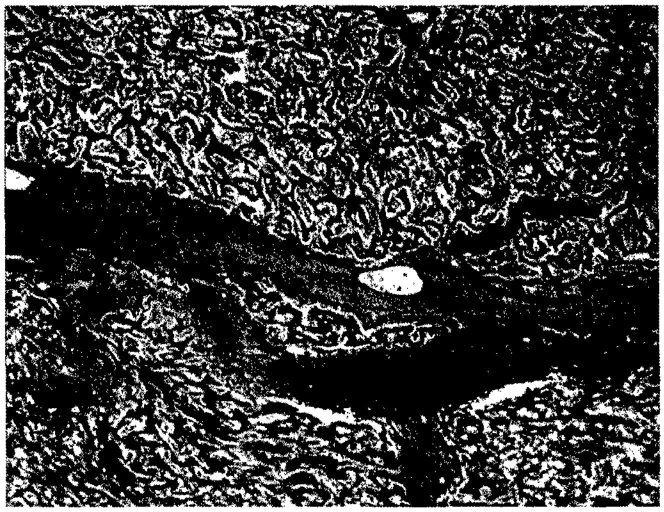

Fig 43. Fibrosis associated with the center hole of defect C was present, but the defect was mostly occupied by extensive new bone formation.

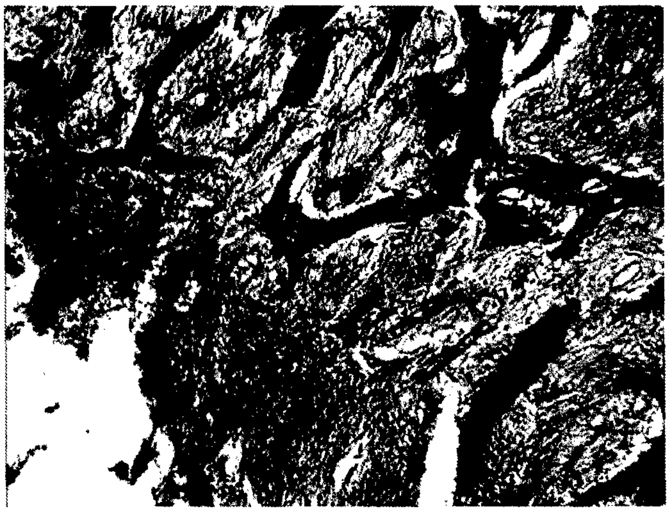

Fig 44. Outside of defect A, new cancellous bone formation was present along the margin of the defect.

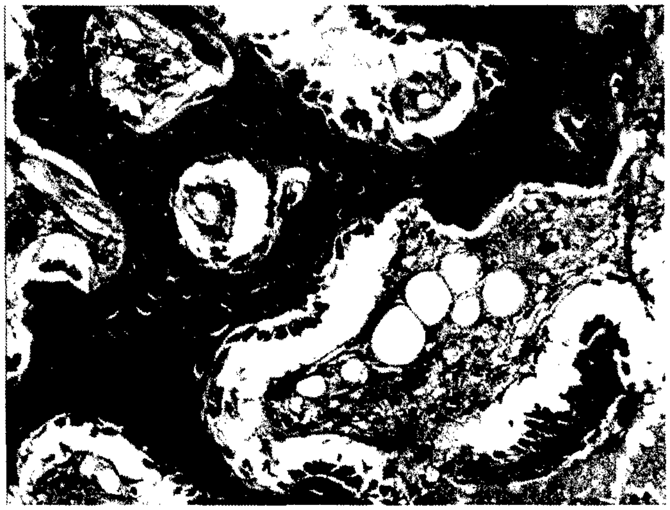

Fig 45. Higher magnification of bone in the defect. A number of osteoblasts were present along the edge of the bone, suggesting extensive new bone formation.

Summary:

Table 2 Histology of the Defect Area

CCF #	Defect	HA Remnant	Voids	Fibrosis	Hematoma	Bone	Inflammation
R01-917	A	65	5	10	20	0	(+)
	B	no HA	20	50	30	0	(-)
	C	30	10	50	10	0	(+)
	D	no HA	15	45	40	0	(-)
R01-974	A	no HA	10	55	5	30	(-)
	B	40	10	15	5	30	(-)
	C	no HA	5	20	5	70	(-)
	D	60	10	10	10	10	(+)

Discussion and Conclusions:

The purpose of this study was to define the baseline performance of Hylan B in the femoral defect model. There were some limitations of this study. Since Hyaluronic acid-based materials are difficult to fix for histology, it was very difficult to cut the specimens with a band saw to keep the materials in the defects. They often fell out of the defect during sectioning, especially of the one-week specimens. Also the routine tissue processing with decalcification caused some shrinkage of the HA materials as well as adjacent tissues, making it difficult to estimate the percent area occupied by each tissue type.

Based on these samples, our histological analysis illustrates the following findings:

1. Most of the hyaluronic acid-based materials remained in the defect until 2 weeks after surgery, although some were partially absorbed or dissolved in vivo. Giant cells and macrophages were associated with these materials, suggesting active cellular resorption.

2. New bone formation was prominent in 2-week specimens, and extended from the outside margin towards to the center of the defect (in both controls and the HA defects)

3. Most of the hematoma was re-organized and by 2 weeks after surgery.

4. Focal acute inflammation was present associated with hyalulonic acid-based beads in the three of four HA-containing defects. The significance of this acute

inflammation is unclear, but either infection or a fundamental issue of biocompatibility should be considered.

Thomas W. Bauer, MD, PhD
Departments of Orthopaedic Surgery and Pathology
The Cleveland Clinic Foundation
9500 Euclid Avenue
Cleveland, Ohio 44195, USA

DEPARTMENT OF DEFENSE
UNITED STATES OF AMERICA

DEPARTMENT OF THE ARMY
US ARMY MEDICAL RESEARCH AND MATERIEL COMMAND
504 SCOTT STREET
FORT DETRICK, MD 21702-5012

REPLY TO
ATTENTION OF

MCMR-RMI-S (70-1y) 15 May 03

MEMORANDUM FOR Administrator, Defense Technical Information Center (DTIC-OCA), 8725 John J. Kingman Road, Fort Belvoir, VA 22060-6218

SUBJECT: Request Change in Distribution Statement

1. The U.S. Army Medical Research and Materiel Command has reexamined the need for the limitation assigned to technical reports written for this Command. Request the limited distribution statement for the enclosed accession numbers be changed to "Approved for public release; distribution unlimited." These reports should be released to the National Technical Information Service.

2. Point of contact for this request is Ms. Kristin Morrow at DSN 343-7327 or by e-mail at Kristin.Morrow@det.amedd.army.mil.

FOR THE COMMANDER:

Phyllis Rinehart

Encl

PHYLLIS M. RINEHART
Deputy Chief of Staff for
Information Management

ADB266022
ADB260153
ADB272842
ADB283918
ADB282576
ADB282300
ADB285053
ADB262444
ADB282296
ADB258969
ADB269117
ADB283887
ADB263560
ADB262487
ADB277417
ADB285857
ADB270847
ADB283780
ADB262079
ADB279651
ADB253401
ADB264625
ADB279639
ADB263763
ADB283958
ADB262379
ADB283894
ADB283063
ADB261795
ADB263454
ADB281633
ADB283877
ADB284034
ADB283924
ADB284320
ADB284135
ADB259954
ADB258194
ADB266157
ADB279641
ADB244802
ADB257340
ADB244688
ADB283789
ADB258856
ADB270749
ADB258933

ADB265793
ADB281613
ADB284934
ADB263442
ADB284977
ADB263437
ADB265310
ADB281573
ADB250216
ADB258699
ADB274387
ADB285530